FIRST-PRINCIPLES STUDY OF MECHANICAL, ELECTRONIC, MAGNETIC AND OPTICAL PROPERTIES OF SELECTED SINGLE AND DOUBLE PEROVSKITES

A DISSERTATION SUBMITTED TO THE

CENTRAL DEPARTMENT OF PHYSICS

INSTITUTE OF SCIENCE AND TECHNOLOGY

TRIBHUVAN UNIVERSITY

NEPAL

FOR THE AWARD OF

DOCTOR OF PHILOSOPHY

IN PHYSICS

BY

PESHAL POKHAREL

JULY 2026

FIRST-PRINCIPLES STUDY OF MECHANICAL, ELECTRONIC, MAGNETIC AND OPTICAL PROPERTIES OF SELECTED SINGLE AND DOUBLE PEROVSKITES

A DISSERTATION SUBMITTED TO THE

CENTRAL DEPARTMENT OF PHYSICS

INSTITUTE OF SCIENCE AND TECHNOLOGY

TRIBHUVAN UNIVERSITY

NEPAL

FOR THE AWARD OF

DOCTOR OF PHILOSOPHY

IN PHYSICS

BY

PESHAL POKHAREL

JULY 2026

TRIBHUVAN UNIVERSITY

Institute of Science and Technology

DEAN'S OFFICE

Kirtipur, Kathmandu, Nepal

Reference No.:

Institute of Science & Technology Dean's Office Kirtipur 2045

30 July, 2026

EXAMINERS

The Title of Ph.D. Dissertation: "First-Principles Study of Mechanical, Electronic, Magnetic and Optical Properties of Selected Single and Double Perovskites"

Name of Candidate: Peshal Pokharel

External Examiners:

1. Prof. Dr. Indra Bahadur Karki
   Retered Prof. Patan Multiple Campus
   Lalitpur, NEPAL

2. Prof. Dr. Prasenjit Sen
   Harish Chandra Research Institute
   Prayagraj, INDIA

3. Dr. Indra D. Sahu
   Campbellsville University
   Campbellsvile, Kentucky, USA

(Dr. Komal Raj Rijal)
Asst. Dean

DECLARATION

Dissertation entitled **"First–Principles Study of Mechanical, Electronic, Magnetic, and Optical Properties of Selected Single and Double Perovskites"** which is being submitted to the Central Department of Physics, Institute of Science and Technology (IoST), Tribhuvan University, Nepal, for the award of the degree of Doctor of Philosophy (Ph.D.), is a research work carried out by me under the supervision of Prof. Dr. Devendra Adhikari of Department of Physics, Mahendra Morang Adarsh Multiple Campus, Tribhuvan University, Biratnagar, Nepal, and co-supervised by Dr. Nurapati Pantha of Central Department of Physics, Tribhuvan University, Kirtipur, Kathmandu, Nepal and Dr. Shashit Kumar Yadav of Department of Physics, Mahendra Morang Adarsh Multiple Campus, Tribhuvan University, Biratnagar, Nepal.

This research is original and has not been submitted earlier in part or full in this or any other form to any university or institute, here or elsewhere, for the award of any degree. I hereby declare that approximately 5% of my dissertation content have been used with artificial intelligence help.

.....

Peshal Pokharel

RECOMMENDATION

This is to recommend that **Peshal Pokharel** has carried out research entitled **"First–Principles Study of Mechanical, Electronic, Magnetic and Optical Properties of Selected Single and Double Perovskites"** for the award of Doctor of Philosophy (Ph.D.) in **Physics** under our supervision. To our knowledge, this work has not been submitted for any other degree, elsewhere.

He has fulfilled all the requirements laid down by the Institute of Science and Technology (IoST), Tribhuvan University, Kirtipur for the submission of the dissertation for the award of Ph.D. degree.

.....

Prof. Dr. Devendra Adhikari
Supervisor
(Professor)
Mahendra Morang Adarsh Multiple Campus
Tribhuvan University
Biratnagar, Nepal

.....

Dr. Nurapati Pantha
Co-supervisor
(Associate Professor)
Central Department of Physics
Tribhuvan University
Kirtipur, Kathmandu, Nepal

.....

Dr. Shashit Kumar Yadav
Co-supervisor
(Assistant Professor)
Mahendra Morang Adarsh Multiple Campus
Tribhuvan University
Biratnagar, Nepal

July 2026

TRIBHUVAN UNIVERSITY
CENTRAL DEPARTMENT OF PHYSICS
Kirtipur, Kathmandu, Nepal

☎ 4331054
cdp.tu.edu.np

Ref. No.: (F. No … ……) CDP …… Date: .....

LETTER OF APPROVAL

Date: 23/02/2026

On the recommendation of **Prof. Dr. Devendra Adhikari**, Department of Physics, Mahendra Morang Adarsh Multiple Campus, Tribhuvan University, Biratnagar, Nepal, **Dr. Nurapati Pantha**, Central Department of Physics, Tribhuvan University, Kathmandu, Nepal, and **Dr. Shashit Kumar Yadav**, Department of Physics, Mahendra Morang Adarsh Multiple Campus, Tribhuvan University, Biratnagar, Nepal, this Ph.D. dissertation submitted by **Peshal Pokharel**, Central Department of Physics, Tribhuvan University, Kathmandu, Nepal, entitled **"First–Principles Study of Mechanical, Electronic, Magnetic and Optical Properties of Selected Single and Double Perovskites"** is forwarded by the Central Department Research Committee (CDRC) to the Dean, IoST, T.U.

Narayan

Dr. Narayan Prasad Adhikari
Professor and Head
Central Department of Physics,
Tribhuvan University
Kirtipur, Kathmandu
Nepal

ACKNOWLEDGMENTS

Firstly, I would like to express my immense gratitude to my research supervisor Prof. Dr. Devendra Adhikari, Mahendra Morang Adarsh Multiple Campus, Tribhuvan University, Biratnagar, Nepal and co-supervisors Dr. Nurapati Pantha, Central Department of Physics, Tribhuvan University, Kirtipur, Nepal and Dr. Shashit Kumar Yadav, Department of Physics, Mahendra Morang Adarsh Multiple Campus, Tribhuvan University, Biratnagar, Nepal for their supports, scientific as well as motivational inspirations, guidance, and mentorship to carry this research work.

I am thankful to Prof. Dr. Narayan Prasad Adhikari (HoD), Prof. Dr. Om Prakash Niraula (former HoD) for their help in completing this work. Similarly, I want to acknowledge Prof. Dr. Shankar Khanal, Dean of IoST, TU, and former Dean, Prof. Dr. Binil Aryal., Prof. Dr. Ishwor Koirala (Director, Research Directorate, TU). I thankfully acknowledge the CDRC members: Prof. Dr. Raju Khanal, Prof. Dr. Hari Prasad Lamichhane and Assoc. Prof. Dr. Balaram Ghimire. I gratefully acknowledge Prof. Dr. Dinesh Raj Bhuju (Mid–West University, Nepal), Assoc. Prof. Dr. Chitra Bd. Baniya (TU, Nepal), Prof. Dr. Nabaraj Khatiwada (NDRI, Nepal) for valuable academic courses and fruitful discussion. Furthermore, I would like to thank Assoc. Prof. Dr. Gopi Chandra Kaphle, Assoc. Prof. Dr. Madhav Prasad Ghimire, Assoc. Prof. Dr. Tika Ram Lamichhane, Dr. Rajendra Prasad Koirala, Dr. Hari Krishna Neupane, and Dr. Hari Shankar Mallik of the Central Department of Physics, Tribhuvan University, Kirtipur, Nepal for valuable suggestions and inspirations. I am also grateful to all the faculty members and nonteaching staffs of the department for their continuous motivational supports.

I would like to extend my special appreciation to Dr. Kapil Adhikari (Gandaki University, Pokhara, Nepal), Dr. Bikash Sharma (Sikkim Manipal Institute of Technology, Sikkim, India), Dr. Mohan Lal Barma (Chhattisgarh Swami Vivekanand Technical University, Bhilai, India), Associate Prof. Dr. Ram Prasad Koirala, Dr. Upendra Mehta, Dr. Ramesh Kumar Gohivar and Mr. Arjun Dhungana, of Department of Physics, Mahendra Morang Adarsh Multiple Campus, Tribhuvan University, Biratnagar, Nepal for their support and insightful suggestions.

I am grateful to the Campus Chief of Central Campus of Technology, Tribhuvan University, Dharan, Nepal for providing study leave during my research work. My sincere thanks also go to all teaching and nonteaching staffs of the Central Campus of Technology, Tribhuvan University, Dharan, Nepal and Mahendra Morang Adarsh Multiple

Campus, Tribhuvan University, Biratnagar, for their valuable suggestions and encouragement.

I am also thankful to my friends, Mr. Manoj Khanal, Mr. Netra Prasad Subedi, Mr. Dipendra Kumar Sah, Mr. Prabhakar Oli, Mr. Shambhu Sharma Bhandari, Mr. Prakash Neupane and other colleagues whose cooperation was very important during my Ph.D. work.

My sincere thanks go to Mrs. Sarita Adhikari for her continuous support, encouragement, and inspiration during this work.

For the love, understanding and support, I would like to thank my beloved wife Mrs. Pratiksha Khatiwada (Pokharel), daughter Miss Prasuna Pokharel and son Mr. Prerak Pokharel for support and good wishes during my ups and downs. Moreover, I would like to show my gratitude to my father-in-law Mr. Khilanath Khatiwada, mother-in-law Mrs. Sita Devi Khatiwada, brothers-in-law Mr. Pankaj and Mr. Pravab and sister-in-law Mrs. Pratima for their continuous support throughout the research period. Last but not least, I would like to show my immense gratitude to my father Mr. Narayan Pokharel for the encouragement and inspiration and my mother, Mrs. Sushila Devi for nurturing and standing by me in all ups and downs of my life.

Peshal Pokharel
July 2026

शोधसार

पेरोव्स्काइट (Perovskite) खनिज क्रिस्टल पदार्थ हो जसलाई सामान्यतया ABX_3 रासायनिक सूत्रद्वारा प्रतिनिधित्व गरिन्छ। यस्ता यौगिकहरूको सरल तथा नियमित ठोस क्रिस्टल संरचनाका कारण तिनीहरूमा संरचनात्मक (structural), यान्त्रिक (mechanical), चालकजन्य (electronic), चुम्बकीय (magnetic), तथा प्रकाशजन्य (optical) जस्ता रोचक भौतिक विशेषताहरू पाइन्छन, जसले गर्दा यी पदार्थहरू बहुआयामिक क्षेत्रमा उपयोगी हुने क्षमता राख्दछन्। यी पदार्थहरू ऊर्जा, अप्टोइलेक्ट्रोनिक, स्पिन्ट्रोनिक, डाटा भण्डारण, सेन्सर तथा उच्च तापक्रमीय उपकरणहरूमा व्यापक रूपमा प्रयोग गरिन्छ। प्रस्तुत शोधकार्यमा आधारभूत सूचनामा आधारित गणितीय मोडेल (first principles calculation) अन्तर्गत इलेक्ट्रोनिक घनत्वमा आधारित गणितीय सिद्धान्त (Density Functional Theory) प्रयोग गरी पेरोव्स्काइट सामग्रीहरू जिरकोनियम सिलिकेट ($ZrSiO_3$), समेरियम म्याङ्गनाइट ($SmMnO_3$) तथा स्ट्रन्टियम जिरकोनियम मोलिब्डेनम अक्साइड (Sr_2ZrMoO_6) का संरचनात्मक, चालकजन्य, चुम्बकीय, यान्त्रिक तथा प्रकाशजन्य गुणहरूको अध्ययन गरिएको छ। गणनाका लागि बल्क संरचनामा Perdew–Burke–Ernzerhof (PBE-GGA) तथा सतह र तहयुक्त संरचनामा Perdew–Burke–Ernzerhof for Solids (PBEsol) एक्सचेन्ज—कोरिलेसन फङ्सनल प्रयोग गरिएको छ। Ultrasoft Vanderbilt Pseudopotential (USPP) र plane-wave basis set को प्रयोग गरी वेभ-फङ्सन तथा चार्ज घनत्वका लागि क्रमशः ७० Ry र ५६० Ry को ऊर्जा सीमा निर्धारण गरिएको छ। कुल ऊर्जा र परमाणु बलका लागि क्रमशः $१०^{-६}$ eV र $१०^{-३}$ eV/Å को अभिसरण सीमा (convergence threshold) निर्धारण गरिएको छ। साथै, पदार्थका यान्त्रिक गुणहरूको अध्ययन गर्न stress–strain विधिबाट प्रत्यास्थता स्थिरांक (elastic constants) गणना गरिएको छ। यस अध्ययनमा $ZrSiO_3$ मा विभिन्न दबाब, सतह-अन्त्य संरचना (surface termination model) तथा एकपत्रीय (monolayer) संरचनाको प्रभाव, $SmMnO_3$ मा युरोपियम (Eu) तथा इट्रियम (Y) प्रतिस्थापनको प्रभाव तथा Sr_2ZrMoO_6 मा उच्च दबाबको प्रभाव अध्ययन गरिएको छ। अध्ययनबाट $ZrSiO_3$ अप्रत्यक्ष ब्यान्ड-ग्याप भएको अर्धचालक पदार्थ रहेको पाइयो। दबाब बढ्दै जाँदा यसको ब्यान्ड-ग्याप बढ्ने, तहहरूको संख्या बढ्दा घट्ने तथा एकपत्रीय संरचनामा तनाव लागू गर्दा (tensile strain) ब्यान्ड- ग्याप घट्ने र सङ्कुचन गर्दा (compressive strain) बढ्ने देखिन्छ। सतह-अन्त्य संरचनाहरूले पनि बल्क संरचनाको तुलनामा कम ब्यान्ड-ग्याप (इलेक्ट्रोन सर्न आवश्यक ऊर्जा) प्रदर्शन गरेका छन्। त्यसैगरी, साबिकका अन्य परमाणु ले प्रतिस्थापन नगरिएको (pristine) $SmMnO_3$ ले फेरोम्याग्नेटिक अर्ध—धात्विक व्यवहार देखाएको छ भने Eu र Y प्रतिस्थापनपछि यसको ब्यान्ड-ग्याप घटेको पाइयो। Sr_2ZrMoO_6 डबल पेरोव्स्काइटले अप्रत्यक्ष ब्यान्ड ग्याप भएको अर्धचालक प्रकृति

देखाउँछ र यसमा फेरोम्याग्नेटिक व्यवहार पाइन्छ। यान्त्रिक विश्लेषणले देखाउँछ कि त्रिआयामिक $ZrSiO_3$ ले ० देखि १०० GPa सम्मको दबाबमा यान्त्रिक स्थायित्व कायम राख्दै लचिलोपन (ductility) प्रदर्शन गर्दछ। साथै सिलिकन तथा जिरकोनियमद्वारा अन्त्य गरिएका सतह—स्ल्याबहरू पनि संरचनात्मक रूपमा स्थिर र लचिलो देखिएका छन्। $ZrSiO_3$ को एकपत्रीय तह संरचनामा –६% देखि +६% सम्मको तनाव अवस्थामा पनि पदार्थ मेकानिकल रूपमा स्थिर रहेको पाइन्छ। $SmMnO_3$ मा Eu तथा Y प्रतिस्थापन गर्दा २५% सम्मको प्रतिस्थापन स्तरमा पनि पदार्थले यान्त्रिक स्थायित्व कायम राख्दै लचिलोपन (ductility) कायम राखेको देखिन्छ। प्रतिस्थापन नगरिएको $SmMnO_3$ को कडापन (stiffness) Eu डोपिङ्ग गर्दा घट्छ भने Y डोपिङ्ग गर्दा बढ्छ। त्यसैगरी Sr_2ZrMoO_6 डबल पेरोव्स्काइटमा ८० GPa सम्मको समदिशीय दबाब अन्तर्गत संरचनात्मक तथा यान्त्रिक दिशात्मक भिन्नता (anisotropy) को अध्ययन गरिएको छ। चुम्बकीय विश्लेषणले देखाउँछ कि $SmMnO_3$ मा Eu प्रतिस्थापन गर्दा कुल चुम्बकीय क्षण र प्रत्येक परमाणुको चुम्बकीय क्षण बढ्छ, जबकि Y प्रतिस्थापन गर्दा यी घट्ने प्रवृत्ति देखिन्छ। साथै Eu प्रतिस्थापन गर्दा क्युरी तापक्रम २५५.३५ K बाट ३१४.२८ K सम्म बढ्छ भने Y प्रतिस्थापन गर्दा यो तापक्रम १८७.६९ K सम्म घट्छ। चुम्बकीय विश्लेषणले देखाउँछ कि $SmM\ nO_3$ मा Eu प्रतिस्थापन गर्दा कुल चुम्बकीय क्षण र प्रत्येक परमाणुको चुम्बकीय क्षण बढ्छ, जबकि Y प्रतिस्थापन गर्दा यी घट्ने प्रवृत्ति देखिन्छ। साथै Eu प्रतिस्थापन गर्दा क्युरी तापक्रम २५५.३५ केल्भिन (K) बाट ३१४.२८ केल्भिन (K) सम्म बढ्छ भने Y प्रतिस्थापन गर्दा यो तापक्रम १८७.६९ केल्भिन (K) सम्म घट्छ। $ZrSiO_3$ को डायइलेक्ट्रिक फङ्सनको वास्तविक (real) र काल्पनिक (imaginary) भाग दबाबसँग बढ्दछ, जससँगै ० देखि १०० GPa सम्म दबाब बढ्दा अवशोषण सीमा (absorption edge) र तीव्र peaks उच्च ऊर्जा तिर सर्छ । $ZrSiO_3$ को अपवर्तन सूचकांक (refractive index) तथा परावर्तन गुण (reflectivity) पनि तनाव तथा सङ्कुचन अवस्था अनुसार परिवर्तन हुने देखिन्छ। Eu तथा Y प्रतिस्थापन गरिएको $SmMnO_3$ मा अपवर्तन सूचकांक र परावर्तन गुण घट्दै जाने प्रवृत्ति देखिन्छ। यी परिणामहरूले देखाउँछ कि संरचनात्मक परिवर्तन, तनाव तथा परमाणु प्रतिस्थापनले इलेक्ट्रोनिक संरचना तथा पदार्थका विद्युत् र प्रकाशसम्बन्धी गुणहरूमा महत्वपूर्ण प्रभाव पार्दछ। यी परिणामहरूले अध्ययन गरिएका पेरोव्स्काइट सामग्रीहरू ऊर्जा, अप्टोइलेक्ट्रोनिक, स्पिन्ट्रोनिक तथा उच्च-दबाबीय उपकरणहरूमा प्रयोग गर्न सकिने सम्भावना रहेको पुष्टि गर्दछ।

मुख्य शब्दहरू : पेरोव्स्काइट पदार्थहरू, आधारभूत सिद्धान्तमा आधारित गणना, इलेक्ट्रोनिक संरचना, प्रकाशजन्य गुण, चुम्बकीय गुण, लोचशील, यान्त्रिक स्थायित्व, एकपत्रीय तह

ABSTRACT

Perovskites are crystalline materials represented by the general formula ABX_3. Their simple crystal structure leads to a broad range of electrical, catalytic, optical, magnetic, piezoelectric, dielectric, and magnetoresistive properties. Due to their remarkable properties, perovskites have been widely utilized in thin-film capacitors, optoelectronic devices, non-volatile memory, solar cells, data storage technologies, spintronic devices, lasers, sensors, high-temperature coatings, and frequency filters. In the present work, we investigate the mechanical, electronic, magnetic, and optical properties of zirconium silicate ($ZrSiO_3$) perovskite (under different hydrostatic pressures, surface terminations, different layer configurations, and its monolayer form); europium (Eu)– and yttrium (Y)–doped samarium manganite ($SmMnO_3$); and the double perovskite strontium zirconium molybdate (Sr_2ZrMoO_6) using first-principles density functional theory (DFT) calculations. For bulk calculations, the Perdew–Burke–Ernzerhof (PBE–GGA) exchange–correlation functional was used, whereas the Perdew–Burke–Ernzerhof for solids (PBEsol) functional was employed for surface and layered structures. Ultrasoft Vanderbilt pseudopotentials (USPPs) were adopted with plane-wave cutoff of 70 Ry for the wavefunctions and 560 Ry for the charge density. Brillouin zone sampling was performed using Monkhorst–Pack grids of $14 \times 14 \times 14$ for bulk property calculations and $14 \times 14 \times 1$ for the monolayer. Convergence thresholds were set to 10^{-6} eV for the total energy and 10^{-3} eV/Å for the atomic forces. The elastic constants were calculated using the stress–strain method. The present study shows that the bulk $ZrSiO_3$ is an indirect band gap semiconductor. Its band gap value increases with rise in pressure and decreases with the increasing number of layers. The termination model has a smaller band gap (2.585 eV for ZrO– and 1.639 eV for SiO_2– termination model) than the bulk model. Electronic band gap of $ZrSiO_3$ monolayer increases under compressive strain and decreases under tensile strain. Pristine $SmMnO_3$ shows ferromagnetic half–metallic behaviour, and has the band gap of 2.72 eV. Its value substantially reduces with the introduction of Eu and Y dopants. The Sr_2ZrMoO_6 double perovskite exhibits an indirect band gap semiconductor with ferromagnetic behaviour. Elastic property calculations confirmed the mechanical stability and ductility of bulk $ZrSiO_3$ up to 100 GPa. Both ZrO– and SiO_2–terminated models of $ZrSiO_3$ are also mechanically stable and ductile. The $ZrSiO_3$ monolayer exhibits mechanical stability and ductility from -6% to +6% strain values. The pristine and Eu– and Y– doped $SmMnO_3$, the material preserves its mechanical stability and ductility, even at a 25% substitution level. The stiffness of pristine $SmMnO_3$ decreases with Eu– doping and increases with Y– doping. Elastic calculations of double perovskite Sr_2ZrMoO_6 under isotropic pressures from 0 to 80 GPa reveal significant elastic anisotropy, with distinct pressure–dependent behaviors.

Magnetic analysis reveals that the magnetic moment of $SmMnO_3$ increases with Eu–doping, whereas Y– doping leads to a reduction. Curie temperature of pristine $SmMnO_3$ raises with Eu– doping, whereas lowers with Y– doping. The real and imaginary parts of dielectric function of $ZrSiO_3$ increase with pressure, with absorption edges and sharp peaks shift to higher energies as pressure increases from 0 to 100 GPa. The refractive index and reflectivity of $SmMnO_3$ decreases with Eu– and Y– dopings. The tunable electronic and optical properties of $ZrSiO_3$ under pressure, mechanical strain, surface termination and 2D form indicated the material is suitable for flexible electronic devices and nano–electronics. The enhanced magnetic and electronic properties of Eu–and Y–doping on $SmMnO_3$ indicate its application in magnetic sensors and data storage devices.

Key words: *Perovskite materials, First-principles calculation, Electronic structure, Optical properties, Magnetic properties, Ductile, Mechanical stability, monolayer*

List of Acronyms and Abbreviations

AFM	: Anti-ferromagnetic
APW	: Augmented Plane Wave
BOA	: Born–Oppenheimer Approximation
BLYP	: Becke–Lee–Yang–Parr
BTP	: BoltzTraP
BZ	: Brillouin Zone
CVD	: Chemical Vapor Deposition
CBM	: Conduction Band Minimum
DFT	: Density Functional Theory
DOS	: Density of States
ESPRESSO	: opEn–Source Package for Research in Electronic Structure, Simulation, and Optimization
FM	: Ferromagnetic
FET	: Field Effect Transistor
FTER	: Fourier Transform Infrared
GGA	: Generalized Gradient Approximation
GGA + U	: Generalized Gradient Approximation with Hubbard U
GPL	: General Public License
HEG	: Homogeneous Electron Gas
HF	: Hartree Fock
HK	: Hohenberg Kohn
HRTEM	: High–Resolution Transmission Electron Microscopy
KS	: Kohn Sham
K.E.	: Kinetic Energy
LDA	: Local Density Approximation
LED	: Light Emitting Diode
MD	: Molecular Dynamics
MAS	: Magic Angle Spinning
MP	: Monkhorst Pack
MV	: Marzarri Vanderbilt
NMR	: Nuclear Magnetic Resonance
NSCF	: Non–selfconsistent Field
Ntype	: Number of Type

ORR : Oxygen Reduction Reaction
PDOS : Projected Density of States
PBE : Perdew Burke Ernzerhof
PBEsol : Perdew–Burke–Ernzerhof for solids
PG – yne : Pentagrphyne
PLD : Pulsed laser deposition
PPs : Pseudopotentials
PW : Plane Wave
PW91 : Perdew-Wang 91
PWSCF : Plane–Wave Self–Consistent Field
QE : Quantum ESPRESSO
QHE : Quantum Hall Effect
QMC : Quantum Monte–Carlo
QTT : Quantum Tunneling Transistor
RRKJ : Rappe Rabe Kaxiras Joannopoulos
RTA : Relaxation Time Approximation
SCF : Self–consistent Field
SEM : Scanning electron microscopy
SDFT : Spin–polarized Density Functional Theory
SOC : Spin Orbic Coupling
SOFC : Solid Oxide Fuel Cell
SWE : Schrödinger Wave Equation
TEM : Transmission Electron Microscopy
TDOS : Total Density of States
TE : Thermoelectric
TF : Thomas Fermi
TF : Thomas–Fermi–Dirac
TMDC : Transition–Metal Dichalcogenide
USPPs : Ultra–Soft Pseudo-Potentials
VBM : Valence Band Maximum
vdWs : van der Waals
XC : Exchange Correlation
XPS : X-ray Photoelectron Spectroscopy
XRD : X-ray Diffraction

LIST OF SYMBOLS

0D	: Zero dimensional
1D	: One dimensional
2D	: Two dimensional
3D	: Three dimensional
Å	: Angstrom
eV	: Electron Volts
E_0	: Ground state energy
E_f	: Fermi energy
E_g	: Bandgap energy
E_s	: Strain energy
E_{corr}	: Correlation energy
E_{xc}	: Exchange energy
GPa	: Gigapascal
H	: Hamiltonian
K_B	: Boltzmann constant
K	: Electronic contribution of thermal conductivity
KHz	: Kilo hertz
m^*	: Effective mass
MPa	: Megapascal
n(r)	: Electron density
Ry	: Rydberg
σ	: Electrical conductivity
τ	: Relaxation time
θ_D	: Debye temperature
μ	: Chemical potential
μ_B	: Bohr magneton
μ_T	: Total magnetic moment
Ψ	: Wave function

List of Tables

Page No.

List of Figures

Page No.

TABLE OF CONTENTS

Chapter 1

1. INTRODUCTION

1.1 General background

Materials science is an interdisciplinary field that influences on multiple areas of modern society. Among various materials, perovskites have gained significant attention because they enable the integration of fundamental scientific research with practical technological applications. Perovskites are not only a development of extant material families, but they also represent a new category of materials with specific characteristics. Perovskites demonstrate improved properties, such as greater efficiency in solar energy conversion and improved performance in optoelectronic devices (Lin, 2016). In the present dissertation, we utilized first-principles approaches to examine mechanical, electronic, optical and magnetic properties of perovskites to optimize them for specific applications. Recent advancements in computational tools and algorithms enable first-principles calculation easier and faster. This helps the researchers to study larger systems and more complex materials. First–principles methods, like density functional theory (DFT), are very useful tools for studying materials at the atomic level. They predict material properties by directly solving the basic quantum mechanical equations which describe the electrons behavior, without the need for empirical parameters (Hautier *et al.*, 2012).

A perovskite crystal structure is a widely studied structure in material science with a general chemical formula ABO_3. In this structure, the A site is typically occupied by alkaline or alkaline-earth, or rare-earth cations with coordination number 12. The transition metal cations with coordination number 6 are located at the B site. X is oxide or halide anion. Most commonly, X site is occupied by oxygen in oxide perovskites or a halide (X = Cl, Br, I) in halide perovskites (Mishra and Parida, 2023). Halide perovskites can be further categorized as alkali halide perovskites and organometallic halide perovskites or hybrid perovskites, based on the nature of the A cation. Usually, the A cation has a larger size than the B cation, and their combination is governed by charge balance and the stoichiometric requirements of the perovskite. The ideal perovskite structure exhibits cubic symmetry, Figure 1. In this configuration, the A ion is coordinate with 12 neighboring atoms, while the B ion coordinates with 6. The structure can be described by a set of BZ_6 octahedra that share corners and have B-Z-B bond angles of 180° (Wang and Cheng, 2013).

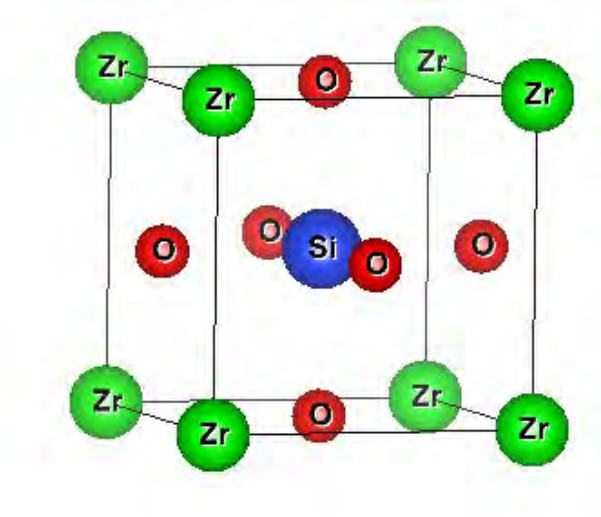

Figure 1: Ideal crystal structure of $ZrSiO_3$ perovskite.

Later, it was studied by Count Lev Alexevich von Perovski, and the name "perovskite" was given in his honor (Rose, 1842). Historically, materials with a crystal structure comparable to $CaTiO_3$ have been referred to as perovskites. Perovskite and perovskite–based materials have great importance in material science due to their simple crystal structure, which allows them to exhibit an extensive range of electrical, catalytic, optical, magnetic, piezoelectric, dielectric, and magnetoresistive properties. These features make them useful in memory devices, solar cells, thin–film capacitors, hard disk read heads, data storage technologies, spintronic devices, infrared-blocking windows, lasers, high-temperature coatings, and frequency filters for wireless technology (Pokharel *et al.*, 2024).

For example, nanosized $BaTiO_3$ perovskite ceramics are widely used in multilayer ceramic capacitors and are also applied in microwave devices, such as antennas (Kumari, 2023). The $PbTiO_3$ perovskite is known for its ferroelectric and piezoelectric properties, which make it suitable for use in medical imaging and energy harvesting devices (Zhang *et al.*, 2015). In addition, $SrFeO_{3-\delta}$, has been investigated for its electrochemical performance and has demonstrated its potential as an electrode material in solid oxide fuel cells (SOFCs) Kumar (2023). Studies on $SrTiO_3$ have also revealed superconducting behavior due to electron–phonon coupling (Kumar, 2023). The magneto-caloric and thermoelectric characteristics of $LaMnO_3$ have been explored for magnetic refrigeration applications near their Curie temperature (Tahiri *et al.*, 2021). Additionally, synthesis methods of $LaCoO_3$ perovskite significantly influence its properties and performance in the catalytic oxidation reforming of diesel fuel (Villoria *et al.*, 2011).

In perovskite structures, the Goldschmidt tolerance factor (t) is a dimensionless parame-

ter used to predict the structural stability and symmetry of perovskite materials. An ideal cubic perovskite structure is formed when t $\approx$ 1. As the tolerance factor drops just below unity, the structure may remain cubic, although minor distortion can occur. In terms of the tolerance factor, oxide perovskites generally maintain a cubic crystal structure when $0.89 < t < 1$, whereas for halide perovskites $0.85 < t < 1$ (Tidrow, 2014). When t is between 0.8 and 0.89, the perovskite structure gets distorted, and the symmetry changes to orthorhombic or tetragonal. When $t > 1$, perovskites tend to adopt hexagonal shapes because the larger A-site cation or smaller B-site cation makes octahedra share faces. Hexagonal perovskites usually have a tolerance factor greater than 1 $t > 1$ (Li, 2016b).

Double perovskite

Double perovskites are generally originate from conventional perovskites of the formula ABX_3. In the conventional perovskite, the B-site cation creates a 3D network of BX_6 octahedra. Double perovskites are produced by replacing two divalent B ions with single monovalent (B) ion and a trivalent (B′) ion, resulting in the formula $A_2BB'X_6$. In double perovskites, the B and B′ cations occupy alternating octahedral sites, while the X anions are located in interstitial positions, Figure 2a. While the A-site cations are located in the spaces between the corner-sharing octahedra (Ji *et al.*, 2024).

Double perovskite structures have two types of octahedra BO_6 and $B'O_6$. These two types of octahedra have different cation electronegativities, which makes the bond lengths and sizes of octahedra different, Figure 2b. This structural distortion reduces the symmetry compared to single perovskites, which exhibit 3D network of uniform octahedra. The double perovskite compounds have been known about since the early 1950s and have become more famous because of their distinctive properties and broad range of industrial uses. More than 1,000 double perovskites have been studied in last few years. Double perovskites have a number of distinct characteristics, such as high-temperature thermoelectric performance, novel electronic, optical and magnetic properties. These have opened up new possibilities in many fields (Roy, 1954). High-temperature thermoelectric qualities in double perovskites have been studied in detail because they can convert thermal waste to useful energy. Their tunable electronic, magnetic and optical properties enable their applications in many electronic devices such as in optoelectronics, spintronic devices and next-generation technologies. The double perovskites such as $Cs_2AgBiBr_6$ and Cs_2NaBiI_6 demonstrate potential uses in optoelectronic device (Chu *et al.*, 2019). In addition to these, double perovskites can be used in solar cells (Kung, 2020), LEDs (Zheng *et al.*, 2024), photocatalysts (Idris *et al.*, 2020), lasers, (Kumar and Radhakrishnan, 2018), photodetectors (Ghosh *et al.*, 2022), scintillators (Zaghrane *et al.*, 2024), field-effect transistors (FET) (Abiram *et al.*, 2022), electrochemical cells (Tarutin *et al.*, 2023), and fuel conversion and energy conversion

devices (Yang *et al.*, 2023).

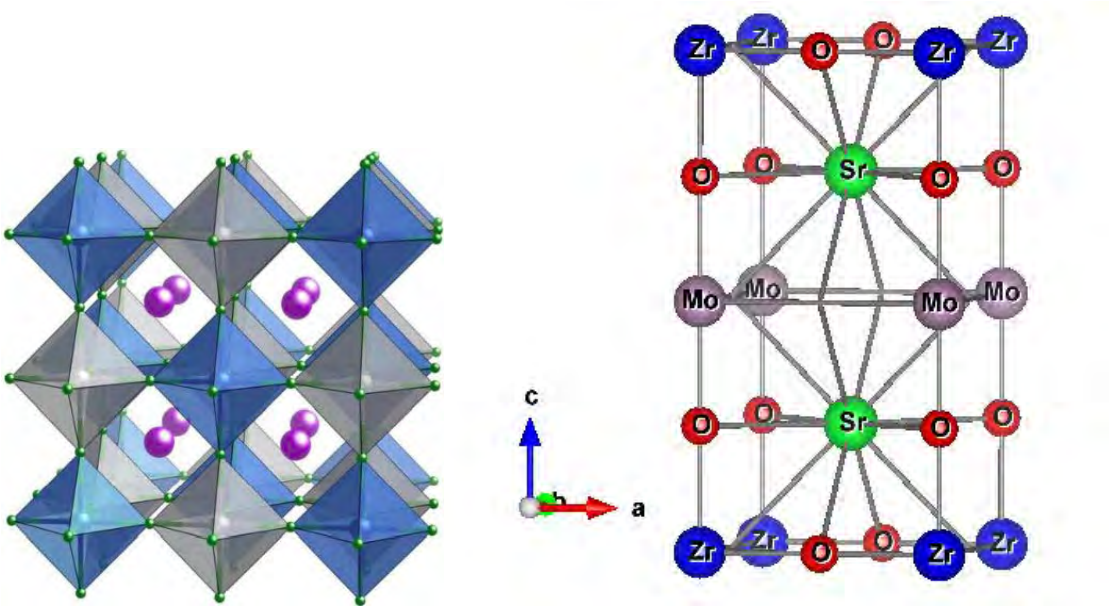

Figure 2: Standard unit cell of double perovskite (a) in polyhedral form, (b) ideal crystal structure (Pokharel *et al.*, 2025).

Surface termination of perovskites

In the surface termination models of perovskites, the atoms constituting the bulk material are distributed in a specific pattern at the outermost layers, which can vary depending on the crystallographic orientation (Tomar *et al.*, 2018). For perovskites, with general formula ABO_3, common surface terminations include AO and BO_2 atomic termination models along certain crystallographic (001) plane. The surface energy, charge distribution, and atomic distortions influence the stability, reactivity, and properties of these types of terminations. Different surface terminations result in unique physical and chemical behaviors due to differences in surface structures, compositions, and charge distributions. For [001] orientation, the slab models are created by slicing bulk material along [001] direction and adding a 15 Å vacuum to prevent periodic images.

Two-dimensional (2D) layered materials

The 2D layered materials are a new class of nanomaterials that possess exceptional physical properties, making them ideal for next-generation electrical appliances. For example graphene, MoS_2, black phosphorus, and 2D perovskites consist of atomically thin layers bonded together in-plane by strong covalent bonds. A perovskite monolayer is an ultra-thin nanostructure composed of a single atomic or molecular layer,

typically made up of inorganic slabs of corner-sharing metal oxide octahedra (Ricciardulli *et al.*, 2021). The slabs are separated by layers of monovalent and divalent cations to get stable and well-ordered atomic arrangements. These monolayers have significant applications in electronics, catalysis, supercapacitors, batteries, and energy technologies.

The layers of 2D perovskites generally consist of inorganic metal-halide octahedral sheets (BX_6) separated by organic cations that act as spacer layers (Dey *et al.*, 2021). The inorganic layers are confined to two dimensions, which restricts the movement of charge carriers and enhance quantum confinement effects (Dey *et al.*, 2021). The inorganic layers are limited to two dimensions, which restricts the movement of charge carriers and makes quantum confinement effects stronger. Strong covalent bonds between the inorganic layers give 2D perovskites structure. Nanosheets, nanoplatelets, and nanodisks of perovskite are examples of two-dimensional (2D) perovskite materials. 2D perovskites exhibits with alternating octahedral stacking pattern, which is different from stacking pattern of graphene and transition metal dichalcogenides (TMDC). In octahedral configuration, the B-site cations maintain their octahedral coordination with the layers. Mixed stacking is a combination of various configurations within a single monolayer, whereas the alternating stacking refers to a periodic repetition of distinct stacking configuration.

Quasi–2D perovskites

Quasi–2D perovskites represent an intermediate structural class between two-dimensional and three-dimensional structures. They consist of n layers of corner-sharing (BX_6) octahedra with organic spacer cations (A') between each layer. This layered structure takes advantage of the better electronic qualities and structural stability of their 3D counterparts.

The general formula for 2D and quasi–2D perovskites is $A'_2A_{(n-1)}B_nX_{3n+1}$, where A' denotes organic spacer and $A_{(n-1)}B_nX_{3n+1}$ represents inorganic slabs. A a mono- or divalent cation responsible for separating the inorganic layers. B represents divalent metal cations, and X is oxide or halide anions that form octahedra with B cations. Where n represents number of inorganic layers of perovskite slab between organic layers. Where, n = 1 represents 2D perovskites, where an isolated layer of BX_6 octahedra is sandwiched between two organic spacer layers. Whereas n = (2– 4) represents quasi-2D perovskites, which have 2 to 4 layers of BX_6 octahedra that balance the quantum confinement of 2D structures with better charge transport properties than that of 3D perovskites (Lee *et al.*, 2025).

Compared to the 3D counterparts, 2D and quasi–2D perovskites have many benefits,

such as tunable electronic properties, and greater structural flexibility. This makes them suitable for solar cells, optoelectronics, and flexible electronic devices.

Structural and mechanical properties of perovskites

The perovskite structure exhibits different shapes and properties due to the presence of distinct cations and anions. The structural properties of perovskites depend upon the atomic radii, atomic arrangement and bonding interactions between the constituents cations and anions. Surface modification, doping with other elements, and changes in dimensionality also influence the structural stability of the material. The mechanical behavior of perovskites plays an important role in determining how they respond to external forces and strain. Which affects its performance across various applications.

The mechanical characteristics of a material are evaluated using different elastic parameters. Young's modulus measures the stiffness or rigidity of materials and indicates its resistance to elastic deformation under applied stress. It is the ratio of normal stress to longitudinal strain in linear elastic region. Bulk modulus is ratio of change in pressure to volumetric strain. It measures the resistance of material to bulk compression. The shear modulus determines how well a material can resist shear deformation and how well it can handle changes in shape without changing its volume. Poisson's ratio describes the bonding characteristics and mechanical behavior of materials. A ratio of shear modulus to bulk modulus (G/B) value lower than the critical value measures ductile to brittle properties of materials. This ratio lower than critical value of 0.57 shows ductility, whereas above 0.57 implies brittleness. Elastic anisotropy refers to the variations in mechanical properties in different crystallographic directions. It is crucial for determining the mechanical stability, crack propagation, and structural reliability of materials.

Electronic properties of perovskites

Electronic properties of perovskites play a crucial role in their performance in electronics and optoelectronic applications. These electronic properties are mainly governed by band structure and density of states of substance. The band structure describes the relationship between electron energy with the wave vector (k) in a crystal lattice. It gives important information regarding the energy bands and band gap E_g, which determine that the material is conductor, semiconductor or insulator.

Optical properties of perovskites

Optical properties of the material are evaluated through their dielectric response, absorption behavior, refractive index, and reflectance. Dielectric function, $\epsilon(\omega)$ =

$\epsilon_1(\omega) + i\epsilon_2(\omega)$ is a complex function that depends on frequency of incident photons. It describes interaction of materials with electromagnetic radiation. The real part of $\epsilon(\omega)$, $\epsilon_1(\omega)$, gives the dispersion and polarization response of a material to an external electromagnetic fields. Whereas the imaginary part $\epsilon_2(\omega)$, highlights the absorption of electromagnetic radiation due to inter–band transitions between occupied and unoccupied electronic states. Refractive index indicates the extent of bending of light when it enters the material. Whereas absorption coefficient describes how strongly the material absorbs incident radiation as a function of photon energy. The reflectivity of a surface relates how much light it reflects back. These properties help determine effectiveness of perovskites in optoelectronic applications.

Magnetic properties of perovskites

The magnetic properties of perovskites, such as paramagnetism, ferromagnetism and antiferromagnetism, are significantly influenced by the arrangement of cations within their crystal structure. These magnetic properties are the result of interactions between unpaired electrons in d-orbitals of transition metal ions that are located at the B-sites in the perovskite lattice. The total magnetic moment of perovskite materials is a vector sum of individual atomic magnetic moments. The study of magnetic properties of perovskites is important for data storage technologies, magnetic sensors, spintronic devices and more.

Novelty and Practical Relevance

Zirconium silicate ($ZrSiO_3$) is a promising zirconium-based perovskite for use under diverse conditions because of its high thermal stability, strong mechanical strength, and tunable electronic and optical properties. Although zirconium-based perovskites have been widely studied, the effects of surface termination, strain and pressure on structural, electronic, elastic, and optical properties of $ZrSiO_3$ are still not well understood. In addition, limited information is available on how strain influences the stability, electronic band structure, and elastic anisotropy of $ZrSiO_3$ monolayers, even though these effects are critical for nanoscale device applications. Both the double perovskite Sr_2ZrMoO_6 and the $ZrSiO_3$ monolayer exhibit elastic anisotropy that affects their stability and thermal behavior, suggesting that Zr-based perovskites may possess similarly significant and useful anisotropic characteristics.

The novelty of this work is first-principles study of effect of hydrostatic pressure, strain, surface termination, and elemental doping on mechanical, electronic, optical, and magnetic properties of selected perovskites. This study addresses existing knowledge gaps and makes reliable predictions. The result suggest that the $ZrSiO_3$ is a strong candidate

for use in scaffold materials. The strain-dependent activity of the $ZrSiO_3$ monolayer points out its potential in nanoelectronics and flexible devices.

1.2 Problem statement

Knowledge of the experimental synthesis of zirconium-based perovskites and double perovskites is essential for the characterization, fabrication, and design of new materials with superior properties. Zirconium-based materials have been extensively studied in various manners, such as zircon-type silicates, amorphous zirconium silicate dielectrics, and zirconate perovskites. In addition, Zr– based double perovskites and atomic substitution on $SmMnO_3$ have attracted significant interest because they have a lot of distinct structural, electronic, magnetic, and mechanical properties. Experimental investigations are difficult and costly for the synthesis and characterization of atomically thin layers, for monitoring surface terminations, and for examining high-pressure or strain-dependent states of these materials. Therefore, we use DFT study of electronic, optical, elastic, and magnetic properties of selected zirconium-based perovskites, double perovskites, and $SmMnO_3$ perovskites under hydrostatic pressure, applied strain, reduced dimensionality, and elemental doping.

1.3 Objectives of the Work

This work will provide detailed theoretical knowledge of fundamental physical properties of selected single and double perovskite materials using first-principles calculations. Perovskites have useful properties, which makes them suitable in electronics, optoelectronics, and spin-based technologies. It is important to understand their structural stability, mechanical response, electronic behavior, and magnetic characteristics for optimizing their performance and guiding future material design. In this context, objectives of the present work are divided into a general and specific objectives, as outlined below:

General Objective

- To study the mechanical, electronic, magnetic, and optical properties of single and double perovskites.

Specific Objectives

- To study the structural stability of single perovskites ($ZrSiO_3$, $SmMnO_3$) and the double perovskite (Sr_2ZrMoO_6) through the tolerance factor, cohesive energy, and formation energy.

- To study the mechanical properties, such as elastic moduli, Poisson's ratio, and anisotropy, of $ZrSiO_3$, $SmMnO_3$, and Sr_2ZrMoO_6 perovskites.
- To study the electronic properties (band structure and density of states) of $ZrSiO_3$, $SmMnO_3$, and Sr_2ZrMoO_6 perovskites.
- To study the magnetic moments and Curie temperature of $SmMnO_3$ and Sr_2ZrMoO_6 perovskites to evaluate their magnetic properties.
- To study the dielectric constant, refractive index, absorptance, and transmittance of $ZrSiO_3$ and $SmMnO_3$ perovskites.

1.4 Organization of the work

This dissertation is arranged in subsequent chapters:
Chapter 1: "Introduction" presents the background of perovskite materials, their significance in materials science, the motivation behind the present work, and the objectives of this thesis.
Chapter 2: "Literature Review" presents the brief review of existing literature helpful for carrying out this work. It also includes research gaps and method we have employed to address the scientific issues.
Chapter 3: "Materials and Methods" presents the theoretical background, necessary formulas and the computational framework employed throughout the entire work. It includes a fundamental overview of DFT too.
Chapter 4: "Results and Discussion" contains the principal findings of this research. Section 4.1 presents and discusses structural electrical and elastic properties of bulk $ZrSiO_3$ under different hydrostatic pressures and for different surface termination models. Section 4.2 presents the findings on structural, electrical, elastic characteristics of $ZrSiO_3$ monolayer. Section 4.3 summarizes structural, electronic, magnetic, and elastic, properties of Eu and Y– doped $SmMnO_3$ perovskite. Section 4.4 discusses and presents the elastic and thermal anisotropy of Sr_2ZrMoO_6 double perovskite.
Chapter 5: "Conclusions and Recommendations" presents the important conclusions drawn from the work along with recommendations for future work.
Chapter 6: "Summary" presents a concise summary of this work.

Chapter 2

2. LITERATURE REVIEW

This study systematically explores structural, electronic, mechanical, optical, and magnetic properties of perovskites using DFT. Researchers have been studying perovskites since 1892 as they can be used in different fields. This chapter gives a short overview of the research on single perovskites ($ZrSiO_3$, $SmMnO_3$) and double perovskite (Sr_2ZrMoO_6).

2.1 Zr–based perovskite

Zirconium–based perovskites are a significant class of functional oxide materials with high structural stability, wide electronic band gaps, and tunable physical properties Li *et al.* (2016). These qualities make them good candidates for optoelectronics, microelectronics, energy devices, and high temperature devices.

Ozkan *et al.* (1974) experimentally synthesized zircon ($ZrSiO_4$) and determined their elastic constants. These measurements showed that the d ifferences in the reported elastic constants of zircon were mainly due to metamictization in natural samples Cheng *et al.* (2004). Natural zircon commonly incorporates uranium and thorium impurities, which induce radiation damage and lead to metamictization, thereby significantly modifying its mechanical response. Ultrasonic pulse superposition and phase comparison techniques were used to redetermine elastic constants of both synthetic zircon crystals and high-purity natural single crystals and verified to be non-metamict. When zircon with lattice parameters a_0 = 6.606 Å and c_0 = 5.980 Å was taken, accurate elastic constants were obtained and metamictization lowered acoustic velocities by approximately 20% relative to structurally intact samples. These findings clearly indicate high sensitivity of Zr–O–Si bonding networks to structural disorder and radiation-induced defects. Although $ZrSiO_4$ crystallizes in a zircon-type structure, which is structurally distinct from the perovskite phase, its mechanical behavior provide valuable guidance for understanding the behavior of $ZrSiO_3$ perovskite systems. The mechanical properties of both perovskite and nonperovskite materials are governed by strength and flexibility of Zr–O polyhedral units. In $ZrSiO_3$, zirconium occupies the B-site within corner-sharing ZrO_6 octahedra; consequently, variations in bond lengths, coordination environment and strain, or surface termination can markedly influence elastic anisotropy and mechanical stability.

Wilk and Wallace (2000) stated that zirconium-based silicate materials are substitutes for standard gate dielectrics since they work well electrically and are very stable at high temperatures. Thin films of zirconium silicate ($ZrSi_xO_y$) with a low zirconium concentration (3–5 atomic percent) were formed directly on silicon substrates and had an equivalent oxide thickness of about 21 Å for a 50 Å film substrates. These films also had very low hysteresis values (<10 mV), which means that contact on the film and the silicon substrate was quite good. These films also have very low leakage current densities of 10^{-6} A/cm^2 at 1.0 V, which indicates they might be used in low-power microelectronics. The dielectric characteristics of $ZrSi_xO_y$ have been found to be significantly influenced by the film composition. Films with $ZrSiO_4$ compositions near stoichiometric demonstrated high permittivity due to stronger Zr–O bonding. Hence, Si–rich $ZrSi_xO_y$ films a good balance between better dielectric performance and structural stability.

Elmore *et al.* (2003) conducted a comprehensive study on various silicate-based materials, such as zirconium silicate, magnesium silicates, aluminosilicates, and other clay minerals frequently used in industrial and cosmetic applications. Silicon and oxygen create a network bonded with metal cations (M), such as Zr, Mg, Al, Ca, or Na, in all of these minerals. Chemical stability of these materials is maintained by metal cation (M)–O–Si bonding network. They simultaneous studied natural and synthesized silicates, and their physical and chemical properties are affected by particle size, composition, crystal structure and moisture content. Zirconium silicate and related silicates demonstrated little toxicity upon oral or skin exposure, with no notable adverse effects identified in either short-term or long-term investigations. The effects of inhalation, however, were shown to depend on the size and form of the particles. Very small particles or fiber-like structures at high concentration had stronger impacts on the lungs. They further found that lungs diseases mainly result from long-term inhalation of mineral dust during mining and processing activities, rather than from the chemical properties of zirconium silicates. This confirms that Zr–O–Si bonds are chemically stable and less reactive.

Shah *et al.* (2024) investigated mechanical, optical and thermoelectric properties of lead-free zirconate perovskites $XZrO_3$ (X = Ca, Sr, Ba) using WIEN2k code. The calculated results agreed with experimental data. The $BaZrO_3$ perovskite was found to be the most stable among the studied compounds. These materials exhibited mechanical stability, ductile behavior and excellent resistance to external stress. These zirconate perovskites possess semiconducting nature with E_g = 3.25, 3.71 and 3.80 eV for $CaZrO_3$, $SrZrO_3$ and $BaZrO_3$, respectively. Furthermore, these materials have favorable optical properties, with refractive index values between 1.0 and 2.0 and high light absorption mostly in the UV region (about 5.0 eV). In addition, these materials exhibit strong ther-

moelectric properties, such as high power factors and large Seebeck coefficients. They also possess good mechanical strength, remarkable optical activity. These combined properties indicate that Zr–based perovskites possess significant potential for various technological applications.

Later, Gupta *et al.* (2024) conducted first-principles calculation to study electronic, optical, mechanical and thermoelectric behaviour of Zr-based perovskites $ZrXH_3$ (X = Zn, Cd). Their findings revealed that these materials have thermodynamic and mechanical stability even at high pressure. These perovskites showed metallic behaviour, and exhibit significant elastic anisotropy. The study also showed that Zr–centered bonding networks which influenced physical properties of these materials under pressure. These findings have drawn concern of modern day researchers towards oxide perovskites such as $ZrSiO_3$.

2.2 Surface termination model

Structural and electronic properties of perovskites also depend upon types of surface terminations. Different terminations in ABO_3 perovskites (AO– and BO_2 –terminated surfaces) can cause significant differences in surface relaxation, electronic band structure, and optical response.

In this regard, de Lazaro and Longo (2004) studied the structural and electronic characteristics of cubic $PbTiO_3$ [001] surfaces with TiO_2– and PbO– terminations by first–principles calculation. They found that surface structure relaxation is significantly influenced by the types of termination. On TiO_2–terminated surfaces, Ti atoms show large displacements, whereas on PbO– terminated surfaces, the Pb atoms on top layer display the greatest displacement.

In addition to this, they investigated the electronic structure, dipole behavior, and bonding characteristics for each termination model. The band gap of the bulk material, TiO_2–terminated, and PbO–terminated models had different values. The TiO_2–terminated surface induced band splitting in conduction bands and PbO–termiated in valence bands. The electron density distribution indicates a covalent nature of both Ti–O and Pb–O bonds, with the Ti–O bonds exhibiting stronger electron sharing than the Pb–O bonds. Their findings showed how surface termination affected atomic relaxation, electronic configuration, and bonding in perovskite oxides. Their concept was used in the present work.

Luo (2015) examined the structural and electronic characteristics of $KNbO_3$ (001) surfaces using DFT method. The structural and electronic properties of $KNbO_3$ perovskite depends upon types of surface terminations, i.e. KO–termination and NbO_2–termination. A detailed analysis of surface energies, atomic relaxations, and charge distributions were carried out for both terminations. The top surface layer had the most atomic displacements for NbO_2–terminated surface, while second layer below the surface had the most atomic displacements for the KO–terminated surface. They further showed that the surfaces were very different in terms of stability. The NbO_2 –termination had a lower surface energy (0.75 eV) than that of the KO–termination (1.21 eV), indicating it to be more stable and easier to fabricate. Electronic properties of the material was significantly influenced by surface termination. The band gap is 1.70 eV for KO–termination and 1.30 eV for NbO_2–termination. Charge study showed that K and O atoms had weaker ionic bonds and Nb and O atoms had stronger covalent bonds.

Sokolovic *et al.* (2025) demonstrated that cubic ABO_3 perovskites exhibit two distinct surface termination models along [001] direction. These are AO–surface termination model and BO_2–surface termination model. Surface termination plays significant role on thin-film growth and surface properties. Therefore, careful control of the growth of each AO or BO_2 layer is essential to control electrical and chemical behavior of perovskites. Pulsed laser deposition is widely employed to create perovskite thin films, but it does not provide precise control over surface composition and termination. On the other hand, oxide molecular beam epitaxy offers atomic–level accuracy and better control of surface chemistry. Therefore, it is more suitable method for surface termination studies. They demonstrated that the resistivity, carrier density, and photoresponse due to AO– terminations model differ from BO_2– type terminations model. Additionally, angle-resolved X-ray photoelectron spectroscopy proved that surface species other than perovskites are mostly linked to the SrO– termination, moreover, TiO_2– terminated surfaces maintained a more stoichiometric perovskite nature.

Most of these insights come from well-studied systems such as $PbTiO_3$, $KNbO_3$, and $SrTiO_3$. While these studies provide useful comparisons, termination-dependent behavior in $ZrSiO_3$ surfaces remains largely unexplored. The knowledge acquired from well-studied systems such as $PbTiO_3$, $KNbO_3$, and $SrTiO_3$ with AO- and BO_2-type terminations, can be easily applied to $ZrSiO_3$ perovskite systems, where ZrO and SiO_2 serve analogous roles.

2.3 2D monolayer of perovskites

Ahn *et al.* (2004) studied the optical properties and interfacial layer formation in ultrathin zirconium silicate films grown on silicon substrates. The microstructure and thickness of interfacial layer were analyzed using variable–angle spectroscopic ellipsometry and high–resolution transmission electron microscopy (HRTEM). Chemical composition of the films were analyzed using X–ray photoelectron spectroscopy (XPS). The films were deposited by pulse-mode metal–organic chemical vapor deposition (CVD) using oxygen–based zirconium and silicon precursors. They also examined the effect of different gases (O_2 or NO) during oxidation and film growth. HRTEM images showed an amorphous layer formed at the interface below the zirconium silicate films. XPS results confirmed that this layer was free from zirconium but was rich in silicon. Ellipsometry analysis showed that the interfacial layer consists of mostly a mixture of SiO_2 and SiO. When an ultrathin oxynitride buffer layer was added under optimized conditions, the thickness of the interfacial layer decreased significantly. However, when oxygen was present during film formation, the interfacial layer got thicker, and it was unable to its further growth. These results show that both factors, interfacial chemistry and growth atmosphere strongly affects the structural quality and optical response of zirconium-based silicates.

Freiman *et al.* (2009) reported the growth of zirconium oxide thin films using a layer-by-layer deposition method. For that purpose diluted zirconium alkoxide solutions were successively applied to silicon substrates. This method made it feasible to control film growth at the molecular level. They observed that film thickness increased gradually and the film density slightly decreased at higher alkoxide concentrations. These thin films demonstrated thermal stability up to 600°C with moderate dielectric constant. These films were suitable for microelectronic applications.

Tsai et al. (2016) demonstrated that layered perovskites are more structurally stable and resistant to damage from the environment compared to three-dimensional perovskites. Their work showed that when perovskites are made into two-dimensional structures, their electronic structure is changed due to quantum confinement. This provides better for the band gap and the transport of charge carriers. These findings have motivated the present computational analysis of their structural, mechanical and electrical properties of perovskite monolayer.

Tsai *et al.* (2016) showed that two-dimensional layered perovskites possess better structural stability and higher resistance to environmental degradation than their three-dimensional counterparts. Their study demonstrated that converting perovskites into

a two-dimensional form modifies their electronic structure because of quantum confinement, making it possible to tune the band gap and charge-carrier transport. These findings have motivated the present computational investigation of inorganic perovskite monolayers to systematically examine the effects of reduced dimensionality on their structural, mechanical, and electronic properties.

Phuc *et al.* (2018) used first-principles calculation to study how biaxial strain affects monolayer phosphorene. They found that strain strongly changed the band gap. Even a small compressive strain of 1% modified the band gap along both x– and y– axes. When compressive strain was further increased, band gap value continuously decreased and reached 0 eV at critical strains of $\epsilon_x = -13\%$. Whereas, direct to indirect band gap transition occurred when the tensile strain along the x-direction exceeded $\epsilon_x = 5\%$. The band gap increased for $0 < \epsilon_x < 5\%$ and then decreased beyond this strain value. However, tensile strain along the y-direction led to a steady increase in the band gap. These results showed that electronic properties of phosphorene are significantly affected by applied strain. The biaxial strain changed the bond lengths and interactions between the orbitals. These changes directly influenced the band structure and optical response. Although this study focused on phosphorene, the underlying mechanism is highly relevant to two-dimensional perovskite monolayers. Similar strain-induced variations in orbital hybridization and lattice distortion can effectively tune the electronic and optical properties of 2D perovskites. Because monolayer perovskites possess reduced dimensionality and a large surface-to-volume ratio, their electronic structure is particularly sensitive to external strain, making strain engineering an effective approach for optimizing band gaps, charge transport, and optoelectronic performance.

Sando (2022) provided a detailed review of ABO_3 perovskite, discussing their key properties such as ferroelectricity, magnetism, strong electronic interactions, superconductivity, and optical behavior, with a focus on thin-film systems. The review showed that when perovskite films were grown on single-crystal substrates, new and unusual phases could appear. These phases are not present in bulk materials. This happens because the substrate imposes mechanical constraints such as lateral strain, crystal orientation, symmetry disorder, and interactions between oxygen octahedra. In addition, the biaxial strain and substrate orientation could break crystal symmetry and trigger phase transitions. These structural changes directly affect the functional properties of the materials. These effects were much stronger in low-dimensional perovskites, such as monolayer structures. In these materials, strain has a more significant and noticeable impact. In this context, the ideas of lateral strain and structural coupling developed for perovskite thin films provided a clear framework in understanding and tuning electronic, and functional properties of perovskite monolayers.

2.4 Doble perovskites

Double perovskites are widely studied for their diverse structural, electronic, magnetic, and dielectric properties. Their behavior can be easily tuned for various applications by applying external effects such as strain, cations doping, or suitable choice of B– and B′ – site cations.

Tellez *et al.* (2013) studied structural, magnetic, ferroelectric, and electronic properties of Sr_2ZrMnO_6 double perovskite. The material was synthesized using a standard solid–state reaction process, and its structure was examined using X–ray diffraction and theoretical optimization method. The results showed that Sr_2ZrMnO_6 exibited a cubic double perovskite structure. Magnetic measurements revealed long-range magnetic ordering at about 53.2 K. Temperature-dependent magnetic susceptibility indicated a transition from a paramagnetic to a ferrimagnetic state, with an effective magnetic moment of approximately 3.3 μ_B. Furthermore, magnetization measurements at 4.0 K displayed clear ferromagnetic hysteresis, confirming magnetic ordering at low temperatures. Polarization–electric field measurements also demonstrated ferroelectric behavior, from which a high dielectric permittivity of about 330 was obtained. To support their experimental results, they performed DFT calculations to study electronic and magnetic properties. The calculations showed that the material was semiconducting, with an effective magnetic moment of 2.84 μ_B. These findings indicated that Zr–containing double perovskites are multifunctional materials. They combine magnetic ordering, ferroelectricity, and semiconducting behavior. Because of these properties, they are promising materials for spintronic and magnetoelectric applications.

Li (2016a) examined structural and electrical characteristics of Sr_2ZnWO_6 double perovskite under high pressure. They employed X-ray diffraction and Raman spectroscopy to investigate how the structure and lattice vibrations changed. They employed AC impedance measurements to evaluate the changes on electrical properties of the material. At ambient pressure, Sr_2ZnWO_6 crystallizes in a monoclinic structure. When pressure increased the crystal structure transformed from monoclinic to triclinic phase at about 9 GPa. This transition was primarily caused by increased distortion of the corner-sharing $(Zn,W)O_6$ octahedra which lowers the crystallographic symmetry. The Raman spectroscopy results further supported this finding, and showed noticeable changes in vibrational modes associated with the WO_6 octahedra. Furthermore, electrical measurements reveal a significant change in transport behavior at higher pressures. Around 11 GPa pressure, the electrical resistivity increased significantly and an electronic transition occurred together with the structural distortion. This phenomenon is due to the fact

that pressure makes O $2p$–W $5d$ hybridization stronger, which makes covalent bonding stronger and reduces the charge-transfer energy and carrier localization.

Bao *et al.* (2019a) examined structural, elastic, and thermal properties of TMIr compounds (TM = Sc, Y, Lu, Ti, Zr, and Hf). The calculated parameters and formation energies were close to experimental data. The results showed that the stability followed the order ScIr > LuIr > HfIr > YIr > TiIr > ZrIr. Their calculations of polycrystalline elastic constants revealed that all TMIr intermetallics were ductile, with elastic anisotropy increasing in the order ZrIr > HfIr > TiIr > LuIr > YIr > ScIr. The Debye temperatures ranged from a maximum of about 370 K for ScIr to a minimum of around 183 K for HfIr. Their results further showed that Zr–containing compounds exhibited enhanced elastic anisotropy and strong ductile behavior. This behavior was attributed to the extended nature of Zr–$4d$ orbitals and strong metal ligand bonding.

Dar *et al.* (2019) studied half–metallic properties of Sr_2MnTaO_6 double perovskite using ab initio DFT calculations. They employed GGA, GGA+U, and mBJ approaches to study spin –polarized band structure. Their results showed that Sr_2MnTaO_6 exhibited half-metallic behavior with ferromagnetic ordering and a total magnetic moment of 4 μ_B. The electronic structure showed metallic behavior in spin-up channel and semiconducting behavior in spin-down channel. Elastic and mechanical properties calculations indicated that Sr_2MnTaO_6 was a hard and stiff material with a brittle nature. The material exhibits high ultraviolet (UV) light absorption, and a suitable refractive index and dielectric constant values. That make its potential for solar and optoelectronic applications. The calculated Debye temperature (θ_D) indicated high thermal conductivity, along with characteristic specific heat capacity behavior. These findings provided a useful comparison for Zr–based double perovskites such as Sr_2ZrMnO_6. Substituting Ta atom with Zr was expected to enhance lattice stability due to stronger Zr–O bonds and to allow tunable elastic anisotropy and thermal properties under pressure.

2.5 Rare earth– based perovskite

Liu (2018) reported an efficient and cost-effective method for synthesizing mesoporous $SmMnO_3$ perovskite sheets using a one-step calcination process, in which citric acid was used to promote perovskite formation and pore generation. Structural and morphological analyses revealed uniformly distributed mesopores across the sheets, which gives the wide surface area of the material. Their studies on the structure of the $SmMnO_3$ sheets indicated that mesopores are equally spaced out across the sheets. The synthesized

$SmMnO_3$ showed excellent catalytic activity for toluene oxidation, and it sustained its performance for 36 hours. These findings demonstrate that $SmMnO_3$ is an environment friendly catalyst that can be produced on a large scale. Furthermore, they also noticed that there was strong link between its electronic structure, magnetic behavior, and metal–oxygen bonding.

Many oxide materials have low redox activity, slow oxygen exchange, and limited chemical stability. This makes them less effective for solar thermochemical CO_2 splitting. Gao *et al.* (2022) demonstrated that cation-doped $SmMnO_3$ perovskites perform better on CO_2 splitting, doping with Ca and Al had the better performance. For example, $Sm_{0.6}Ca_{0.4}Mn_{0.8}Al_{0.2}O_3$ produce lots of CO, 595.56 mol g^{-1} at 1100°C – 1350°C. This value has remained consistent over multiple cycles and is nearly four times of pristine $SmMnO_3$. The better performance is due the oxygen vacancies form which spread more easily in the perovskite lattice. These processes are primarily influenced by the electronic structure, defect formation, and metal–oxygen bonding. In addition, doped $SmMnO_3$ shows strong absorption of solar-light, emphasizing the key role of its optical properties.

Mahalik *et al.* (2023) demonstrated that rare–earth perovskite oxides are suitable non-precious metal catalysts for energy applications. They used hydrothermal method at 200 °C to synthesize $SmMnO_3$ perovskite and then evaluated its oxygen reduction reaction (ORR) activity on alkaline medium. XRD, FTIR, SEM, TEM, and XPS all showed that the material had a well– crystallized perovskite structure. When tested with a rotating ring–disk electrode (RRDE), the $SmMnO_3$ carbon catalyst exhibits lower onset potential and higher current density than commercial Pt/C catalyst. It also showed higher stability and tolerance to methanol. The composite material can behave as an effective and stable ORR catalyst in alkaline medium according to these findings. Magnetic ordering in $SmMnO_3$ may also affect charge transport by changing the spin polarization and exchange interactions. The strong mechanical stability of the perovskite helps it to remain stable during long-term use.

Electronic and magnetic properties of rare-earth manganites had been effectively tuned through A-site cation substitution. Vedmid *et al.* (2024) demonstrated that when the ratio of Mn^{3+}/Mn^{4+} was altered when the Sm site in $SmMnO_3$ was substituted with a Sr atom. As a result, double-exchange interactions became stronger and the Jahn-Teller distortion occurred. In a similar way, doping on $SmMnO_3$ with Eu or Y at the Sm site was expected to slightly change the lattice distortions and bond angles. Even small

structural distortion strongly affect the electronic structure and magnetic behavior of the material.

2.6 Research gaps

Zirconium–based materials have been studied in various forms, such as zircon-type silicates, amorphous zirconium silicate dielectrics, and zirconate perovskites. However, most of the existing research are focused only on specific compound. A complete understanding of Zr-based perovskites is still missing. In particular, Zircon ($ZrSiO_4$) and other Zr–based perovskites have been studied for their elastic, dielectric, and chemical properties. The perovskite phase of $ZrSiO_3$ has received much less attention.

First-principles studies on zirconium–based perovskite oxides, particularly Zr–containing perovskites such as $BaZrO_3$, $SrZrO_3$, and $ZrSiO_3$, have attracted considerable attention because of their excellent structural stability, wide band gaps, and tunable physical properties. Furthermore, comprehensive DFT investigations that simultaneously explore structural stability, electronic structure, optical behavior, elastic anisotropy, and pressure effects in $ZrSiO_3$ are still limited. Therefore, more study is necessary to comprehend how pressure influences its mechanical properties, electronic band structure, phase stability, and potential applications in high-pressure optoelectronics, biomedical devices, and catalysis (Mahmood et al., 2019)(Mahmood *et al.*, 2019).

Even though, previous experimental and first-principles studies on surface termination (AO- and BO_2-terminations) in ABO_3 perovskites have shown significant effects on surface relaxation, stability, electronic behaviors, and optical response. However, well-studied systems such as $PbTiO_3$, $KNbO_3$, and $SrTiO_3$ provide most of these insights. While these studies provide useful comparisons, termination-dependent behavior in $ZrSiO_3$ surfaces remains largely unexplored. Therefore, a comprehensive DFT investigation of $ZrSiO_3$ surface terminations is essential to understand and predict its surface-dependent electronic, mechanical, and optical properties.

Previous experimental and first-principles studies have shown that surface termination (AO- and BO_2-terminated surfaces) strongly influences the structural stability, electronic structure, and optical properties of ABO_3 perovskites. However, these studies have mainly focused on well-known materials such as $PbTiO_3$, $KNbO_3$, and $SrTiO_3$, whereas the surface properties of $ZrSiO_3$ remain largely unexplored. Similarly, most investigations of zirconium-based oxides and silicates have concentrated on thin films, dielectric properties, and microelectronic applications, with limited attention given to

crystalline and low-dimensional $ZrSiO_3$. In particular, the effects of surface termination, quantum confinement, and external strain on the structural, electronic, optical, and mechanical properties of $ZrSiO_3$ monolayers have not been systematically investigated. Therefore, a comprehensive density functional theory (DFT) study is needed to understand these properties and evaluate the potential of $ZrSiO_3$ for nanoelectronic and optoelectronic applications.

Extensive research has been conducted on rare–earth (RE)–based perovskites such as $SmMnO_3$, but most studies have focused on synthesis methods, morphology, and general properties, despite their high catalytic and thermochemical performances. The effects of isovalent R–E doping with elements like Eu and Y at the atomic level remain largely unexplored. Therefore, a comprehensive DFT study of both pristine and Eu/Y–doped $SmMnO_3$ is essential to elucidate the structure–property relationships and guide their practical applications.

In double perovskites, strong coupling can occur between magnetic and dielectric properties, while structural variations primarily influence electronic, elastic, and dielectric behavior. Experimental and theoretical studies, particularly on Sr_2ZrMnO_6, have revealed its multifunctional behavior, including magnetic ordering, ferroelectricity, and semiconducting characteristics. Pressure–dependent studies of related double perovskites highlight the key role of B-site cations in controlling structural property. First-principles investigations of other double perovskites show that elastic anisotropy, thermal stability, and spin-polarized electronic states are highly sensitive to cation chemistry. However, a systematic understanding of Zr-based double perovskites is still lacking. In particular, comprehensive DFT studies that simultaneously examine structural stability, electronic and magnetic behavior, elastic and thermal responses, and their evolution under pressure or strain is limited. This gap limits the ability to establish clear structural property correlations and to rationally design Zr-based double perovskites for spintronic, magnetoelectric, and high-stability applications.

To address these gaps, this study uses first–principles DFT computations to systematically analyze:

- Pressure-dependent properties of Zr-based perovskites: ($ZrSiO_3$).
- Surface termination effects in $ZrSiO_3$ surface
- Strain-engineered behavior of 2D $ZrSiO_3$ monolayers.

- The impact of Eu– and Y– doping on $SmMnO_3$ perovskite.
- Elastic anisotropy and thermal properties of the Sr_2ZrMoO_6 double perovskite.

Chapter 3

3. MATERIALS AND METHODS

This chapter presents methods employed to accomplish objectives of the current study. Initially, the theoretical foundations underlying the systems under investigation are outlined. The Hamiltonian and Schrödinger equations for electronic and nuclear contributions of many-body systems are explained. Several approximations are then discussed to address the challenges of solving many–body Schrödinger wave equation (SWE), including Born–Oppenheimer approximation (BOA) (Born & Oppenheimer, 1927), Hartree approximation (Hartree, 1928), Hartree–Fock approximation (Fock, 1930), and Thomas–Fermi (TF) approach (Fermi, 1927). Finally, a concise overview of density functional theory is presented, including derivation of Kohn–Sham equation (Kohn & Sham, 1965). There are many different exchange-correlation functionals that can be used to describe how electrons interact with each other. Some of them are Local Density Approximation and Generalized Gradient Approximation. Overall, above theoretical foundations provide a foundational basis for computational study of physical properties of perovskite and double perovskite materials under hydrostatics pressure, mechanical strain, dimensional variation, and atomic substitution.

3.1 Many-body Schrödinger wave equation

For a many-body system, Hamiltonian is expressed as (Martin, 2004)

$$\hat{H}\psi_i\left(r_1\sigma_1,\ldots r_N\sigma_N,R_1,R_2\ldots R_N\right)=E_i\psi_i\left(r_1\sigma_1,\ldots r_N\sigma_N,R_1,R_2\ldots R_N\right) \tag{3.1}$$

Here, r_i and σ_i denote the position and spin states of the electrons, respectively, while R_i represents the positions of the nuclei. The operator $\hat{H}$ corresponds to Hamiltonian of system containing N electrons and M nuclei. Wave function, ψ_i, describes the i^{th} state of a system of $3N$ electronic and $3M$ nuclear degrees of freedom.

In terms of electrons and nuclei, the SWE for a many-body system is (Born and Oppenheimer, 1927)

$$\hat{H}=-\sum_{i=1}^{N}\frac{\hbar^2}{2m_e}\nabla_i^2-\sum_{I=1}^{N_c}\frac{\hbar^2}{2M_I}\nabla_I^2+\sum_{i<j}\frac{e^2}{|\mathbf{r}_i-\mathbf{r}_j|}-\sum_{i,I}\frac{Z_Ie^2}{|\mathbf{r}_i-\mathbf{R}_I|}+\sum_{I<J}\frac{Z_IZ_Je^2}{|\mathbf{R}_I-\mathbf{R}_J|} \tag{3.2}$$

The index i, j denotes electrons, while I, J denotes nuclei. In this context, m_e represents

mass of electron, while M_I denotes mass of nuclei. So, the Hamiltonian is expressed as

$$\hat{H} = \hat{T}_e + \hat{V}_{\text{int}} + \hat{V}_{\text{ext}} + \hat{T}_N + \hat{V}_{II} \tag{3.3}$$

with the following definitions:

$$\hat{T}_e = -\sum_{i=1}^{N} \frac{\hbar^2}{2m_e} \nabla_i^2; \qquad \text{(Kinetic energy of electrons)}$$

$$\hat{V}_{\text{int}} = \sum_{i<j} \frac{e^2}{|\mathbf{r}_i - \mathbf{r}_j|}; \qquad \text{(Electron-electron Coulomb repulsion energy)}$$

$$\hat{V}_{\text{ext}} = -\sum_{i,I} \frac{Z_I e^2}{|\mathbf{r}_i - \mathbf{R}_I|} \qquad \text{(Electron-nuclei Coulomb attraction energy)}$$

$$\hat{T}_N = -\sum_{I=1}^{N_c} \frac{\hbar^2}{2M_I} \nabla_I^2; \qquad \text{(Kinetic energy of nuclei)}$$

$$\hat{V}_{II} = \sum_{I<J} \frac{Z_I Z_J e^2}{|\mathbf{R}_I - \mathbf{R}_J|} \qquad \text{(Nuclei-nuclei Coulomb repulsion energy)}$$

and the Hamiltonian:

$$\hat{H}\Psi(\{\mathbf{R}_I\}, \{\mathbf{r}_i\}) = E\Psi(\{\mathbf{R}_I\}, \{\mathbf{r}_i\}) \tag{3.4}$$

SWE gives complete description of the system but it has high computational cost. To overcome this limitation, the Born-Oppenheimer approximation (BOA), introduced in 1927, separates the nuclear and electron motion based on their mass differences (Born and Oppenheimer, 1927).

3.2 Born-Oppenheimer approximation (BOA)

This approximation simplifies complex interactions between electrons and nuclei in a molecule by assuming that their motions can be separated due to the significant difference in their masses. Since electrons move much faster and are significantly lighter than nuclei, the nuclear motion can be treated as stationary. Consequently, the total wave function is written as distinct nuclear and electronic components (Born and Oppenheimer, 1927) as

$$\Psi(\{\mathbf{R}_I\}, \{\mathbf{r}_i\}) = \Phi(\{\mathbf{R}_I\})\psi(\{\mathbf{R}_I\}, \{\mathbf{r}_i\}) \tag{3.5}$$

where, $\Phi(\{\mathbf{R}_I\})$ describes the state function of nuclei and $\psi(\{\mathbf{R}_I\}, \{\mathbf{r}_i\})$ are for the

electrons. The electronic Hamiltonian, accounting for electron interactions in a static nuclear potential, is expressed as (Born and Oppenheimer, 1927)

$$\hat{H}_e = -\sum_{i=1}^{N} \frac{\hbar^2}{2m_e}\nabla_i^2 - \sum_{i,I} \frac{Z_I e^2}{|\mathbf{r}_i - \mathbf{R}_I|} + \sum_{i<j} \frac{e^2}{|\mathbf{r}_i - \mathbf{r}_j|} \tag{3.6}$$

Thus, the SWE for electronic and nuclear components of the Hamiltonian becomes

$$\left[-\sum_{i=1}^{N} \frac{\hbar^2}{2m_e}\nabla_i^2 - \sum_{i,I} \frac{Z_I e^2}{|\mathbf{r}_i - \mathbf{R}_I|} + \sum_{i<j} \frac{e^2}{|\mathbf{r}_i - \mathbf{r}_j|}\right] \psi(\{\mathbf{R}_I\}, \{\mathbf{r}_i\}) = V(\{\mathbf{R}_I\})\psi(\{\mathbf{R}_I\}, \{\mathbf{r}_i\}) \tag{3.7}$$

$$\left[-\sum_{I=1}^{N_c} \frac{\hbar^2}{2M_I}\nabla_I^2 + V\{\mathbf{R}_I\}\right] \Phi(\{\mathbf{R}_I\}) = E\Phi\{\mathbf{R}_I\} \tag{3.8}$$

The energy eigenvalues of the nuclear part, $V(R_I)$, are obtained by solving Equation (3.6). These eigenvalues, when utilized in Equation (3.7), describes the nuclear motion.

3.3 Single-particle approximation

The single-particle approximation simplifies the many-body interactions by assuming that each particle travels independently under the effective potential provided by other particles. Which reduces computational cost for calculations of ground state physical characteristics. There are two main methods to use this approximation:
(a) Wave–function method: In this method, each particle is describe by its own wave function, which is influenced by an effective potential due to the interaction with other particles.
(b) Density–functional theory (DFT): It describes the system using electron density rather than individual wave functions. This makes it widely used and efficient method for studying systems with many–electrons.

3.4 Wave funcion method

3.4.1 Hartree approximation

The Hartree approximation assumes that each electron moves independently in an average electric field produced by the nuclei and the other electrons, without considering direct electron–electron exchange and correlation effects (Hartree 1928). Additionally, total wave function is product of individual wave functions for each electron and is expressed as

$$\Psi(r_1, r_2, \ldots, r_n) = \psi_1(r_1)\psi_2(r_2)\ldots\psi_n(r_n) \tag{3.9}$$

And the total energy can be given as

$$\hat{H}\Psi(r_1, r_2, \ldots, r_n) = E\Psi(r_1, r_2, \ldots, r_n) \tag{3.10}$$

A self-consistent variational approach is used to determine its solution.

3.4.2 Hartree-Fock approximation

The Hartree–Fock (HF) method simplifies the many–electron SWE by using a single Slater determinant of N orbitals to describe the total wave function. It ensures the antisymmetric nature of wave function, and is consistent with Pauli exclusion principle. The wave function can be expressed as (Slater, 1937; Fock, 1930)

$$\Psi_{HF} = \frac{1}{\sqrt{N!}} \begin{vmatrix} \psi_1(x_1) & \psi_2(x_1) & \ldots & \psi_N(x_1) \\ \psi_1(x_2) & \psi_2(x_2) & \ldots & \psi_N(x_2) \\ \vdots & \vdots & \ddots & \vdots \\ \psi_1(x_N) & \psi_2(x_N) & \ldots & \psi_N(x_N) \end{vmatrix} \tag{3.11}$$

Thus, the Hamiltonian then becomes

$$\left[-\frac{1}{2}\nabla^2 + V_{\text{ext}} + \int d^3r' \frac{\rho(\mathbf{r}')}{|\mathbf{r} - \mathbf{r}'|} - \sum_j^N \frac{\langle \psi_j | \psi_i \rangle}{|\mathbf{r} - \mathbf{r}'|} \right] \psi_i(\mathbf{r}) = \epsilon_i \psi_i(\mathbf{r}) \tag{3.12}$$

This Hamiltonian incorporates the exchange potential, and is defined as

$$V_x[\psi_i, \psi_j] = -\sum_{j=1}^{N} \frac{\psi_j^*(\mathbf{r})\psi_i(\mathbf{r}')\psi_j(\mathbf{r})}{|\mathbf{r} - \mathbf{r}'|} \tag{3.13}$$

By incorporating both Hartree and exchange contributions, the Hartree-Fock approximation is expressed as (Fock, 1930)

$$\left[-\frac{1}{2}\nabla^2 + V_{\text{ext}} + V_{\text{sc}} \right] \psi_i = \epsilon_i \psi_i \tag{3.14}$$

where,

$$V_{\text{sc}} = V_H + V_x \tag{3.15}$$

In Equation (3.14), the 1^{st} term is K.E. of electrons, 2^{nd} term corresponds to electron–ion interaction, and 3^{rd} term describes electron–electron interaction, including self–interaction contribution.

3.5 Density–based approach: Density-Functional Theory

DFT uses electron density, $n_0(\mathbf{r})$, as the central variable rather than many–electron SWE. The electronic structure of atoms, molecules, and solids can be extensively studied using this well known quantum mechanical approach. Concept of DFT originated from Thomas and Fermi (Thomas, 1927; Fermi, 1928) and was improved by Dirac (Dirac, 1930) by adding exchange and correlation effects. The later formulation of the HK theorems and KS formalism established DFT as a powerful and widely used tool in modern computational physics and chemistry.

3.5.1 Thomas–Fermi-Dirac approximation

Thomas and Fermi proposed that the electron density could serve as the central quantity for describing a system of interacting particles, rather than conventional wave functions approach. Within this framework, the total energy, $E_{\mathrm{TF}}[n(\mathbf{r})]$ is formulated as a function of electron density (Thomas, 1927; Fermi, 1928) in the form

$$E_{\mathrm{TF}}[n(\mathbf{r})] = C_1 \int d^3r\, n(\mathbf{r})^{5/3} + \int d^3r\, V_{\mathrm{ext}}(\mathbf{r}) n(\mathbf{r}) + \frac{1}{2} \int \frac{n(\mathbf{r}) n(\mathbf{r}')}{|\mathbf{r} - \mathbf{r}'|}\, d^3r\, d^3r' \quad (3.16)$$

In homogeneous electron gas (HEG), initial term represents K. E. of non-interacting electrons and expressed in atomic units with the coefficient $C_1 = \frac{3}{10}(3\pi^2)^{2/3}$. Second term represents the interaction of the electrons with the external potential, whereas the third term represents the classical electrostatic repulsion between electrons, known as the Hartree energy.

The K. E. of the HEG is derived by integrating the kinetic energy over the free–electron energy states of Fermi wave vector, $k_F = [3\pi^2 n(\mathbf{r})]^{1/3}$ as

$$T_0[n(\mathbf{r})] = \frac{2}{(2\pi)^3} \int_0^{k_F} \frac{\hbar^2 k^2}{2m}\, 4\pi k^2\, dk = C_1 \int n(\mathbf{r})^{5/3}\, d^3r \quad (3.17)$$

The Thomas-Fermi model initially ignored electron exchange and correlation. In 1930, Dirac added a local exchange term on this model, $C_2 \int n(\mathbf{r})^{4/3}\, d^3r$, where $C_2 = \frac{3}{4}(3/\pi)^{1/3}$. This modification led to the Thomas-Fermi-Dirac (TFD) equation and is expressed as (Dirac, 1930)

$$\begin{aligned} E_{\mathrm{TFD}}[n(\mathbf{r})] = C_1 \int n(\mathbf{r})^{5/3}\, d^3r + \int V_{\mathrm{ext}}(\mathbf{r}) n(\mathbf{r})\, d^3r \\ + \frac{1}{2} \int \frac{n(\mathbf{r}) n(\mathbf{r}')}{|\mathbf{r} - \mathbf{r}'|}\, d^3r\, d^3r' + C_2 \int n(\mathbf{r})^{4/3}\, d^3r. \end{aligned} \quad (3.18)$$

For all densities, $n(\mathbf{r})$, the energy functional maintains the total number of electrons,

N, while predicting ground–state properties N. This is achieved using the method of Lagrange's multiplier, expressed as

$$\left[E_{\mathrm{TFD}}[n(\mathbf{r})] - \mu\left(\int n(\mathbf{r})\, d^3r - N\right)\right] = 0 \tag{3.19}$$

Here, μ is the Lagrange multiplier, that corresponds to the Fermi energy at absolute zero temperature (0 K). Thus, the Thomas–Fermi–Dirac equation becomes (Tomishima, 1959)

$$\frac{5}{3}C_1 n(\mathbf{r})^{2/3} + V_{\mathrm{ext}}(\mathbf{r}) + \int \frac{n(\mathbf{r}')}{|\mathbf{r}-\mathbf{r}'|}\, d^3r' + \frac{4}{3}C_2 n(\mathbf{r})^{1/3} = \mu \tag{3.20}$$

Solving above equation gives the ground–state electron density. While Thomas-Fermi-Dirac model was a significant step forward in DFT, it has limitations in atomic shell structures and molecular bonding. The predictions regarding the electronic structure of solids using this model are less accurate.

3.5.2 Hohenberg-Kohn theorems

The HK theorems form the foundation of DFT. In this approach, electron density is the key parameter for describing interacting particles under an external potential (Hohenberg and Kohn, 1964).

Theorem I: The ground-state particle density $n_0(\mathbf{r})$ of any interacting many-particle system in an external potential $V_{\mathrm{ext}}(\mathbf{r})$ uniquely determines the external potential, except for an arbitrary constant. Therefore, all ground-state properties of the system can be determined if the ground-state particle density $n_0(\mathbf{r})$ is known. For an N-electron system, if two potentials $V_1(\mathbf{r})$ and $V_2(\mathbf{r})$ generate same ground–state electron density, then they correspond to two different Hamiltonians, H_1 and H_2. These Hamiltonians are expressed as (Hohenberg and Kohn, 1964)

$$H_1 = T + U + \sum_i V_1(\mathbf{r}_i) \tag{3.21}$$

$$H_2 = T + U + \sum_i V_2(\mathbf{r}_i) \tag{3.22}$$

where, K.E. operator (T) is;

$$T = -\frac{1}{2}\sum_i \nabla_i^2 \tag{3.23}$$

and the inter-electronic potential U is

$$U = \frac{1}{2}\sum_{i\neq j} \frac{1}{|\mathbf{r}_i - \mathbf{r}_j|} \tag{3.24}$$

The SWE for these two Hamiltonians are $H_1\Psi_1 = E_1\Psi_1$ and $H_2\Psi_2 = E_2\Psi_2$. If Ψ_2 yields similar electron density like Ψ_1, then

$$n(\mathbf{r}) = N \int |\Psi_2(\mathbf{r}, \mathbf{r}_2, \ldots, \mathbf{r}_N)|^2 \, d^3r_2 \ldots d^3r_N \tag{3.25}$$

Now, let us consider the energy expectation values of the forms (Hohenberg and Kohn, 1964)

$$E_1 = \langle \Psi_1 | H_1 | \Psi_1 \rangle < \langle \Psi_2 | H_1 | \Psi_2 \rangle \tag{3.26}$$

and

$$E_2 = \langle \Psi_2 | H_2 | \Psi_2 \rangle < \langle \Psi_1 | H_2 | \Psi_1 \rangle \tag{3.27}$$

This leads to the following inequalities

$$E_1 < E_2 + \int n(\mathbf{r})[V_1(\mathbf{r}) - V_2(\mathbf{r})] \, d^3r \tag{3.28}$$

and

$$E_2 < E_1 + \int n(\mathbf{r})[V_2(\mathbf{r}) - V_1(\mathbf{r})] \, d^3r \tag{3.29}$$

Sum of Equation (3.28) and (3.29) gives

$$E_1 + E_2 < E_2 + E_1 \tag{3.30}$$

This contradiction, demonstrates that the $n_0(\mathbf{r})$ has a simple influence on $V_{\text{ext}}(\mathbf{r})$.

Theorem II: The exact ground–state energy in an external potential, $V_{\text{ext}}(\mathbf{r})$, is derived from the global minimum of the energy functional, $E[n]$. The density that minimizes $E[n]$ is the exact ground–state density, $n(\mathbf{r})$. The Hohenberg–Kohn energy functional, excluding nuclear–nuclear interactions is (Hohenberg and Kohn, 1964)

$$E_{\text{HK}}[n(\mathbf{r}); V_{\text{ext}}] = T[n(\mathbf{r})] + E_{\text{int}}[n(\mathbf{r})] + \int V_{\text{ext}}(\mathbf{r}) n(\mathbf{r}) \, d^3r \tag{3.31}$$

Here $T[n(\mathbf{r})]$ is K.E. and $E_{\text{int}}[n(\mathbf{r})]$ represents electron–electron interaction energy. Both are universal functionals and are independent on external potential. They can be combined into a single functional as

$$F[n(\mathbf{r})] = T[n(\mathbf{r})] + E_{\text{int}}[n(\mathbf{r})] \tag{3.32}$$

If $\int V_{\text{ext}}(\mathbf{r})$ describes interaction between electrons and external potential, then energy functional is expressed as

$$E_{\text{HK}}[n(\mathbf{r}); V_{\text{ext}}] = F[n(\mathbf{r})] + \int V_{\text{ext}}(\mathbf{r}) n(\mathbf{r})\, d^3r \tag{3.33}$$

It can be achieved by minimizing Equation (3.21) with variations in $n(\mathbf{r})$, which enables the computation of all ground–state properties of the system.

3.5.3 Kohn-Sham equations

The KS formalism, proposed by Kohn and Sham in 1965 (Kohn and Sham, 1965), provides a mathematical framework for performing electronic structure calculations. It replaces the interacting system with an equivalent non–interacting one which have same $n_0(\mathbf{r})$. It overcomes the difficulty of directly solving interacting system by introducing exchange–correlation functional to represent electron–electron interactions. Whose exact form remains unknown and must be approximated to evaluate the energy functional. The precision of DFT results is strongly affected by selection of the exchange–correlation functional. They have demonstrated wide applicability across diverse materials, including semiconductors, metals, and insulators (Martin, 2004). In addition, the introduction of hybrid functionals (Becke, 1993; Adamo and Barone, 1999) and approaches incorporating van der Waals interactions (Klimeš and Michaelides, 2012) has further extended the scope of DFT by addressing its limitations in specific systems.

In KS approach, true ground-state electron density is replaced with a comparable density from a hypothetical system of non–interacting particles. Within the system, electrons possess an effective potential, $V_{\text{KS}}(\mathbf{r})$, rather than the complex potential from the interactive system. The corresponding Kohn–Sham Hamiltonian is (Kohn and Sham, 1965)

$$\hat{H}_{\text{KS}} = \frac{1}{2} \sum_i \nabla_i^2 + V_{\text{KS}}(\mathbf{r}) \tag{3.34}$$

The Schrödinger equations for N non–interacting electrons is

$$\left(\frac{1}{2} \nabla_i^2 + V_{\text{KS}}(\mathbf{r}) \right) \psi_i(\mathbf{r}) = \epsilon_i \psi_i(\mathbf{r}) \tag{3.35}$$

and the ground state electron densities can be obtained by solving this equation iteratively. Each electron is assigned to an orbital with the minimum available eigen values ϵ_i. The electron–density of the auxiliary system is expressed as

$$n(\mathbf{r}) = \sum_{i=1}^{N} |\psi_i(\mathbf{r})|^2 \tag{3.36}$$

The ground–state energy functional for a many–body interacting system utilizing the KS model (Kohn and Sham, 1965) can be expressed in terms of orbital density as

$$E[n(\mathbf{r})] = T_s[n(\mathbf{r})] + E_H[n(\mathbf{r})] + E_{\mathrm{XC}}[n(\mathbf{r})] + \int V_{\mathrm{ext}}(\mathbf{r})n(\mathbf{r})\, d^3r \tag{3.37}$$

In this case, $T_s[n(\mathbf{r})]$ represents K.E. of the non–interacting particles, $E_H[n(\mathbf{r})]$ represents Hartree energy while $E_{\mathrm{XC}}[n(\mathbf{r})]$ represent exchange-correlation energy for a many–body interacting system.

To find ground–state energy functional, the above expression can be minimized with respect to $n(\mathbf{r})$ with same numbers of electrons. This method can be employed to calculate the equivalent Kohn–Sham one–particle potential, which yields (Kohn and Sham, 1965)

$$\begin{aligned} V_{\mathrm{KS}}(\mathbf{r}) &= V_{\mathrm{ext}}(\mathbf{r}) + V_{\mathrm{H}}(\mathbf{r}) + V_{\mathrm{XC}}(\mathbf{r}) \\ &= V_{\mathrm{ext}}(\mathbf{r}) + \frac{\partial E_{\mathrm{H}}[n(\mathbf{r})]}{\partial n(\mathbf{r})} + \frac{\partial E_{\mathrm{XC}}[n(\mathbf{r})]}{\partial n(\mathbf{r})} \end{aligned} \tag{3.38}$$

where $V_{\mathrm{H}}(\mathbf{r}) = \frac{\partial E_{\mathrm{H}}[n(\mathbf{r})]}{\partial n(\mathbf{r})}$, is the functional derivative of the Hartree energy with respect to the electron density and is called the Hartree potential. Similarly, $V_{\mathrm{XC}}(\mathbf{r}) = \frac{\partial E_{\mathrm{XC}}[n(\mathbf{r})]}{\partial n(\mathbf{r})}$ is the functional derivative of the exchange–correlation (X_C) energy with respect to the electron density and is called the exchange–correlation (X_C) potential.

The Equations (3.36), (3.37), and (3.38) are known as the Kohn-Sham equations. The KS potential V_{KS} depends on electron density, and this potential is utilized to solve KS equations to get new electron density. The exchange-correlation functional must be approximated to acquire reliable results on the KS approach in DFT calculations. The Kohn–Sham technique depends on universal energy functional along with various empirical parameters, that are independent to the material system.

3.5.4 Exchange-correlation functionals

The Kohn–Sham requires a mathematical representation of the electron density as primary variable in DFT. The charge density is calculated from self–consistent method, which depends on the KS potential. The KS potential has complex function because it includes the exchange and correlation effects. Among the available exchange–correlation functionals, LDA and the GGA are popular functionals (Perdew and Wang, 1992).

3.5.4.1 Local density approximation (LDA)

In the Local Density Approximation (LDA), the exchange–correlation energy depends only on the electron density at each point in space (Langreth and Perdew, 1980). LDA is based on the homogeneous electron gas (HEG) model. For real materials, where the electron density is not uniform, LDA assumes that each point in the system behaves locally like a HEG with the same electron density. The total exchange–correlation energy is then obtained by integrating the local exchange–correlation energy over the entire space. LDA is most accurate for systems in which the electron density changes slowly. Therefore, it is widely used in electronic structure calculations and geometry optimization. Although LDA is a simple approximation, it often provides reliable results because the errors in the exchange and correlation energies tend to partially cancel each other. In case of HEG, the exchange-correlation functional ($E_{\mathrm{LDA}}[n]$) is expressed as (Kohn and Sham, 1965; Martin, 2004):

$$E_{\mathrm{LDA}}[n] = \int n(\mathbf{r})\, \epsilon_{\mathrm{XC}}[n(\mathbf{r})]\, d^3r \tag{3.39}$$

where $\epsilon_{\mathrm{XC}}[n(\mathbf{r})]$ represents the exchange-correlation energy per electron in a HEG with electron density $n(\mathbf{r})$.

The exchange, $E_X[n]$ and correlation, $E_C[n]$, contributions to the total exchange-correlation functional, E_{XC}, is given as

$$E_{\mathrm{XC}}[n] = E_X[n] + E_C[n] \tag{3.40}$$

And energy functional is given as (Dirac, 1930),

$$E^X_{\mathrm{LDA}}[n] = \int n(\mathbf{r})\, \epsilon_X[n(\mathbf{r})]\, d^3r \tag{3.41}$$

where,

$$\epsilon_X[n] = -\frac{3}{4}\left(\frac{3}{\pi}\right)^{1/3} [n(\mathbf{r})]^{1/3} \tag{3.42}$$

The correlation energy of a HEG is complex and only works accurately well at high concentrations.

At low electron densities, electron–electron interactions become stronger, resulting in enhanced electron correlation and a tendency for electrons to arrange themselves into a Wigner crystal-like structure. Ceperley and Alder (1980) obtained accurate correlation energies over a wide range of electron densities using Quantum Monte Carlo simulations. Their results were subsequently used to develop several widely adopted Local Density Approximation (LDA) exchange–correlation functionals, including the

Vosko–Wilk–Nusair (VWN) functional (Vosko *et al.*, 1980), Perdew–Zunger (PZ81) functional (Perdew and Zunger, 1981) and Cole-Perdew (CP) (Cole and Perdew, 1982).

3.5.4.2 Generalized gradient approximation (GGA)

The LDA assumes that electron density is locally uniform, which is not true for real systems with changing electron density. To overcome this limitation, GGA improves upon LDA by including gradient–based corrections to electron density, which makes it more accurate for system with non-uniform electron distributions.

In GGA, the functional E_{XC}^{GGA} is given as (Perdew, 1986)

$$E_{XC}^{GGA}[n(r)] = \int f[n(r), \nabla n(r)]\, d^3r, \tag{3.43}$$

Here, f is functional of $n(r)$ and $\nabla n(r)$ is its spatial gradient.

Similar to LDA, the GGA exchange–correlation functional, E_{XC}^{GGA} is splited within the exchange component, E_X^{GGA}, and the correlation component, E_C^{GGA}, and is expressed as (Perdew *et al.*, 1996)

$$E_{XC}^{GGA} = E_X^{GGA} + E_C^{GGA}. \tag{3.44}$$

Several methods have been used to build DFT exchange–correlation functionals. The Perdew–Burke–Ernzerhof functional (PBE) (Perdew *et al.*, 1996), Perdew–Burke–Ernzerhof for solids (PBEsol) (Perdew *et al.*, 2008), and BLYP exchange–correlation functional (Tozer and Handy, 1998) are popular and common GGA functionals. To improve the accuracy of DFT calculations, several other GGA-type functionals have been proposed and created. Beyond GGA, more advanced approximations such as the modified Becke–Johnson potential (mBJ), meta-Generalized Gradient Approximation (meta-GGA), and hyper-Generalized Gradient Approximation (hyper-GGA) are employed to achieve more accurate and realistic results. These approaches use different parameters to describe the exchange–correlation energy in certain point in space.

3.5.4.3 GGA with hubbard potential (GGA+U)

LDA and GGA are effective for studying the electronic and magnetic properties of weakly correlated system, particularly those do not contain partially filled 3d, 4d, 5d, or 4f/5f orbitals. However, for materials containing 3d and 4f electrons, LDA and GGA tend to give inaccurate results because they cannot accurately describe the strong interactions between these localized electrons. The GGA+U approach includes an on–site Coulomb correction term (Hubbard parameter U), to better describe strongly correlated systems

(Anisimov *et al.*, 1991) and is expressed as

$$E_{\text{GGA+U}} = E_{\text{GGA}} + E_U \tag{3.45}$$

where, E_U is the Hubbard correction term that takes into consideration the Coulomb interaction between localized electrons. According to (Anisimov *et al.*, 1991) E_U is given by

$$E_U = \frac{U - J}{2} \sum_{m,\kappa} \left[n_{m,\kappa}(1 - n_{m,\kappa}) \right] \tag{3.46}$$

Here, U stands for the screened on–site Coulomb interaction, J stands for the on–site exchange (Hund's) interaction, and $n_{m,\kappa}$ denotes the occupation number of the electrons in the localized orbital m with spin κ. The summation runs over all correlated orbitals and spin channels. The effective on–site Coulomb parameter U_{eff} = U - J, which reduces fractional orbital occupancies and provides a better description of strongly correlated d- and f-electron systems.

3.6 Solution of the Kohn-Sham equations

The KS technique addresses many–electron problem through an iterative, self-consistent procedure. It simplifies the complex many-electron interactions by modelling them as an equivalent non-interacting system with the same ground–state electron density. The KS approach begins with an initial guess for the electron density. This guess is usually made by adding up the densities of individual atoms. This initial density is utilized to generate Kohn-Sham potential, V_{KS}, to solve the KS equations. Then, the electron density is compared to density obtained from last iteration to assess self-consistency. The system is considered to converge when a gap between these values decreases below a specified threshold, and the desired results can be extracted, Figure 3. This procedure is repeated until convergence is achieved (Kohn and Sham, 1965).

3.7 Pseudopotentials

A basis set is constructed by combining basic mathematical functions to describe molecular or electronic orbitals. A minimum basis set is the smallest number of functions needed to represent all electrons in an atom. In KS framework, different basis sets are employed to represent electronic orbitals. In this study, we utilize orthogonalized plane–wave basis sets in a pseudopotential framework, is ideal for systems with periodic boundary conditions. Other commonly used basis sets in materials simulations include Gaussian functions (Frisch and Hanebeck, 2021), Augmented Plane Waves (APW) (Loucks and Slater, 1967), and Localized Atomic Orbitals (Soler *et al.*, 2002).

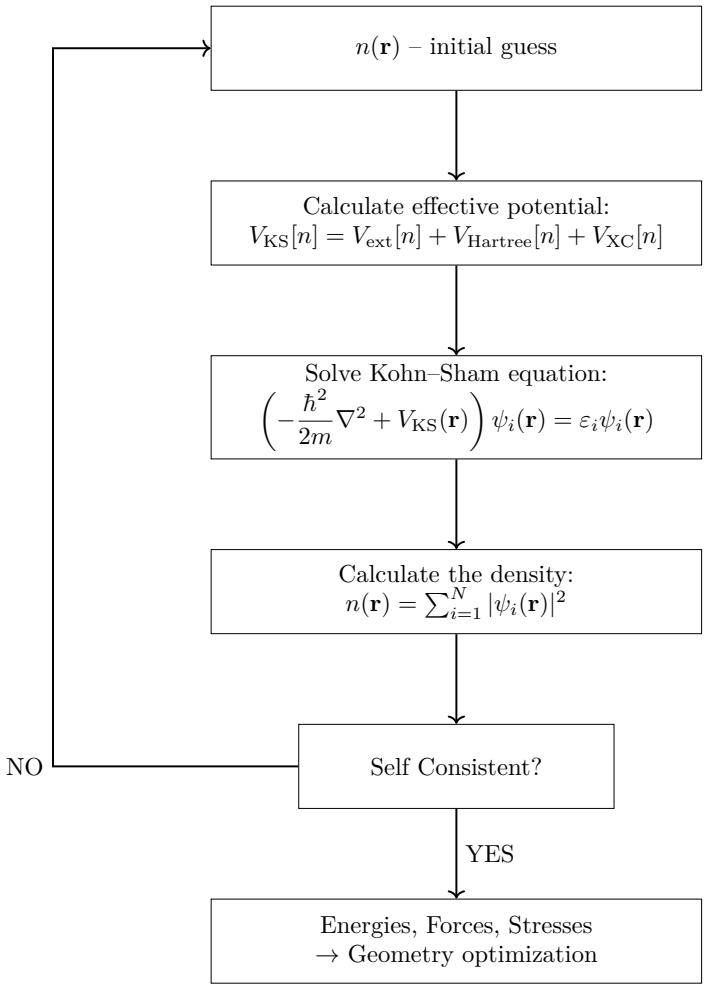

Figure 3: Self-consistency flowchart showing the iterative procedure in Kohn-Sham method.

Bloch's theorem states that

$$\psi_{\mathbf{k}}(\mathbf{r}) = u_{\mathbf{k}}(\mathbf{r})\exp^{i\mathbf{k}\cdot\mathbf{r}}, \tag{3.47}$$

Herein, $u_{\mathbf{k}}(\mathbf{r})$ represents periodic part of the wave function that reflects translational symmetry of the unit cell. Each wave vector in reciprocal space must be evaluated independently with respect to the SWE. When the core potentials are replaced with pseudopotentials, plane waves become the preferred basis set in periodic systems, is explained below. Orthogonal plane waves are unaffected by atomic locations and energy levels. The KS equations are rewritten as a matrix eigenvalue problem in DFT. This simplifies the calculation of the expansion coefficients. In practice, its expansion is limited by a kinetic energy cutoff (E_{cut}). It is important to choose the E_{cut} carefully so that the wave functions are smooth and physical measurements like total energy converges. Consequently, a balance between computational cost and the desired accuracy is required.

DFT calculations need many basis functions to describe both core and valence electrons.

Core electron wave functions are highly oscillatory and tightly confined, so they require many Fourier components. Valence electron wave functions are smoother in bonding regions but show complex nodal behavior near atomic nuclei. These features require a higher plane-wave cutoff, which increases the computational expense. To simplify calculations, the valence wave functions are smoothed near the atomic core and neglect the explicit treatment of core electrons, as they have little effect on most physical properties of the substance. However, their influence is incorporated into an effective potential known as a pseudopotential. The pseudopotential replaces strong electrostatic potential of core electrons with a smoother effective potential, thereby avoiding singularities at the nucleus. This technique minimizes the size of the matrices that need to be diagonalized and number of plane waves used by smoothing the valence wave functions.

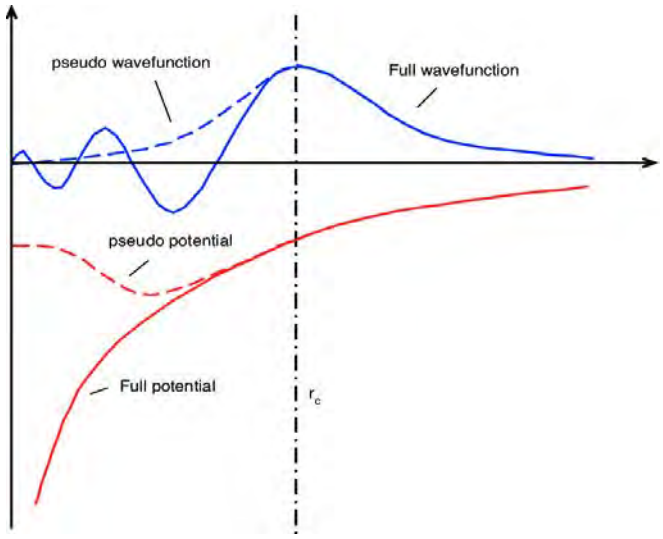

Figure 4: Schematic diagram of a pseudopotential (Ning, 2011).

The solid lines represent the smoother pseudopotential and its corresponding pseudo wave function, while the dashed lines depict the Coulomb potential and the highly oscillatory all-electron wave function in the vicinity of the atomic nuclei, Figure 4. In the pseudopotential approach, pseudo–potential and pseudo–wave function are designed to align with actual all–electron behavior beyond a certain cutoff radius r_c. This method avoids the difficulties that arise due to severe singularities and quick oscillations of the wave functions around the atomic nuclei (Bachelet and Filippetti, 2005). In the pseudopotential framework, the strong Coulomb potential is substituted with a weaker effective potential which precisely represents the system beyond the core region. This method eliminates problems such as singularities and complicated nodal structures around the nucleus, which makes calculations easier by focusing on the most important features and not getting stuck in the details of core electrons and high–frequency oscillations in the valence wave functions. Pseudopotentials are classified as either hard (small r_c, requiring more plane waves) or soft (large r_c, requiring fewer plane waves). The

ideal pseudopotential should be easy to use in calculations (soft), work well in various chemical environments (transferable), and computationally efficient (Vanderbilt, 1990).

Norm–conserving pseudopotentials preserve electronic charge of the system and are highly transferable, but they are computationally expensive (Hamann *et al.*, 1979). On the other hand, ultrasoft–pseudopotentials (Vanderbilt, 1990) reduce computational costs by using suitable charge density and kinetic energy cutoff values. The choice of pseudopotential depends on balance between accuracy and computational cost.

3.8 Spin–orbit coupling (SOC)

The motion of an electron around the nucleus (orbital motion) and its intrinsic spin, both generate magnetic fields. Interaction between spin of electron and its orbital motion is called spin–orbit coupling. It is a relativistic effect. SOC is very important that strongly influences the magnetic, electronic, and transport properties of solids and is important for spintronic applications (Hoffmann, 2013).

In the non–relativistic limit of the Dirac equation, the SOC Hamiltonian for a free electron moving in an electric field $\mathbf{E}$ is expressed as (Saue, 2005)

$$H_{\mathrm{SOC}} = \frac{e\hbar}{4m^2c^2}\,\boldsymbol{\sigma}\cdot(\mathbf{E}\times\mathbf{p}) \tag{3.48}$$

where, $\mathbf{p}$ is the electron momentum, m is the electron mass, c is the speed of light, and $\boldsymbol{\sigma}$ represents the vector of Pauli matrices. This interaction can be interpreted as an effective Zeeman coupling in the rest frame of a moving electron, in which the electric field produces an effective magnetic field

$$\mathbf{B}_{\mathrm{eff}} = \frac{1}{2mc^2}(\mathbf{E}\times\mathbf{p}) \tag{3.49}$$

which interacts with the electron's spin. In crystals, electric field arises from gradient of the crystal potential, $\mathbf{E} = -\nabla V(\mathbf{r})$, and is strongest near the atomic nuclei. Therefore, SOC mainly originates from regions close to the atoms.

SOC becomes particularly important in materials that lacking inversion symmetry. In crystals possessing both time–reversal and inversion symmetry, the electronic bands have spin-degenerate, such as $E(\mathbf{k},\uparrow) = E(\mathbf{k},\downarrow)$. Time-reversal symmetry requires $E(\mathbf{k},\uparrow) = E(-\mathbf{k},\downarrow)$, while inversion symmetry enforces $E(\mathbf{k},\uparrow) = E(-\mathbf{k},\uparrow)$. When inversion symmetry is broken, SOC can lift this spin degeneracy even in absence of external magnetic field, creating $E(\mathbf{k},\uparrow) \neq E(\mathbf{k},\downarrow)$. This gives rise to spin–momentum locking and chiral spin textures, which are central to many spintronic phenomena. Inversion symmetry often breaks at surfaces and interfaces.

The Au(111) surface is a well–known example where Rashba spin splitting was first seen (LaShell *et al.*, 1996). At a surface, electrons experience a confinement potential, $V(z)$, normal to the surface, creating an electric field $\nabla V = E_{\perp}\hat{z}$. For an electron moving in the surface plane with momentum $\mathbf{k}$, this produces an effective magnetic field proportional to $\nabla V \times \mathbf{k}$. The resulting spin–orbit interaction is described by the Rashba Hamiltonian (Rashba and Sheka, 1991)

$$H_R = \alpha_R \boldsymbol{\sigma} \cdot (\hat{z} \times \mathbf{k}) \tag{3.50}$$

where, α_R is the Rashba coupling strength.

Tight–binding and first–principles calculations have shown that the Rashba effect is not determined solely by the surface electric field. Instead, breaking inversion symmetry modifies orbital hybridization near the atomic nuclei, which makes the electron wavefunctions asymmetric and enhances SOC (Hortamani and Wiesendanger, 2012). As a result, magnitude of Rashba splitting strongly depends on local atomic structure and chemical environment at the surface.

3.9 Computational details

The calculations were performed with Quantum ESPRESSO code (see appendix A2) (Giannozzi *et al.*, 2009), which employs pseudopotential plane-wave methods within DFT (Thomas, 1927; Fermi, 1928). The PBE functional (Perdew *et al.*, 1996) was used for bulk materials, and PBEsol functional (Perdew *et al.*, 2008) was used for surface and layer calculations. We used a plane–wave expansion to show the wavefunctions with energy cutoff $E_{\text{cut}} = 70\,\text{Ry}$ and charge density cutoff $\rho_{\text{cut}} = 560\,\text{Ry}$ (see Appendix A4.1, Figure A_1). Ultra-soft Vanderbilt-type pseudopotentials (USPPs) were employed to implement valence electron–atomic core interactions (Langreth and Perdew, 1980). We used a $14 \times 14 \times 14$ k-point mesh for bulk calculations in the first Brillouin zone (see Appendix A4.2, Figure A_2) (Monkhorst and Pack, 1976). $12 \times 12 \times 1$ was used for surface calculations and a $14 \times 14 \times 1$ mesh was used for monolayer calculations. For Eu– and Y–doped $SmMnO_3$, a $14 \times 14 \times 14$ mesh was used for bulk calculations, while a $12 \times 12 \times 12$ mesh was adopted for Sr_2ZrMoO_6 to calculate its elastic and thermal properties. The convergence thresholds were set to $E_{tot} = 10^{-6}$ eV and 10^{-3} eV/Å for atomic forces.

The stress–strain method was employed to determine the elastic constants by introducing small distortions to optimise unit cells (Golesorkhtabar *et al.*, 2013). The Debye temperature was determined using the average sound velocity derived from longitudinal and transverse elastic wave velocities (Anderson, 1963). A vacuum gap of 15 Å was incorporated for surface and layer computations of $ZrSiO_3$ to avoid interactions between periodic images in surface and two dimensional systems. GGA+U and SOFC methods were used

to study the magnetic characteristics of pure and Eu and Y doped $SmMnO_3$. The GGA (Perdew *et al.*, 1996) was applied to calculate electronic band structures for $ZrSiO_3$, Sr_2ZrMoO_6, and Eu– and Y– doped $SmMnO_3$. To account for strong electron-electron interactions in Mn–3d and Sm–4f orbitals, the GGA+U approach (Anisimov *et al.*, 1991) was employed. We performed non–self-consistent calculations to obtain the DOS and PDOS (see Appendix A3.3). For bulk $ZrSiO_3$, pressure-dependent properties were studied under isotropic pressures ranging from 0–100 GPa, while pressures from 0 to 80 GPa were applied to Sr_2ZrMoO_6.

Chapter 4

4. RESULTS AND DISCUSSION

We describe the basic findings of the current study with reference to relevant experimental findings in this chapter. This study examines structural, electronic, optical, mechanical, and magnetic behavior of Zr–based two–and three–dimensional perovskites, double perovskites, and $SmMnO_3$ perovskite materials. Computational analyses were conducted using spin-polarized DFT in Quantum ESPRESSO (QE) package. We did systematic convergence tests to find the best values for kinetic energy cutoff, k-points, and lattice parameters for stable structures. We analysed the electronic and magnetic properties via band structure, DOS, and PDOS analysis. Stress–strain method was employed to determine elastic constants.

This chapter addressed following sections:

- **Section 4.1**: Structural stability of bulk $ZrSiO_3$ at varying pressures, its layered configurations, surface terminations, and the structural properties of Eu- and Y-doped $SmMnO_3$ and Sr_2ZrMoO_6 perovskites.
- **Section 4.2**: Electronic properties of the studied materials based on band structure calculations.
- **Section 4.3** : Optical properties , including dielectric constants, refractive indices, reflectance, and absorptance of the study materials.
- **Section 4.4**: Elastic properties of the investigated materials.
- **Section 4.5** : Thermal properties and related analysis.
- **Section 4.6**: Magnetic properties of Eu– and Y– doped $SmMnO_3$ and Sr_2ZrMoO_6 perovskites.

4.1 Structral properties

4.1.1 Bulk $ZrSiO_3$ at different pressures

The $ZrSiO_3$ perovskite structure exhibits the symmetric cubic structure with $Pm\bar{3}m$ space group.

Table 1: Lattice constant (a_0), ground-state energy (E_0), minimum volume (V_0), cohesive energy (ΔE), and bond lengths of $ZrSiO_3$ under different pressures.

P (GPa)	a_0 (Å)	E_0 (Ry) $\times 10^{-3}$	V_0 (Å^3)	(ΔE) (eV/atom)	Zr–O (Å)	Si–O (Å)	Zr–Si (Å)
0	3.627	-472.512	47.707	-7.592	2.547	1.801	3.119
20	3.617	-472.512	47.321	-7.592	2.547	1.801	3.119
40	3.607	-472.513	46.948	-7.593	2.547	1.801	3.119
60	3.598	-472.513	46.594	-7.594	2.547	1.801	3.098
80	3.589	-472.514	46.249	-7.596	2.542	1.801	3.098
100	3.581	-472.516	45.917	-7.602	2.540	1.801	3.077

Table 1 displays the structural parameters of the optimized structure of bulk $ZrSiO_3$, which includes the lattice constant (a_0), ground state energy (E_0), minimum volume (V_0), cohesive energy (ΔE), and bond lengths at pressure range 0 – 100 GPa. As shown in Figure 5a, the linear compressibility of this compound can be explained by the gradual decline in ratio of a/a_0 and V/V_0 as pressure increases.

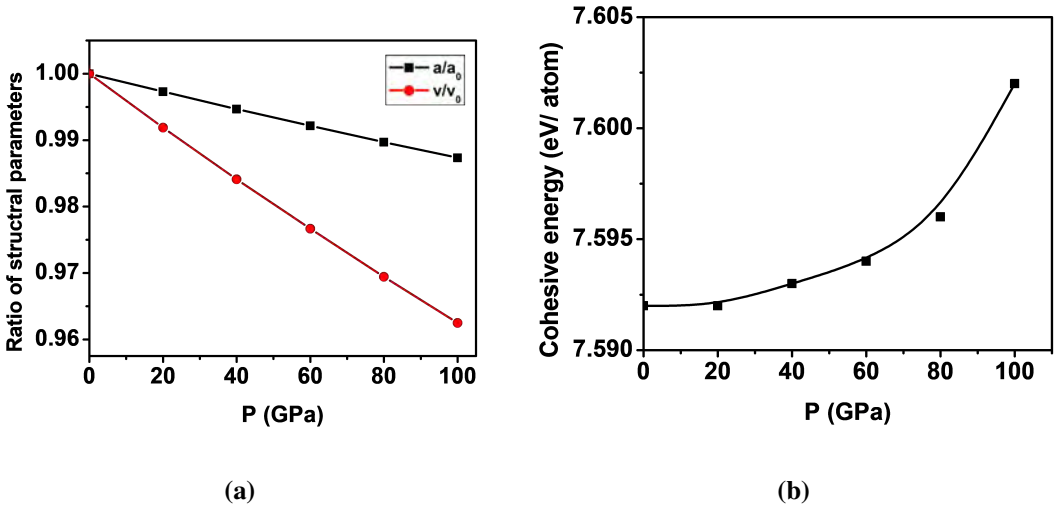

Figure 5: (a) Ratios of structural parameters (a/a_0 and V/V_0), (b) cohesive energy for bulk $ZrSiO_3$ under different pressures (Pokharel *et al.*, 2024).

The covalent nature of the silicon–oxygen tetrahedra in $ZrSiO_3$ leads to decrease in

bond length under isotropic pressure. Figure 5b shows a nonlinear relationship between cohesive energy and pressure. The cohesive energy increases as a result of the reductions in bond lengths and the strength of interactions. For instance, the Zr–O bond length decreases from 2.547 Å to 2.540 Å when pressure increases from 0 GPa to 100 GPa. Similarly, the Zr–Si bond length decreases from 3.119 Å at 0 GPa to 3.077 Å at 100 GPa. This consistently decrease in bond length with increasing pressure is due to lattice contraction and increased covalent character (Hao *et al.*, 2015). After removal of pressure, the material retains its initial state that indicates the absence of hysteresis loss during alternate compression–expansion cycles.

4.1.2 Different layered configurations

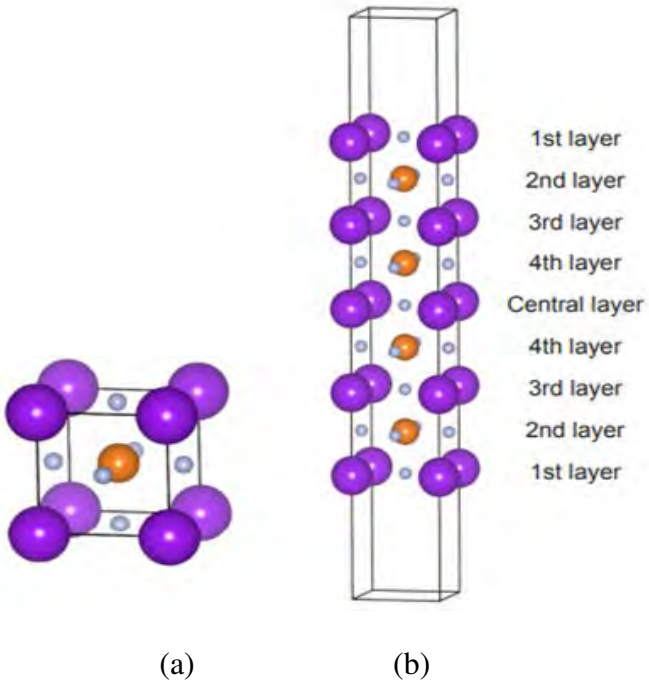

Figure 6: (a) Primitive unit cell, (b) four-layer unit cell of the $ZrSiO_3$ (Pokharel *et al.*, 2024).

The primitive unit cell of $ZrSiO_3$ has chemical formula ABX_3, it has three different atomic locations. Zirconium (Zr) occupies in the A site, where it lies in the middle of an octahedral coordination environment and forms bonds with nearby oxygen atoms. Silicon (Si) is typically located on the corners of the structure (B) site, where it forms silicon–oxygen tetrahedra that constitute a tetrahedral network. The oxygen atoms are located at the X–sites, where they make both the silicon–oxygen tetrahedra and the Zr-centered octahedral coordination, Figure 6a.

A 4-layered unit cell is formed by alternating SiO_2 and ZrO layers in a specific sequence, such as SiO_2-ZrO-SiO_2-ZrO, or in the reverse order. This configuration results in a

layered structure with periodic repetition of SiO_2 and ZrO layers. The SiO_2 layer is made up of a tetrahedral network of Si–O bonds, with each Si atom bonded to 4 oxygen atoms, which keeps the structural stable. In ZrO layer, oxygen atoms interact with Zr, with the Zr atoms situated between the SiO_2 layers, enhancing the overall stability and integrity of the compound, Figure 6b.

4.1.2.1 Surface energy

Surface energy estimates energy associated with formation of surface due to bonds breaking. It is the amount of work per unit area that is needed to break the bonds between molecules and create a new surface (Meyer *et al.*, 1999). To determine the appropriate slab model thickness, the surface energy was evaluated for slabs consisting of different numbers of layers. The surface energy (γ) of the material is given by (Ishikawa and Uemori, 1999)

$$\gamma = \frac{E_{\text{slab}} - nE_{\text{bulk}}}{2A} \tag{4.1}$$

where A is minimum surface area, E_{slab} and E_{bulk} are the energies of slab layer and bulk, respectively and n is number of layers.

Table 2: Surface area (A), total energy (E_{tot}), energy per-atom (E_0), and surface energy (E_s) of $ZrSiO_3$ of different layers

No of layers	Area A ($\times 10^{-20}$ m^2)	E_{bulk} (Ry)	E_{Tot} (Ry)	E_0 per atom (Ry)	Surface energy (J/m^2)
1	5.915	-472.512	-472.411	-94.482	2.975
2	5.915	-472.512	-944.902	-94.490	3.274
3	5.915	-472.512	-1417.407	-94.494	3.382
4	5.915	-472.512	-1889.912	-94.496	3.356
5	5.915	-472.512	-2362.452	-94.498	3.357

The calculated values of A, E_{Tot}, E_0, and E_s for different layers of $ZrSiO_3$ are presented in Table 2. The stability of [001] surface termination was generally examined by surface energy calculations, which exhibit a distinct convergence with increasing slab thickness. The surface energy increases rapidly upto third layer and beyond this layer it remains constant, Figure 7a. This shows that the surface energy has converged for the three layers. Consistent with this observation, the cohesive energy decreases significantly upto three layer and then becomes stable with the increases in number of layers, Figure 7b. Cohesive energy convergence provides further evidence that bulk-like bonding is sufficiently restored after three layers. These results show that a three-layer slab is

sufficient to describe the surface geometry of both ZrO–terminated and SiO_2–terminated slab models along the [0 0 1] direction.

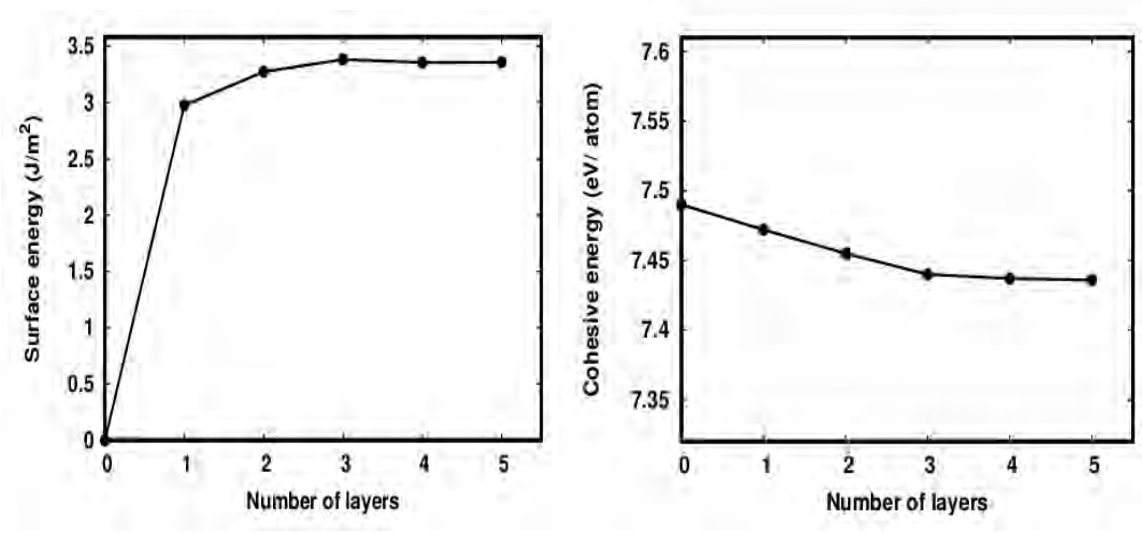

(a) **(b)**

Figure 7: (a) Surface energy per cell, (b) cohesive energy per atom versus the number of layers in $ZrSiO_3$ (Pokharel *et al.*, 2024).

4.1.2.2 Surface relaxation of $ZrSiO_3$

In the slab model, surface relaxation occurs when atoms or ions rearrange relative to their bulk positions due to reduced coordination and the tendency to minimize surface energy. Consequently, surface relaxation alters the spacing between adjacent layers near the slab surface (Sun *et al.*, 2002). In this study, we investigate surface and atomic relaxations of $ZrSiO_3$ (001) surfaces with ZrO– and SiO_2– terminations. The atomic relaxation (ΔZ_i) of the i^{th} layer can be given as (Beeler *et al.*, 2020)

$$\Delta Z_i = Z_{i,\text{relaxed}} - Z_{i,\text{unrelaxed}} \tag{4.2}$$

where, $Z_{i,\text{unrelaxed}}$ is the unrelaxed Z-coordinate and $Z_{i,\text{relaxed}}$ is the relaxed Z-positions of Zr, Si, and O atoms in the i^{th} layer. Positive values signify relaxations toward the vacuum region, and negative values suggest relaxations toward the bulk (de Lazaro and Longo, 2004). In the same way, if $Z_i > Z_{\text{unrelaxed}}$, the atom has relaxed toward the vacuum region, whereas if $Z_i < Z_{\text{unrelaxed}}$, indicates that the atom has relaxed toward the bulk (Skriver and Rosengaard, 1992).

For the first layer from the surface, the calculated ΔZ values for both Zr and O atoms are 0.001 Å, indicating a slight outward relaxation toward the vacuum region. The Si atom shows a very small outward movement (ΔZ = 0.001 Å). In the first layer, the Si atom shows a very small outward movement (ΔZ = 0.001 Å). In the second layer, the atomic

displacements were slightly larger with Zr, Si, and O atoms, each moving outward by ΔZ = 0.002 Å. This means the outward relaxation is stronger than in first layer. In the third layer, the atomic displacements of Zr, Si, and O atoms were again small (ΔZ = 0.001 Å). This suggests only minor outward relaxation toward the vacuum region, the Si atom shows a very small outward movement. Overall, these results indicate that atoms undergo systematic outward relaxation as they approach the surface of $ZrSiO_3$. Such behavior reflects the tendency of surface atoms to rearrange to minimize surface energy of the structure.

Bader charge analysis shows how electronic charge is spread around in a system. The calculated values of Q for Zr, Si, and O atoms in bulk $ZrSiO_3$ material are +0.27|e|, +1.02|e|, and −0.43|e|, respectively. This shows how charge is transferred and localized around each atomic species. For the surface layers, the Bader charges (Q) of Zr, Si, and O atoms in the 1^{st}, 2^{nd}, 3^{rd}, and 4^{th} layers are calculated. The corresponding Bader charges are $(+0.32\,|e|,\ +1.08\,|e|,\ -0.48\,|e|)$, $(+0.51\,|e|,\ +1.19\,|e|,\ -0.47\,|e|)$, $(+0.56\,|e|,\ +1.07\,|e|,\ -0.44\,|e|)$, and $(+0.76\,|e|,\ +0.91\,|e|,\ -0.46\,|e|)$, respectively. This difference in Bader charges between layers confirms the redistribution of electronic charge near the surface, which demonstrates the layer–dependent electronic behavior of $ZrSiO_3$ perovskite.

4.1.3 Surface termination models and their relaxations

In the surface termination models of perovskites, the atoms constituting the bulk material are distributed in a specific pattern at the outermost layers, which can vary depending on the crystallographic orientation (Tomar *et al.*, 2018). For $ZrSiO_3$ in (001) orientation, the termination slab models are constructed by cleaving bulk material along [001] direction and adding a vacuum of 15 Å to prevent periodic images. Oxygen (O) atoms form Zr-O and Si-O bonds and resulting in two distinct termination models: silicon-dominant SiO_2 – termination and zirconium-dominant ZrO– termination models (Pokharel *et al.*, 2024). The ZrO-terminated slab comprised a supercell with 17 atoms, Figure 8a, while the SiO_2-terminated slab contained 18 atoms, Figure 8b. The surface energy for several slab thicknesses were then estimated to decide the size of the slab models. Surfaces with two possible terminations emerged concurrently when surface energy was distributed equally on both surfaces. The electronic states of perovskites are significantly influenced by surface termination, which further influences the behaviour of charge carriers and overall properties of the material.

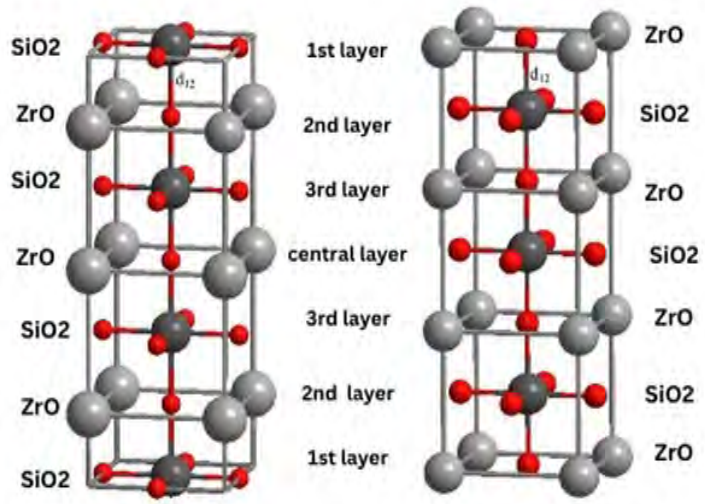

(a) (b)

Figure 8: (a) SiO_2-terminated, (b) ZrO-terminated three-layer slab of $ZrSiO_3$ (Pokharel *et al.*, 2024).

To analyze the slab model more precisely, total energy per atom and surface energy were examined as functions of slab thickness. Relaxation analysis was performed on the [0 0 1] surfaces of $ZrSiO_3$, allowing all atoms in each layer on both sides of this slab to move freely along directions orthogonal to the surface. Surface and atomic relaxations for the $ZrSiO_3$ [0 0 1] surfaces were analyzed for both ZrO–and SiO_2–terminated configurations. The atomic relaxations relative to the bulk lattice positions were evaluated for these terminations. Due to inherent symmetry of the slab, atomic displacements (Δz) in top three layers mirrored those in the bottom three layers. For SiO_2-terminated surfaces, both oxygen (O) and silicon (Si) atoms in the first layer (Δz = -1.175 Å for O and Δz = -1.256 Å for Si) and third layer (Δz = -0.395 Å for O and Δz = -0.675 Å for Si) experienced inward relaxation, whereas in the second layer, O atoms (Δz = 0.753 Å) experienced outward relaxation and that of Si (Δz = -1.030 Å) still experienced inward relaxation. For ZrO-terminated slabs, atoms of O in all three layers exhibited outward relaxations, with (Δz = 0.047 Å, 0.061 Å, 0.030 Å for the 1^{st}, 2^{nd}, and 3^{rd} layers, respectively), whereas Zr exhibited inward relaxations, with Δz = -0.041 Å, -0.098 Å, and -0.329 Å for the corresponding layers. Notably, the second layer of ZrO–terminated surface displayed the most significant atomic relaxations, while for the SiO_2–terminated surface largest atomic relaxations were observed in the first-layer atoms.

To verify the convergence of charge distribution with slab thickness, Bader charge

distributions were calculated for different model geometries (Cargnoni *et al.*, 2000). The analysis expressed in Table 3, revealed that the charge distribution converge to values lower than the formal ionic charges of $+4|e|$ for oxygen, $+4|e|$ for silicon, and $-2|e|$ for zirconium. The charge difference between the bulk and the internal layers was small, being less than $+0.1|e|$, $+0.2|e|$, $+0.1|e|$ for O, Si, and Zr atoms, respectively. The SiO_2 molecule with a terminated surface model has partial charges of $+0.39|e|$ on Si and partial negative charges of $-0.43|e|$ on O. This charge distribution showed that the Si–O bonds are polar covalent, meaning that the electrons are not shared evenly, which gives Si a little positive charge and O a small negative charge (Sethi and Satake, 2010).

Table 3: Atomic displacements (Δz) and Bader charge distribution (Q) for ZrO– and SiO_2–terminated $ZrSiO_3$ slabs

	SiO_2 termination		ZrO termination	
	Si	O	Zr	O
1^{st} layer				
Δz (Å)	-1.256	-1.175	-0.041	0.047
Q ($\|e\|$)	0.911	7.570	10.309	7.572
2^{nd} layer				
Δz(Å)	-1.030	0.753	-0.098	0.061
Q ($\|e\|$)	10.176	7.571	0.927	7.571
3^{rd} layer				
Δz (Å)	-0.675	-0.395	-0.329	0.030
Q ($\|e\|$)	1.181	7.513	10.483	7.513
Central layer				
Q ($\|e\|$)	0.932	7.585	10.398	7.585
Bulk				
Q ($\|e\|$)	1.017	7.570	10.398	-

In the ZrO– termination model, Zr had a partial positive charge of $+1.19|e|$, and oxygen O had a partial negative charge of $-0.43|e|$. The charge distributions indicate that both SiO_2–and ZrO– terminated surfaces exhibit partially covalent Si–O bonds, while the Zr–O bonds show a comparatively weaker covalent nature (Pokharel *et al.*, 2024). Due to inherent symmetry, the relaxation analysis revealed that atomic displacements in the upper three layers were comparable to those in the lower three layers. In particular, oxygen atoms in topmost layer of ZrO-terminated surfaces relaxed outward, whereas

those in the 1^{st} layer relaxed inward. Both ZrO– and SiO_2–terminated $ZrSiO_3$ [001] surfaces show outward relaxation of second-layer oxygen atoms, while SiO_2–terminated surfaces exhibit the largest relaxations in the first layer.

4.1.4 $ZrSiO_3$ monolayer

Our study examines the formation of the monolayer of $ZrSiO_3$ from its 3D perovskite structure using visualization and modeling tools such as VESTA. First, the 3D bulk structure of $ZrSiO_3$, consisting of an arrangement of corner-sharing BX_6 octahedra was optimized.

To construct the monolayer, the interlayer linkages among the octahedra are removed by manipulating the crystal along the z-axis, and introducing a 15 Å vacuum layer in VESTA to simulate the isolation of a single layer. This vacuum stops interaction between repeated slab images and ensures the system behaves like an isolated monolayer. In this stage, the $ZrSiO_3$ monolayer slab was optimized so that the atomic positions could relax to the minimum total energy state. This technique considers structural modifications that happen when dimensions are reduced, changes in bond lengths or bond angles within the monolayer.

As shown in Figure 9, the 2D crystalline structure contains BX_6 shared X anions that connect octahedra in a plane. The standard formula of two-dimensional layered perovskites looks like $(A')_mA_nB_nX_{3n+1}$, in which A′ represents heavy cation that is divalent when $m = 1$ or monovalent when $m = 2$, which determines whether the structure forms a bilayer or monolayer. A denotes a smaller cation located within the perovskite layer, while B is a metal cation positioned at center of the BX_6 octahedra. X is an anion, typically a halide or oxygen, that coordinates with the B cation. The parameter m indicates number of A′ cations, and n indicates number of BX_6 octahedral layers.

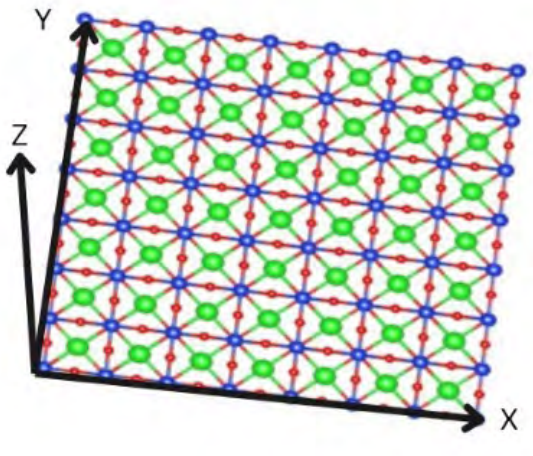

Figure 9: Optimize monolayer of $ZrSiO_3$ (Pokharel *et al.*, 2024b).

Table 4: Strain energy (ΔU), cohesive energy (ΔE), and bond lengths of a $ZrSiO_3$ monolayer at different strain

Strain (%)	ΔU (eV)	ΔE (eV/atom)	Zr–O (Å)	Si–O (Å)	Zr–Si (Å)
6	2.765	7.625	2.722	2.041	3.265
4	1.106	7.699	2.672	2.004	3.235
2	0.394	7.748	2.620	1.965	3.208
0	0.000	7.763	2.569	1.927	3.182
-2	0.410	7.739	2.517	1.889	3.121
-4	1.088	7.666	2.466	1.849	3.046
-6	2.766	7.525	2.415	1.811	2.937

After relaxation of $ZrSiO_3$ monolayer, the optimized structural properties, such as bond length, strain energy, and cohesive energy at different strain percentages (±6%), were computed and are summarized in Table 4. The tabulated values show that compressive strain brings atoms closer, shortening the bond lengths, Figure 10a, whereas tensile strain pushes atoms apart, resulting in longer bond lengths.

In general, cohesive energy measures the bonding strength and mechanical stability of materials. Higher cohesive energy means that stronger interatomic interactions and greater structural stability. Whereas lower values correspond to weaker bonds and less stable structure. For the monolayer, it is given by (Voigt, 1928)

$$E_{\text{coh}} = E_{\text{tot}} - \sum_i n_i E_i \tag{4.3}$$

where E_{coh} is cohesive energy, E_{tot} represents total energy of monolayer, E_i represents energy for an isolated atom, n_i represents number of atoms. The cohesive energy decreases as the applied strain deviates from the equilibrium state, indicating a reduction in the structural stability of the $ZrSiO_3$ monolayer under both compressive and tensile strains. However, the decrease in cohesive energy is smaller under compressive strain than under tensile strain, suggesting that the monolayer retains slightly higher stability under compression. Furthermore, the consistency of the cohesive energy values at ±2% strains suggest that the material responds symmetrically to both compressive and tensile strains, as illustrated in Figure 10b.

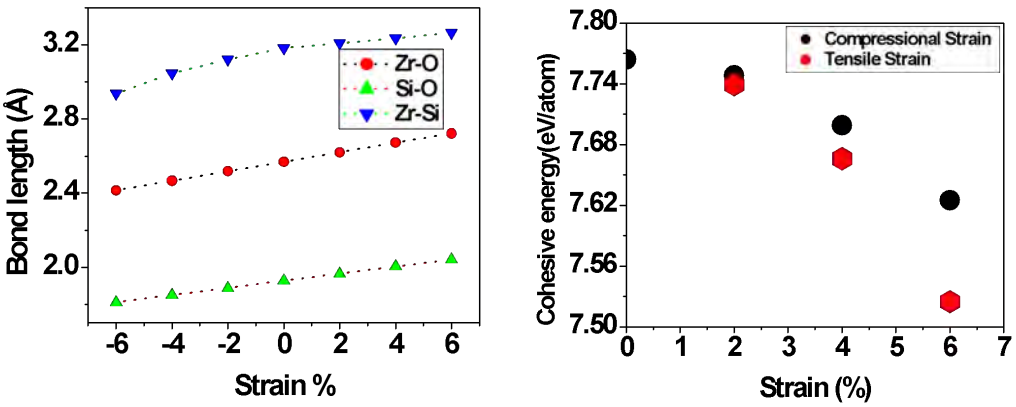

(a) **(b)**

Figure 10: Variation of (a) bond length, (b) cohesive energy with strain (Pokharel *et al.*, 2024b).

Strain energy

In the monolayers, there are no bulk interactions, therefore all atoms are exposed at the surface, and there are no interior atoms to protect the material from strain. Also, 2D materials are capable of handling bigger elastic deformations than their bulk counterparts. The study of strain energy gives us important information about how strain affects the mechanical and structural stability of materials when they deform. The strain energy per atom (E_s) is given by (Huang *et al.*, 2015)

$$E_s = \frac{E_{\text{tot}} - E_0}{n} \tag{4.4}$$

where E_{tot} stands for the total energy under strain, E_0 is total energy without strain, and n represents number of atoms.

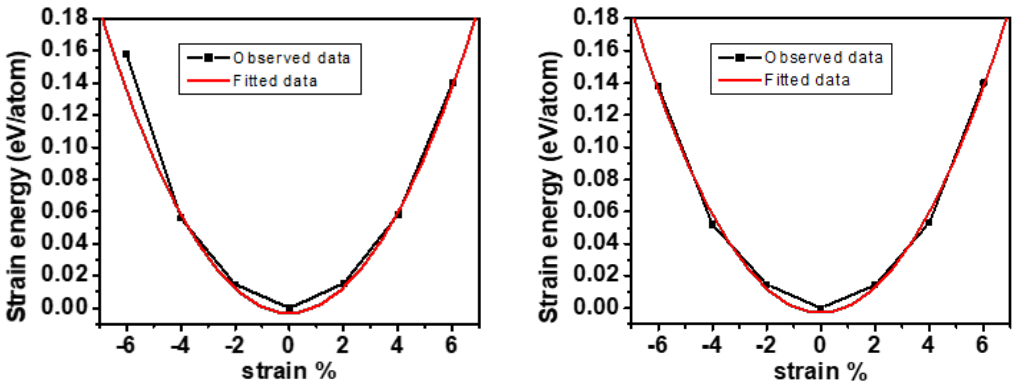

(a) **(b)**

Figure 11: Variation of strain energy of $ZrSiO_3$ monolayer with strain in the (a) x and (b) y directions (Pokharel *et al.*, 2024b).

The uniaxial strain (ϵ_1) was applied on both the x and y directions in increments of 2%, ranging from −6% to +6%, in order to analyze the strain energy under small elastic deformations. The strain energy versus strain graphs for both directions are displayed in Figure 11(a, b). This study shows that with a zero strain value ($\epsilon = 0$), the system reaches its minimum energy state, which shows that the system is in equilibrium at that state and strain energy increases in both compressive and tensile strains. This material exhibits harmonic approximation with a linear stress-strain relationship within -2% to +2% strain. Beyond this range, the presence of the higher-order term causes the curves to deviate from harmonic behavior. A smaller area on the x–direction curve means greater material stability in that direction.

4.1.5 Eu– and Y– doped $SmMnO_3$ perovskite

This section discusses the effects of substitutional doping of europium (Eu) and yttrium (Y) in the $SmMnO_3$ compound. The pristine $SmMnO_3$ material has a general formula of ABO_3, with Sm occupying A–site and Mn as B-site, Figure 12a. If cations of various dimensions are substituted at either A or B sites, the cubic structure symmetry may be changed to tetragonal, orthorhombic, or monoclinic (Jayakrishnan *et al.*, 2021). Since, the atomic radii of Eu and Y are close to that of Sm; the substitution at the Sm atom results only in slight variations in the lattice parameters, thereby preserving the cubic structural symmetry Figure 12b.

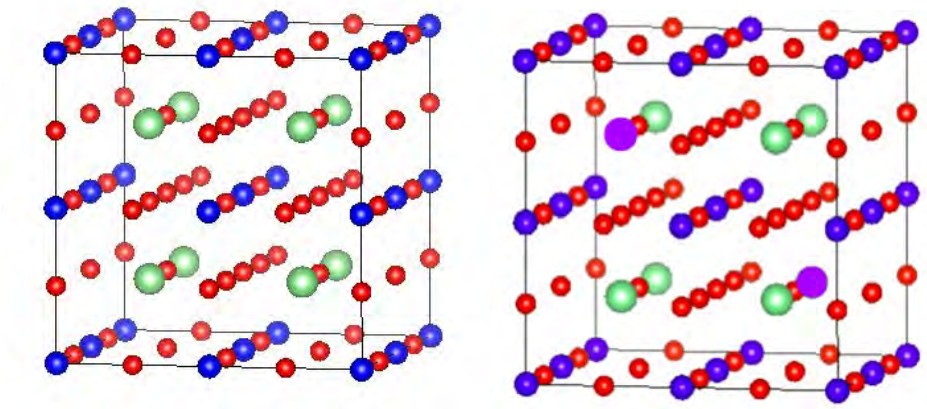

(a) **(b)**

Figure 12: Supercell models of (a) pristine, (b) Eu- or Y-substituted $SmMnO_3$ (Pokharel *et al.*, 2024c).

The Goldschmidt tolerance factor (t) for a doped perovskite is given by (Tidrow, 2014)

$$t = \frac{(1-x)r_A + xr_{A'} + r_O}{\sqrt{2}\,(r_B + r_O)}, \tag{4.5}$$

where x is the concentration of the dopant ion at the A-site, r_A is the ionic radius of the

original A-site cation, $r_{A'}$ is the ionic radius of the substituted (dopant) A-site cation, r_B is the ionic radius of the B-site cation, and r_O is the ionic radius of the oxygen anion. For a doped perovskite, the ideal value of the tolerance factor is $t = 1$, which corresponds to an ideal cubic perovskite structure. The ideal value remains the same for both doped and undoped systems. However, doping changes the calculated tolerance factor because it modifies the average ionic radius of the A-site cation through partial substitution. The calculated tolerance factors for pristine and Eu- and Y-doped $SmMnO_3$ lie within this range, Table 5, confirming that the perovskite structure remains stable at a 25% doping level. The tolerance factor goes down at higher amounts of Eu and Y doping. This shows that the shape of $SmMnO_3$ becomes less stable. When Eu is added, the tolerance factor decreases linearly as the amount of dopant increases. This means that the lattice geometry changes slowly and uniformly. However, Y substitution results in a more rapid and nonlinear decrease of the tolerance factor, indicating that the crystal structure responds more strongly and rapidly to Y– doping, Figure 13a.

The cohesive energy (ΔE) examines the stability of the complex by measuring the energy needed to separate into individual atoms. It is given by (Philipsen and Baerends, 1996)

$$\Delta E = \frac{E_{\text{tot}} - \left(E_A + E_B + E_{\text{O}_2}\right)}{n} \tag{4.6}$$

where E_{tot} is total energy of compound, E_A, E_B and E_{O_2} are energies of isolated atoms of A-site, B-site cations, and oxygen, respectively and and n represents numbers of atoms in the formula unit. The negative cohesive energies observed for pristine and doped materials suggest that they are thermodynamically stable.

Table 5: Lattice constants, tolerance factor, and cohesive energies of pure and Eu– or Y–doped $SmMnO_3$

Compound	Lattice Constant (Å)	Tolerance Factor (t)	Cohesive Energy (eV/atom)
Bulk $SmMnO_3$	7.391	0.873	-6.135
12.5% Eu doped	7.384	0.876	-6.429
25.0% Eu doped	7.375	0.879	-6.525
12.5% Y doped	7.379	0.870	-7.265
25.0% Y doped	7.367	0.867	-7.856

The value of t for both Eu– and Y– doped $SmMnO_3$ increases with decreasing bond lengths as dopant concentrations increase. The cohesive energy of $SmMnO_3$ increases continuously as the concentrations of Eu– and Y– doping increase (6.135, 6.429, and 6.525 eV/atom for Eu–doping while are 6.135, 7.265 and 7.856 eV/atom for Y–doping), which suggests higher structural stability with doping. When Eu is introduced, the cohesive energy increases gradually because ionic radius of Eu^{3+} is little less than that of Sm^{3+}. It represents a modest lattice contraction and stronger Eu–O bonding without inducing significant structural distortion. In contrast, the cohesive energy increases more rapidly for Y– doping because Y^{3+} has a smaller ionic radius, which causes more lattice deformation. These results indicate that doped $SmMnO_3$ exhibits more structural stability than the pristine $SmMnO_3$, Figure 13b.

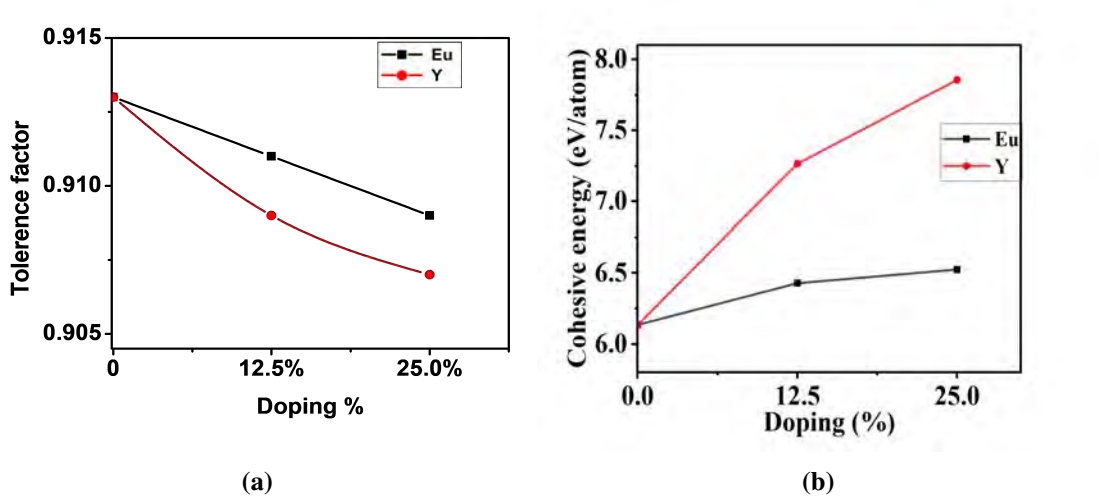

Figure 13: Variation of (a) tolerance factor and (b) cohesive energy of Eu- and Y-doped $SmMnO_3$ (Pokharel *et al.*, 2024b)

4.1.6 Sr_2ZrMoO_6 double perovskite at different pressure

The pressure-dependent structural parameters of tetragonal Sr_2ZrMoO_6, including the lattice constants (a and c), ground state energy (E_0), minimum volume (V_0), heat of formation (ΔH), were evaluated in the range 0–80 GPa. The relative lattice parameters a/a_0, c/c_0, and V/V_0 exhibit monotonic decrement with rise in pressure, which shows the expected compression of the crystal lattice, Figure 14a. At lower pressures it follows a linear trend, but at higher pressures it starts to deviate slowly because the lattice becomes stiffer under compression.

The tolerance factor values of Sr_2ZrMoO_6 at different pressures have been evaluated using Equation (4.5), indicating structural stability and deformation tolerance. This material remains stable across the preferred pressure range. This small variation in the tolerance factor (t) reflects the reliability of Sr_2ZrMoO_6 under varying pressure

conditions.

The formation energy (ΔH_f) of Sr_2ZrMoO_6 perovskite is expressed as (Ray *et al.*, 2021)

$$\Delta H_f = \frac{E_{\text{total}}(Sr_2ZrMoO_6) - (2E_{Sr} + E_{Zr} + E_{Mo} + 6E_O)}{6} \tag{4.7}$$

Here, $E_{\text{total}}(Sr_2ZrMoO_6)$ is the equilibrium energy of the Sr_2ZrMoO_6 perovskite, while E_{Sr}, E_{Zr}, E_{Mo}, and E_O represent respective energies for strontium, zirconium, molybdenum, and oxygen atoms in their bulk forms.

Table 6: Lattice constants (a_0, c_0), volume (V_0), normalized ratios (a/a_0, c/c_0, V/V_0), and heat of formation (ΔH) of tetragonal Sr_2ZrMoO_6 under different pressures

P (GPa)	a (Å)	c (Å)	V (Å^3)	a/a_0	c/c_0	V/V_0	ΔH (eV/atom)
0	4.066	8.232	136.086	1.000	1.000	1.000	-3.251
20	4.046	8.174	133.908	0.995	0.993	0.984	-3.249
40	4.025	8.133	132.819	0.990	0.988	0.976	-3.248
60	4.009	8.092	132.040	0.986	0.983	0.970	-3.244
80	3.993	8.059	131.459	0.982	0.979	0.966	-3.240

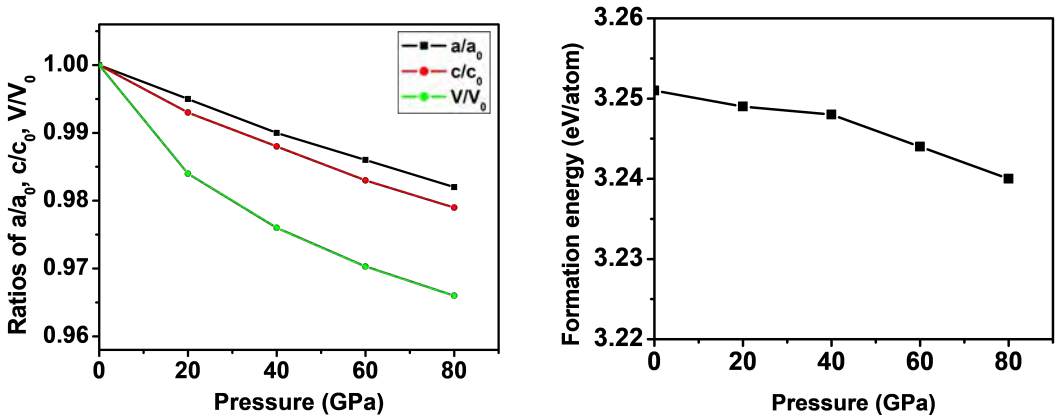

(a) **(b)**

Figure 14: Variation of (a) lattice parameter, (b) formation energy of Sr_2ZrMoO_6 with pressure (Pokharel *et al.*, 2025).

The formation energy (ΔH_f) of Sr_2ZrMoO_6 ranges from -3.251 to -3.240 eV/atom, Table 6. This negative value of ΔH_f confirms thermodynamic stability of Sr_2ZrMoO_6, which indicates that the compound can be synthesized experimentally under pressures up to 80 GPa. The formation energy exhibits a nonlinear decrement with increasing pressure. This tendency has been related to the decrease in structural distortion along with the stabilization of bond lengths and bond angles, Figure 14b. Furthermore, the same pattern of variation has been noticed on decreasing pressure, indicating no hysteresis loss during the expansion and compression cycles.

4.2 Electronic properties

4.2.1 The bulk material at different pressures

The electronic band structure and PDOS of cubic $ZrSiO_3$ perovskite are studied along the Γ–X–M–R path in the first Brillouin zone. At zero pressure, $ZrSiO_3$ exhibits an indirect band gap of 3.164 eV. This gap grows steadily with pressure, reaching up to 3.261, 3.287, 3.318, 3.328, and 3.339 eV at 20, 40, 60, 80, and 100 GPa, respectively, Figure 15(a–f).

When pressure increases 0 –100 GPa, due to compression the atoms of $ZrSiO_3$ move closer to each other, which increases orbital overlap. This increased overlap makes the bonding and anti–bonding interactions stronger. This results in an upward shift of CBM and downward shift of the VBM. Consequently, E_g value progressively increases from 3.164 eV to 3.339 eV. The similar tendency has been observed for cesium lead iodide perovskites (Cao *et al.*, 2018).

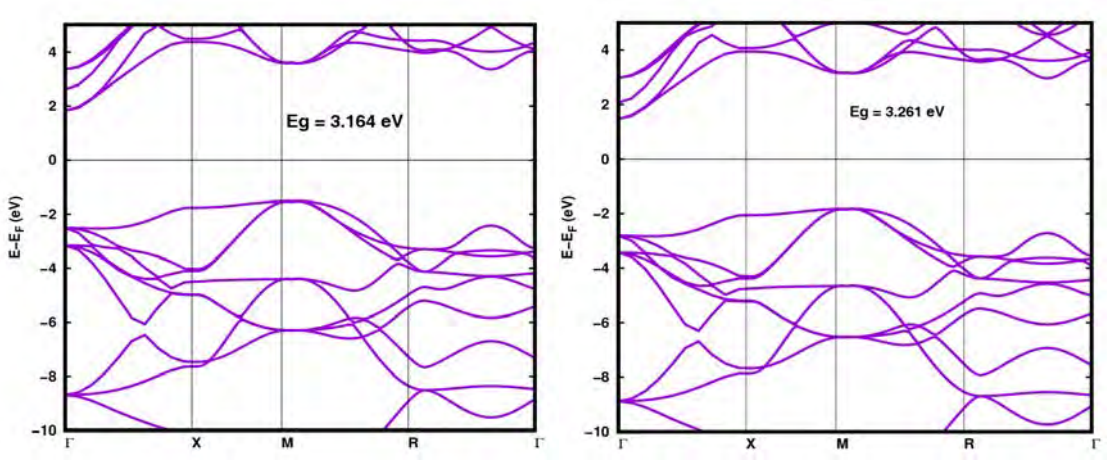

(a) **(b)**

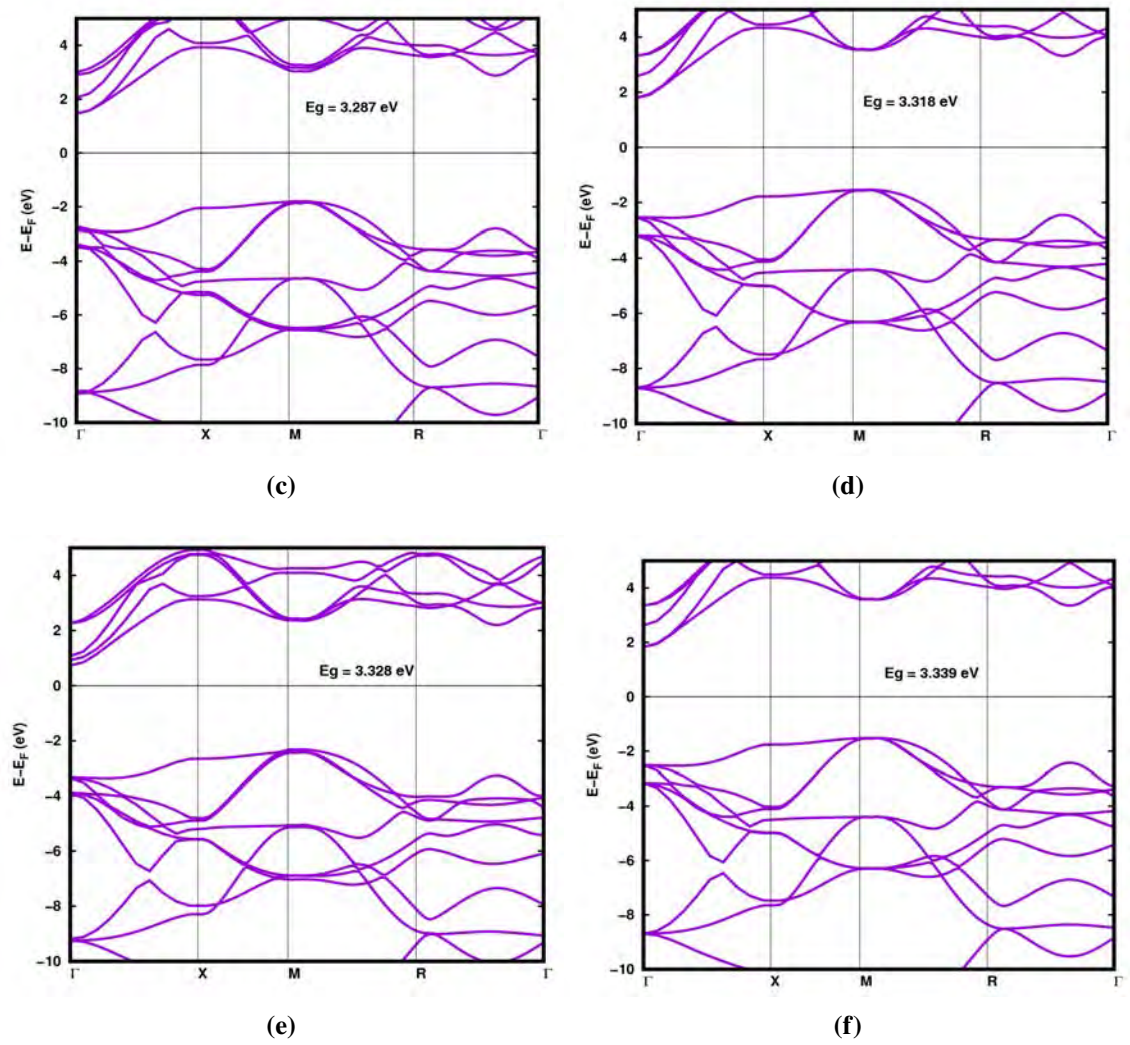

Figure 15: Band structures of bulk $ZrSiO_3$ at (a) 0 GPa, (b) 20 GPa, (c) 40 GPa, (d) 60 GPa, (e) 80 GPa, and (f) 100 GPa pressures (Pokharel *et al.*, 2024).

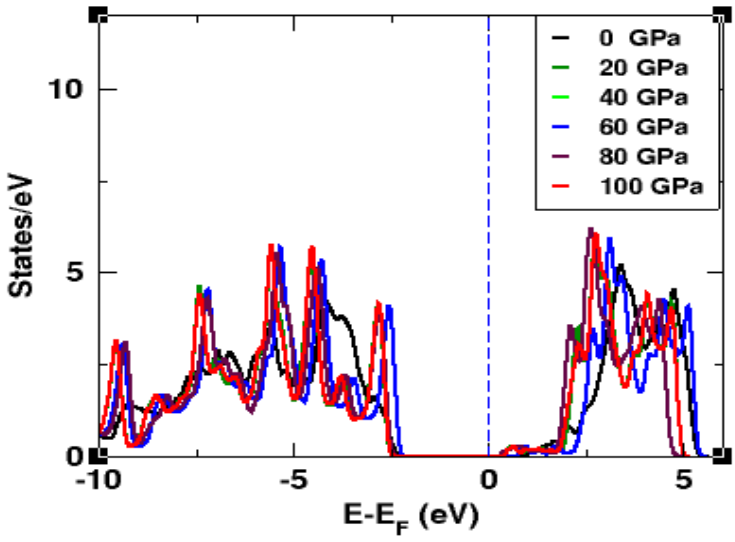

Figure 16: Total density of states of bulk $ZrSiO_3$ at different pressures

Figure 16 shows the density of states at from 0 to 100 GPa, which is according to band structure results. As pressure rises, peaks of DOS systematically move toward higher energies, indicating that electronic states are pushed to higher energy levels and more electronic states are available at those energies.

4.2.2 Different layered configurations

In this subsection, we analyze the band structure of the bulk and layered $ZrSiO_3$, considering structures with up to four layers and are evaluated using their respective high-symmetry points. The results show that the bulk $ZrSiO_3$ exhibits an indirect band gap, that is also preserved in the different layered configurations, Figure 17(a–e). Band gap value decreases with increase in number of layers, Figure 17f. This decrement is due to quantum confinement and interlayer interactions caused by van der Waals forces. This layer–dependent change in the band gap is in agreement with what other researchers have found in 2D materials like MoS_2 and phosphorene (López-Suárez, 2016; Cai *et al.*, 2014).

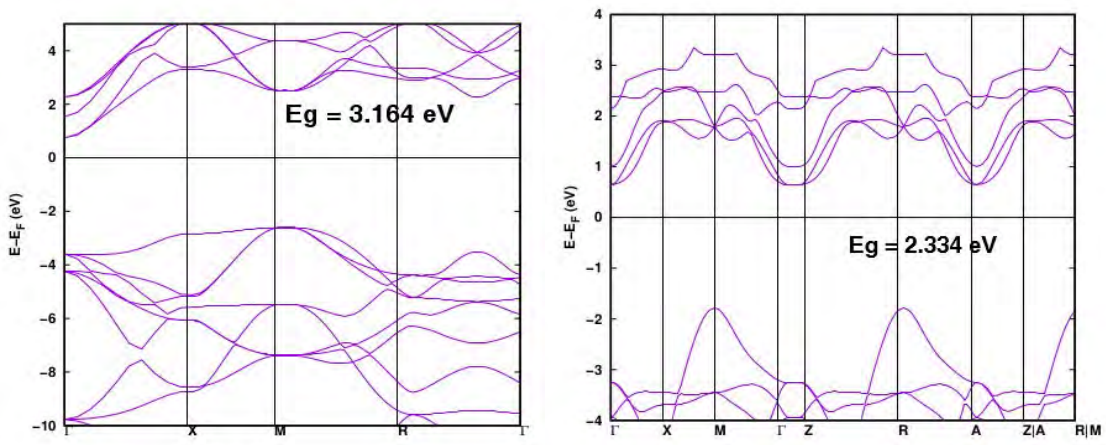

(a) **(b)**

(c) **(d)**

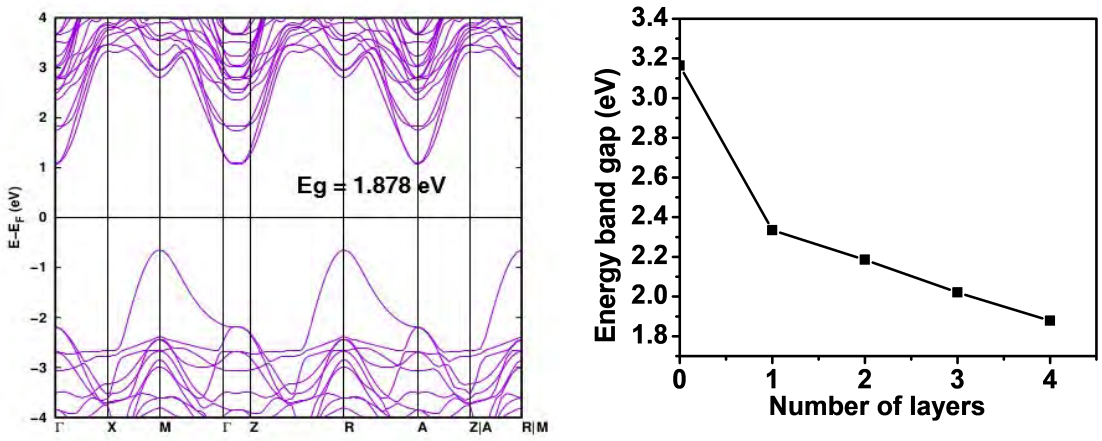

(e) **(f)**

Figure 17: Band structures of different layers of $ZrSiO_3$ (a–e) one to four layers, (f) variation of band gap with number of layers (Pokharel *et al.*, 2024).

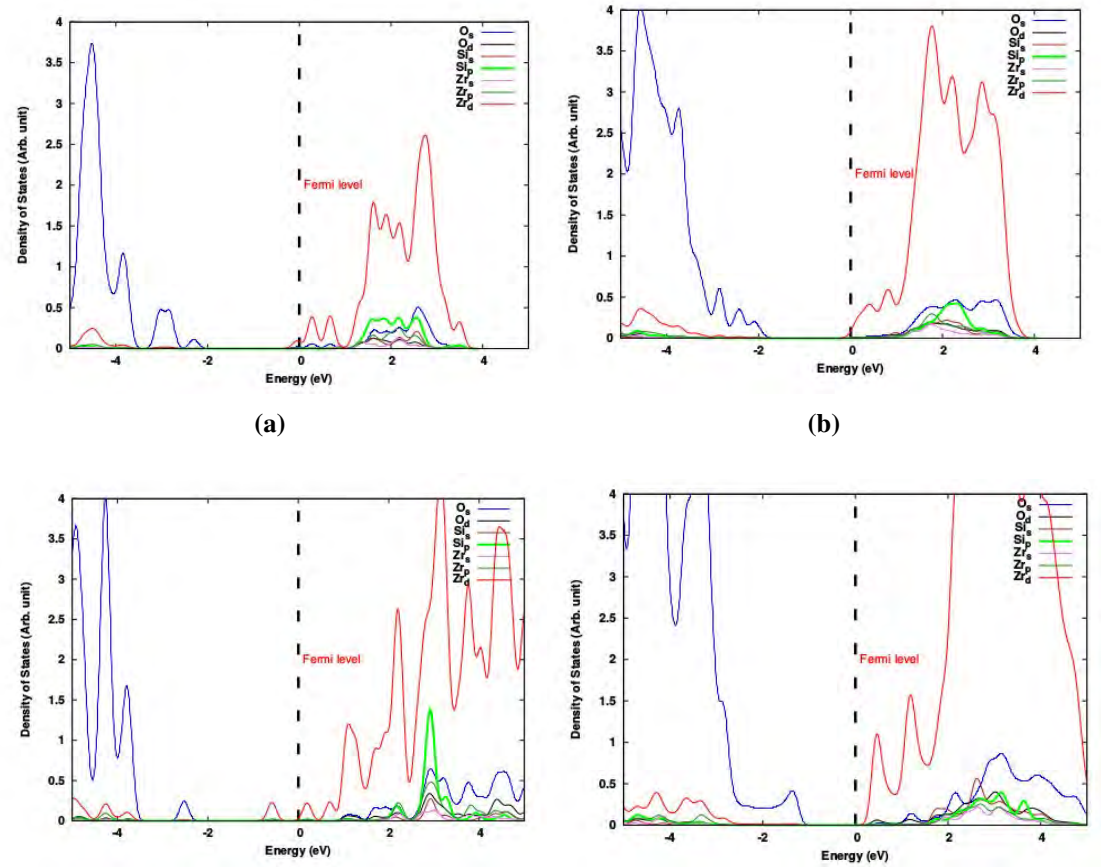

(a) **(b)**

(c) **(d)**

Figure 18: PDOS of (a) first, (b) second, (c) third, (d) fourth layers of $ZrSiO_3$ (Pokharel *et al.*, 2024).

The PDOS for different layered configurations of $ZrSiO_3$ were computed using the

GGA approximation with ultrasoft pseudopotentials. The PDOS calculations reveal the contributions from the Zr–4d, Si–3s, and O–2p orbitals. We observed sharp peaks in the O–2p states within the valence bands, indicating strongly localized oxygen 2p orbitals that actively participate in bonding with both silicon and zirconium atoms. Similarly, sharp peaks were identified in the Zr–4d states within the conduction band, suggesting the significant role of localized zirconium 4d orbitals on the conduction band. These observations are clearly illustrated in the PDOS plots for different $ZrSiO_3$ layers, Figures (18a–d).

4.2.3 Termination model

The band structures of the ZrO-terminated and SiO_2-terminated slabs were computed along the path Γ–X–M–Γ–Z–R–A–Z–R|M. The predicted band gaps for ZrO-terminated slab and SiO_2-terminated slab are 2.585 eV, and 1.639 eV, respectively, Figure 19(a, b). In termination slab model, the surface relaxation, reconstruction, and charge redistribution gives rise to localized electronic states. As a result the termination model has a smaller band gap than the bulk model. The SiO_2–terminated model has more influence on the conduction band with formation of a relaxed surface state near conduction band minimum (CBM) and a lower band gap value compared to ZrO-terminated model. These results indicate that the surface termination has a pronounced effect on the electronic structure of the material.

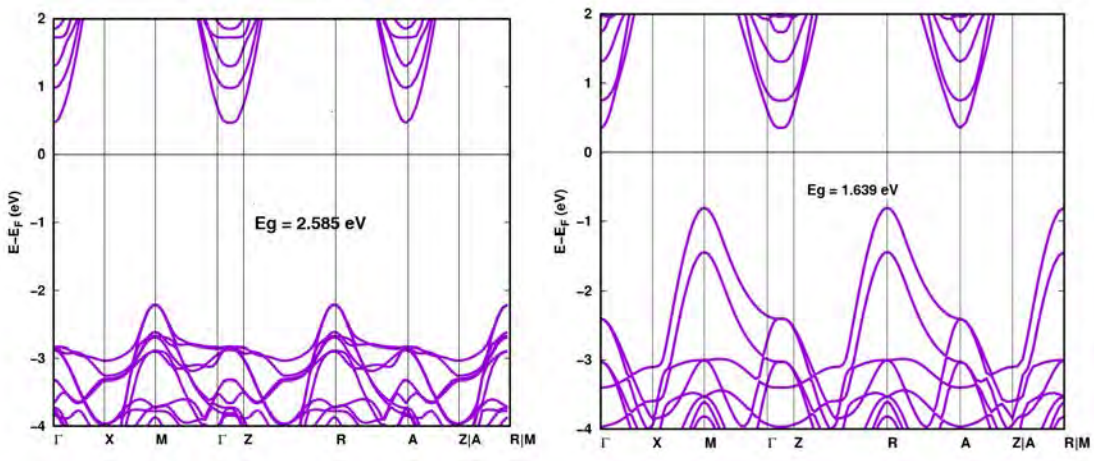

Figure 19: Band structures of (a) ZrO–, (b) SiO_2– surface terminations of $ZrSiO_3$ slab (Pokharel *et al.*, 2024).

PDOS of different atomic orbitals of Zr, Si and O atoms in different layers of both Zr– ans Si_2– termination models have different contributions. The Zr atom in the 2^{nd} layer shows a higher PDOS peak compared to the central layer, suggesting greater electron

occupancy, Figure 20a.

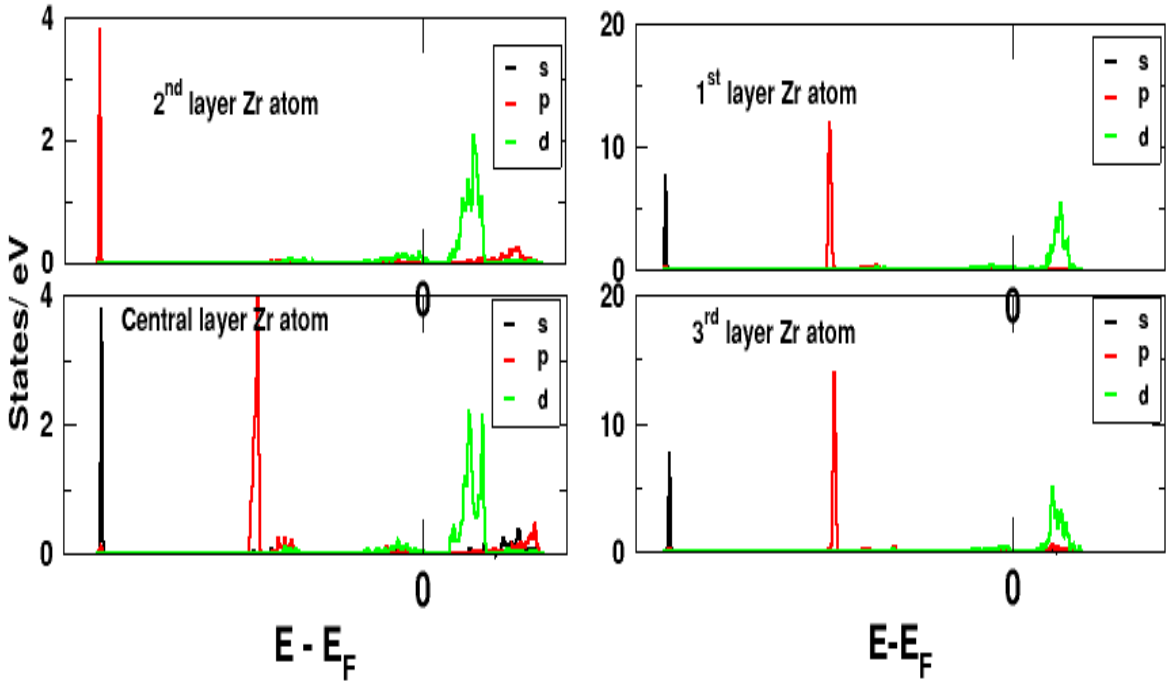

(a)

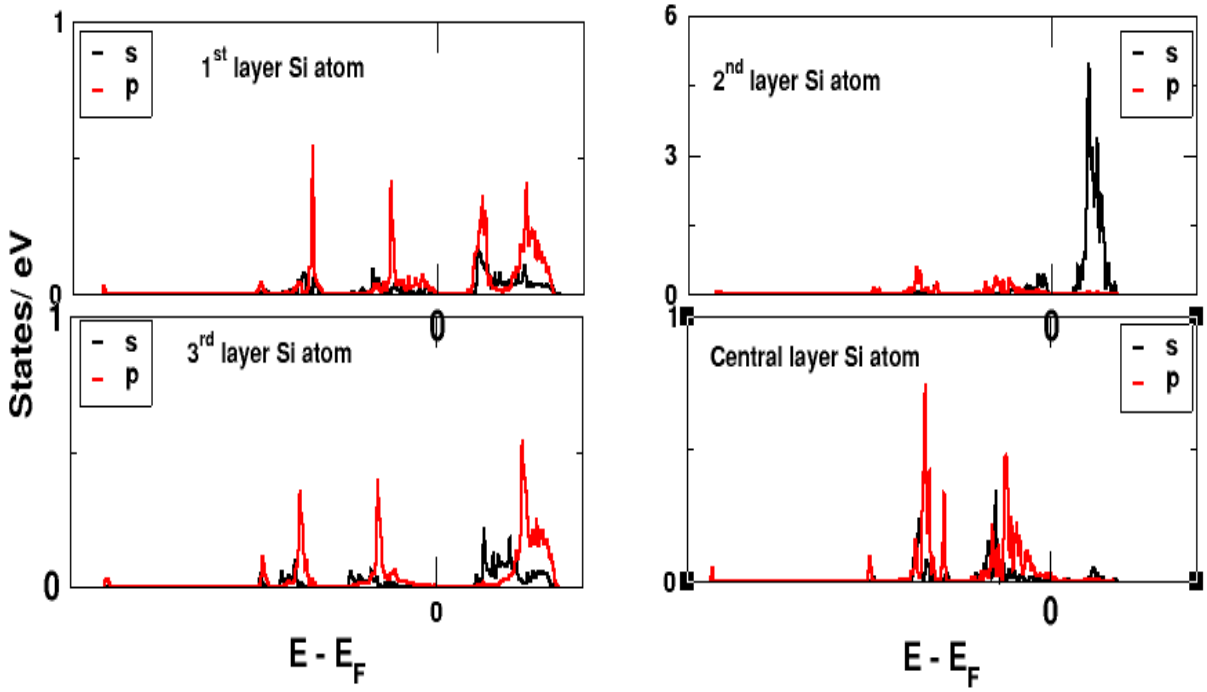

(b)

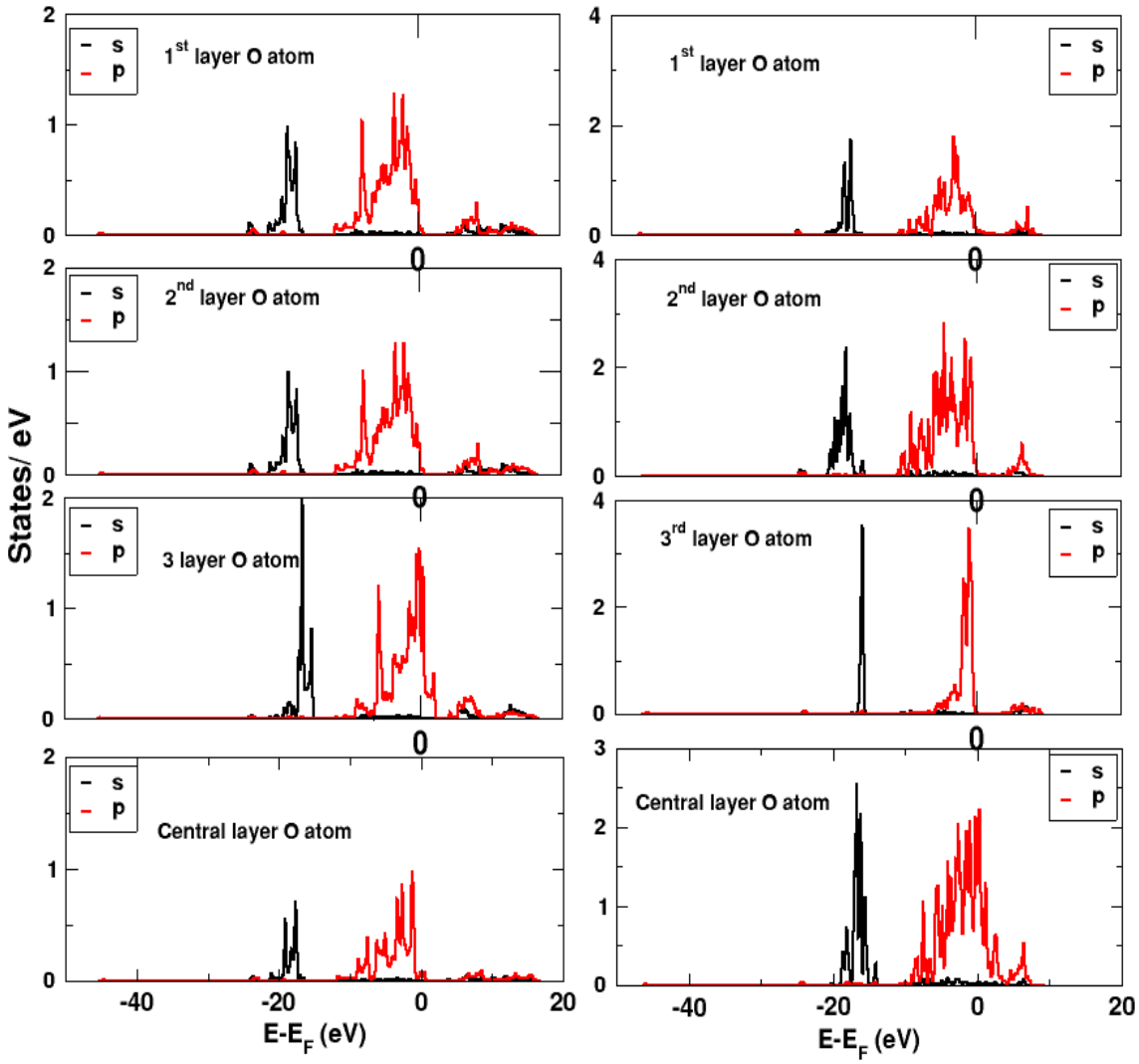

Figure 20: PDOS contributions of (a) Zr (b) Si and (c) O atoms in termination models (Pokharel *et al.*, 2024).

The high PDOS peak for the Zr atom in the 2^{nd} layer suggests a probability of electron localization, and the energy inequality among s, p, and d orbitals of Zr atom are typical characteristic of transition metals. The d orbitals are more spread out in space and contain more energy than the s and p orbitals. This energy difference can have a big effect on electrical conductivity of the material.

The 3^{rd} layer of oxygen atoms has the largest electron density, which means that the bonding connections are the strongest. The 2^{nd} layer has fewer bonding interactions. The 1^{st} and central layers have electron concentrations that are in the middle, corresponding to moderate bonding strength. In the case of the ZrO-termination slab, the Zr–d orbitals exhibit higher energy levels than the s and p orbitals, and the Zr atom in 3^{rd} layer has a higher PDOS peak than in the 1^{st} layer, indicating a higher probability of

electron occupancy in its orbitals, Figure 20c. PDOS study of oxygen atoms in different levels shows that the 2^{nd} layer has the highest electron density, the 1^{st} layer lowers has the least, and the 3^{rd} and central layers have intermediate values. The central layer of silicon atoms has higher energy states, whereas the 2^{nd} layer has a more stable electronic configuration with lower energy levels.

4.2.4 $ZrSiO_3$ monolayer

Spin-polarized band structure and PDOS calculations were carried out to examine electronic properties of $ZrSiO_3$ monolayer under strain. As shown in Figure 21a, the electronic band structures for both channels completely overlap throughout the Brillouin zone, indicating the absence of spin splitting. This observation is further supported by the PDOS plots in Figure 21b, where identical contributions from both spin states are observed across the entire energy range. The perfect symmetry between the both spin channels suggests that the $ZrSiO_3$ monolayer remains non-magnetic.

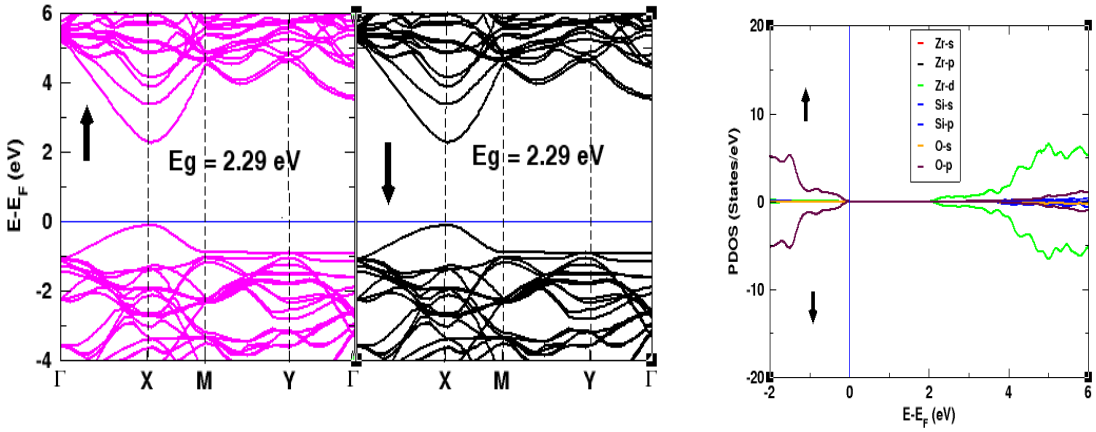

(a) **(b)**

Figure 21: Spin–polarized (a) band structure, (b) PDOS of $ZrSiO_3$ monolayer (Pokharel *et al.*, 2024b).

At zero strain, the $ZrSiO_3$ monolayer has band gap of 2.29 eV with semiconducting nature. Conduction band is dominated by Zr–4d orbitals, whereas valence band is primarily contributed by O–2p orbitals as shown in Figure 21b. Compared with the bulk structure, noticeable changes in band structure are observed in $ZrSiO_3$ monolayer. These differences arises from the reduction in dimensionality, quantum confinement effect and the absence of k_z dispersion in the two–dimensional system. As a result, the electronic structure of the monolayer differs significantly from that of the bulk phase.

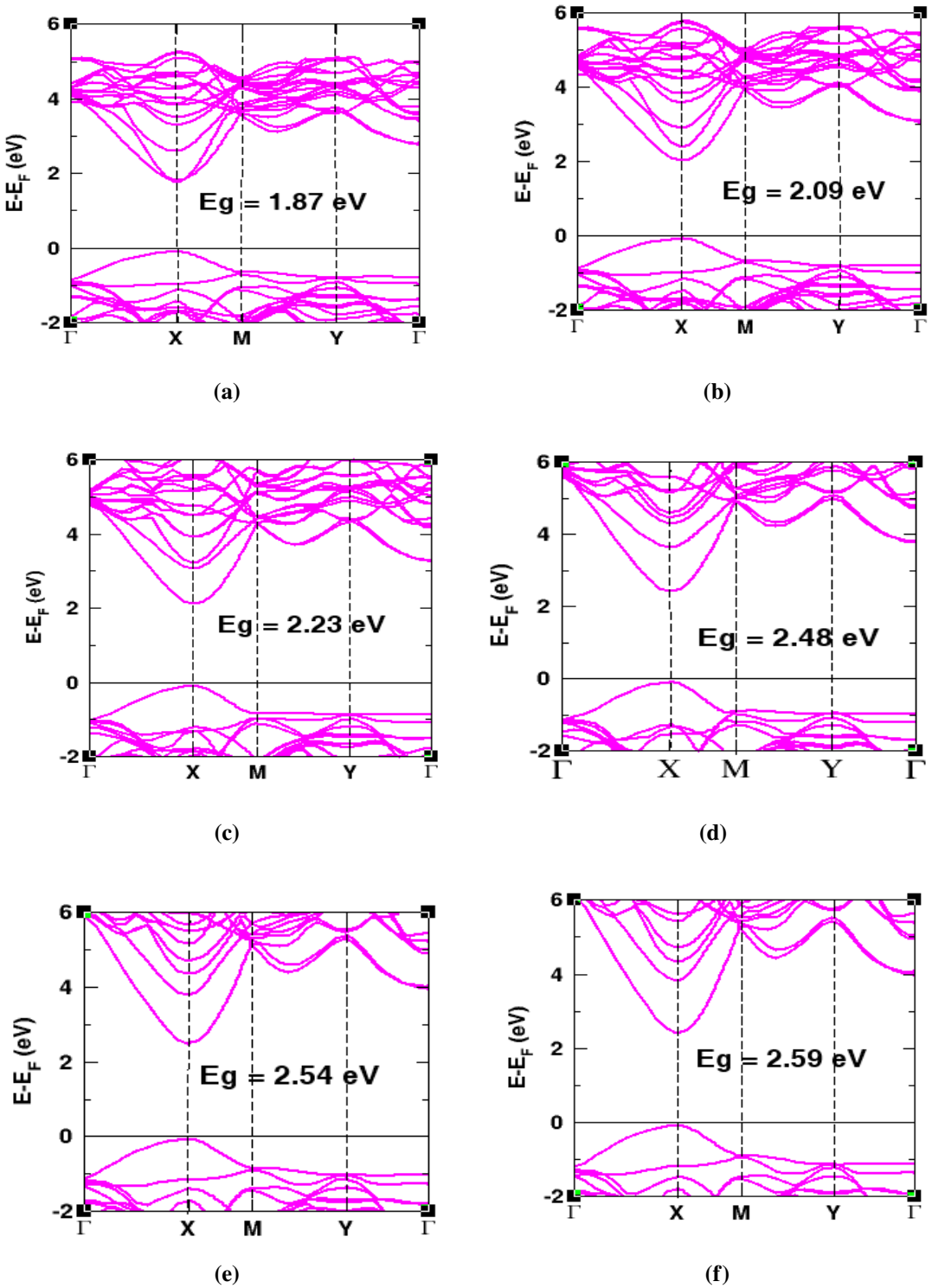

Figure 22: Strain dependent band structure of $ZrSiO_3$ monolayer (a–f) (Pokharel *et al.*, 2024b).

Figures 22(a–f) illustrate electronic band structures of $ZrSiO_3$ monolayer. Under compressive strain, the in–plane atoms move closer to each other which increases orbital overlapping. This increased orbital overlap makes the bonding and anti–bonding interactions stronger. This results the VBM shifts downward and the CBM shifts upward.

Consequently, E_g value progressively increases from 2.29 to 2.59 eV. Tensile strain causes the in–plane atoms move farther apart from each other, which reduces the orbital overlap. This reduced overlap weakens the bonding–antibonding interactions. Consequently, a shift of CBM to higher energy and the VBM to lower energy states take place. Consequently, the E_g value gradually decreases from 2.29 to 1.87 eV. The monolayer exhibits strain-tunable wide band gap, which makes it perfect for strain-sensitive devices, optoelectronics, and flexible electronics (Deb *et al.*, 2024). The total density of states (TDOS) plots support this trend.

When tensile strain is applied (0% to +6%), the band gap decreases due to weaker orbital interactions, Figure 23a. Whereas, compressive strain (0% to −6%) increases the band gap because the stronger orbitals overlap, Figure 23b. Based on these findings, $ZrSiO_3$ monolayers may be suitable for tunable band gap material by mechanical strain.

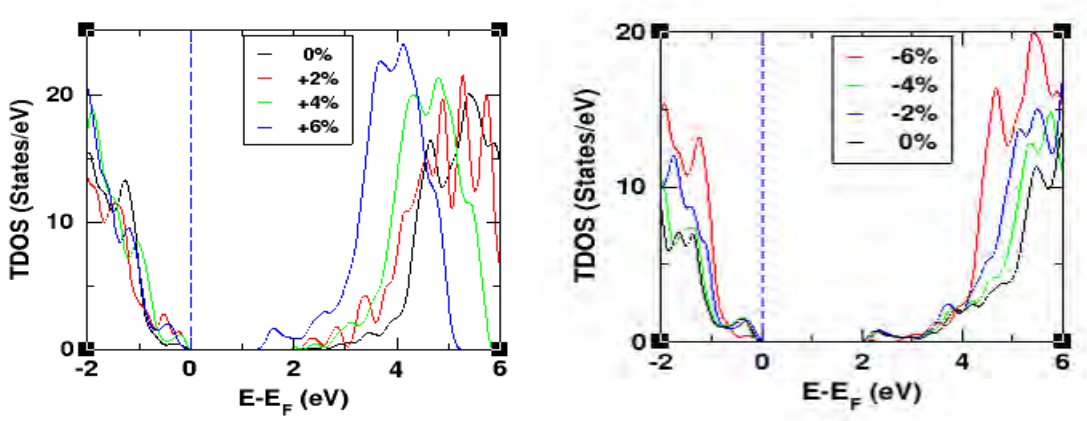

Figure 23: TDOS of $ZrSiO_3$ monolayer under (a) tensile, (b) compressive strain (Pokharel *et al.*, 2024b).

4.2.5 Eu– and Y– doped $SmMnO_3$

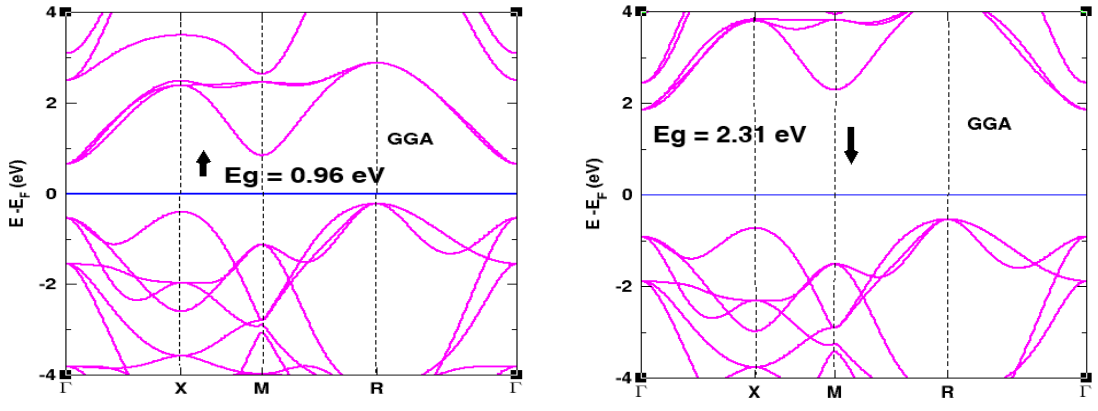

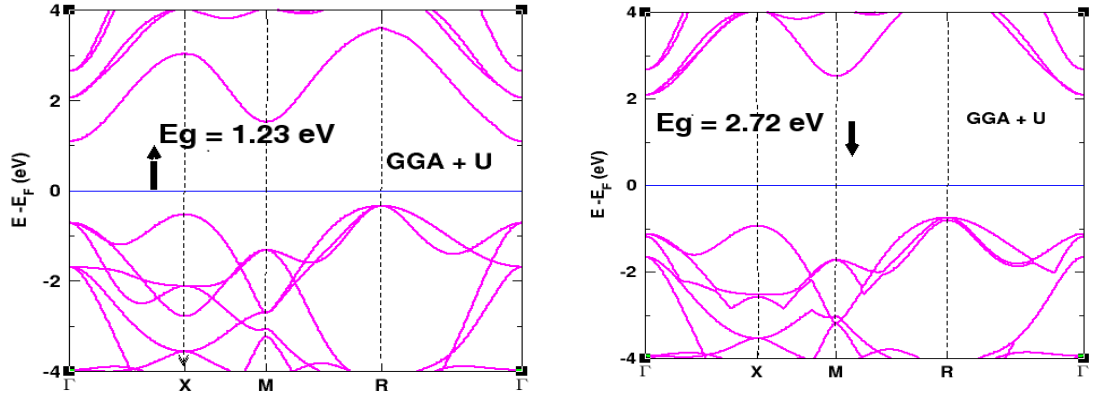

(c) **(d)**

Figure 24: Band structure of pristine $SmMnO_3$ (a–b) using GGA, (c–d) using GGA + U approach (Pokharel *et al.*, 2024c).

The band structure and DOS of pristine and Eu-doped $SmMnO_3$ were examined using spin-polarized GGA and GGA+U approaches. The band structure calculations were performed across path Γ–X–M–Γ–R. The GGA+U approach uses the Hubbard U parameter to enhance localization of electron interactions in partially filled Mn–3d and Eu–4f orbitals. This change makes it easier for GGA+U to appropriately describe electronic band structure and PDOS of the material.

For pristine $SmMnO_3$, the calculated band gap is 2.31 eV with, GGA, Figure 24b and 2.72 eV with GGA+U, Figure 24d. These values are consistent with the experimental measurement of 2.8 eV (Saad H.-E and Alsobhi, 2022). When a Eu atom having partially filled 4f orbitals ($[Xe]4f^7 6s^2$) are doped into $SmMnO_3$, it creates new energy levels that interact with electronic structure of the original material and lowers the E_g value.

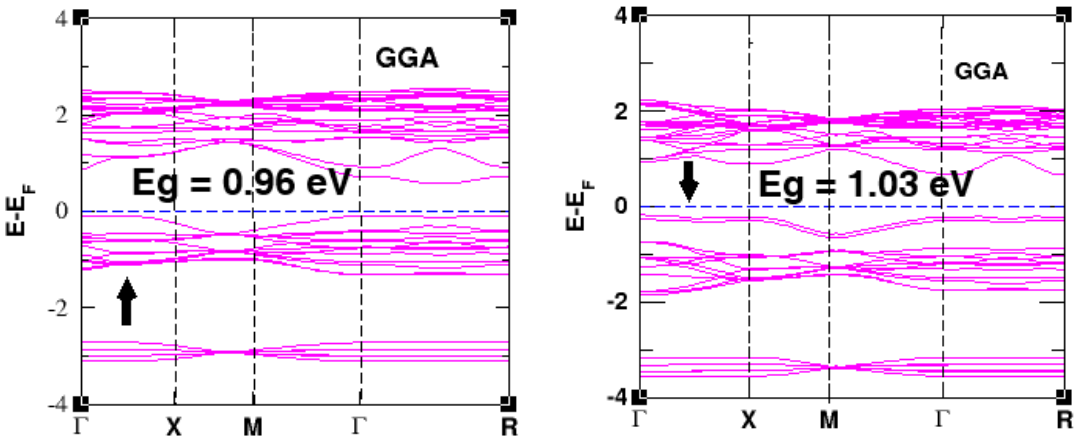

(a) **(b)**

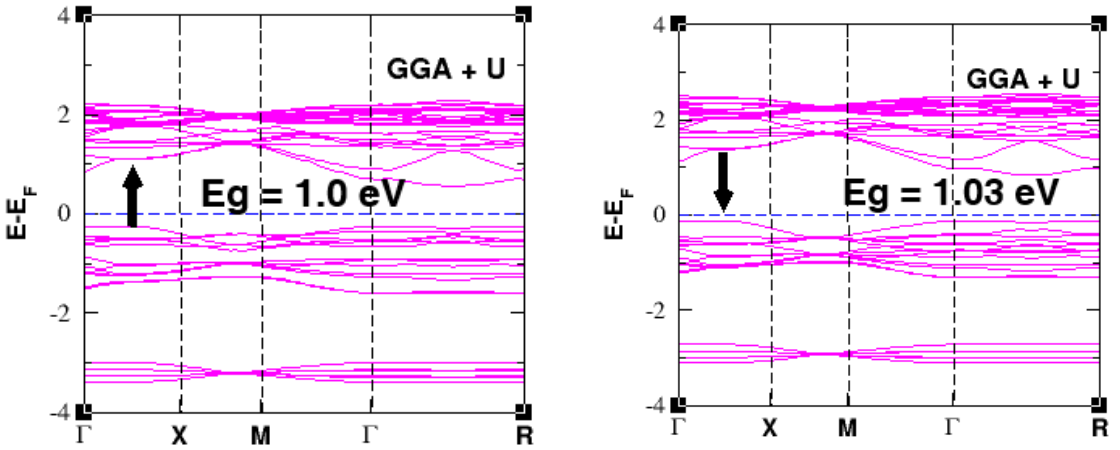

(c) **(d)**

Figure 25: Band structure of 12.5% Eu-doped $SmMnO_3$ (a–b) using GGA, (c–d) using GGA + U approach (Pokharel *et al.*, 2024c).

The band gap declines to 1.03 eV at 12.5% Eu doping, Figures 25(a–b) and further reduces to 0.40 eV at 25% Eu doping on both GGA and GGA+U calculations, Figures 26(a–b). These results suggest that both approximations change electronic structure. Similarly, Y–doping, which involves partially filled 4d orbitals ($[Kr]4d^1 5s^2$), also lowers the band gap value. Figures 27(a–d) indicate that the electronic band gap drops to 1.30 eV with 12.5% Y doping, and it drops even more to 0.76 eV with 25.0% Y doping (Figures 28a–d).

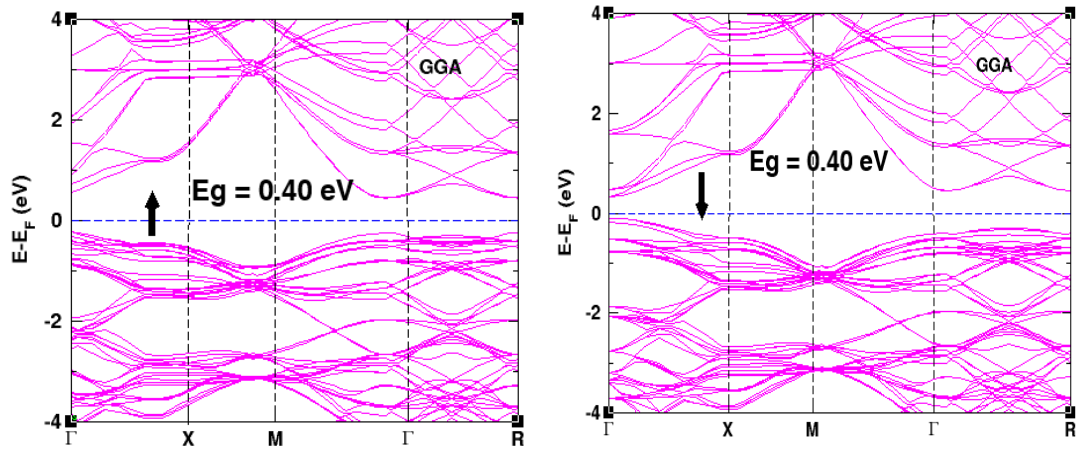

(a) **(b)**

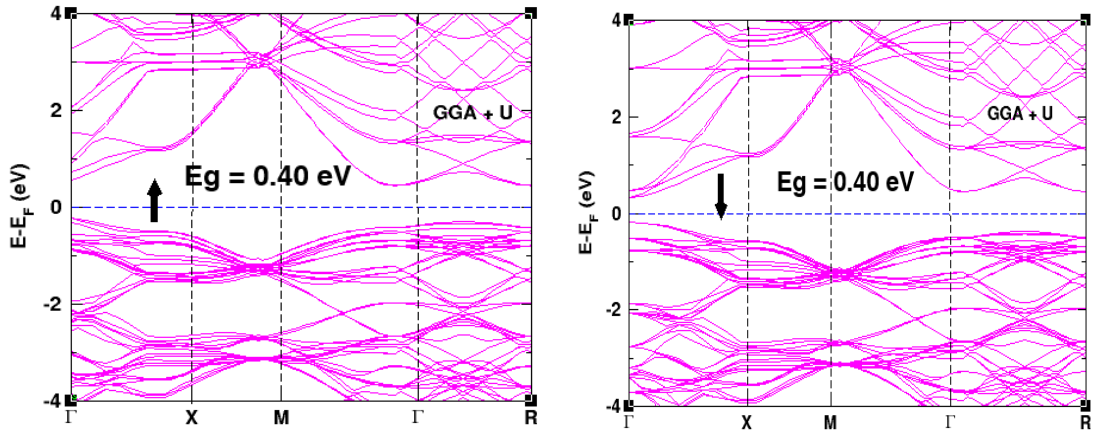

(c) (d)

Figure 26: Band structure of 25% Eu-doped $SmMnO_3$ (a–b) using GGA, (c–d) using GGA + U approach (Pokharel *et al.*, 2024c).

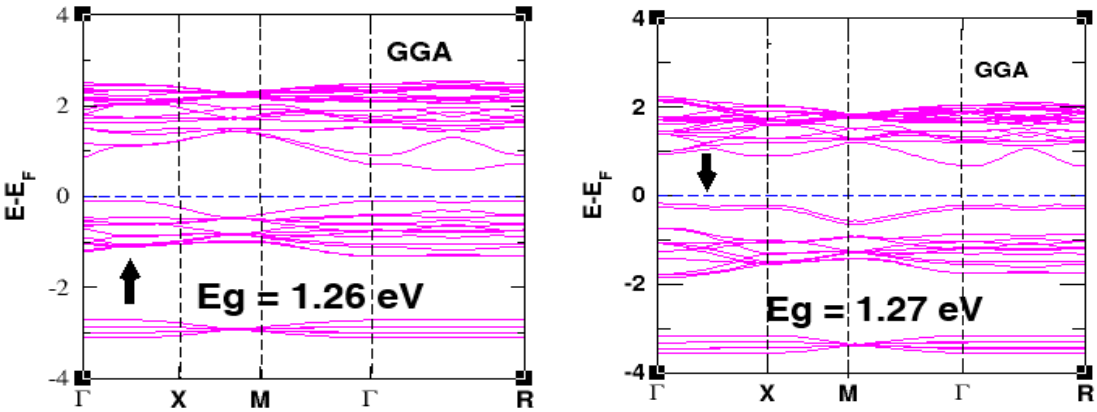

(a) (b)

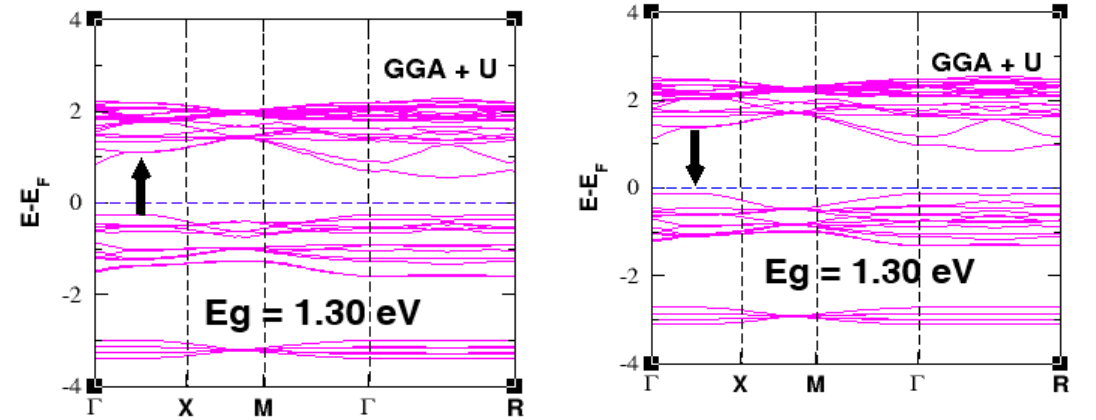

(c) (d)

Figure 27: Band structure of 12.5% Y–doped $SmMnO_3$ (a–b) using GGA, (c–d) using GGA + U approach (Pokharel *et al.*, 2024c).

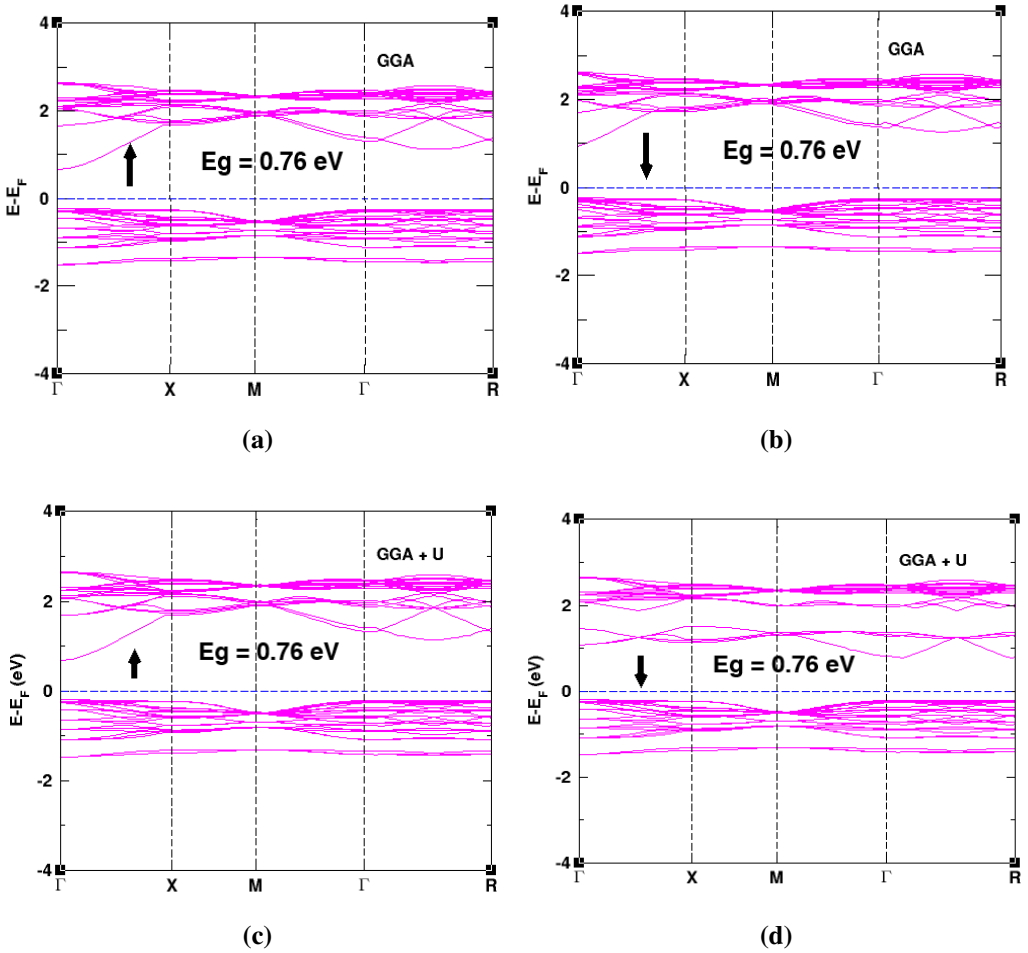

Figure 28: Band structure of 25% Y–doped $SmMnO_3$ (a–b) using GGA, (c–d) using GGA + U approach (Pokharel *et al.*, 2024c).

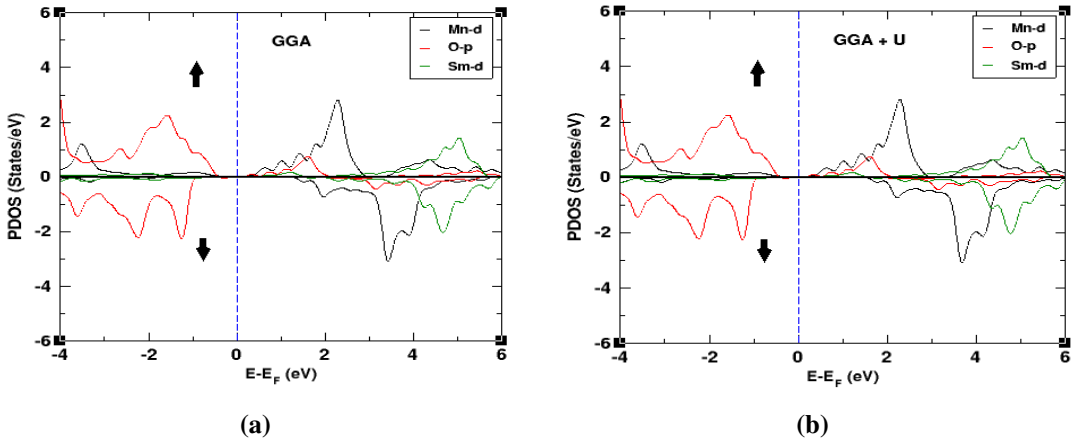

Figure 29: PDOS of pristine $SmMnO_3$ using (a) GGA, (b) GGA + U (Pokharel *et al.*, 2024c).

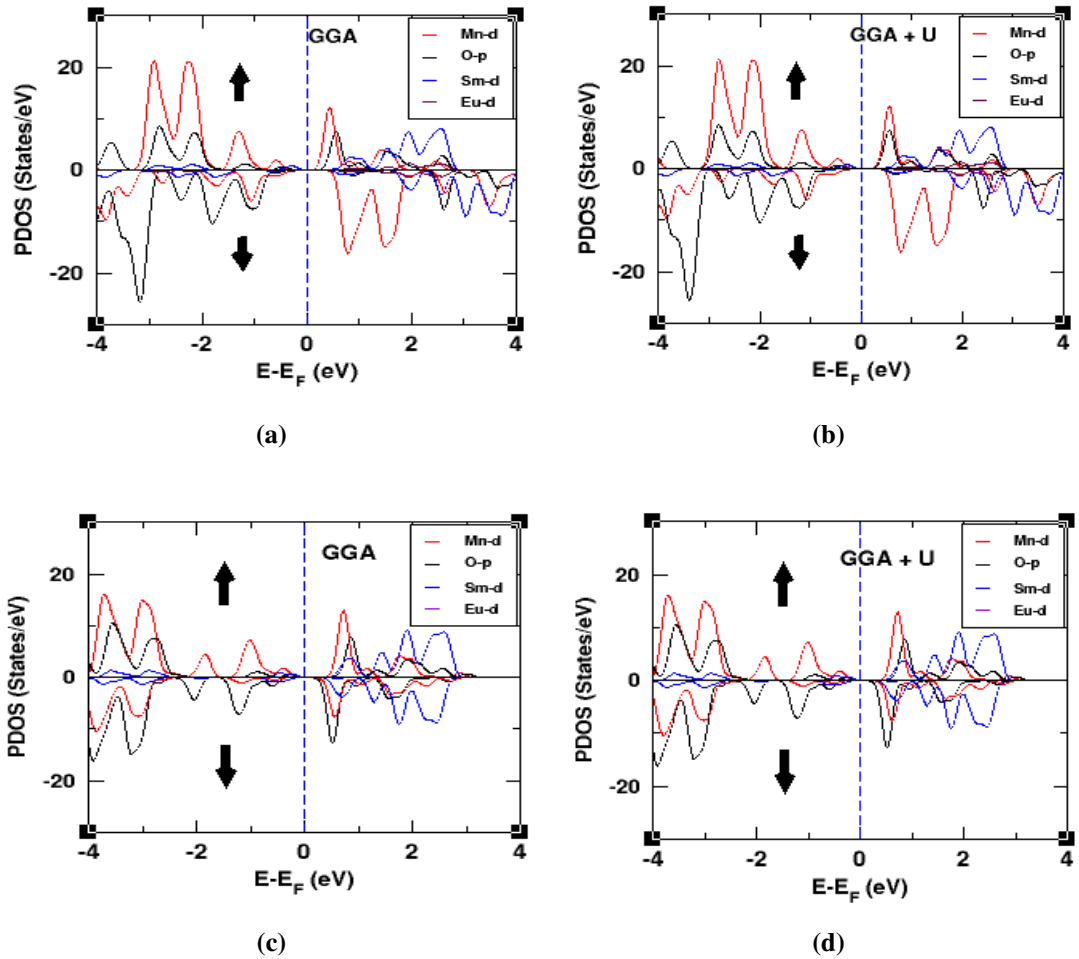

Figure 30: PDOS of Eu-doped $SmMnO_3$ using (a) GGA 12.5%, (b) GGA + U 12.5%, (c) GGA 25.0%, (d) GGA + U 25.0% (Pokharel *et al.*, 2024c)

The PDOS results of pristine $SmMnO_3$ shown in Figures 29a and 29b support the band structure calculations shown in Figure 24. The valence band is dominated by states whereas conduction band is contributed by Mn–3d states. These contributions are responsible for the band gap observed in the material.

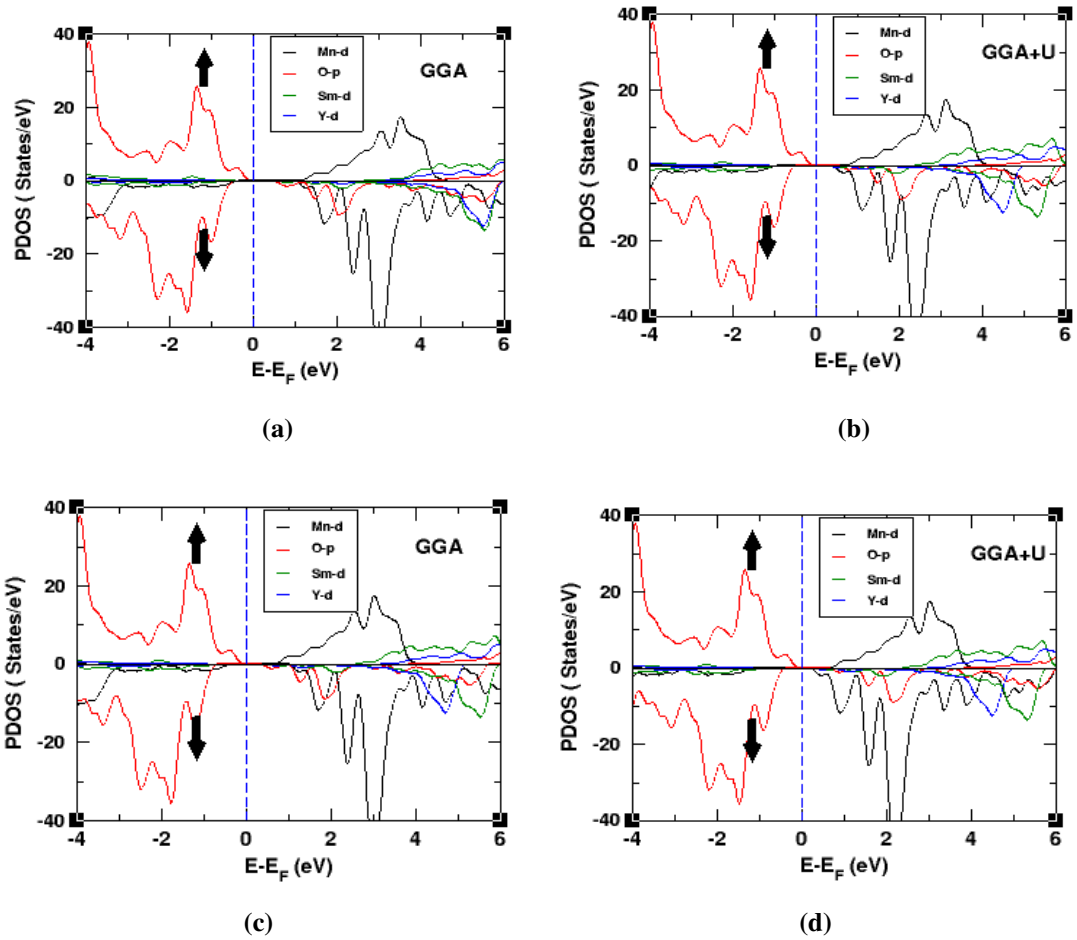

Figure 31: PDOS using (a) GGA, (b) GGA + U for 12.5% Y-doped, (c) GGA, (d) GGA + U for 25.0% Y-doped $SmMnO_3$ (Pokharel *et al.*, 2024c).

As Eu– doping increases, influence of O–2p and Mn–3d states to both the valence and conduction bands decrease, Figure 30(a–d). Similar trends are observed with different concentrations of Y– doping, Figure 31(a–d). These findings suggest that Eu and Y doping can reduce and tune the band gap of $SmMnO_3$, indicating the material's potential applications in various fields.

4.2.6 Sr_2ZrMoO_6 double perovskite

In this study, band structure of Sr_2ZrMoO_6 was computed along high-symmetry k-points. Inclusion of on–site Coulomb potential in the GGA method makes it easier to deal with interaction of localized electron in the partially filled Mo–4d orbitals. This modification enables a precise analysis of band structure and PDOS of substance. The estimated band gap is 1.03 eV in spin up channel, Figure 32a and 1.42 eV in spin down, Figure 32b. This band gap value observed in Sr_2ZrMoO_6 is consistant with those reported by Roknuzzaman et al. for Cs_2BiCuI_6 (Roknuzzaman *et al.*, 2019).

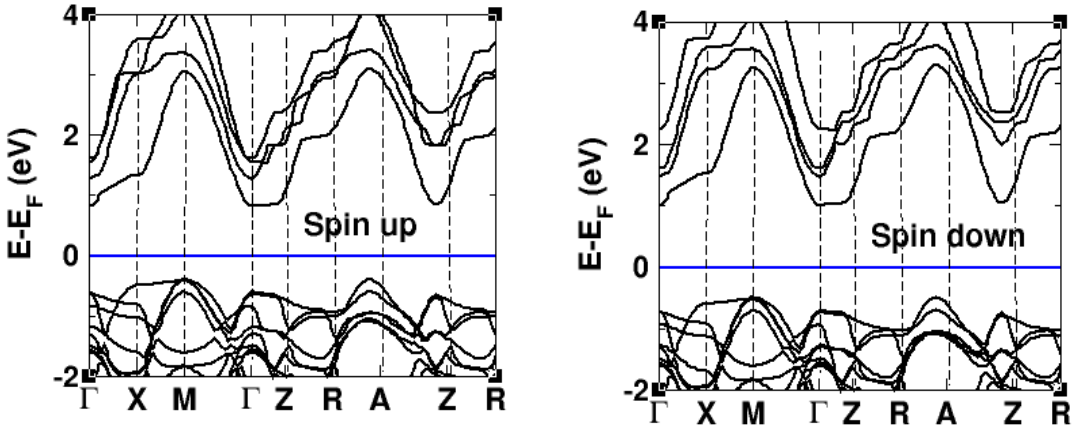

(a) **(b)**

Figure 32: Band structure of Sr_2ZrMoO_6 double perovskite (Pokharel *et al.*, 2025).

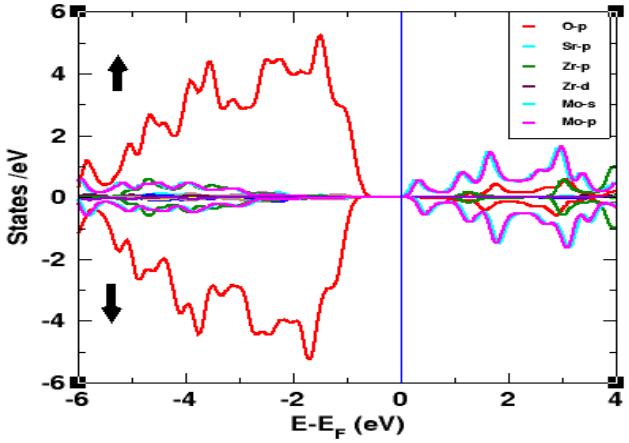

Figure 33: PDOS of Sr_2ZrMoO_6 using GGA + U approach (Pokharel *et al.*, 2025).

Figure 33 illustrates that the PDOS study of Sr_2ZrMoO_6 indicates the conduction band is primary influenced by Mo–4d orbitals and valence band is contributed by O–2p orbitals. Additionally, the asymmetry between the two spin channels indicates the magnetic behavior of material.

4.3 Optical properties of materials

The dielectric function is closely correlated with the behavior of the substance that interacts with electromagnetic waves, particularly light waves. The dielectric constant, $\epsilon(\omega)$, which includes both the real part, $(\epsilon_1(\omega))$ and the imaginary part, $(\epsilon_2(\omega))$ is

expressed as (Deb and Sarkar, 2021)

$$\epsilon(\omega) = \epsilon_1(\omega) + i\epsilon_2(\omega) \tag{4.8}$$

Mathematically, $\epsilon_1(\omega)$ is calculated using an expression obtained from the Kramers-Kronig transformation equations (Harmel *et al.*, 2015) and is expressed as

$$\epsilon_1(\omega) = 1 + \frac{2}{\pi}\mathcal{P}\int_0^\infty \frac{\omega'\epsilon_2(\omega')}{\omega'^2 - \omega^2}d\omega' \tag{4.9}$$

where $\mathcal{P}$ denotes principal value of integral.
$\epsilon_2(\omega)$ is calculated using following formula (Lu, 2021)

$$\epsilon_2(\omega) = \frac{4\pi^2 e^2}{\omega^2 m^2}\sum_n \sum_{n'} \int_{\mathrm{BZ}} |P_{nn'}(k)|^2 f_{kn}(1 - f_{kn'})\delta(E_{nk} - E_{n'k} - \hbar\omega)d^3k \tag{4.10}$$

Here, $\mathrm{f_{kn}}$ represents the Fermi-Dirac distribution function, while $P_{nn'}(k)$ denotes the projection of the momentum matrix elements on the direction of the field for the initial and final states. The symbol E_{nk} represents energy of a single electron, ω is angular frequency, $\hbar$ represents reduced Planck's constant, m indicates electron mass and e represents the elementary charge.
Alternatively, $\epsilon_2(\omega)$ can be written in terms of the transition dipole matrix elements as (Gajdovs *et al.*, 2006)

$$\epsilon_2(\omega) = \frac{4\pi^2 e^2}{m^2\omega^2}\sum_{i,j} \left|\langle D_{ij}\rangle\right|^2 f_i(1 - f_i)\delta(E_f - E_n - \hbar\omega)d^3k \tag{4.11}$$

where, D_{ij} is transition dipole matrix element. E_n is energy of electron in n^{th} state, f_i represents Fermi distribution function. The refractive index ($n(\omega)$), reflectivity ($R(\omega)$) and absorptance ($\alpha(\omega)$) can be determined using the dielectric functions, $\epsilon_1(\omega)$ and $\epsilon_2(\omega)$. $R(\omega)$ is given by the equation (Egerton, 2009)

$$R(\omega) = \left[\frac{\sqrt{\epsilon_1(\omega) + i\epsilon_2(\omega)} - 1}{\sqrt{\epsilon_1(\omega) + i\epsilon_2(\omega)} + 1}\right]^2 \tag{4.12}$$

Standard formula for $n(\omega)$ is (Lu, 2021)

$$n(\omega) = \left[\frac{\epsilon_1(\omega) + \sqrt{\epsilon_1(\omega)^2 + \epsilon_2(\omega)^2}}{2}\right]^{1/2} \tag{4.13}$$

and the absorptance is given by (Gajdovs *et al.*, 2006)

$$\alpha(\omega) = \frac{2\omega}{c}\left[\frac{\sqrt{\varepsilon_1^2(\omega)+\varepsilon_2^2(\omega)}-\varepsilon_1(\omega)}{2}\right]^{1/2} \tag{4.14}$$

4.3.1 $ZrSiO_3$ at different pressures

The static dielectric constant, $\epsilon_1(0)$, represents the value of the dielectric function at zero photon energy. The dielectric function, expressed in Equation (4.9), which describes response of material to electromagnetic radiation at different photon energies. Figure 34a demonstrates the variation of $\epsilon_1(\omega)$ with photon energy. The static dielectric constant $\epsilon_1(0)$ at different pressures about 3.6–3.8 from 0 – 100 GPa. A sharp increase in $\epsilon_1(\omega)$ is observed at 4.4 – 4.8 eV at different pressures.

Imaginary part of dielectric function, $\epsilon_2(\omega)$, reveals the ability of material to absorb electromagnetic radiation. Figure 34b shows that $\epsilon_2(\omega)$ approaches zero when the photon energy is close to zero. This suggests that the material does not absorb much energy when there are no incident photons present. After the photon energy threshold has been crossed, $\epsilon_2(\omega)$ increases rapidly due to the onset of inter-band electronic transitions. At 0 Gpa $ZrSiO_3$ has an absorption edge at about 3.15 eV, comparable to calculated electronic band gap of 3.164 eV. As pressure increases 20 – 100 GPa, onset values increase from 3.25 – 3.32. The sharp peak are observed at 4.13, 4.37, 4.49, 4.78, 4.90 and 4.92 eV at pressure 0, 20, 40, 60, 80 and 100 GPa respectively. These findings demonstrate that pressure significantly changes electronic structure and optical response of material.

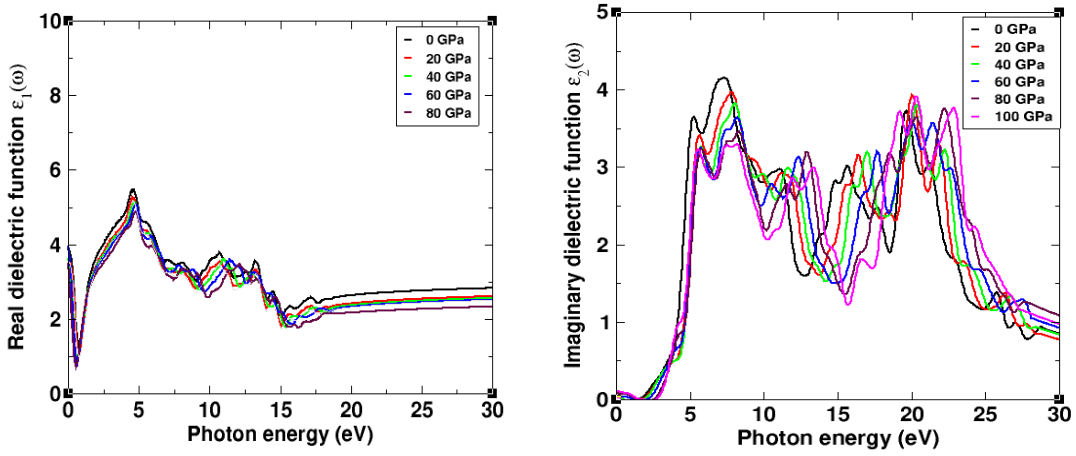

(a) **(b)**

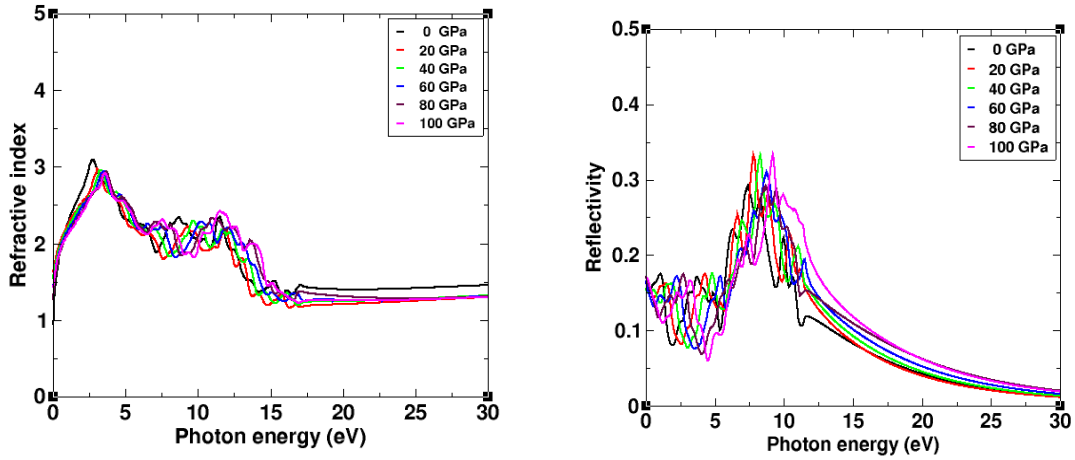

(c) **(d)**

Figure 34: Variation of (a) $\epsilon_1(\omega)$, (b) $\epsilon_2(\omega)$ (c) refractive index and (d) reflectivity of $ZrSiO_3$ perovskite

The calculated refractive index n(ω) for ZrsiO3 at different pressure are shown in Figure 34c. The refractive index describes how fast electromagnetic waves travel through the material and gives important information about its optical response and electronic polarization. The static refractive index values n(0) at different pressures are same (1.38–1.39). The higher peaks are observed in low photon energy range of 2.78–3.62 eV form 0 to 100 GPa.

The reflectivity spectra exhibit relatively low reflectance in the visible region. As the photon energy increases, the reflectivity spectra exhibit clear peaks in ultraviolet region around 7.42 – 9.25 eV, corresponding to strong inter-band electronic transitions. As shown in Figure 34d, the $ZrSiO_3$ compound shows the highest peak reflectivity of approximately 0.29 at 7.42 eV at 0 GPa, whereas the peak intensities of about 0.34 observed from 7.80 – 9.25 eV for 20 – 100 GPa pressure values.

4.3.2 Eu– and Y– doped $SmMnO_3$

The optical behavior of pristine and Eu– and Y– doped $SmMnO_3$ has been analyzed through the calculation of the dielectric response, refractive index, and reflectivity. Figure 35a illustrates the variation of the $\varepsilon_1(\omega)$ with photon energy. The calculated static dielectric constant, $\varepsilon_1(0)$, for the pristine compound is 1.58. After Eu doping, the static dielectric constant slightly decreases to 1.33 at 12.5% doping and further drop to 1.28 at 25%. For Y–doping, the decrease is even more noticeable, with values of 1.20 and 1.15 for 12.5% and 25% doping, respectively. The 25% Y-doped material shows the lowest static dielectric constant and the smallest peak value of $\varepsilon_1(\omega)$ among all the studied materials. This low peak indicates that 25% Y-doped material has a lower electronic

polarizability than other doped systems.

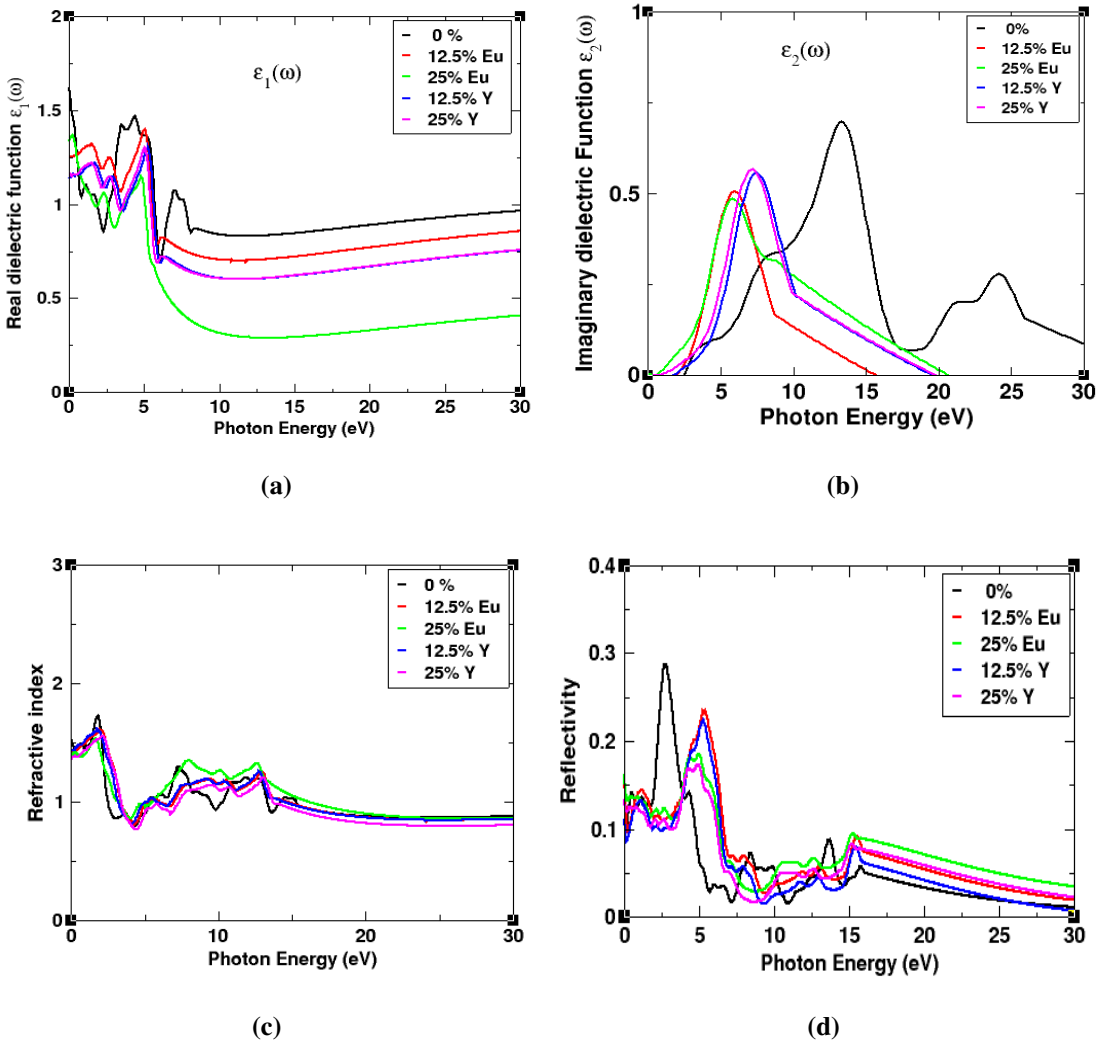

Figure 35: Variation of (a) real and (b) imaginary parts of dielectric function (c) refractive index, (d) reflectivity of pristine and Eu/Y–doped $SmMnO_3$ (Pokharel *et al.*, 2024c).

Figure 35b shows that $\varepsilon_2(\omega)$ is almost zero for low photon energy. When the photon energy exceeds the threshold value, $\varepsilon_2(\omega)$ increases rapidly due to onset of interband transitions. The pristine system shows an absorption edge at 2.5 eV, comparable to calculated electronic band gap of 2.73 eV. This shows that the material is a semiconductor. Eu– and Y– doped materials show strong peaks at 5–7 eV photon energy in the ultraviolet region. This peak arises from high-energy interband transitions from O-2p states to Mo-3d states. This indicates that the doped materials absorb photons in the ultraviolet region. The absorption edge of $\varepsilon_2(\omega)$ for the 12.5% Eu-doped system appears near 0.95 eV, comparable to estimated band gap 1.03 eV. In addition, higher peaks appear in the 3–6 eV energy range, indicating stronger optical transitions within

the visible region. A similar behavior is seen in the Y-doped systems. The absorption edge is around 1.2 eV for 12.5% Y doping and about 0.7 eV for 25% Y doping, indicating a significant enhancement of low-energy optical transitions compared with the pristine system.

Figure 35c displays the calculated refractive index $n(\omega)$ for pristine and Eu- and Y-doped materials. The static refractive index values $n(0)$ of pristine, 12.5% Eu-doped, 25% Eu-doped, 12.5% Y-doped, and 25% Y-doped compounds are 1.45, 1.43, 1.41, 1.39, and 1.36, respectively. All the materials show strong peaks in the low photon energy value between 1.8 and 2.5 eV. This peak is due to strong electronic polarization due to interband transitions. The maximum refractive index value of approximately 1.70 is observed for pristine $SmMnO_3$ near 1.8 eV, whereas the Eu- and Y-doped systems show slightly lower peak values. This decrease in the peak intensity of $n(\omega)$ after doping indicates the doped materials have lower optical polarizability. This is due to modifications in the electronic structure of pristine material when Eu and Y atoms replace Sm atoms.

The reflectivity spectra provide insight into the surface optical behavior of the investigated compounds. Static reflectivity values R(0) for pristine, 12.5% Eu-doped, 25% Eu-doped, 12.5% Y-doped, and 25% Y-doped compounds are 0.14, 0.13, 0.15, 0.10, and 0.12, respectively. The reflectivity spectra exhibit pronounced peaks in the ultraviolet region around 3–6 eV, corresponding to strong interband electronic transitions, Figure 35d. The pristine compound shows the highest peak reflectivity of approximately 0.28 near 3 eV, whereas the doped systems display slightly reduced peak intensities. This reduction suggests that Eu and Y doping modifies the electronic structure and weakens the reflection of incident electromagnetic radiation. The relatively low reflectivity in the visible region indicates minimal energy loss due to reflection, suggesting that these materials are promising candidates for photovoltaic applications.

4.3.3 Sr_2ZrMoO_6 double perovskite

Optical behavior of Sr_2ZrMoO_6 is studied by evaluating the $\varepsilon_1(\omega)$, and $\varepsilon_2(\omega)$, and the refractive index, with the energy of the photons. Figure 36a demonstrates the variation of $\varepsilon_1(\omega)$ with photon energy. The static dielectric constant $\varepsilon_0(\omega)$, for the compound is 4.9. The peak value of $\varepsilon_1(\omega)$ is 10.7 at 1.8 eV, indicates the significant electrical polarizability of the material.

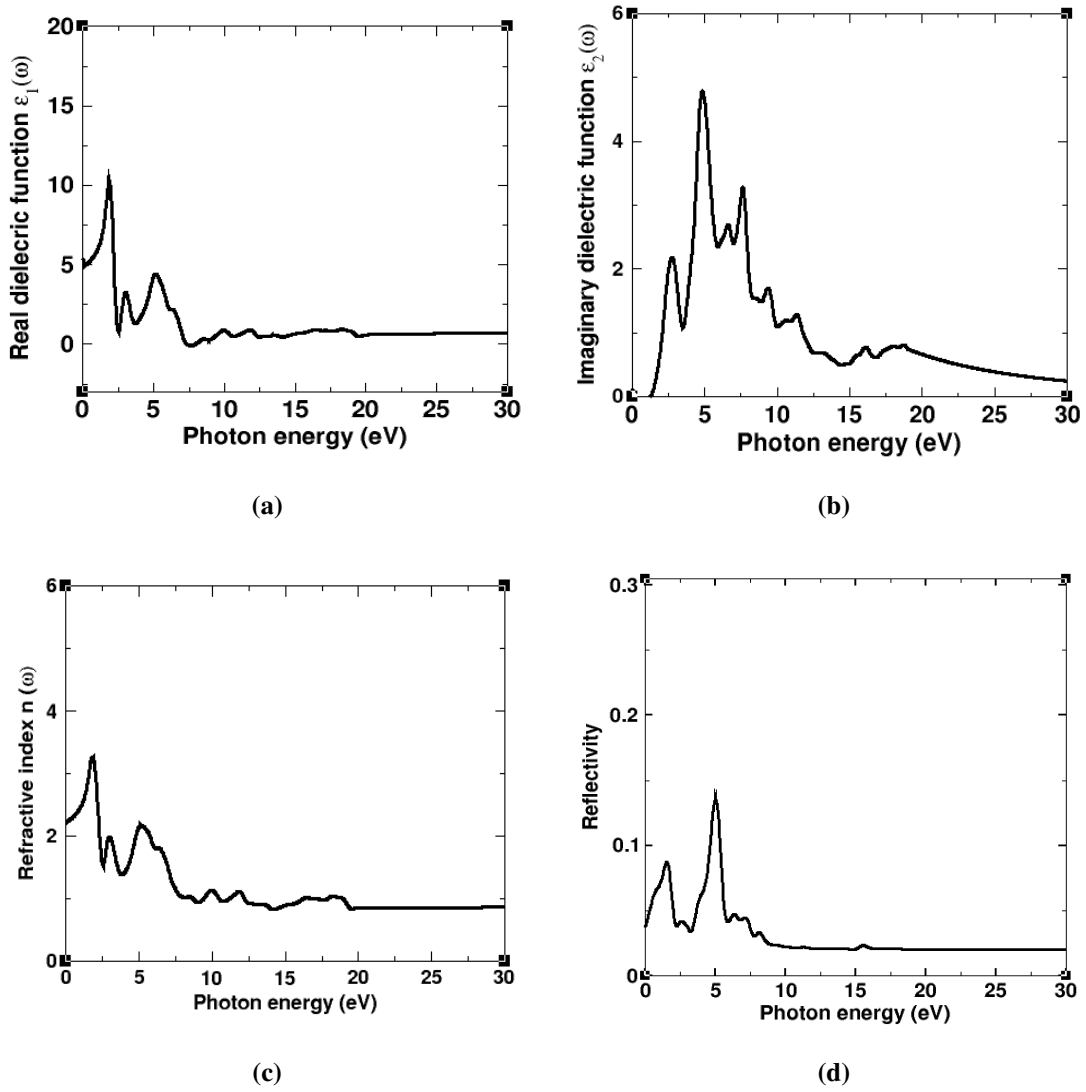

Figure 36: Variation of (a) real and (b) imaginary parts of dielectric function, (c) refractive index and (d) reflectivity of Sr_2ZrMoO_6 (Pokharel *et al.*, 2025).

The $\varepsilon_2(\omega)$ spectra illustrate that the material always absorbs electromagnetic radiation throughout a range of energy levels, with positive values in all directions. As shown in Figure 36b, $\varepsilon_2(\omega)$ approaches zero when the photon energy tends to zero, indicating there is negligible absorption in the absence of incident photons. After the photon energy threshold has been crossed, $\varepsilon_2(\omega)$ increases rapidly due to the onset of inter-band electronic transitions. The pristine system has an absorption edge at about 1.36 eV, comparable to calculated electronic band gap 1.40 eV. This confirms that the material is a semiconductor. For this material, there is also the highest peak in the 4.6 eV , UV region of the spectrum, which means that optical transitions are stronger in the UV range.

The refractive index shows how much the wave bends when it enters the crystal structure.

It follows a pattern that is comparable to the $\varepsilon_1(\omega)$ spectra. From Figure 36c, the refractive index is 2.2, which means the material is optically dense and interacts strongly with light.

Reflectivity spectra exhibit relatively low reflectance in visible region. The reflectivity spectra exhibit pronounced peaks in ultraviolet region around 5.2 eV, corresponding to strong inter-band electronic transitions. As shown in Figure 36d, the Sr_2ZrMoO_6 compound shows the highest peak reflectivity of approximately 0.29 at 5.2 eV indicating strong optical response in the ultraviolet region.

4.4 Elastic properties

The elastic stiffness tensors C_{11}, C_{12}, and C_{44} are key parameters for evaluating the mechanical properties and stability of simple cubic perovskites. Specifically, C_{11} characterizes the resistance to longitudinal (length) deformation, while C_{12} and C_{44} represent the resistance to shear or shape deformation (Birch, 1947). The pressure-dependent elastic constants for $ZrSiO_3$ are calculated through the stress-strain method (Wang *et al.*, 2018) based on the following relations.

According to Hooke's law, the stress tensor is linearly related to the strain tensor through the fourth-rank elastic stiffness tensor as (Golesorkhtabar *et al.*, 2013)

$$\sigma_{ij} = C_{ijkl}\varepsilon_{kl}, \tag{4.15}$$

where σ_{ij} and ε_{kl} represent the stress and strain tensor components, respectively, and C_{ijkl} is the fourth-rank elastic stiffness tensor. Since the stress and strain tensors are symmetric, the fourth-rank tensor C_{ijkl} can be represented in Voigt notation by an equivalent 6×6 elastic stiffness matrix, C_{ij}. The mechanical properties of cubic system are determined using second order elastic tensors C_{11}, C_{12} and C_{44}. Based on these C_{ij} values, the system is confirmed to be mechanically stable under the specified conditions. That is it satisfies the Born–Huang generalized elastic stability criteria for cubic crystals are given by (Jamal *et al.*, 2014)

$$\begin{cases} C_{11} - |C_{12}| > 0, \\ C_{11} + 2C_{12} > 0, \\ C_{12} < B < C_{11}, \\ C_{44} > 0 \end{cases} \tag{4.16}$$

The bulk modulus (B), shear modulus (G), and Young's modulus (E) are evaluated using the Voigt–Reuss–Hill (VRH) approximation. In this approach, the Voigt approximation

assumes a uniform strain throughout the crystal and provides the upper bound of the elastic moduli (Voigt, 1928). Accordingly, the Voigt bulk modulus (B_V) is expressed as

$$B_V = \frac{C_{11} + 2C_{12}}{3}, \tag{4.17}$$

where C_{ij} are the elastic stiffness constants.

The Reuss approximation assumes a uniform stress throughout the crystal and provides the lower bound of the elastic moduli (Reuss, 1929). The corresponding Reuss bulk modulus (B_R) is given by

$$B_R = \frac{1}{3S_{11} + 6S_{12}}, \tag{4.18}$$

where S_{ij} are the elastic compliance constants.

Similarly, the Voigt shear modulus (G_V) and the Reuss shear modulus (G_R) are given by

$$G_V = \frac{C_{11} - C_{12} + 3C_{44}}{5}, \tag{4.19}$$

$$G_R = \frac{5C_{44}(C_{11} - C_{12})}{4C_{44} + 3(C_{11} - C_{12})}. \tag{4.20}$$

Hill proposed that the actual elastic moduli of a polycrystalline material can be approximated by the arithmetic mean of the Voigt and Reuss bounds (Hill, 1952). Therefore, the bulk modulus (B) and shear modulus (G) are calculated as

$$B_H = \frac{B_V + B_R}{2} \tag{4.21}$$

$$G_H = \frac{G_V + G_R}{2} \tag{4.22}$$

The Young's modulus (E) is further given as

$$E = \frac{9BG}{3B + G} \tag{4.23}$$

The Poisson's ratio (ν) is expressed as (Jamal *et al.*, 2014)

$$\nu = \frac{3B - 2G}{2(3B + G)} \tag{4.24}$$

and, Cauchy's pressure (P_C) is given as (Poniznik *et al.*, 2008)

$$P_C = C_{12} - C_{44} \tag{4.25}$$

The nature of bonding in a compound can be inferred from the sign of Cauchy's pressure (Poniznik *et al.*, 2008) and the value of Poisson's ratio (Pachori *et al.*, 2022). Cauchy's pressure is typically negative for covalent bonds and positive for ionic bonds. For covalent compounds, Poisson's ratio (ν) < 0.25, while for ionic compounds, it is close to or exceeds 0.25 (Surucu *et al.*, 2019). The generalized Born-Huang's mechanical criteria for tetragonal systems are expressed in following inequalities (Born and Huang, 1955)

$$\begin{cases} \mathrm{C_{11}} > 0, \\ \mathrm{C_{33}} > 0, \\ \mathrm{C_{11} + C_{33} - 2C_{12}} > 0, \\ \mathrm{C_{44}} > 0, \\ \mathrm{C_{66}} > 0, \\ \mathrm{C_{11} - C_{12}} > 0, \\ \mathrm{2C_{11} + 2C_{12} + C_{33} + 4C_{13}} > 0 \end{cases} \tag{4.26}$$

The tetragonal Voigt bounds are derived from the Voigt approximation or uniform strain assumption (Voigt, 1928). The bulk modulus (B_V) is defined in terms of C_{ij} as

$$\mathrm{B_V} = \frac{1}{9}[\mathrm{2C_{11} + C_{33} + 2C_{12} + 4C_{13}}] \tag{4.27}$$

The Reuss approximation gives the lower bound bulk modulus (B_R) as

$$\mathrm{B_R} = \frac{\mathrm{C^2}}{\mathrm{M}} \tag{4.28}$$

with $\mathrm{M} = [\mathrm{C_{11} + C_{12} + 2C_{33} - 4C_{44}}]$
and $\mathrm{C^2} = (\mathrm{C_{11} + C_{12}})\mathrm{C_{33}} - 2\mathrm{C_{13}^2}$
Similarly, the Voigt approximation provides the upper bound of the shear modulus, known as the Voigt shear modulus (G_V), which is expressed as (Voigt, 1928)

$$G_V = \frac{1}{30}\left[M + 3C_{11} - 3C_{12} + 12C_{44} + 6C_{66}\right]. \tag{4.29}$$

The Reuss approximation provides the lower bound of the shear modulus, known as the Reuss shear modulus (G_R), and is given by (Reuss, 1929)

$$G_R = \frac{15}{\left(\frac{18B_R}{C^2} + \frac{6}{C_{11}+C_{12}} + \frac{6}{C_{44}} + \frac{3}{C_{66}}\right)}. \tag{4.30}$$

According to Hill, the effective bulk and shear moduli of a polycrystalline material are obtained by taking the arithmetic mean of the Voigt and Reuss bounds (Hill, 1952). Therefore, the Hill bulk modulus (B_H) and Hill shear modulus (G_H) are given by

$$B_H = \frac{B_V + B_R}{2}, \tag{4.31}$$

$$G_H = \frac{G_V + G_R}{2}. \tag{4.32}$$

The Cauchy pressure along X-axis (P_a^{Cauchy}) and y-axis (P_b^{Cauchy}) of a tetragonal system can be obtained as (Chen *et al.*, 2020)

$$P_a^{Cauchy} = C_{13} - C_{44}, \quad P_b^{Cauchy} = C_{12} - C_{66} \tag{4.33}$$

4.4.1 Bulk $ZrSiO_3$ at different pressures

This subsection discusses the mechanical properties and dynamic stability of $ZrSiO_3$ under different pressures. Second-order elastic constants, C_{11}, C_{12}, C_{44} can be determined with the stress-strain method employing small strain distortions. These C_{ij} values are used to obtain different mechanical properties of the compound, including mechanical strength, ductility, toughness, brittleness, Poisson's ratio, and anisotropy (Pokharel *et al.*, 2024).

Table 7: Elastic stiffness tensors (C_{ij}), elastic moduli (B, G, and E), Poisson's ratio (ν) and G_H / B_H ratio of bulk $ZrSiO_3$ at different pressures

P (GPa)	C_{11} (GPa)	C_{12} (GPa)	C_{44} (GPa)	E (GPa)	B (GPa)	G (GPa)	ν -	G/B -
0	205.28	169.58	36.92	78.75	181.48	27.58	0.427	0.152
20	207.46	170.17	36.96	80.08	182.60	28.06	0.426	0.154
40	209.13	170.24	37.18	81.69	183.10	28.65	0.425	0.156
60	211.04	171.53	37.39	82.54	184.70	28.95	0.425	0.157
80	213.01	171.54	37.51	84.45	185.10	29.68	0.424	0.161
100	214.84	171.61	37.78	85.94	186.02	29.08	0.423	0.156

Values of C_{11}, C_{12}, and C_{44} of $ZrSiO_3$ at various pressures are presented in Table 7. The calculated C_{ij} values satisfy the stability criteria described in Equation (4.16), indicating it to be mechanically stable up to 100 GPa.

The C_{11} values increase gradually with increasing pressure, whereas C_{12} and C_{44} increase slightly with pressure, which is due to slight decrease in anisotropy of the substance with pressure, Figure 37a. Increase in elastic moduli with pressure indicates that the material becomes stiffer at higher pressure and improves its resistance to isotropic compression, shear deformation, and overall mechanical rigidity of the material over the studied pressure range.

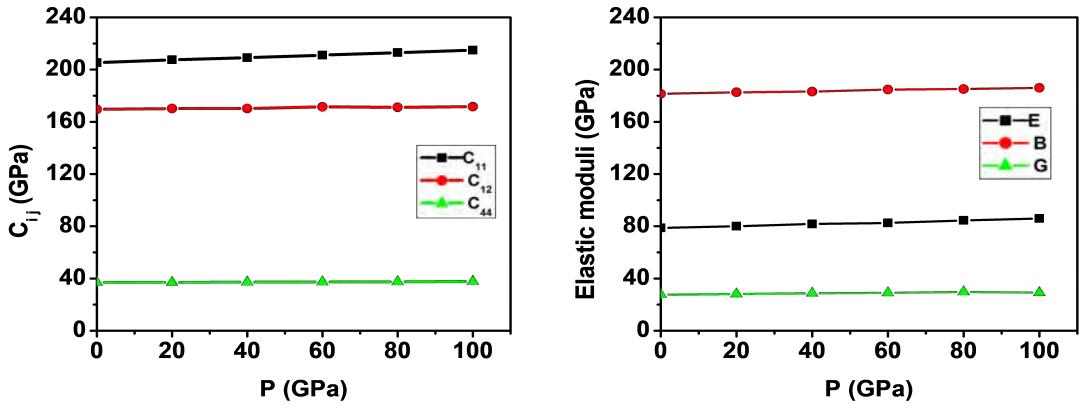

(a) **(b)**

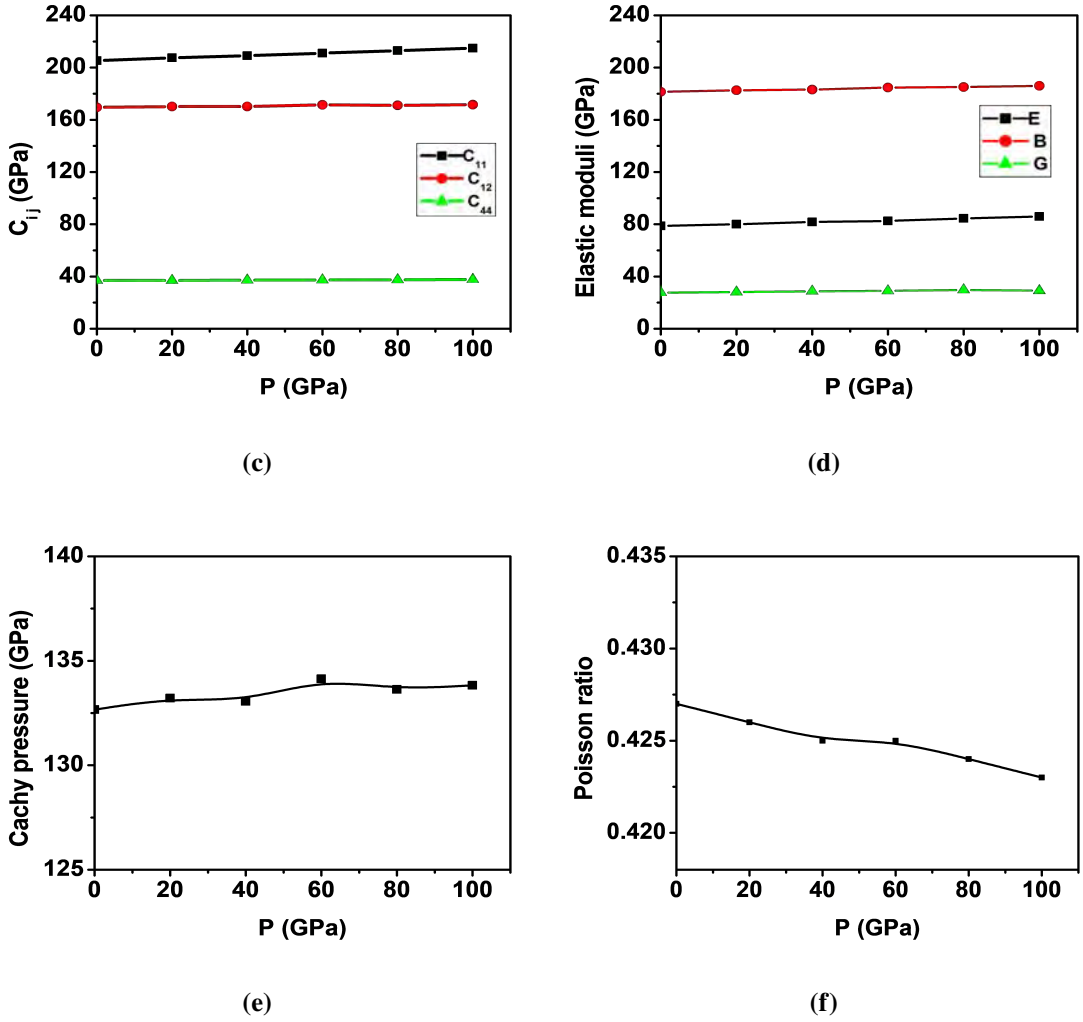

Figure 37: Pressure-dependent (a) C_{ij} values, (b) elastic moduli (B, G, E), (c) Cauchy pressure, (d) Poisson's ratio of $ZrSiO_3$ (Pokharel *et al.*, 2024).

As per Pugh's criteria, a material exhibits ductile behavior when the ratio $G/B < 0.57$ and brittle behavior when $G/B > 0.57$ (Pugh, 1954; Mouhat and Coudert, 2014). At all applied pressures, the calculated Pugh ratio for bulk $ZrSiO_3$ is found to be below 0.57, indicating that the material is ductile. The Young's and bulk moduli of $ZrSiO_3$ increase with increasing pressure, while the shear modulus remains nearly constant due to the material's resistance to shear deformation, Figure 37b. The positive Cauchy pressure indicates that the material is ductile and has metallic bonding characteristics. As the pressure of the sample is gradually increased, the Cauchy pressure remains almost constant, Figure 37c. This suggests that which suggests that the bonding nature of the material remains stable.

The Poisson's ratio decreases with pressure, Figure 37d. This result revealed that $ZrSiO_3$ shows less compressibility in the lateral direction compared to the axial direction.

4.4.2 Termination model

A surface slab was constructed from the (001) plane of bulk cubic $ZrSiO_3$ by introducing a vacuum region to avoid interactions between periodically repeated slab images. The bulk $ZrSiO_3$ crystal exhibits cubic symmetry with lattice parameters $a = b = c$. The introduction of the vacuum region extends the lattice parameter along the z-direction while maintaining periodicity in the x–y plane, resulting in a tetragonal slab geometry with $a = b \neq c$. The resulting slab consists of alternating SiO_2 and ZrO layers separated by the vacuum region.

The stress–strain approach was applied to evaluate elastic stiffness tensors, as previously mentioned in Section 4.5.1. The mechanical behaviour of a tetragonal system was characterized by six independent elastic stiffness tensors. The calculated C_{ij} values for the ZrO-terminated models are C_{11} = 135.39 GPa, C_{12} = 102.29 GPa, and C_{13} = 66.02 GPa, C_{33} = 28.86 GPa, C_{44} = 90.26 GPa, and C_{66} = 41.39 GPa, and those for the SiO_2-termination model are C_{11} = 130.56 GPa, C_{12} = 78.09 GPa, C_{13} = 73.91 GPa, C_{33} = 16.06 GPa, C_{44} = 91.28 GPa, and C_{66} = 41.17 GPa.

Table 8: Elastic moduli (B, G, E), Poisson's ratio (ν), G_H/B_H ratio, and Cauchy's pressure (P_C) of bulk $ZrSiO_3$, ZrO-terminated slab, and SiO_2-terminated slab (Pokharel *et al.*, 2024)

Compound	B (GPa)	B_R (GPa)	B_H (GPa)	G (GPa)	G_R (GPa)	G_H (GPa)	E (GPa)	ν	G_H/B_H	P_C (GPa)
Bulk	181.30	181.28	181.29	29.55	14.06	21.80	62.88	0.479	0.12	132.06
ZrO-terminated	92.19	42.06	67.12	33.22	25.34	29.28	76.69	0.309	0.44	37.16
SiO_2-terminated	89.36	24.84	57.09	30.82	19.77	25.29	66.13	0.307	0.443	57.85

The mechanical properties of bulk $ZrSiO_3$ and its ZrO-terminated and SiO_2–terminated slab models were calculated and are summarized in Table 8. Both the ZrO- and SiO_2–terminated slab models fulfill the mechanical stability criteria. However, the SiO_2–terminated slab exhibit higher elasticity and stability compared to the ZrO-terminated slab. The values of $G_H/B_H < 0.57$, Poisson's ratio $\nu > 0.33$ and positive values of Cauchy's pressures of ZrO-terminated and SiO_2-terminated slab model confirm that both termination models exhibit ductile nature.

4.4.3 Eu– and Y– doped $SmMnO_3$

This section provides a detailed study of the mechanical behavior of europium (Eu) and yttrium (Y) doped $SmMnO_3$. The study focuses on how doping influences the mechanical properties of pure $SmMnO_3$.

The presented C_{ij} values in Table 9 satisfy the Born–Huang generalized mechanical stability criterion as describe in Equation (4.16) for all pristine and doped materials. Mechanical properties of $SmMnO_3$ are significantly altered by substitution of Eu and Y. The Eu– doping results in significant decrease in both the shear and Young's moduli. In particular, value of E decreases from 187.78 GPa (bulk) to 123.90 GPa and G decreases from 72.34 GPa to 44.34 GPa when 12.5% Eu doping is implemented (Table 10). At 25% Eu doping, the value of E further decreases to 138.07 GPa and G is approximately 49.82 GPa. This decrement shows that the material becomes less stiff. In both cases, bulk modulus increases and the material becomes less compressible due to higher atomic radii of Eu and Y compared to Sm. This difference in size causes lattice distortions within the crystal structure, which makes the material harder to compress.

Table 9: Elastic moduli (B, G and E), Poisson's ratio (ν), and G_H/B_H ratio of $SmMnO_3$ at different doping levels of europium and yttrium (Pokharel *et al.*, 2024c)

Compounds	B_V (GPa)	B_R (GPa)	B_H (GPa)	G_V (GPa)	G_R (GPa)	G_H (GPa)	E (GPa)	ν	$\frac{G_H}{B_H}$
Pristine $SmMnO_3$	154.89	154.89	154.89	72.68	71.99	72.34	187.78	0.323	0.47
12.5% Eu doped	200.56	200.56	200.56	51.31	37.38	44.34	123.90	0.365	0.22
25% Eu doped	201.09	201.09	201.09	56.55	43.09	49.82	138.07	0.386	0.25
12.5% Y doped	185.09	185.09	185.09	90.25	73.85	82.05	214.46	0.307	0.44
25% Y doped	182.47	182.47	182.47	89.86	74.58	82.22	214.45	0.304	0.45

The Poisson's ratio values ($\nu > 0.26$) for pure and doped $SmMnO_3$ demonstrate distinct trends depending on the dopant. The calculated values of ν are 0.323 for pure $SmMnO_3$, 0.365 for 12.5% Eu doping, 0.386 for 25% Eu doping, 0.307 for 12.5% Y doping, and 0.304 for 25% Y doping. These values reveal that ν increases with europium doping, while it decreases with yttrium doping. Because of the difference in atomic radii, the Eu doping increases the lateral expansion when the material is compressed longitudinally. The increasing Poisson's ratio with Eu doping indicates the material becomes more ductile. Conversely, the decrease in Poisson's ratio with Y– doping results in an increase in stiffness of the material. Pugh's criterion shows that, the calculated values of Pugh's

ratio ($\frac{G}{B} > 1.75$) and positive Cauchy pressure $C_{12} - C_{44}$ indicate that all pristine and doped compounds remain ductile.

4.4.4 Sr_2ZrMoO_6 at different pressures

This section studies mechanical characteristics and dynamic stability of Sr_2ZrMoO_6 at different pressure conditions. Pressure–dependent C_{ij} values of Sr_2ZrMoO_6 are provided in Table 10. From these C_{ij} values, the elastic compliance constants, S_{ij}, were derived (Table 11). The mechanical stability criteria of materials under hydrostatic pressure were determined using generalized Born-Huang's lattice conditions, with the C_{ij} values must meet following inequalities (Born and Huang, 1955)

$$\begin{cases} C_{11} - P > 0, \\ C_{33} - P > 0, \\ C_{44} - P > 0, \\ C_{66} - P > 0, \\ C_{11} - C_{12} - 2P > 0, \\ C_{11} + C_{33} - 2C_{13} - 4P > 0, \\ 2C_{11} + 2C_{12} + C_{33} + 4C_{13} + 3P > 0 \end{cases} \tag{4.34}$$

Based on the data presented in Table 10, this equation confirms that the studied compound satisfies the mechanical stability criteria within 0–80 GPa.

Table 10: Elastic stiffness tensors (C_{ij}) of the Sr_2ZrMoO_6 double perovskite at different pressures (Pokharel *et al.*, 2025)

P (GPa)	C_{11} (GPa)	C_{12} (GPa)	C_{13} (GPa)	C_{22} (GPa)	C_{23} (GPa)	C_{33} (GPa)	C_{44} (GPa)	C_{55} (GPa)	C_{66} (GPa)
0	313.21	95.11	85.66	313.21	85.66	332.62	98.46	98.46	135.32
20	321.71	95.83	87.72	321.71	87.72	335.16	98.24	98.24	137.45
40	327.66	96.19	90.49	327.66	90.49	341.69	98.09	98.09	140.22
60	330.85	96.85	93.32	330.85	93.32	343.29	97.83	97.83	143.22
80	332.57	97.03	95.66	332.57	95.66	350.04	97.67	97.67	147.89

Elastic constants show how a material resists stress from different directions. Specifically, C_{11}, C_{22}, and C_{33} describe stiffness of the crystal along the a, b, and c axes,

respectively. A higher value of C_{11} indicates high resistance under compression along a-axis, which makes the material less compressible and stiffer in that direction. Likewise, higher values of C_{22} and C_{33} have more significant responses to compressive stress along the b- and c-axes, respectively (Bao *et al.*, 2020).

Table 11: Elastic compliance matrix (S_{ij}) of the Sr_2ZrMoO_6 double perovskite

P (GPa)	S_{11} (GPa^{-1})	S_{12} (GPa^{-1})	S_{13} (GPa^{-1})	S_{22} (GPa^{-1})	S_{23} (GPa^{-1})	S_{33} (GPa^{-1})	S_{44} (GPa^{-1})	S_{55} (GPa^{-1})	S_{66} (GPa^{-1})
0	0.004	-0.001	-0.001	0.004	0.001	0.003	0.010	0.010	0.007
20	0.004	-0.001	-0.001	0.004	0.001	0.003	0.010	0.010	0.007
40	0.003	-0.001	-0.001	0.003	0.001	0.003	0.010	0.010	0.007
60	0.003	-0.001	-0.001	0.003	0.001	0.003	0.010	0.010	0.007
80	0.003	-0.001	-0.001	0.003	0.001	0.003	0.010	0.010	0.007

The elastic constants E, B, G and ν were computed applying Equations (4.28) – (4.32), as discussed in Section 4.5.

Table 12: Elastic moduli (B, G, E), Poisson's ratio (ν), and G_H/B_H ratio of Sr_2ZrMoO_6 double perovskite at different pressures (Pokharel *et al.*, 2025)

P (GPa)	B_V (GPa)	B_R (GPa)	B_H (GPa)	G_V (GPa)	G_R (GPa)	G_H (GPa)	E (GPa)	ν	G_H/B_H
0	165.76	165.73	165.75	112.31	110.51	111.41	273.04	0.225	0.67
20	169.01	169.00	169.01	113.78	111.82	112.79	276.81	0.227	0.67
40	172.37	172.35	172.36	115.27	113.09	114.18	280.58	0.229	0.66
60	174.66	174.64	174.65	116.04	113.67	114.86	282.62	0.230	0.66
80	176.88	176.79	176.84	117.42	114.68	116.05	285.66	0.231	0.66

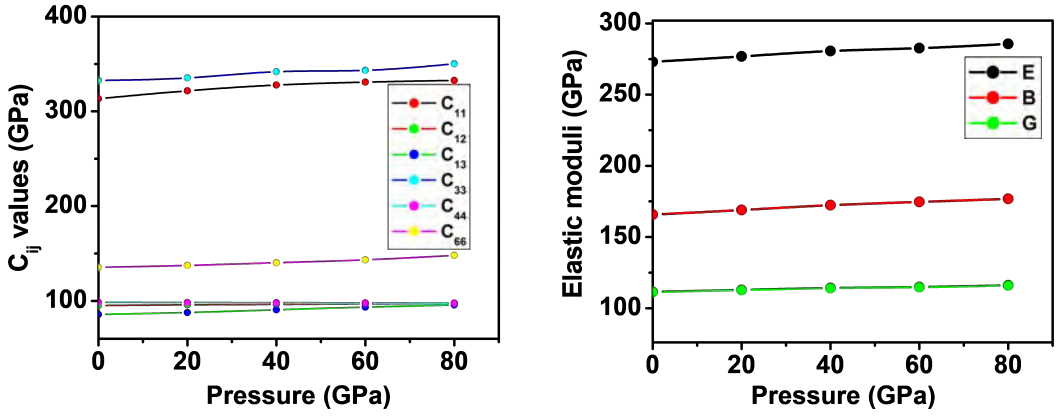

(a) **(b)**

Figure 38: Elastic properties of Sr_2ZrMoO_6 at different pressures (a) C_{ij}, (b) E, B, G (Pokharel *et al.*, 2025).

Figure 38a illustrates that, C_{11} and C_{33} consistently show the highest values across all pressure levels, indicating that Sr_2ZrMoO_6 demonstrates strong resistance to uniaxial compression. Furthermore, it is observed that C_{33} consistently exceeds C_{11} across the entire pressure range, indicating stronger atomic bonding in [001] direction than [100] direction. The C_{44} and C_{66} values vary significantly with pressure and are not equal, indicating that the shear moduli exhibit strong anisotropy (Table 10).

Figure 38b illustrates that elastic moduli (E, B, G) increase steadily with pressure up to 80 GPa. When pressure increases, the atoms move closer together and their bonds become stronger. This makes Sr_2ZrMoO_6 stiffer and more resistant to deformation at high-pressure conditions.

Even at 80 GPa, the G/B ratio remained above 0.57 (Table 12). This shows that tetragonal Sr_2ZrMoO_6 is brittle. The negative Cauchy constant with low Poisson's ratio (0.225 to 0.231) further verify that the material is brittle, with covalent bonding up to 80 GPa. The Vickers hardness (H_V) of the material can be determined using a semi-empirical equation proposed by Tian et al.(Tian *et al.*, 2012) as

$$H_V = 0.92 \left(\frac{G}{B}\right)^{1.137} G^{0.708} \tag{4.35}$$

The capacity of a material to resist fracture expansion is expressed by its fracture toughness (K_{IC}). It can be calculated using the following formula (Wu *et al.*, 2022)

$$K_{IC} = V_0^{1/6} G \left(\frac{B}{G}\right)^{1/2} \tag{4.36}$$

where V_0 is the volume of a single atom (in m^3).

To assess the damage resistance of the compound, the brittleness index (M) is used, which is expressed in terms of H_V and K_{IC} as (Boccaccini, 1997)

$$M = \frac{H_V}{K_{IC}} \tag{4.37}$$

The materials with high K_{IC} values strongly resist crack propagation. Materials with small M values demonstrate better damage tolerance and are less brittle. The moderate fracture toughness (K_{IC}) value of Sr_2ZrMoO_6 ranges from 3.61 to 3.73 MPa·$m^{1/2}$ at pressures of 0-80 GPa (Table 13). The fracture toughness value for Sr_2ZrMoO_6 is more than those of many superhard materials such as diamond (Field and Freeman, 1981) but slightly less than cubic boron nitride (c-BN) (Monteiro *et al.*, 2013). It resists cracking growth better than many brittle ceramics and superhard materials.

Table 13: Fracture toughness (K_{IC}) and brittleness index (M) of the Sr_2ZrMoO_6

P (GPa)	H_V (GPa)	K_{IC} (MPa·$m^{1/2}$)	M ($\mu m^{-1/2}$)
0	16.64	3.61	4.61
20	16.74	3.64	4.60
40	16.97	3.66	4.64
60	17.02	3.67	4.64
80	17.02	3.73	4.61

Moreover, the brittleness index (M) values for the material are between 4.60 to 4.64 $\mu m^{-1/2}$. The relatively low M value, along with moderate fracture toughness, indicates that Sr_2ZrMoO_6 is less brittle and possesses moderate toughness. This combination of reduced brittleness and outstanding fracture toughness highlights its potential for high-performance applications in structural, thermal, and electronic fields.

4.4.5 Elastic anisotropy

Elastic anisotropy of perovskite materials refers to the variation of mechanical properties along different crystallographic directions. It is commonly evaluated using several anisotropy indices. One of the most widely used is the universal anisotropy index (A^U), which quantifies the overall deviation of a material from ideal isotropic elastic behavior

(Ranganathan and Ostoja-Starzewski, 2008). In addition, the compressional anisotropy index (A_{comp}) and shear anisotropy index (A_{shear}) are used to evaluate anisotropy in the bulk and shear responses, respectively. These indices are determined from the differences between the Voigt and Reuss bounds of the corresponding elastic moduli. For an isotropic material, the Voigt and Reuss bounds are identical, resulting in $A_{\text{comp}} = 0$ and $A_{\text{shear}} = 0$. As the difference between these bounds increases, the values of A_{comp} and A_{shear} increase, indicating stronger elastic anisotropy. Therefore, these indices provide a quantitative measure of the directional dependence of the compressional and shear responses of perovskite materials. They are defined as follows (Nye and Lindsay, 1984).

$$A^U = \frac{5B_V}{B_R} + \frac{G_V}{G_R} - 6 \tag{4.38}$$

$$A^Z = \frac{2C_{44}}{C_{11} - C_{12}} \tag{4.39}$$

$$A_{\text{comp}} = \frac{B_V - B_R}{B_V + B_R} \tag{4.40}$$

$$A_{\text{shear}} = \frac{G_V - G_R}{G_V + G_R} \tag{4.41}$$

Isotropic properties are characterized by A^U, $A_{\text{comp}}, A_{\text{shear}} = 0$, and $A^Z = 1$, whereas any deviation from these values indicates anisotropy. Furthermore, an increase in A^U, A_{comp}, A_{shear}, and $|A^Z - 1|$ correspond to a greater degree of anisotropy.

4.4.5.1 Eu or Y-doped $SmMnO_3$ perovskite

Table 14: Elastic anisotropy indices (A^U, A^Z, A_{comp}, A_{shear}) of $SmMnO_3$ at different doping levels of europium and yttrium (Pokharel *et al.*, 2024c)

Compounds	A^U	A^Z	A_{comp}	A_{shear}
Pristine $SmMnO_3$	0.009	6.098	0.000	0.005
12.5% Eu doped	0.373	16.228	0.000	0.157
25% Eu doped	0.312	14.821	0.000	0.135
12.5% Y doped	0.222	12.649	0.000	0.099
25% Y doped	0.204	12.224	0.000	0.093

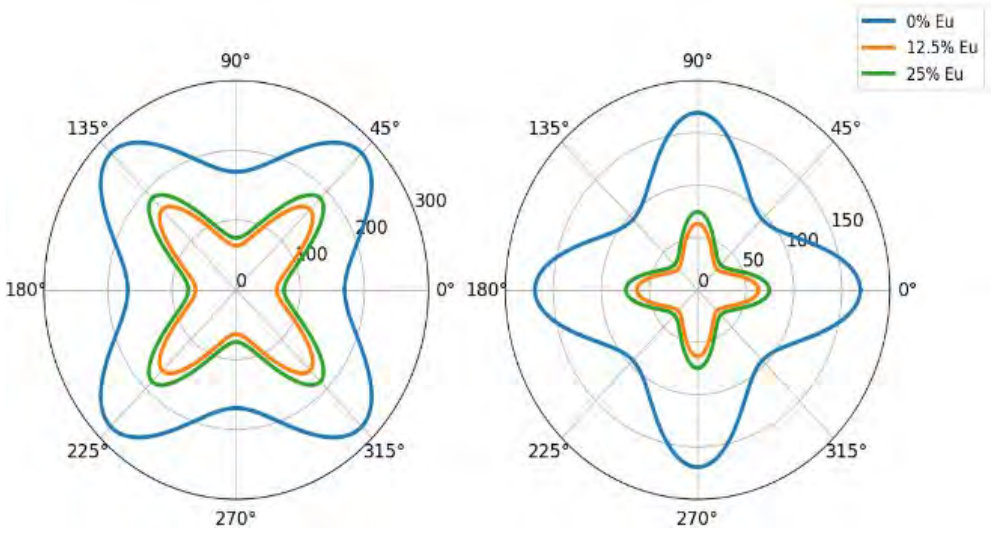

(a)

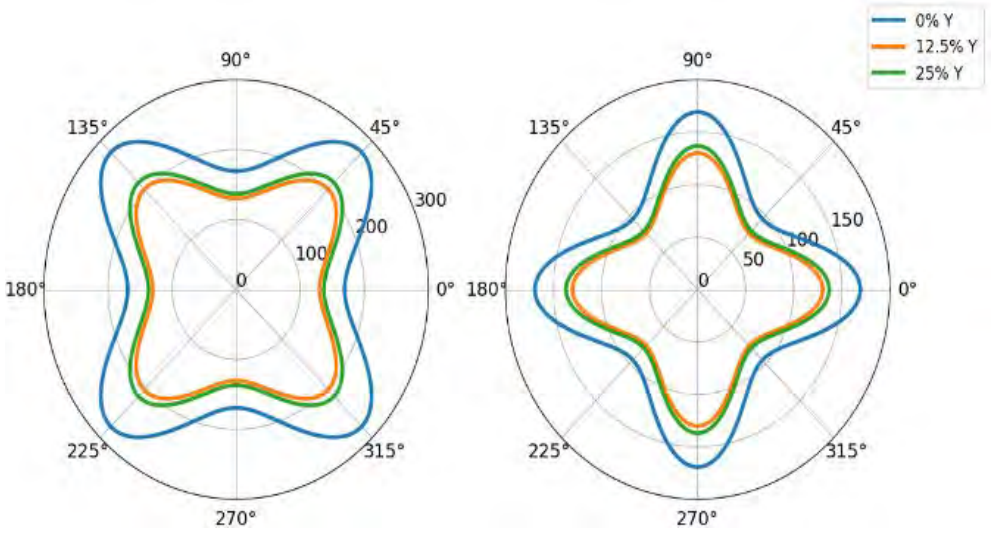

(b)

Figure 39: Polar plots of Young's and shear modulii for (a) Eu–doped, (b) Y-doped $SmMnO_3$ at different doping levels (Pokharel *et al.*, 2024c).

These pristine and Eu– or Y– doped compounds have an isotropic bulk modulus and a perfect spherical shape. The values of A_{shear} and A^Z in (Table 14) are not same, and they demonstrate high anisotropy. Compared with pristine $SmMnO_3$, all anisotropy indices increase markedly for both 12.5% and 25% Eu and Y doping levels. This indicates that Eu– doping enhances the material's elastic anisotropy, but Y– doping has a lesser effect than Eu. Figures 39a and 39b present directional dependent Young's and shear moduli of the complexes using polar plots. These graphs show that the complexes are elastically anisotropic.

4.4.5.2 Sr_2ZrMoO_6 at different pressures

In a tetragonal crystal, apart from elastic anisotropy indices (A^U, A^Z, A_{comp}, A_{shear} other anisotropy factors $A_{[100]}$, $A_{[010]}$, and $A_{[001]}$ also have significant meanings. These anisotropy factors are defined as (Ravindran *et al.*, 1998)

$$A_1 = A_{[100]} = \frac{4C_{44}}{C_{11} + C_{33} - 2C_{13}} \tag{4.42}$$

$$A_2 = A_{[010]} = \frac{4C_{55}}{C_{22} + C_{33} - 2C_{23}} \tag{4.43}$$

$$A_3 = A_{[001]} = \frac{2C_{66}}{C_{11} - C_{12}} \tag{4.44}$$

These equations further highlight the anisotropic behavior of the shear modulus along different crystallographic directions. Elastic anisotropy of Sr_2ZrMoO_6 under pressures of 0 to 80 GPa, is evaluated using several indices. The universal anisotropy index (A^U) is a comprehensive estimation of overall anisotropy (Ranganathan and Ostoja-Starzewski, 2008). Additionally, the bulk anisotropy index (A_{comp}) and the shear anisotropy index (A_{shear}) provides insights into the specific anisotropies in compression and shear, respectively, and describe the elastic anisotropy of double perovskites at the applied isotropic pressure (Nye and Lindsay, 1984).

Isotropic properties are represented by $A^U = 0$ and $A_{comp} = A_{shear} = 0$, whereas any non-zero values imply anisotropy. Furthermore, degree of anisotropy rises for higher values of A^U, A_{comp} and A_{shear}.

Table 15: Elastic anisotropy indices (A^U, A^Z, A_{comp}, A_{shear}, A_1, A_2, A_3) for the Sr_2ZrMoO_6 double perovskite at different pressures (Pokharel *et al.*, 2025)

Pressure (GPa)	A^U	A_{comp}	A_{shear}	A_1	A_2	A_3
0	0.082	0.000	0.008	0.823	0.823	1.241
20	0.088	0.000	0.009	0.813	0.813	1.217
40	0.097	0.000	0.009	0.803	0.803	1.212
60	0.104	0.000	0.010	0.806	0.806	1.224
80	0.119	0.002	0.012	0.802	0.802	1.256

Table 15 presents the computed values of A^U, A_{comp}, and A_{shear} of Sr_2ZrMoO_6 double perovskite at different pressures.

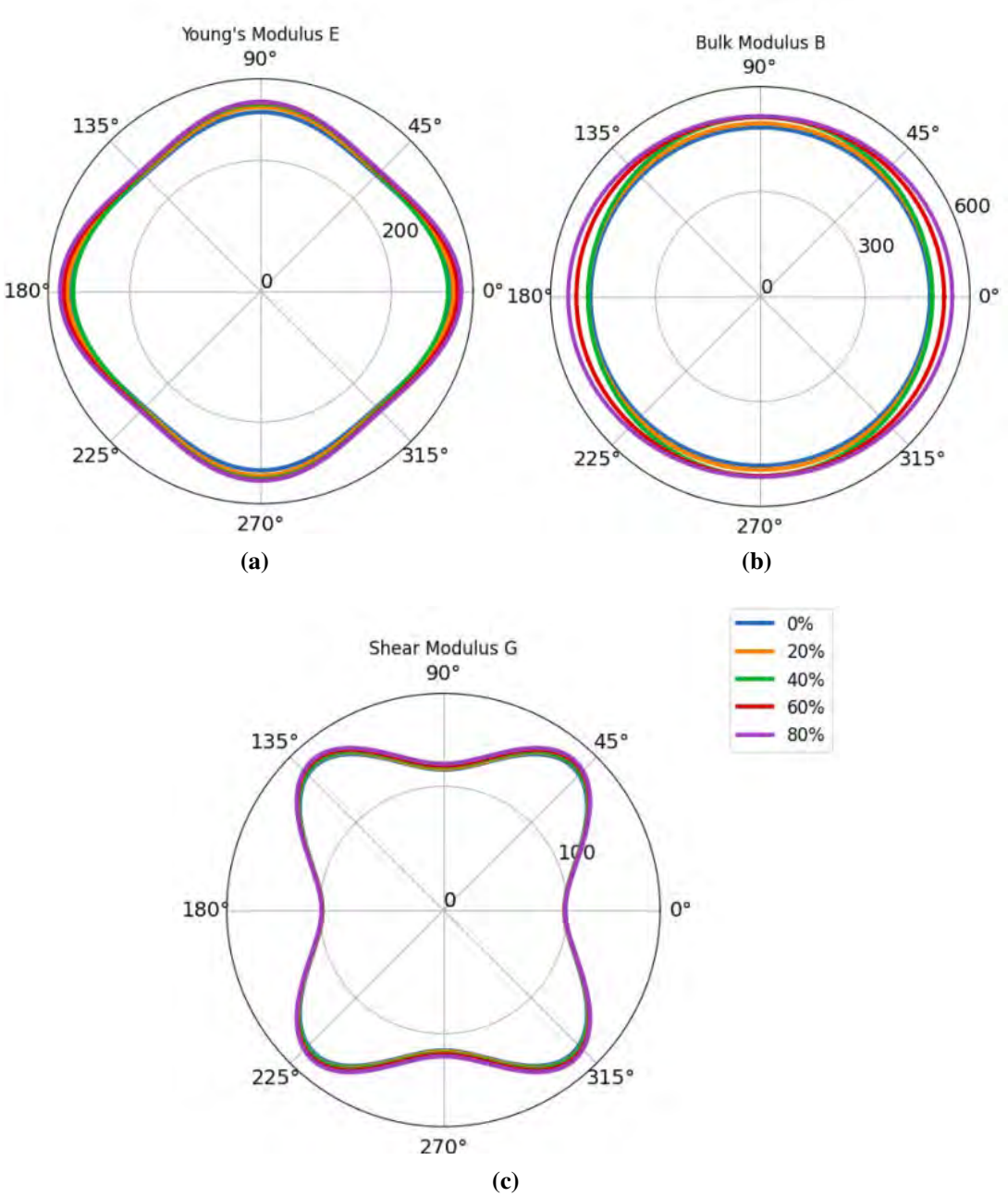

Figure 40: Polar plots of variation of elastic moduli (E, B, G) of Sr_2ZrMoO_6 at different pressures (Pokharel *et al.*, 2025).

To better illustrate elastic anisotropy of the material under the given conditions, 2D polar plots of the elastic moduli were generated. These plots are derived from the elastic compliance constants (S_{ij}) and directional cosines (l_i) (Ning, 2011; Pokharel *et al.*, 2025)

and given as

$$\frac{1}{E} = S_{11}(l_1^4 + l_2^4) + (2S_{13} + S_{44})(l_2^2 l_3^2 + l_1^2 l_3^2) + S_{33} l_3^4 + (2S_{12} + S_{66}) l_1^2 l_2^2 \tag{4.45}$$

$$\frac{1}{B} = (S_{11} + S_{12} + S_{13}) - (S_{11} + S_{12} - S_{13} - S_{33})\, l_3^2 \tag{4.46}$$

$$\begin{aligned}\frac{1}{G} = {} & \frac{1}{2}(S_{44} + S_{66})(l_1^4 + l_2^4) + S_{44} l_3^4 + l_1^2 l_2^2 \left[4(S_{11} - S_{12}) + (S_{44} - S_{66})\right] \\ & + l_3^2(1 - l_3^2) \times \left[2(S_{11} + S_{12} - 2S_{13}) + \frac{1}{2}(S_{66} - S_{44})\right]\end{aligned} \tag{4.47}$$

The 2D polar plots demonstrate that the elastic moduli are direction-dependent, indicating that their values vary within the material based on direction. The bulk modulus plot may appear more circular under different conditions, suggesting that the bulk modulus remains nearly isotropic across the pressure range. In contrast, the non-circular polar plots of Young's and shear moduli reveal a moderate level of anisotropy under these conditions. Figure 40 shows that the elastic moduli are direction-dependent, indicating that their values vary with direction. The bulk modulus plot may become more circular as pressure increases, suggesting that the bulk modulus remains nearly isotropic across the pressure range. In contrast, Young's and shear moduli display a moderate level of anisotropy as pressure increases.

4.4.5.3 Sound velocities at different isotropic axes

In a tetragonal structure, transverse and longitudinal wave modes are feasible only along specific symmetry directions, such as [100], [010], and [110]. The waves are composed of a combination of longitudinal and transverse modes in other orientations. The velocities can be expressed as (Bao *et al.*, 2019a)

$$[100]\, v_l = [010]\, v_l = \sqrt{\frac{C_{11}}{\rho}};\ [001]\, v_{t_1} = \sqrt{\frac{C_{44}}{\rho}};\ [001]\, v_{t_2} = \sqrt{\frac{C_{66}}{\rho}} \tag{4.48}$$

$$[001]\, v_l = \sqrt{\frac{C_{33}}{\rho}};\ [100]\, v_{t_1} = [010]\, v_{t_2} = \sqrt{\frac{C_{66}}{\rho}};\ \text{and} \tag{4.49}$$

$$\begin{aligned}&[100]\, v_l = \sqrt{\frac{C_{11} + C_{12} + 2C_{66}}{\rho}}, \qquad [001]\, v_{t_1} = \sqrt{\frac{C_{44}}{\rho}}, \\ &[110]\, v_{t_2} = \sqrt{\frac{C_{11} - C_{12}}{\rho}}.\end{aligned} \tag{4.50}$$

In a tetragonal structure, sound velocities depend on the path of wave propagation relative to crystallographic axes. Transverse and longitudinal wave modes are allowed only along specific symmetry directions, such as [100], [010], and [110]. In other

orientations, both transverse and longitudinal modes coexist (Bao *et al.*, 2019b). The calculated sound velocities (v_l, v_{t_1}, v_{t_2}) for Sr_2ZrMoO_6 at various pressures clearly demonstrate this anisotropy.

Table 16: Longitudinal (v_l) and transverse (v_t) sound velocities ($m\,s^{-1}$) of Sr_2ZrMoO_6 under different pressures and directions

P	ρ	[100] direction			[001] direction			[110] direction		
(GPa)	(g/cm^3)	v_l (m/s)	v_{t_1} (m/s)	v_{t_2} (m/s)	v_l (m/s)	v_{t_1} (m/s)	v_{t_2} (m/s)	v_l (m/s)	v_{t_1} (m/s)	v_{t_2} (m/s)
0	5.591	7485.35	4179.98	4920.11	7713.79	4920.11	4920.11	7792.88	4179.99	4416.89
20	5.678	7525.89	4150.13	4919.24	7681.61	4919.24	4919.24	7807.32	4150.13	4459.17
40	5.722	7568.57	4141.09	4951.16	7728.91	4951.16	4951.16	7846.26	4141.09	4498.15
60	5.759	7578.87	4129.84	4986.44	7720.04	4986.44	4986.44	7873.46	4129.84	4506.94
80	5.782	7585.38	4127.31	5058.48	7782.07	5058.48	5058.48	7921.54	4127.31	4513.92

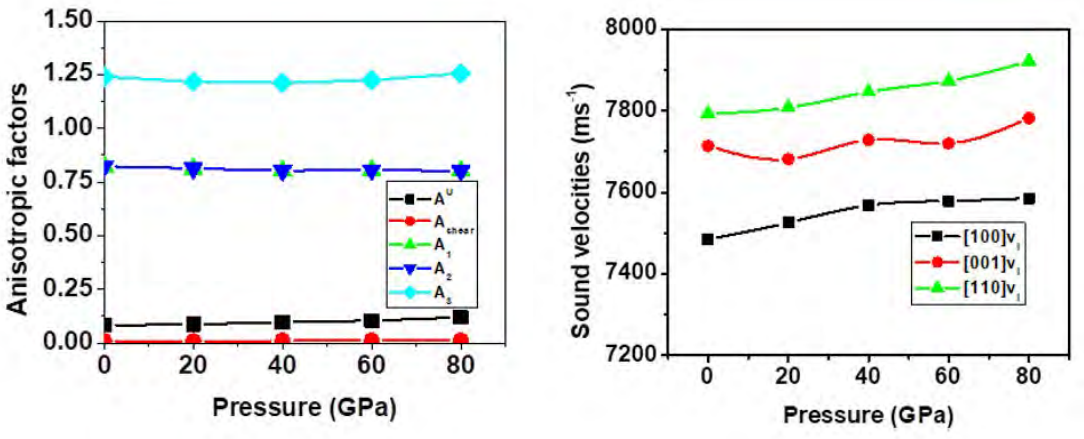

(a) **(b)**

Figure 41: (a) Anisotropy factor, (b) sound velocities of Sr_2ZrMoO_6 at different pressures

The longitudinal velocity increases gradually with pressure in the [100] direction, from 7485.35 m/s at 0 GPa to 7585.38 m/s at 80 GPa (Table 16). The transverse velocities (v_{t_1} and v_{t_2}) exhibit similar trends, with v_{t_1} decreasing slightly from 4179.98 m/s to 4127.31 m/s, while v_{t_2} increases from 4920.11 m/s to 5058.48 m/s over the same pressure range. According to these findings, the wave propagation is significantly more sensitive to pressure in transverse direction than in longitudinal direction, particularly along the direction of [100]. In the [001] direction, the variation in both longitudinal and transverse velocities follow a different pattern than in the [100] direction and on the [110]

direction, the longitudinal velocity (v_l) increases more sharply than in other directions. This difference is because the material is stiffer in the [001] direction. Overall, the pressure-induced increase in sound velocities confirms that Sr_2ZrMoO_6 becomes stiffer during compression, which influences longitudinal and transverse modes along various crystallographic axes, Figure 41b.

4.5 Debye temperature

Debye temperature (θ_D) describes thermal properties of substances. A higher value of θ_D indicates that the material possesses higher thermal conductivity and a high melting temperature (Verma *et al.*, 2012). In this study, θ_D was computed from average sound velocity using established methods and elastic constant data, expressed as (Anderson, 1963)

$$\theta_D = \frac{h}{k_B}\left[\frac{3n}{4\pi}\left(\frac{N_A\rho}{M}\right)\right]^{1/3} v_m \tag{4.51}$$

where h represents Planck's constant, k_B is Boltzmann's constant, N_A is Avogadro's number, M is molecular mass, ρ is density, and v_m is the average sound velocity. The average sound velocity is expressed in terms of longitudinal and transverse velocities by the relation (Wu *et al.*, 2020). It is expressed as

$$v_m = \left[\frac{1}{3}\left(\frac{2}{v_t^3} + \frac{1}{v_l^3}\right)\right]^{-1/3} \tag{4.52}$$

Navier's equation gives longitudinal and transverse velocities using the bulk (B) and shear (G) moduli (Wu *et al.*, 2021).

$$v_l = \left[\frac{3B + 4G}{3\rho}\right]^{1/2}, \quad v_t = \left[\frac{G}{\rho}\right]^{1/2} \tag{4.53}$$

4.5.1 Bulk $ZrSiO_3$ at different pressures

Table 17 presents the computed values of v_l, v_t and v_m, indicating minimal change with increasing pressure, Figure 42a. Figure 42b illustrates that the Debye temperature (θ_D) rises gradually under pressure. This rise in θ_D is attributed to the compression of the atomic structure, reducing interatomic distances and strengthening bonding forces, which leads to higher vibrational energy and frequencies. Since covalent bond strength is proportional to θ_D, the computed values suggest that $ZrSiO_3$ exhibits the strongest covalent character up to 100 GPa. Similar trends were observed by Tian et al. (2017) in the Al_7Cu_2Fe alloy (Tian *et al.*, 2017) and by Daoud in the thallium-phosphide (Daoud,

2017) using DFT.

Table 17: Pressure dependent density (ρ), acoustic velocities (v_l, v_t, v_m) and Debye temperature (θ_D) of bulk $ZrSiO_3$

P (GPa)	ρ (g cm^{-3})	v_l (m s^{-1})	v_t (m s^{-1})	v_m (m s^{-1})	θ_D (K)
0	5.823	6127.39	2187.66	2485.47	348.22
20	5.871	6121.70	2186.21	2483.87	348.85
40	5.917	6118.38	2200.77	2500.02	352.14
60	6.007	6097.12	2195.35	2493.80	353.02
80	6.033	6117.60	2216.92	2517.92	356.95
100	6.050	6115.49	2234.12	2536.98	360.00

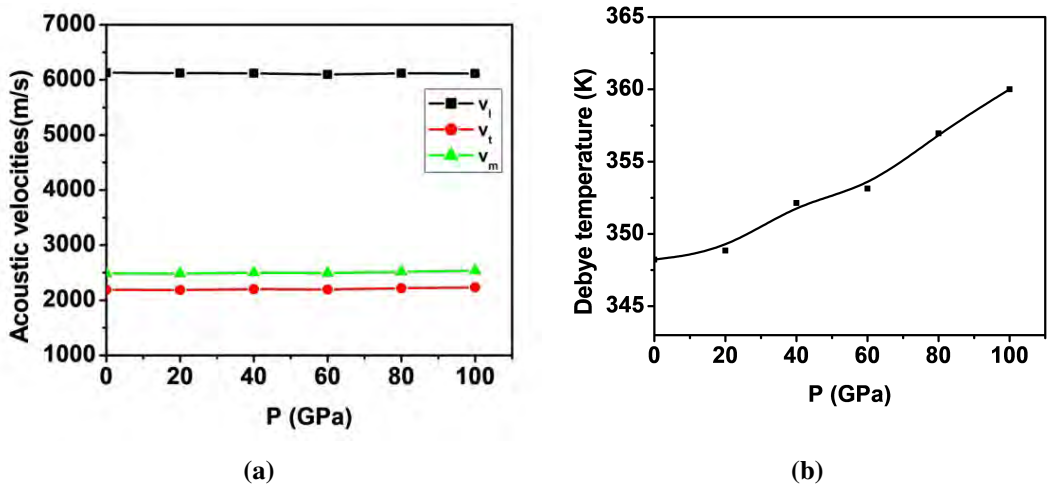

(a) **(b)**

Figure 42: Pressure-dependent (a) acoustic velocities, (b) Debye temperature (θ_D) of bulk $ZrSiO_3$ (Pokharel *et al.*, 2024).

4.6 Termination model

The calculated values of ρ are 7.040 g/cm³ for bulk $ZrSiO_3$, 2.724 g/cm^3 for the ZrO–terminated slab, and 2.278 g/cm^3 for the SiO_2–terminated slab. As expected, the bulk structure showed the highest density, followed by the ZrO–terminated slab, while the SiO_2–terminated slab exhibits the lowest density.

Table 18: Calculated density (ρ), acoustic velocities (v_l, v_t, v_m), and Debye temperature (θ_D) of bulk and slabs of $ZrSiO_3$

Compound	ρ (g cm^{-3})	v_l (m s^{-1})	v_t (m s^{-1})	v_m (m s^{-1})	θ_D (K)
Bulk	7.040	5974.06	3206.22	3550.02	438.04
ZrO-terminated	2.724	5877.07	2935.30	3293.08	321.09
SiO_2-terminated	2.278	7429.31	3280.83	3703.21	359.17

Similarly, the sound velocities (v_l, v_t, v_m) are calculated to be (5974.06, 3206.22, 3550.02 m/s) for the bulk and (5877.07, 2935.30, 3293.08 m/s) for the ZrO-terminated slab and (7429.31, 3280.83, 3703.21 m/s) for the SiO_2–terminated slab, Table 18. The bulk phase has the lowest sound velocity of the three systems, whereas the SiO_2–terminated slab has the highest. The calculated values of the Debye temperatures (θ_D) are 438.04 K, 321.09 K, and 359.17 K for bulk $ZrSiO_3$, ZrO–, and SiO_2–terminated slab models, respectively. These findings suggest that the bulk compound possesses the maximum thermal conductivity and melting temperature, indicated by its higher Debye temperature. The SiO_2–terminated slab has an intermediate Debye temperature, whereas the ZrO–terminated slab has the least value. These results predict that surface termination reduces the thermal conductivity and melting temperature.

4.6.1 Eu– and Y– doped $SmMnO_3$

Table 19: Density (ρ), acoustic velocities (v_l, v_t, v_m) and Debye temperature (θ_D) of $SmMnO_3$ at different doping levels of Eu and Y (Pokharel *et al.*, 2024c)

Compounds	ρ (g cm^{-3})	v_l (m s^{-1})	v_t (m s^{-1})	v_m (m s^{-1})	θ_D (K)
Pristine $SmMnO_3$	7.042	5974.06	3206.22	3550.00	438.04
12.5% Eu doped	8.194	5994.44	2711.99	3058.01	418.62
25% Eu doped	8.225	5703.09	2461.14	2780.55	380.55
12.5% Y doped	7.996	6068.78	3203.36	3551.98	487.39
25% Y doped	7.676	6168.66	3278.78	3628.80	496.44

The longitudinal, transverse, and average sound velocities of pristine $SmMnO_3$ decrease with Eu– doping, whereas Y– doping leads to an increase in all acoustic velocities, Figure 43a. In the same way, the Debye temperature (θ_D) decreases with increasing Eu content, while Y– doping significantly raises θ_D, Figure 43b.

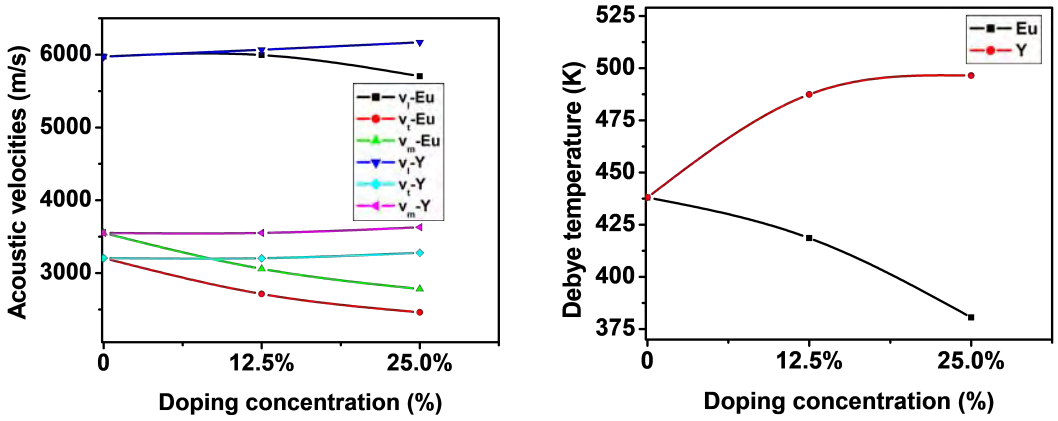

(a) **(b)**

Figure 43: Variation of (a) acoustic velocities, (b) Debye temperature of $SmMnO_3$ with different Eu and Y doping levels (Pokharel *et al.*, 2024c).

4.6.2 Sr_2ZrMoO_6 double perovskite at different pressures

The Debye temperature (θ_D) represents the vibrational characteristics of a solid. Above (θ_D), all vibrational modes are active, whereas below θ_D, quantum effects become significant. A higher θ_D value generally indicates that the material has a high melting temperature and enhanced thermal conductivity (Anderson, 1963; Pokharel *et al.*, 2024b). In this study, we have computed θ_D using Equation (4.52) and elastic constants data.

Table 20: Density (ρ), acoustic velovities (v_l, v_t, v_m) and Debye temperature (θ_D) of Sr_2ZrMoO_6 at different pressures (Pokharel *et al.*, 2025)

Pressure (GPa)	ρ (g/cm^3)	v_l (m/s)	v_t (m/s)	v_m (m/s)	θ_D (K)
0	5.591	7498.32	4464.33	4942.32	531.55
20	5.678	7498.79	4456.16	4934.17	533.50
40	5.722	7533.14	4467.83	4948.01	536.25
60	5.759	7543.82	4465.53	4946.36	537.32
80	5.782	7574.01	4480.83	4963.57	539.81

The Debye temperature (θ_D) and calculated sound velocities for Sr_2ZrMoO_6 at different pressures are presented in Table 20. As pressure increases, both Debye temperature and acoustic velocities increase slightly. Variation in the acoustic velocities are nearly linear, Figure 44a. At low pressure there is harmonic effects on lattice but at high pressure show anharmonic effects and cause the non-linear increase (θ_D) with pressure, Figure 44b.

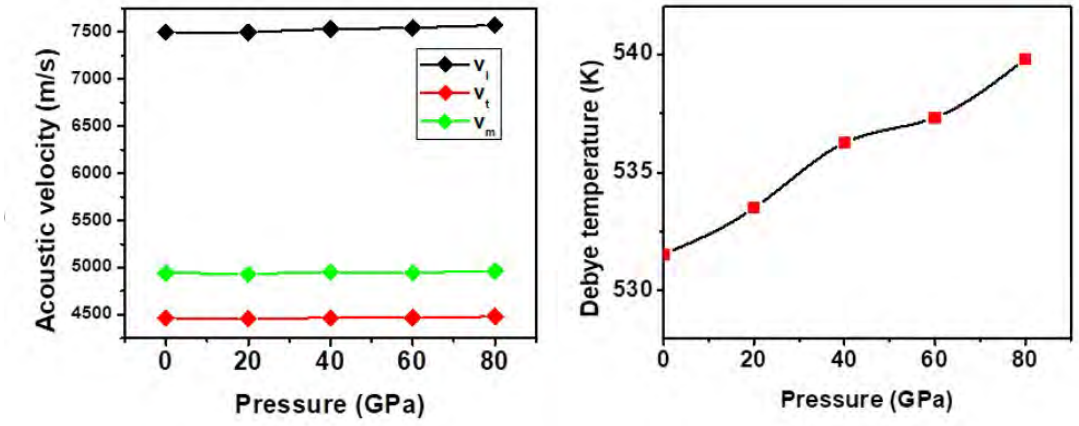

(a) **(b)**

Figure 44: Variation of (a) acoustic velocities, (b) Debye temperature of Sr_2ZrMoO_6 under different pressures (Pokharel *et al.*, 2025).

4.7 Mechanical properties of $ZrSiO_3$ monolayer

To examine the mechanical strength and stability of the of $ZrSiO_3$ monolayer, elastic constants (C_{ij}) are computed using the finite distortion method (Li, 2020), and are given by (Faghihnasiri *et al.*, 2019)

$$C_{ij} = \frac{1}{S_0}\left(\frac{\partial^2 E_s}{\partial \epsilon_i \partial \epsilon_j}\right) \tag{4.54}$$

where E_s, ϵ, and S_0 represent the strain energy, the applied strain, and the area of the strain-free monolayer, respectively. σ_j can be expressed as

$$\begin{bmatrix}\sigma_1\\ \sigma_2\\ \sigma_6\end{bmatrix} = \begin{bmatrix}C_{11} & C_{12} & 0\\ C_{12} & C_{22} & 0\\ 0 & 0 & C_{66}\end{bmatrix}\begin{bmatrix}\epsilon_1\\ \epsilon_2\\ \epsilon_6\end{bmatrix} \tag{4.55}$$

For the crystal symmetry of the 2D square lattice, only C_{11}, C_{22}, C_{12}, and C_{66} are identified as significant independent elastic stiffness constants and the total energy is

expressed as (Le Page and Saxe, 2002)

$$E = \frac{1}{2}\left(C_{11}\epsilon_{xx}^2 + C_{22}\epsilon_{yy}^2 + 2C_{12}\epsilon_{xx}\epsilon_{yy} + 2C_{66}\epsilon_{xy}^2\right) \tag{4.56}$$

Two-dimensional Young's modulus (Y_a and Y_b) are given by (Sharma *et al.*, 2022)

$$Y_a = \frac{C_{11}^2 - C_{12}^2}{C_{11}} \quad \text{and} \quad Y_b = \frac{C_{22}^2 - C_{12}^2}{C_{22}}, \tag{4.57}$$

The corresponding Poisson ratios (ν_a, ν_b) are expressed as

$$\nu_a = \frac{C_{12}}{C_{11}} \quad \text{and} \quad \nu_b = \frac{C_{12}}{C_{22}}, \tag{4.58}$$

And the 2D shear modulus is given by

$$G = C_{66} \tag{4.59}$$

Poisson's ratio (ν) and 2D Young's modulus (Y^{2D}) are used to calculate in-plane stiffness (K) and shear modulus (G) (Politano and Chiarello, 2015) as

$$K = \frac{Y^{2D}}{2(1-\nu)}, \quad \text{and} \quad G = \frac{Y^{2D}}{2(1+\nu)} \tag{4.60}$$

where bulk modulus denotes resistance to compression, and shear modulus denotes resistance of a 2D material to deformation. Stiffness, in this context, measures the resistance to elastic deformation.

The calculated elastic constants under zero strain (Table 21) closely match those reported for single-layer B_2SSe, but they differ substantially from those of the α-Ga_2S_3 and α-Ga_2Se_3 monolayers (Yan *et al.*, 2022; Hu and Huang, 2017). Our findings illustrate that strain has significant impacts on the elastic characteristics of $ZrSiO_3$ monolayer. The estimated values of C_{11}, C_{22}, C_{12}, and C_{66}, within the -6% to 6% strain range, meet the mechanical stability criteria of 2D material (Mouhat and Coudert, 2014), stated as

$$C_{11}C_{22} - C_{12}^2 > 0 \quad \text{and} \quad C_{66} > 0 \tag{4.61}$$

Table 21: Elastic stiffness coefficients (C_{ij}), elastic moduli (Y, K, G), Poisson's ratio (ν), and mechanical stability conditions of $ZrSiO_3$ monolayer (Pokharel *et al.*, 2024b)

Strain	C_{11}	C_{22}	C_{12}	C_{66}	Y_a	Y_b	ν_a	ν_b	K_a	K_b
%		(N/m)				(N/m)			(N/m)	
6	156.74	139.01	49.92	77.02	140.84	107.39	0.318	0.349	103.25	82.48
4	158.57	141.41	50.39	78.65	142.56	110.09	0.317	0.356	104.36	85.48
2	169.52	148.82	52.24	80.73	153.42	114.55	0.308	0.351	100.85	88.29
0	196.52	159.82	59.63	81.33	178.43	111.88	0.303	0.373	127.99	88.22
-2	205.04	165.13	56.79	82.04	189.31	117.26	0.277	0.344	130.92	89.37
-4	211.04	171.53	57.39	82.54	195.43	123.81	0.272	0.334	134.27	92.95
-6	219.52	186.08	59.92	83.73	203.16	141.38	0.273	0.322	139.73	104.26

For 2D materials, longitudinal and transverse sound velocities are computed using following relationships (Bolen *et al.*, 2021)

$$v_l = \sqrt{\frac{B+G}{\rho_{2D}}}, \quad v_t = \sqrt{\frac{G}{\rho_{2D}}} \tag{4.62}$$

where ρ_{2D} represents mass density per unit area for 2D material. The longitudinal velocity (v_l) represents the speed of pressure waves, while the transverse velocity (v_t) represents the speed of shear waves.

In addition, Table 21 does not include strain values that exceed ±6% as a result of mechanical instability. The Young's moduli (Y_a and Y_b) increase with compressive strain, indicating that the material is stiffer under compression (Table 21). However, tensile strain lowers the Young's moduli, indicating that the material becomes less stiff under tension, which supports the anisotropic behavior of the monolayer due to compression and tension. Similarly, bulk moduli (K_a and K_b) of the material rise under compression and decrease under tension. The shear modulus is diminished by tensile strain, and enhanced by compressive strain. Which indicates the substance is less sensitive against shear distortion during compression. Poisson's ratio remains approximately 0.3 for both tensile and compressive strains, indicating ductile and flexible nature of the monolayer. Notably, Poisson's ratio increases from approximately 0.303 to 0.318 as the tensile strain is raised from 0% to 6%. This gradual rise reveals that the material can expand more laterally under tensile deformation, which shows that it could be good for strain-sensitive sensor applications.

Table 22: Calculated sound velocities (v_l, v_t, v_m) and Debye temperatures (θ_D) of $ZrSiO_3$ monolayer under strain

Strain (%)	v_l (m s^{-1})	v_t (m s^{-1})	v_m (m s^{-1})	θ_D (K)
6	8629.17	5812.12	6818.15	1181.82
4	8721.86	5873.29	6889.60	1194.18
2	8767.05	5950.45	6962.87	1206.87
0	9102.59	5972.52	7061.97	1224.05
-2	9167.59	5998.54	7098.14	1230.42
-4	9262.37	6016.79	7135.66	1236.82
-6	9490.12	6060.01	7223.11	1251.98

The equation presented below is employed to determine average sound velocity (v_m) in terms of v_l and v_t expressed as (Kong, 2009)

$$\frac{1}{v_m} = \sqrt{\frac{1}{2}\left(\frac{1}{v_l^2} + \frac{1}{v_t^2}\right)} \tag{4.63}$$

The Debye model is utilized to investigate the thermodynamic characteristics of 2D materials in further detail. This model includes determining the frequency distribution function of phonon in the material. The frequency distribution function is given by (Xue *et al.*, 2024)

$$\int_0^{\omega_m} g(\omega)\, d\omega = \int_0^{\omega_m} \frac{\omega\, S}{\pi v_m^2} d\omega = 2N, \tag{4.64}$$

where ω_m is the maximum phonon frequency, and S is surface area of the 2D material.

θ_D for monolayer can be expressed as

$$\theta_D = \frac{\hbar\omega_m}{k_B} = \frac{\hbar}{k_B}.\left(\frac{4\pi N}{S}\right)^{1/2} v_m \tag{4.65}$$

where the symbols carry their usual meanings. Both longitudinal and transverse sound velocities increase with increasing compressive strain. Additionally, the Debye temperature rises with compressive strain and falls under tensile strain (Table 22). A significantly higher Debye temperature is observed for the $ZrSiO_3$ monolayer (1224.05 K) compared with the bulk structure (348.22 K). The θ_D = 1224.05 K is larger than that of MoS_2

monolayer (642 K)and less than that of graphene (1813 K)

Mechanical anisotropy in 2D materials can be measured by Li's methodologies (Li, 2020). Specifically, we examine the universal, Ranganathan (Ranganathan and Ostoja-Starzewski, 2008), and Kube (Kube and De Jong, 2016) anisotropy coefficients. Elastic constants are used to express these anisotropy coefficients. For this purpose, the following formulae are utilized to determine the bulk (K^V, K^R) and shear moduli (G^V, G^R) (Voigt, 1928; Reuss, 1929)

$$K^V = \frac{C_{11} + C_{22} + 2C_{12}}{4} \tag{4.66}$$

$$G^V = \frac{C_{11} + C_{22} - 2C_{12} + 4C_{66}}{8} \tag{4.67}$$

$$K^R = \frac{1}{S_{11} + S_{22} + 2S_{12}} \tag{4.68}$$

$$G^R = \frac{1}{S_{11} + S_{22} - 2S_{12} + S_{66}} \tag{4.69}$$

where S_{ij} reciprocal of C_{ij} matrix known as compliance matrix (Nagy and Siegel, 2020). Further mechanical anisotropy indices are derived using the formulas below.

$$A^{SU} = \begin{cases} 0, & \text{for isotropic systems} \\ \left[\frac{1}{4}(C_{11} + C_{22} + 2C_{12})(S_{11} + S_{22} + 2S_{12}) - 1\right]^2 \\ \quad +2\left[\frac{1}{16}(C_{11} + C_{22} - 2C_{12} + 4C_{66})(S_{11} + S_{22} - 2S_{12} + S_{66})\right]^2, \\ & \text{for anisotropic systems} \end{cases} \tag{4.70}$$

$$A^{\text{Ranganathan}} = \begin{cases} 0, & \text{for isotropic systems} \\ \frac{K^V}{K^R} + 2\frac{G^V}{G^R} - 3, & \text{for anisotropic systems} \end{cases} \tag{4.71}$$

$$A^{\text{Kube}} = \begin{cases} 0, & \text{for isotropic systems} \\ \sqrt{\left(\ln \frac{K^V}{K^R}\right)^2 + 2\left(\ln \frac{G^V}{G^R}\right)^2}, & \text{for anisotropic systems} \end{cases} \tag{4.72}$$

Table 23: Elastic anisotropy and bulk (K^V, K^R), shear (G^V, G^R) moduli of a $ZrSiO_3$ monolayer under strain

Strain (%)	G^V (N/m)	G^R (N/m)	K^V (N/m)	K^R (N/m)	A^{SU}	$A^{Ranganathan}$	A^{Kube}
6	62.99	59.73	98.89	98.49	0.188	0.114	0.033
4	64.23	60.85	100.19	99.82	0.186	0.115	0.033
2	67.09	64.14	105.71	105.21	0.181	0.097	0.028
0	70.30	68.09	118.90	117.48	0.175	0.077	0.020
-2	73.09	71.48	120.94	119.39	0.169	0.058	0.015
-4	74.74	73.45	124.34	122.88	0.167	0.047	0.012
-6	77.58	76.79	131.36	130.38	0.162	0.028	0.007

And the directional dependent Young's modulus and Poisson's ratio as function of orientation angles θ are expressed as

$$E(\theta) = \frac{C_{11}C_{22} - C_{12}^2}{C_{22}\cos^4(\theta) + A\cos^2(\theta)\sin^2(\theta) + C_{11}\sin^4(\theta)} \tag{4.73}$$

$$\nu(\theta) = \frac{C_{12}\cos^4(\theta) - B\cos^2(\theta)\sin^2(\theta) + C_{12}\sin^4(\theta)}{C_{22}\cos^4(\theta) + A\cos^2(\theta)\sin^2(\theta) + C_{11}\sin^4(\theta)} \tag{4.74}$$

$$\begin{aligned}\frac{1}{G(\theta)} &= [S_{11} + S_{22} - S_{12}]\cos^2(\theta)\sin^2(\theta) \\ &\quad + \frac{1}{4}S_{66}\left[\cos^4(\theta) + \sin^4(\theta) - 2\cos^2(\theta)\sin^2(\theta)\right]\end{aligned} \tag{4.75}$$

where

$$A = \frac{(C_{11}C_{22} - C_{12}^2)}{C_{66}} - 2C_{11}, \quad \text{and} \quad B = C_{11} + C_{22} - \frac{(C_{11}C_{22} - C_{12}^2)}{C_{66}} \tag{4.76}$$

Figures 45a, 45b, and 45c present 2D diagrams that illustrate the elastic anisotropy of the two-dimensional material under different strain values, offering more clear and detailed overview of its behavior. The anisotropic behavior under both tensile and compressive strain conditions are more easily visualized and analyzed through the use of these graphs.

The anisotropy values of the $ZrSiO_3$ monolayer expressed in Table 23 demonstrates its mechanical stability and elastic anisotropy. Positive values of $A^{Ranganathan}$ and A^{Kube} indicate significant anisotropy and stability, as per Ranganathan and Kube's criteria.

This anisotropic behavior is further illustrated by polar graphs, Figure 45(a–c).

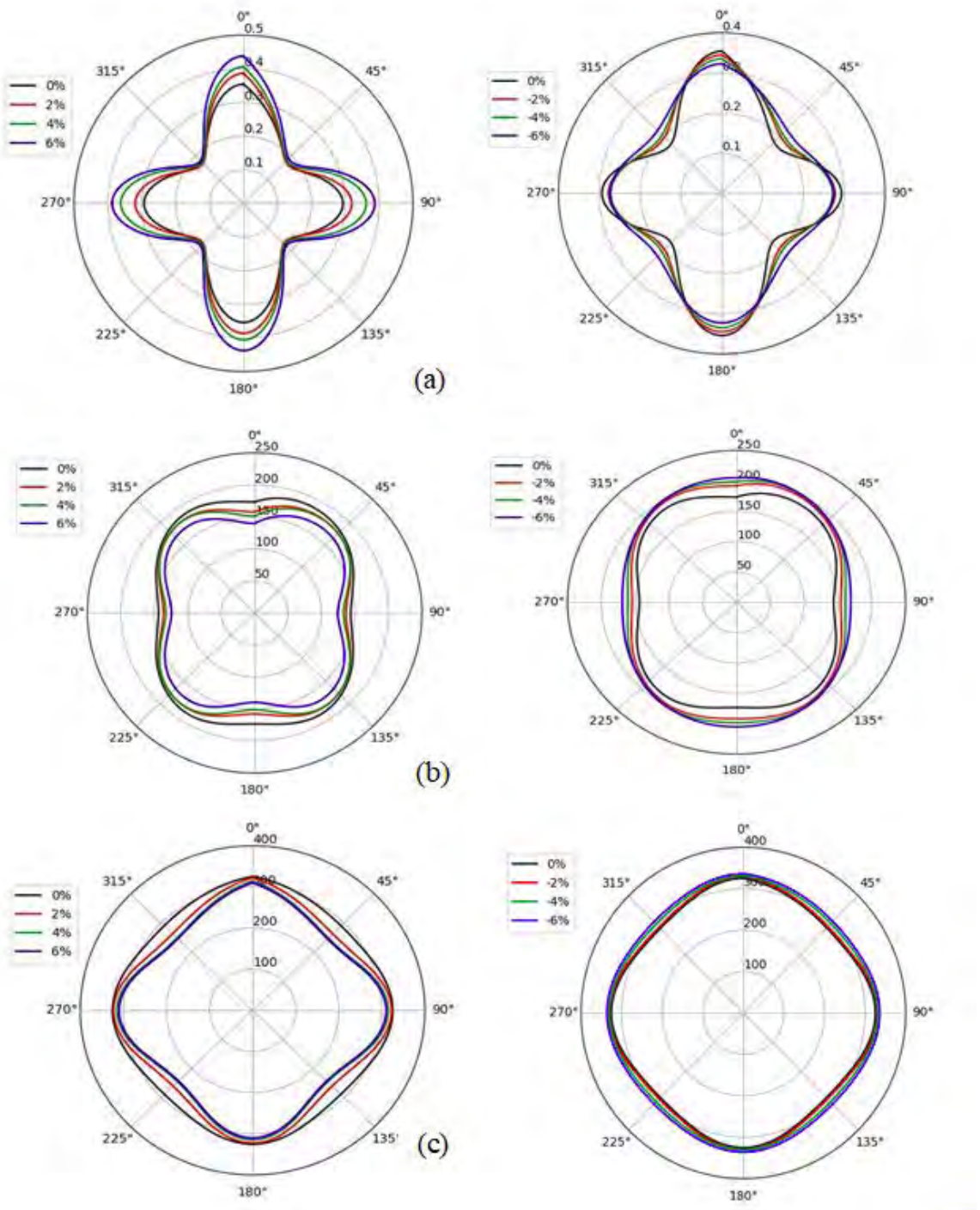

Figure 45: 2D polar plot of (a) Poisson's ratio, (b) Young's modulus, (c) shear modulus of $ZrSiO_3$ monolayer under strains (Pokharel *et al.*, 2024b).

4.8 Magnetic properties

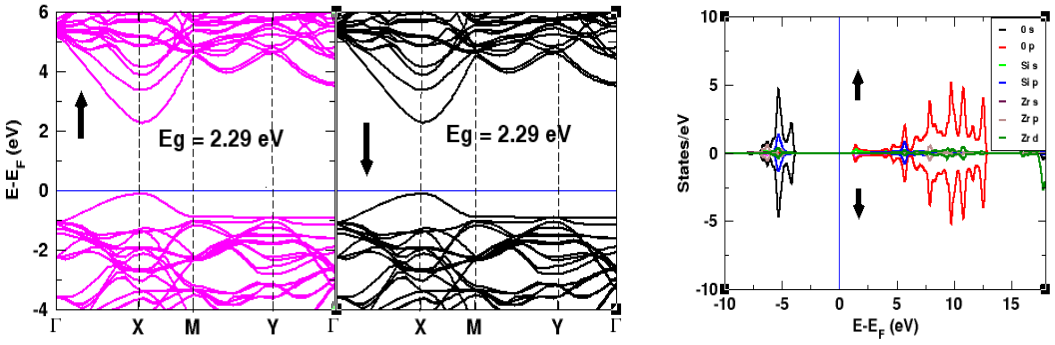

(a) **(b)**

Figure 46: Spin polarized (a) band structure, (b) PDOS of bulk $ZrSiO_3$ (Pokharel *et al.*, 2024).

To examine the magnetic properties of $ZrSiO_3$ monolayer, spin–polarized electronic band structure calculations and PDOS analyses were conducted across the path Γ - X - M - Y - Γ. Figure 46a shows that the electronic band structures for both spin channels are identical across the Brillouin zone, which indicates the absence of spin splitting. This observation is further supported by the PDOS plots in Figure 46b, where identical contributions from both spin states are observed. The perfect symmetry on both spin channels result in non–magnetic behavior of $ZrSiO_3$ monolayer under strain, which is further confirmed by calculated zero magnetic moment.

4.8.0.1 Eu– and Y-doped $SmMnO_3$

The $SmMnO_3$ perovskite exhibits strong magnetic properties, especially when doped with Eu and Y. To study the magnetic properties of $SmMnO_3$, the lattice parameters of the pristine and doped systems were optimized for different magnetic configurations using the Birch–Murnaghan equation of state (see Appendix A4.3). As illustrated in Figure 47(a–e) the calculated results reveal ferromagnetic state is the most stable configuration for both pure and Eu- or Y-doped $SmMnO_3$.

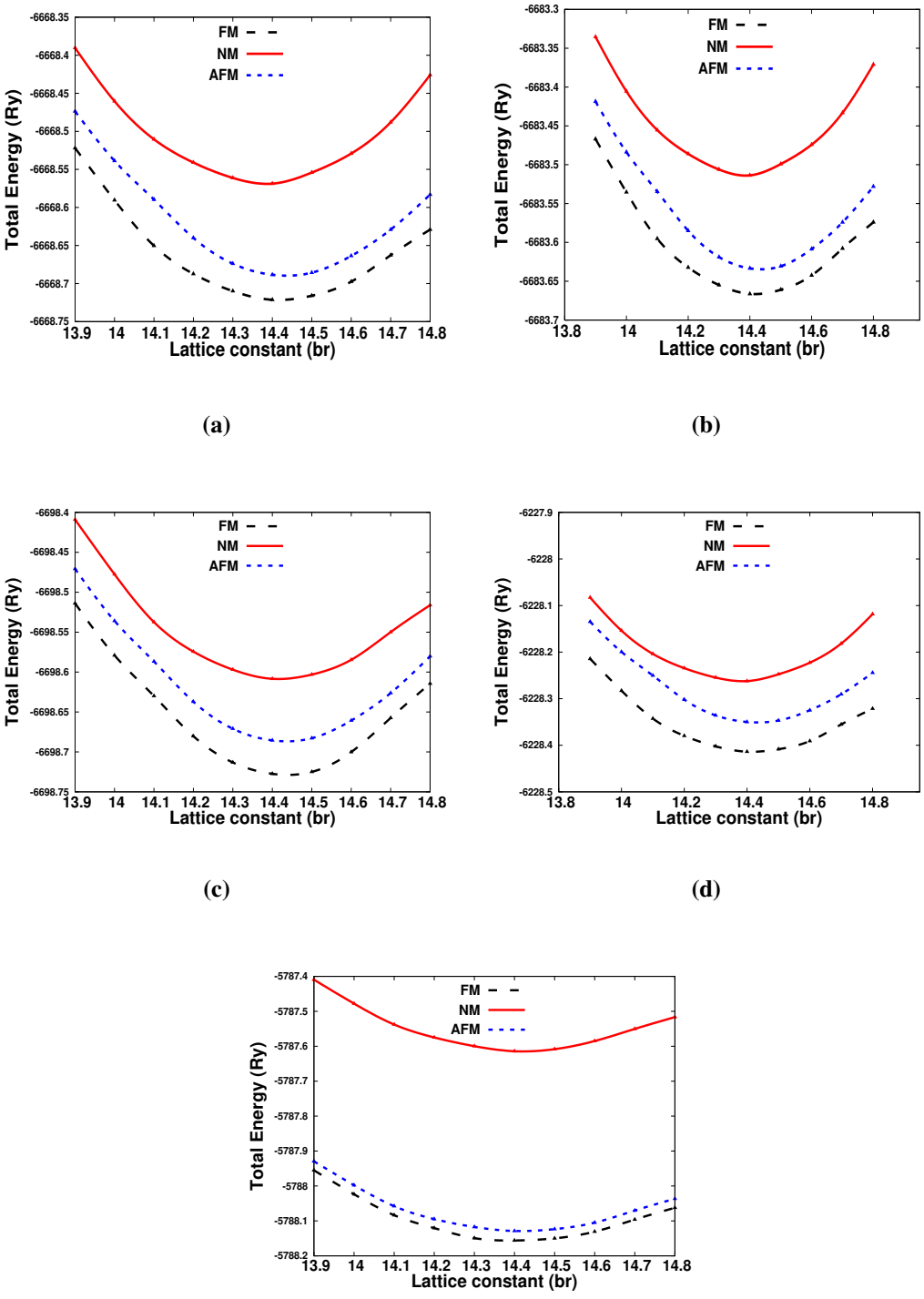

Figure 47: Total energy versus lattice constant of pristine and Eu/Y-doped $SmMnO_3$ (a–e) under different magnetic configurations.

In general, the europium atom exhibits paramagnetic behavior due to the unpaired electrons in its partially filled 4f orbitals (Nereson *et al.*, 1964). However, when doped into $SmMnO_3$, it induces ferromagnetic ordering. Similarly, while yttrium is paramagnetic

in its elemental state, its incorporation into $SmMnO_3$ also triggers the emergence of ferromagnetic properties. These changes are caused by the interactions among Mn-3d states, Sm-4f states, along with the participation of Eu-4f and Y-4d states.

Table 24: Total magnetic moment (M_{Tot}) and atomic magnetic moments of Sm (M_{Sm}), Mn (M_{Mn}), Eu (M_{Eu}), Y (M_Y), and O (M_O) sites in $SmMnO_3$ at different doping levels of Eu and Y (Pokharel *et al.*, 2024c)

Configuration	Compound	M_{Sm} (μ_B)	M_{Eu} (μ_B)	M_Y (μ_B)	M_{Mn} (μ_B)	M_O (μ_B)	M_{Tot} (μ_B)
GGA	Bulk $SmMnO_3$	0.011	–	–	2.935	0.054	3.620
	12.5% Eu doped	0.012	0.012	–	2.941	0.056	3.661
	25% Eu doped	0.012	0.012	–	2.957	0.055	3.767
	12.5% Y doped	0.011	–	0.013	2.507	0.054	3.248
	25.0% Y doped	0.011	–	0.013	2.501	0.054	3.224
GGA+U	Bulk $SmMnO_3$	0.011	–	–	3.276	0.002	3.886
	12.5% Eu doped	0.019	0.019	–	3.292	0.005	3.908
	25.0% Eu doped	0.018	0.019	–	3.293	0.005	3.916
	12.5% Y doped	0.014	–	0.014	2.526	0.055	3.234
	25.0% Y doped	0.011	–	0.014	2.518	0.055	3.207
GGA+U+SOC	Bulk $SmMnO_3$	0.011	–	–	3.583	0.002	4.010
	12.5% Eu doped	0.019	0.019	–	3.849	0.005	4.045
	25.0% Eu doped	0.018	0.019	–	3.855	0.005	4.081
	12.5% Y doped	0.014	–	0.014	2.572	0.055	3.248
	25.0% Y doped	0.011	–	0.014	2.441	0.055	3.229

The GGA+U approach effectively accounts for strong electron–electron interactions in partially filled d and f orbitals. However, the GGA frequently underestimates these interactions, leading to inaccurate predictions of electron localization and magnetic behavior. The addition of on–site Coulomb interaction for electrons in localized partially filled d and f orbitals increase the local and hence total magnetic moment of the compound. For Eu–doped $SmMnO_3$, where both Mn and Eu have partially filled d and f orbitals,

respectively. So the GGA+U approach exhibits stronger electron–electron interactions, and exhibit high magnetic moments as compared to pristine and Y– doped $SmMnO_3$. The inclusion of spin–orbit coupling further increases the total magnetic moment, suggesting that combination of electron–electron interactions and relativistic spin effects strengthening the magnetic behavior of the material. The data in Table 24 indicate that Eu and Y doping have distinct effects on the magnetic behavior of $SmMnO_3$.

4.8.0.2 Sr_2ZrMoO_6 double perovskite

Table 25: Total (M_{Tot}) and atomic magnetic moments of Sr, Zr, Mo, and O sites in Sr_2ZrMoO_6 double perovskite

Configuration	$M_{\mathbf{Sr}}$ (μ_{B})	$M_{\mathbf{Zr}}$ (μ_{B})	$M_{\mathbf{Mo}}$ (μ_{B})	$M_{\mathbf{O}}$ (μ_{B})	$M_{\mathbf{Tot}}$ (μ_{B})
GGA	0.001	0.001	0.805	0.006	1.561
GGA + U	0.001	0.001	1.122	0.095	2.432
GGA + U + SOC	0.001	0.003	1.448	0.036	3.601

The study of magnetic properties revealed that the Sr_2ZrMoO_6 double perovskite is stable in the ferromagnetic phase. The magnetic moments were computed using GGA, GGA+U and SOC approaches.

The magnetism in Sr_2ZrMoO_6 is primarily contributed by the Mo site, whereas the contribution from Sr, O and Zr atoms to overall magnetic moment of the compound is minimal. The addition of on–site Coulomb interaction of electrons in the localized Mo–4d orbitals in GGA method increases the local magnetic moments, thereby increasing the total magnetic moment of the compound. Furthermore, the inclusion of spin–orbit coupling further increases the total magnetic moment, suggesting that combination of electron–electron interactions and relativistic spin effects strengthening the magnetic behavior of the material (Table 25).

4.8.0.3 Curie temperature

The temperature at which magnetic characteristics of material significantly change is known as the Curie temperature (T_C). Below T_C, the magnetic dipoles align in a specific direction resulting in stable magnetic ordering. When the temperature exceeds the Curie temperature, the dipoles are disoriented and travel in a random direction due to the thermal energy. Most perovskites have a low Curie temperature. This temperature

can be calculated using following equation (Kubler, 2007)

$$k_B T_C = \frac{2}{3}\Delta E = \frac{2}{3}\left(\frac{E_{\mathrm{FM}} - E_{\mathrm{AFM}}}{2}\right) \tag{4.77}$$

Table 26: Ground-state energies (E_0) of Eu- and Y-doped $SmMnO_3$ in paramagnetic (PM), ferromagnetic (FM), and antiferromagnetic (AFM) phases

Compound	NM (10^{-3} Ry)	FM (10^{-3} Ry)	AFM (10^{-3} Ry)	$\Delta E = E_{\mathrm{FM}} - E_{\mathrm{AFM}}$ (10^{-3} Ry)	T_C (K)
Pristine $SmMnO_3$	-6667.386	-6668.694	-6668.659	0.035	255.35
12.5% Eu doped	-6682.632	-6683.751	-6683.714	0.037	268.63
25% Eu doped	-6697.236	-6698.699	-6698.656	0.043	314.28
12.5% Y doped	-6227.853	-6228.395	-6228.363	0.031	227.70
25% Y doped	-5787.614	-5788.156	-5788.129	0.026	187.69

The T_C values of undoped, 12.5% Eu-doped, and 25% Eu–doped $SmMnO_3$ are 255.35 K, 268.63 K, and 314.28 K, respectively (Table 26). Conversely, the values for Y–doped samples are 187.69 K and 227.70 K. Figure 48 shows that Y– doping on $SmMnO_3$ substantially decreases the Curie temperature, while Eu– doping leads to a sudden increment.

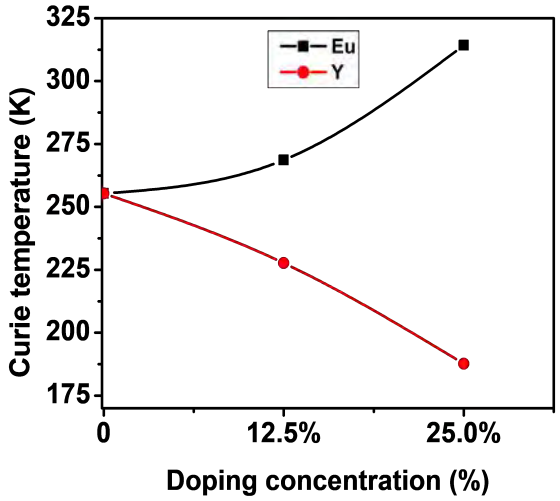

Figure 48: Curie temperature of Eu– and Y– doped $SmMnO_3$ at different doping levels (Pokharel *et al.*, 2024c).

Chapter 5

5. CONCLUSIONS AND RECOMMENDATIONS

5.1 Conclusions

In this work, we systematically investigated the electronic, elastic, optical, and magnetic properties of $ZrSiO_3$ perovskite under different pressures and surface terminations, as well as monolayer $ZrSiO_3$, Eu- and Y-doped $SmMnO_3$, and the Sr_2ZrMoO_6 double perovskite using density functional theory (DFT) calculations. The calculated cohesive and formation energies, together with elastic stability analyses, confirmed the structural stability of all investigated materials under the considered external conditions.

The results demonstrate that hydrostatic pressure, mechanical strain, surface termination, and rare-earth doping are effective approaches for tailoring the physical properties of perovskite materials. Bulk $ZrSiO_3$ is an indirect band-gap semiconductor whose electronic, optical, and elastic properties can be systematically tuned by pressure, strain, and surface termination. The ZrO-terminated surface exhibits higher elasticity and a smaller electronic band gap than the SiO_2-terminated surface, whereas the $ZrSiO_3$ monolayer remains mechanically stable and ductile throughout the investigated strain range. These findings highlight its strong potential for optoelectronic devices and scaffold materials.

The investigation of Eu- and Y-doped $SmMnO_3$ revealed that rare-earth doping significantly modifies the electronic, magnetic, elastic, and optical properties of the parent material. Eu doping enhances ductility and reduces the band gap and Debye temperature, whereas Y doping increases stiffness and Debye temperature while preserving structural stability. These results indicate that doped materials have the potential for multifunctional and magnetoelectric devices.

For Sr_2ZrMoO_6, the calculations confirmed structural and mechanical stability up to 80 GPa and revealed significant elastic anisotropy. The material exhibits an indirect band-gap ferromagnetic semiconductor behavior, suggesting its potential for advanced electronic and spintronic applications under high-pressure conditions.

5.2 Recommendations

The findings of this study establish a foundation for future studies on these perovskite materials, both theoretical and experimental investigations. Collaboration with experimental researchers is recommended for the fabrication and characterisation of $ZrSiO_3$, based on the computational results. Experimental validation is necessary to substantiate the anticipated structural, electrical, and mechanical properties across different pressures, surface terminations, and low-dimensional configurations. Such combined theoretical and experimental work will help to transfer these predictions into practical applications.

Further theoretical and experimental studies are also recommended to investigate the high-pressure behavior of the Sr_2ZrMoO_6 double perovskite and to verify its predicted mechanical, electronic, magnetic, and optical properties. The present computational results can serve as a valuable reference for the experimental fabrication of novel perovskite-based materials, including flexible electronic devices.

Chapter 6

6. SUMMARY

This dissertation presents an extensive first-principles examination of mechanical, electronic, optical and magnetic properties of zirconium-based perovskites, including bulk and two-dimensional $ZrSiO_3$, Eu- and Y-doped $SmMnO_3$, and the Sr_2ZrMoO_6 double perovskite. We used spin-polarized DFT method within the Quantum ESPRESSO software package to carry out the calculations. The PBE functional was employed for bulk materials, and the PBESOL functional was used for surface and layer analysis. Interactions between valence electrons and atomic cores were described using ultrasoft Vanderbilt pseudopotentials. We performed systematic convergence tests for kinetic energy cutoff, k-point sampling, and lattice parameters to verify accuracy. The elastic properties were calculated by stress–strain method.

This study examines different properties of these materials under different conditions. The main results are summarised as follows:

1. Mechanical stability: Bulk $ZrSiO_3$ and its surface-terminated forms (ZrO- and SiO_2-terminated) demonstrate mechanical stability and ductility up to 100 GPa pressure. The SiO_2-terminated form shows superior elasticity.

2. Electronic properties: $ZrSiO_3$ is an indirect band gap semiconductor. Its band gap increases with increasing pressure and decreases with increasing number of layers. These results demonstrate that $ZrSiO_3$ possesses a tunable band gap.

3. Strain effects: The $ZrSiO_3$ monolayer exhibits linear elastic behavior up to ±2% strain and remains mechanically stable within the strain range of ±6%. Tensile strain reduces the band gap, whereas compressive strain increases it.

4. Eu– and Y– doping: Doping with europium and yttrium on $SmMnO_3$ significantly modifies its electronic, magnetic and optical properties. The magnetic moment and Curie temperature of $SmMnO_3$ increases with Eu–doping and decreases with Y–doping.

5. Elastic behavior: Bulk $ZrSiO_3$ shows mechanical stability and ductility up to

100 GPa pressure. Whereas $ZrSiO_3$ monolayer shows strain sensitive elastic anisotropy. The Sr_2ZrMoO_6 double perovskite shows moderate resistance to crack propagation (K_{IC}) and low brittleness index.

REFERENCES

Abiram, G., Gourji, F. H., Pitchaiya, S., Ravirajan, P., Murugathas, T., & Velauthapillai, D. (2022). Air processed $Cs_2AgBiBr_6$ lead-free double perovskite high-mobility thin-film field-effect transistors. *Scientific Reports*, **12**(1): 2455–2462. doi: https://doi.org10.1038/s41598-022-06319-z

Adamo, C., & Barone, V. (1999). Toward reliable density functional methods without adjustable parameters: The PBE0 model. *The Journal of Chemical Physics*, **110**(13): 6158–6170. doi: https://doi.org10.1063/1.478522

Ahn, H., Chen, H.-W., Landheer, D., Wu, X., Chou, L., & Chao, T.-S. (2004). Characterization of interfacial layer of ultrathin zr silicate on si (100) using spectroscopic ellipsometry and hrtem. *Thin Solid Films*, **455**: 318–322. doi: https://doi.org10.1016/j.tsf.2004.01.017

Anderson, O. L. (1963). A simplified method for calculating the debye temperature from elastic constants. *Journal of Physics and Chemistry of Solids*, **24**(7): 909–917. doi: https://doi.org10.1016/0022-3697(63)90067-2

Anisimov, V. I., Zaanen, J., & Andersen, O. K. (1991). Band theory and Mott insulators: Hubbard U instead of Stoner I. *Physical Review B*, **44**: 943–954. doi: https://doi.org10.1103/PhysRevB.44.943

Bachelet, G. B., & Filippetti, A. (2005). Electronic structure: The pseudopotential method. In *Encyclopedia of Materials Science and Technology* (p. 431-440). doi: https://doi.org10.1016/B0-12-369401-9/00453-8

Bao, L., Kong, Z., Qu, D., & Duan, Y. (2020). Revealing the elastic properties and anisotropies of MgX (X = Si, Ge, and Sn) with different structures from a first-principles calculation. *Materials Today Communications*, **24**: 101337–1–11. doi: https://doi.org10.1016/j.mtcomm.2020.101337

Bao, W., Liu, D., Li, P., & Duan, Y. (2019). Elastic anisotropies and thermal properties of cubic TMIr (TM= Sc, Y, Lu, Ti, Zr and Hf): A DFT calculation. *Materials Research Express*, **6**(8): 086574–1–12. doi: https://doi.org10.1088/2053-1591/ab1f01

Bao, W. Z., Liu, D., Li, P., & Duan, Y. H. (2019). Structural properties, elastic anisotropies, and thermal conductivities of tetragonal LnBc (Ln = rare earth) compounds from first-principles calculations. *Ceramics International*, **45**: 1857–1867. doi: https://doi.org10.1016/j.ceramint.2018.10.077

Baroni, S., De Gironcoli, S., Dal Corso, A., & Giannozzi, P. (2001). Phonons and related crystal properties from density-functional perturbation theory. *Reviews of Mod-ern Physics*, **73**(2): 515–562. doi: https://doi.org10.1103/RevModPhys.73.515

Becke, A. D. (1993). A new mixing of hartree-fock and local density-functional theories. *The Journal of Chemical Physics*, **98**(2): 1372–1377. doi: https://doi.org10.1063/1.464304

Beeler, B., Casagranda, A., Aagesen, L., Zhang, Y., & Novascone, S. (2020). Atomistic calculations of the surface energy as a function of composition and temperature in γ u–zr to inform fuel performance modeling. *Journal of Nuclear Materials*, **540**: 152271–1–19. doi: https://doi.org10.1016/j.jnucmat.2020.152271

Birch, F. (1947). The finite elastic strain of cubic crystals. *Physical Review*, **71**(11): 809–824. doi: https://doi.org10.1103/PhysRev.71.809

Boccaccini, A. (1997). Machinability and brittleness of glass-ceramics. *Journal of Materials Processing Technology*, **65**(1-3): 302–304. doi: https://doi.org10.1016/S0924-0136(96)02275-3

Bolen, E., Deligoz, E., & Ozisik, H. (2021). Origin of low thermal conductivity in monolayer PbI_2. *Solid State Communications*, **327**: 114223–1–7. doi: https://doi.org10.1016/j.ssc.2021.114223

Born, M., & Huang, K. (1955). *The dynamical theory of crystal lattices*. Oxford University Press.

Born, M., & Oppenheimer, R. (1927). Zur quantentheorie der molekeln. *Annalen der Physik*, **389**(20): 457–484. doi: https://doi.org10.1002/andp.19273892002

Cai, Y., Zhang, G., & Zhang, Y. W. (2014). Layer-dependent band alignment and work function of few-layer phosphorene. *Scientific Reports*, **4**(1): 6677–6682. doi: https://doi.org10.1038/srep06677

Cao, Y., Qi, G., Liu, C., Wang, L., Ma, Z., Wang, K., & Zou, B. (2018). Pressure-tailored band gap engineering and structure evolution of cubic cesium lead iodide perovskite nanocrystals. *The Journal of Physical Chemistry C*, **122**(17): 9332–9361. doi: https://doi.org10.1021/acs.jpcc.8b01673

Cargnoni, F., Gatti, C., May, E., & Narducci, D. (2000). Geometrical reconstructions and electronic relaxations of silicon surfaces. *The Journal of Chemical Physics*, **112**(2): 887–899. doi: https://doi.org10.1063/1.480616

Ceperley, D. M., & Alder, B. (1980). Ground state of the electron gas by a stochastic method. *Physical Review Letters*, **45**(7): 566–569. doi: https://doi.org10.1103/PhysRevLett.45.566

Chen, S.-B., Zeng, Z.-Y., Chen, X.-R., & Yao, X.-X. (2020). Strain-induced electronic structures, mechanical anisotropy, and piezoelectricity of transition-metal dichalcogenide monolayer CrS_2. *Journal of Applied Physics*, **128**(12): 125111–1–12. doi: https://doi.org10.1063/5.0022429

Cheng, D., Wang, S., & Ye, H. (2004). First-principles calculations of the elastic properties of zrc and zrn. *Journal of alloys and compounds*, **377**(1-2): 221–224.

Chu, L., Ahmad, W., Liu, W., Yang, J., Zhang, R., Sun, Y., & Li, X. (2019). Lead-free halide double perovskite materials: a new superstar toward green and stable optoelectronic applications. *Nano-Micro Letters*, **11**: 1-18. doi: https://doi.org10.1007/s40820-019-0244-6

Cole, L. A., & Perdew, J. (1982). Calculated electron affinities of the elements. *Physical Review A*, **25**(3): 1265-1271. doi: https://doi.org10.1103/PhysRevA.25.1265

Daoud, S. (2017). Thermal properties of cubic zincblende thallium-phosphide. *International Journal of Physical Research*, **5**(1): 14–16.

Dar, S. A., Srivastava, V., & Sakalle, U. K. (2019). Structural and electronic investigation of sr_2mntao_6. *Journal of Magnetism and Magnetic Materials*, **484**: 298–306.

Deb, J., Singh, N. B., & Sarkar, U. (2024). Density functional theory study of pentagraphyne nanotubes. *Physical Chemistry Chemical Physics*, **26**(21): 15484–15493.

Deb, S., & Sarkar, U. (2021). Boron-nitride doped twin-graphene. *Applied Surface Science*, **541**: 148657.

de Lazaro, S., & Longo, E. (2004). Structural and electronic properties of $pbtio_3$ slabs. *Surface Science*, **552**: 149–159.

Dey, A., Ye, J., De, A., Debroye, E., Ha, S. K., Bladt, E., ... others (2021). State of the art and prospects for halide perovskite nanocrystals. *ACS nano*, **15**(7): 10775–10981.

Dirac, P. A. (1930). Note on exchange phenomena in the thomas atom. In *Mathematical proceedings of the cambridge philosophical society* (Vol. 26, pp. 376–385).

Egerton, R. F. (2009). Electron energy-loss spectroscopy in the TEM. *Reports on Progress in Physics*, **72**: 016502–25. doi: https://doi.org10.1088/0034-4885/72/1/016502

Elmore, A. R., et al. (2003). Final report on the safety assessment of aluminum silicate, calcium silicate, magnesium aluminum silicate, magnesium silicate, magnesium trisilicate, sodium magnesium silicate, zirconium silicate, attapulgite, bentonite, fuller's earth, hectorite, kaolin, lithium magnesium silicate, lithium magnesium sodium silicate, montmorillonite, pyrophyllite, and zeolite. *International Journal of Toxicology*, **22**: 37–102. doi: https://doi.org10.3109/10915818209018017

Faghihnasiri, M., Jafari, H., Ramazani, A., Shabani, M., Estalaki, S. M., & Larson, R. G. (2019). Nonlinear elastic behavior and anisotropic electronic properties of two-dimensional borophene. *Journal of Applied Physics*, **125**(14): 145107–1–14. doi: https://doi.org10.1063/1.5079932

Fermi, E. (1928). A statistical method for determining some properties of the atoms. *Zeitschrift für Physik*, **48**: 7379–7385.

Field, J., & Freeman, C. (1981). Strength and fracture properties of diamond. *Philosophical Magazine A*, **43**(3): 595–618. doi: https://doi.org10.1080/01418618108240397

Fock, V. (1930). Bemerkung zum virialsatz. *Zeitschrift für Physik*, **63**(11-12): 855–858. doi: https://doi.org10.1007/BF01339281

Freiman, G., Barboux, P., Perriere, J., & Giannakopoulos, K. (2009). Layer by layer deposition of zirconium oxide onto silicon. *Thin Solid Films*, **517**(8): 2670–2674. doi: https://doi.org10.1016/j.tsf.2008.10.112

Frisch, D., & Hanebeck, U. D. (2021). Gaussian mixture estimation from weighted samples. In *2021 ieee international conference on multisen-sor fusion and integration for intelligent systems (mfi)* (pp. 1–5). doi: https://doi.org10.1109/MFI52462.2021.9591161

Gajdovs, M., Hummer, K., Kresse, G., Furthmuller, J., & Bechstedt, F. (2006). Linear optical properties in the projector-augmented wave methodology. *Physical Review B—Condensed Matter and Materials Physics*, **73**(4): 045112-045120. doi: https://doi.org10.1103/PhysRevB.73.045112

Gao, K., Liu, X., Jiang, Z., Zheng, H., Song, C., Wang, X., ... Xuan, Y. (2022). Direct solar thermochemical CO_2 splitting based on Ca-and Al-doped $SmMnO_3$

perovskites: Ultrahigh CO yield within small temperature swing. *Renewable Energy*, **194**: 482–494. doi: https://doi.org10.1016/j.renene.2022.05.105

Ghosh, J., Sellin, P. J., & Giri, P. K. (2022). Recent advances in lead-free double perovskites for x-ray and photodetection. *Nanotechnology*, **33**(31): 312001–1–26. doi: https://doi.org10.1088/1361-6528/ac6884

Giannozzi, P., Baroni, S., Bonini, N., Calandra, M., Car, R., Cavazzoni, C., & Corso, D. (2009). Quantum espresso: a modular and open-source software project for quantum simulations of materials. *Journal of Physics: Condensed Matter*, **21**(39): 395502–1–20. doi: https://doi.org10.1088/0953-8984/21/39/395502

Golesorkhtabar, R., Pasquale, P., Jurgen, S., Peter, P., & Claudia, D. (2013). Elastic: A tool for calculating second-order elastic constants from first principles. *Computer Physics Communications*, **184**(7): 1861–1873. doi: https://doi.org10.1016/j.cpc.2013.03.010

Gupta, S. L., Kumar, S., Panwar, S., et al. (2024). Ab initio studies of newly proposed zirconium based novel combinations of hydride perovskites $ZrXH_3$ (X= Zn, Cd) as hydrogen storage applications. *International Journal of Hydrogen Energy*, **55**: 1465–1475. doi: https://doi.org10.1016/j.ijhydene.2023.11.286

Hamann, D., Schlüter, M., & Chiang, C. (1979). Norm-conserving pseudopotentials. *Physical Review Letters*, **43**(20): 1494-1497. doi: https://doi.org10.1103/PhysRevLett.43.1494

Hao, R., Zhang, X., Qin, J., Zhang, S., Ning, J., Sun, N., ... Liu, R. (2015). Theoretical prediction of structural stability, electronic and elastic properties of $ZrSi_2$ under pressure. *RSC Advances*, **5**(46): 36779–36786. doi: https://doi.org10.1039/C5RA01964H

Harmel, M., Khachai, H., Hoddou, A., Khenata, R., Murtaza, G., Abbar, B., & Khalfa, M. (2015). Ab initio study of the mechanical, thermal and optoelectronic properties of the cubic $CsBaF_3$. *Acta Physica Polonica A*, **128**: 33-42. doi: https://doi.org10.12693/APhysPolA.128.34

Hautier, G., Jain, A., & Ong, S. P. (2012). From the computer to the laboratory: materials discovery and design using first-principles calculations. *Journal of Materials Science*, **47**: 7317-7340. doi: https://doi.org10.1007/s10853-012-6424-0

Hill, R. (1952). The elastic behavior of a crystalline aggregate. *Proceedings of the Physical Society. Section A*, **65**(5): 349–355. doi: https://doi.org10.1088/0370-1298/65/5/307

Hoffmann, A. (2013). Spin hall effects in metals. *IEEE Transactions on Magnetics*, **49**(10): 5172–5193. doi: https://doi.org10.1109/TMAG.2013.2262947

Hohenberg, P., & Kohn, W. (1964). Inhomogeneous electron gas. *Physical Review*, **136**(3B): B864-B871. doi: https://doi.org10.1103/PhysRev.136.B864

Hortamani, M., & Wiesendanger, R. (2012). Role of hybridization in the Rashba splitting of noble metal monolayers on W (110). *Physical Review B—Condensed Matter and Materials Physics*, **86**(23): 235437–1–7. doi: https://doi.org10.1103/PhysRevB.86.235437

Hu, L., & Huang, X. (2017). Peculiar electronic, strong in-plane and out-of-plane second harmonic generation and piezoelectric properties of atom-thick -M_2X_3 (M= Ga, In; X= S, Se). *RSC Advances*, **7**(87): 55034-55043. doi: https://doi.org10.1039/C7RA11014F

Huang, L., Chen, Z., & Li, J. (2015). Effects of strain on the band gap and effective mass in two-dimensional monolayer GaX (X= S, Se, Te). *RSC Advances*, **5**(8): 5788–5794. doi: https://doi.org10.1039/C4RA12107D

Idris, A. M., Liu, T., Hussain Shah, J., Malik, A. S., Zhao, D., Han, H., & Li, C. (2020). Sr_2NiWO_6 double perovskite oxide as a visible-light-responsive water oxidation photocatalyst. *ACS Applied Materials and Interfaces*, **12**(23): 25938–25948. doi: https://doi.org10.1021/acsami.0c05576

Ishikawa, K., & Uemori, T. (1999). Surface relaxation in ferroelectric perovskites. *Physical Review B*, **60**(17): 11841–11845. doi: https://doi.org10.1103/PhysRevB.60.11841

Jamal, M., Asadabadi, S. J., Ahmad, I., & Aliabad, H. R. (2014). Elastic constants of cubic crystals. *Computational Materials Science*, **95**: 592–599. doi: https://doi.org10.1016/j.commatsci.2014.08.027

Jayakrishnan, V. B., Mishra, S. K., & Sastry, P. U. (2021). Role of a and b site doping on antiferrodistortive phase transition in sodium bismuth titanate. *Materials Research Bulletin*, **144**: 111499–1–8. doi: https://doi.org10.1016/j.materresbull.2021.111499

Ji, Y., Lin, P., Ren, X., & He, L. (2024). Geometric and electronic structures of Cs_2BBJX_6 double perovskites. *Physical Review Research*, **6**(3): 033172–1–033172–12. doi: https://doi.org10.1103/PhysRevResearch.6.033172

Klimeš, J., & Michaelides, A. (2012). Advances in van der Waals dispersion forces in DFT. *The Journal of Chemical Physics*, **137**(12): 120901–1–13. doi: https://doi.org10.1063/1.4754130

Kohn, W., & Sham, L. J. (1965). Self-consistent equations including exchange and correlation effects. *Physical Review*, **140**(4A): A1133–A1138. doi: https://doi.org10.1103/PhysRev.140.A1133

Kokalj, A. (1999). XCrySDen program for displaying crystalline structures. *Journal of Molecular Graphics and Modelling*, **17**(3-4): 176–179. doi: https://doi.org10.1016/S1093-3263(99)00028-5

Kong, B. D. e. a. (2009). Lattice thermal conductivity in graphene. *Physical Review B*, **80**(3): 033406–1–4. doi: https://doi.org10.1103/PhysRevB.80.033406

Kube, C. M., & De Jong, M. (2016). Elastic constants of polycrystals. *Journal of Applied Physics*, **120**(16): 165105–1–15. doi: https://doi.org10.1063/1.4965867

Kubler, J. e. a. (2007). Curie temperatures of Co_2 Heusler compounds. *Physical Review B*, **76**: 024414–1–7. doi: https://doi.org10.1103/PhysRevB.76.024414

Kumar, N. R., & Radhakrishnan, R. (2018). Electronic, optical and mechanical properties of double perovskites. *Materials Letters*, **227**: 289–291. doi: https://doi.org10.1016/j.matlet.2018.05.082

Kumar, S. e. a. (2023). Electrochemical performance of $SrFeO_3$. *ACS Applied Energy Materials*, **6**(3): 2049–2062. doi: https://doi.org10.1021/acsaem.2c04034

Kumari, M. e. a. (2023). Synthesis of $LaFeO_3/BaTiO_3$ heterojunctions. *IEEE Sensors Journal*, **23**(10): 10301–10307. doi: https://doi.org10.1109/JSEN.2023.3263622

Kung, P.-K. e. a. (2020). Lead-free double perovskites for solar cells. *Solar RRL*, **4**(2): 1900306–1–71. doi: https://doi.org10.1002/solr.201900306

Langreth, D. C., & Perdew, J. P. (1980). Theory of nonuniform electronic systems. *Physical Review B*, **21**(2): 5469–5493. doi: https://doi.org10.1103/PhysRevB.21.5469

LaShell, S., McDougall, B. A., & Jensen, E. (1996). Spin splitting of an au(111) surface state band. *Physical Review Letters*, **77**(16): 3419–3422. doi: https://doi.org10.1103/PhysRevLett.77.3419

Lee, H., Moon, T., Lee, Y., & Kim, J. (2025). Structural mechanisms of quasi-2d perovskites for next-generation photovoltaics. *Nano-Micro Letters*, **17**(1): 139–173. doi: https://doi.org10.1007/s40820-024-01609-9

Le Page, Y., & Saxe, P. (2002). Least-squares extraction of elastic data. *Physical Review B*, **65**(10): 104104–1–14. doi: https://doi.org10.1103/PhysRevB.65.104104

Li, N. e. a. (2016). Pressure-induced structural and electronic transition in Sr_2ZnWO_6. *Inorganic Chemistry*, **55**(13): 6770–6775. doi: https://doi.org10.1021/acs.inorgchem.6b01091

Li, R. e. a. (2020). Elastic anisotropy measure for 2d crystals. *Extreme Mechanics Letters*, **34**: 100615–1–7. doi: https://doi.org10.1016/j.eml.2019.100615

Li, Z. e. a. (2016). Stabilizing perovskite structures by tuning tolerance factor. *Chemistry of Materials*, **28**(1): 284–292. doi: https://doi.org10.1021/acs.chemmater.5b04107

Lin, Q. e. a. (2016). Organohalide perovskites for solar energy conversion. *Accounts of Chemical Research*, **49**(3): 545–553. doi: https://doi.org10.1021/acs.accounts.5b00483

Liu, L. e. a. (2018). Mesoporous structured $SmMnO_3$ perovskites sheets. *Materials Letters*, **212**: 107–110. doi: https://doi.org10.1016/j.matlet.2017.10.048

Loucks, T., & Slater, J. C. (1967). Augmented plane wave method. *Physics Today*, **20**(11): 92–93. doi: https://doi.org10.1063/1.3034041

Lu, Y. e. a. (2021). First-principles calculations of electronic properties. *Vacuum*, **191**: 110324–1–11. doi: https://doi.org10.1016/j.vacuum.2021.110324

Luo, B. e. a. (2015). Structural and electronic properties of cubic $KNbO_3$. *Applied Surface Science*, **351**: 558–564. doi: https://doi.org10.1016/j.apsusc.2015.05.140

López-Suárez, M. e. a. (2016). Band gap engineering of MoS_2 upon compression. *Journal of Applied Physics*, **119**(16): 165105–1–5. doi: https://doi.org10.1063/1.4948376

Mahalik, R. R., Hota, I., Soren, S., Debnath, A. K., Muthe, K. P., & Parhi, P. (2023). Efficient oxygen reduction reaction of rare earth perovskite $smmno_3$. *Inorganic Chemistry Communications*, **154**: 110924. doi: https://doi.org10.1016/j.inoche.2023.110924

Mahmood, Q., Haq, B. U., Yaseen, M., Ramay, S. M., Ashiq, M. G. B., & Mahmood, A. (2019). The first-principle study of mechanical, optical and thermoelectric

properties of snzro3 and snhfo3 for renewable energy applications. *Solid State Communications*, **292**: 17–23.

Malakkal, L., Szpunar, B., Zuniga, J. C., Siripurapu, R. K., & Szpunar, J. A. (2016). First principles calculation of thermo-mechanical properties of thoria using quantum espresso. *International Journal of Computational Materials Science and Engineering*, **5**(2): 1650008. doi: https://doi.org10.1142/S2047684116500081

Martin, R. M. (2004). *Electronic structure: Basic theory and practical methods*. Cambridge, UK: Cambridge University Press. doi: https://doi.org10.1017/CBO9780511805769

Meyer, B., Padilla, J., & Vanderbilt, D. (1999). Theory of $pbtio_3$, $batio_3$, and $srtio_3$ surfaces. *Faraday Discussions*, **114**: 395–405. doi: https://doi.org10.1039/a903029h

Mishra, S., & Parida, S. (2023). An overview and recent progress of single and double perovskite metal oxides. In *Perovskite Metal Oxides* (p. 55-80). Elsevier. doi: https://doi.org10.1016/B978-0-323-99529-0.00002-3

Momma, K., & Izumi, F. (2011). Vesta 3 for three-dimensional visualization of crystal, volumetric and morphology data. *Journal of Applied Crystallography*, **44**(6): 1272–1276. doi: https://doi.org10.1107/S0021889811038970

Monkhorst, H. J., & Pack, J. D. (1976). Special points for brillouin-zone integrations. *Physical Review B*, **13**: 5188–5192. doi: https://doi.org10.1103/PhysRevB.13.5188

Monteiro, S. N., Skury, A. L. D., de Azevedo, M. G., & Bobrovnitchii, G. S. (2013). Cubic boron nitride competing with diamond as a superhard engineering material: An overview. *Journal of Materials Research and Technology*, **2**(1): 68–74. doi: https://doi.org10.1016/j.jmrt.2013.03.004

Mouhat, F., & Coudert, F. X. (2014). Necessary and sufficient elastic stability conditions in various crystal systems. *Physical Review B*, **90**(22): 224104. doi: https://doi.org10.1103/PhysRevB.90.224104

Nagy, K. S., & Siegel, D. J. (2020). Anisotropic elastic properties of battery anodes. *Journal of The Electrochemical Society*, **167**(11): 110550–1–17. doi: https://doi.org10.1149/1945-7111/aba54c

Nereson, N. G., Olsen, C. E., & Arnold, G. P. (1964). Magnetic structure of europium. *Physical Review*, **135**(1A): A176–A189. doi: https://doi.org10.1103/PhysRev.135.A176

Ning, Z. (2011). *First principles quantitative modeling of molecular devices* ((Ph.D. Thesis)). Department of Molecular Physics, McGill University, Montreal, Canada.

Nye, J. F., & Lindsay, R. B. (1984). *Physical properties of crystals: Their representation by tensors and matrices*. Oxford, UK: Oxford University Press.

Ozkan, H., Cartz, L., & Jamieson, J. C. (1974). Elastic constants of nonmetamict zirconium silicate. *Journal of Applied Physics*, **45**(2): 556–562. doi: https://doi.org10.1063/1.1663283

Pachori, S., Agarwal, R., Prakash, B., Kumari, S., & Verma, A. S. (2022). Fundamental Physical Properties of Nontoxic Tin-Based Formamidinium $FASnX_3$ (X= I, Br, Cl) Hybrid Halide Perovskites: Future Opportunities in Photovoltaic Applications. *Energy Technology*, **10**(2): 2100709–1–13. doi: https://doi.org10.1002/ente.202100709

Perdew, J. P. (1986). Density-functional approximation for the correlation energy of the inhomogeneous electron gas. *Physical Review B*, **33**(12): 8822–8824. doi: https://doi.org10.1103/PhysRevB.33.8800

Perdew, J. P., Burke, K., & Ernzerhof, M. (1996). Generalized gradient approximation made simple. *Physical Review Letters*, **77**(18): 3865–3868. doi: https://doi.org10.1103/PhysRevLett.77.3865

Perdew, J. P., Ruzsinszky, A., Csonka, G. I., Vydrov, O. A., Scuseria, G. E., Constantin, L. A., ... Burke, K. (2008). Restoring the density-gradient expansion for exchange in solids and surfaces. *Physical Review Letters*, **100**(13): 136406–1–4. doi: https://doi.org10.1103/PhysRevLett.100.136406

Perdew, J. P., & Wang, Y. (1992). Accurate and simple analytic representation of the electron-gas correlation energy. *Physical Review B*, **45**(23): 13244–13249. doi: https://doi.org10.1103/PhysRevB.45.13244

Perdew, J. P., & Zunger, A. (1981). Self-interaction correction to density-functional approximations for many-electron systems. *Physical Review B*, **23**(10): 5048–5079. doi: https://doi.org10.1103/PhysRevB.23.5048

Philipsen, P. H. T., & Baerends, E. J. (1996). Cohesive energy of 3d transition metals: density functional theory atomic and bulk calculations. *Physical Review B*, **54**(8): 5326–5333. doi: https://doi.org10.1103/PhysRevB.54.5326

Phuc, H. V., Hieu, N. N., Ilyasov, V. V., Phuong, L. T., & Nguyen, C. V. (2018). First principles study of the electronic properties and band gap modulation of two-dimensional phosphorene monolayer: Effect of strain

engineering. *Superlattices and Microstructures*, **118**: 289–297. doi: https://doi.org10.1016/j.spmi.2018.04.018

Pokharel, P., Yadav, S. K., Pantha, N., & Adhikari, D. (2024). First-Principles Investigations of Structural, Electronic, and Elastic Properties of $ZrSiO_3$ Perovskite: Layer Dependence, Surface Termination, and Pressure Effects. *Physica Status Solidi (B)*, **261**(8): 2400156–1–15. doi: https://doi.org10.1002/pssb.202400156

Pokharel, P., Yadav, S. K., Pantha, N., Sharma, B., & Adhikari, D. (2025). Elastic Anisotropy and Thermal Properties of Sr_2ZrMoO_6 Double Perovskite under Different Pressure. *Physica Status Solidi (B)*, **262**(5): 2400625–1–10. doi: https://doi.org10.1002/pssb.202400625

Pokharel, P., Yadav, S. K., Sharma, B., Pantha, N., & Adhikari, D. (2024). Structural, electronic, optical, magnetic, and mechanical properties of $SmMnO_3$ perovskite with europium and yttrium doping: A first-principles study. *AIP Advances*, **14**(12): 125309–1–14. doi: https://doi.org10.1063/5.0232439

Politano, A., & Chiarello, G. (2015). Probing young's modulus and poisson's ratio in graphene/metal interfaces and graphite: A comparative study. *Nano Research*, **8**: 1847–1856. doi: https://doi.org10.1007/s12274-014-0691-9

Poniznik, Z. V., Basista, M., & Gross, D. (2008). Effective elastic properties of interpenetrating phase composites. *Computational Materials Science*, **44**(2): 813–820. doi: https://doi.org10.1016/j.commatsci.2008.06.010

Ranganathan, S. I., & Ostoja-Starzewski, M. (2008). Universal elastic anisotropy index. *Physical Review Letters*, **101**: 055504–1–4. doi: https://doi.org10.1103/PhysRevLett.101.055504

Rashba, E., & Sheka, V. (1991). Electric-dipole spin resonances. In *Modern problems in condensed matter sciences* (Vol. **27**, pp. 131–206). Elsevier. doi: https://doi.org10.1016/B978-0-444-88535-7.50011-X

Ravindran, P., Fast, L., Korzhavyi, P. A., Johansson, B., Wills, J., & Eriksson, O. (1998). Density functional theory for calculation of elastic properties of orthorhombic crystals: Application to $TiSi_2$. *Journal of Applied Physics*, **84**(9): 4891–4904. doi: https://doi.org10.1063/1.368733

Ray, R. B., Kaphle, G. C., Rai, R. K., Yadav, D. K., Paudel, R., & Paudyal, D. (2021). Strain-induced electronic structure, and magnetic and structural properties in quaternary heusler alloys ZrRhTiZ (Z = Al, In). *Journal of Alloys and Compounds*, **867**: 158906–1–10. doi: https://doi.org10.1016/j.jallcom.2021.158906

Reuss, A. (1929). Calculation of the flow limits of mixed crystals based on the plasticity of monocrystals. *Journal of Applied Mathematics and Mechanics*, **9**: 49–58. doi: https://doi.org10.1002/zamm.19290090104

Ricciardulli, A. G., Yang, S., Smet, J. H., & Saliba, M. (2021). Emerging perovskite monolayers. *Nature Materials*, **20**(10): 1325–1336. doi: https://doi.org10.1038/s41563-021-01029-9

Roknuzzaman, M., Zhang, C., Ostrikov, K., Du, A., Wang, H., Wang, L., & Tesfamichael, T. (2019). Electronic and optical properties of lead-free hybrid double perovskites for photovoltaic and optoelectronic applications. *Scientific Reports*, **9**(1): 718–727. doi: https://doi.org10.1038/s41598-018-37132-2

Rose, G. (1842). *Journey to the urals, the altai and the caspian sea* (Vol. **2**). Berlin: G. Reimer.

Roy, R. (1954). Multiple ion substitution in the perovskite lattice. *Journal of the American Ceramic Society*, **37**(12): 581–588. doi: https://doi.org10.1111/j.1151-2916.1954.tb13992.x

Saad H.-E, M. M., & Alsobhi, B. (2022). Consequences of tuning rare-earth RE^{3+}-Site and exchange–correlation energy U on the optoelectronic, mechanical, and thermoelectronic properties of cubic manganite perovskites $REMnO_3$ for spintronics and optoelectronics applications. *ACS Omega*, **7**(32): 27903–27917. doi: https://doi.org10.1021/acsomega.2c01511

Sando, D. (2022). Strain and orientation engineering in ABO_3 perovskite oxide thin films. *Journal of Physics: Condensed Matter*, **34**(15): 153001–1–27. doi: https://doi.org10.1088/1361-648X/ac4c61

Saue, T. (2005). Spin-interactions and the non-relativistic limit of electrodynamics. In *Advances in quantum chemistry* (Vol. **48**, pp. 383–405). Elsevier. doi: https://doi.org10.1016/S0065-3276(05)48020-X

Scandolo, S., Giannozzi, P., Cavazzoni, C., de Gironcoli, S., Pasquarello, A., & Baroni, S. (2005). First-principles codes for computational crystallography in the quantum-espresso package. *Zeitschrift fur Kristallographie–Crystalline Materials*, **220**(5-6): 574–579. doi: https://doi.org10.1524/zkri.220.5.574.65062

Sethi, M., & Satake, M. (2010). *Chemical bonding*. Discovery Publishing House.

Shah, S. Z. A., Hussain, D., Abbas, Z., Niaz, S., Parveen, A., Sifuna, J., . . . Chaudhry, A. R. (2024). Unveiling the DFT perspectives on structural, elastic, optoelectronic, and thermoelectric properties of zirconate perovskites $XZrO_3$ (X=

Ca, Sr, Ba). *Inorganic Chemistry Communications*, **163**: 112304–1–8. doi: https://doi.org10.1016/j.inoche.2024.112304

Sharma, S. B., Bhatta, R., Adhikari, R., & Paudyal, D. (2022). Strain-dependent electronic and optical responses of penta-BCN monolayer. *Carbon Trends*, **7**: 100162–1–11. doi: https://doi.org10.1016/j.cartre.2022.100162

Skriver, H. L., & Rosengaard, N. M. (1992). Theoretical study of the structural and electronic properties of transition metals. *Physical Review B*, **46**: 7157–7168. doi: https://doi.org10.1103/PhysRevB.46.7157

Slater, J. C. (1937). Wave functions in a periodic potential. *Physical Review*, **51**(10): 846–851. doi: https://doi.org10.1103/PhysRev.51.846

Sokolovic, I., Schmid, M., Diebold, U., & Setvin, M. (2025). How to cleave cubic perovskite oxides. *Review of Scientific Instruments*, **96**(3): 035113–1–11. doi: https://doi.org10.1063/5.0233747

Soler, J. M., Artacho, E., Gale, J. D., & García, A. (2002). The SIESTA method for ab initio order-N materials simulation. *Journal of Physics: Condensed Matter*, **14**: 2745–2779. doi: https://doi.org10.1088/0953-8984/14/11/302

Sun, C. Q., Tay, B., Zeng, X., Li, S., Chen, T., Zhou, J., & Jiang, E. (2002). Bond-order-bond-length-bond-strength (bond-ols) correlation mechanism for the shape-and-size dependence of a nanosolid. *Journal of Physics: Condensed Matter*, **14**(34): 7781–7795. doi: https://doi.org10.1088/0953-8984/14/34/301

Surucu, G., Candan, A., Gencer, A., & Isik, M. (2019). First-principle investigation for the hydrogen storage properties of $NaXH_3$ (X= Mn, Fe, Co) perovskite type hydrides. *International Journal of Hydrogen Energy*, **44**(57): 30218–30225. doi: https://doi.org10.1016/j.ijhydene.2019.09.201

Tahiri, N., Dahbi, S., Dani, I., El Bounagui, O., & Ez-Zahraouy, H. (2021). Magnetocaloric and thermoelectric properties of the perovskite $LaMnO_3$ material: a DFT study and Monte Carlo technique. *Phase Transitions*, **94**(11): 826–834. doi: https://doi.org10.1080/01411594.2021.1974860

Tarutin, A. P., Filonova, E. A., Ricote, S., Medvedev, D. A., & Shao, Z. (2023). Chemical design of oxygen electrodes for solid oxide electrochemical cells: A guide. *Sustainable Energy Technologies and Assessments*, **57**: 103185–1–18. doi: https://doi.org10.1016/j.seta.2023.103185

Tellez, D. L., Toro, C. D., Rebaza, A. V. G., Roa-Rojas, J., et al. (2013). Struc-tural, magnetic, multiferroic and electronic properties of Sr_2ZrMnO_6 dou-

ble perovskite. *Journal of Molecular Structure*, **1034**: 233–237. doi: https://doi.org10.1016/j.molstruc.2012.10.023

Thomas, L. H. (1927). The calculation of atomic fields. *Mathematical Proceedings of the Cambridge Philosophical Society*, **23**: 542–548. doi: https://doi.org10.1017/S0305004100011683

Tian, J., Zhao, Y., Wen, Z., Hou, H., & Han, P. (2017). Physical properties and Debye temperature of Al_7Cu_2Fe alloy under various pressures analyzed by first-principles. *Solid State Communications*, **257**: 6–10. doi: https://doi.org10.1016/j.ssc.2017.02.011

Tian, Y., Xu, B., & Zhao, Z. (2012). Microscopic theory of hardness and design of novel superhard crystals. *International Journal of Refractory Metals and Hard Materials*, **33**: 93–106. doi: https://doi.org10.1016/j.ijrmhm.2012.02.021

Tidrow, S. C. (2014). Mapping comparison of goldschmidt's tolerance factor with perovskite structural conditions. *Ferroelectrics*, **470**(1): 13–27. doi: https://doi.org10.1080/00150193.2014.922372

Tomar, R., Wadehra, N., Budhiraja, V., Prakash, B., & Chakraverty, S. (2018). Realization of single terminated surface of perovskite oxide single crys-tals and their band profile: $(LaAlO_3)_{0.3}$, $(Sr_2AlTaO_6)_{0.7}$, $SrTiO_3$ and $KTaO_3$ case study. *Applied Surface Science*, **427**: 861–866. doi: https://doi.org10.1016/j.apsusc.2017.08.101

Tomishima, Y. (1959). Thomas-fermi-dirac theory with correlation correction. *Progress of Theoretical Physics*, **22**(1): 1–11. doi: https://doi.org10.1143/PTP.22.1

Tozer, D. J., & Handy, N. C. (1998). The development of new exchange-correlation functionals. *The Journal of Chemical Physics*, **108**(6): 2545–2555. doi: https://doi.org10.1063/1.475638

Trangenstein, J. A. (2017). *Scientific Computing*. New York: Springer.

Tsai, H., Nie, W., Blancon, J.-C., Stoumpos, C. C., Asadpour, R., Harutyunyan, B., . . . Mohite, A. D. (2016). High-efficiency two-dimensional Ruddlesden–Popper perovskite solar cells. *Nature*, **536**: 312–316. doi: https://doi.org10.1038/nature18306

Vanderbilt, D. (1990). Soft self-consistent pseudopotentials in a generalized eigenvalue formalism. *Physical Review B*, **41**(11): 7892–7895. doi: https://doi.org10.1103/PhysRevB.41.7892

Vedmid, L., Fedorova, O., Fetisov, A., & Uporov, S. (2024). Effect of Low-level Doping With Strontium On Structure, Magnetism, and Electron States in $SmMnO_3$ Manganite. *Journal of Superconductivity and Novel Magnetism*, **37**(8): 1429–1442. doi: https://doi.org10.1007/s10948-024-06768-9

Verma, A., Sharma, S., Bhandari, R., Sarkar, B., & Jindal, V. (2012). Elastic properties of chalcopyrite structured solids. *Materials Chemistry and Physics*, **132**(2-3): 416–420. doi: https://doi.org10.1016/j.matchemphys.2011.11.047

Villoria, J., Alvarez-Galvan, M., Al-Zahrani, S., Palmisano, P., Specchia, S., Specchia, V., & Navarro, R. (2011). Oxidative reforming of diesel fuel over $LaCoO_3$ perovskite derived catalysts: Influence of perovskite synthesis method on catalyst properties and performance. *Applied Catalysis B: Environmental*, **105**(3-4): 276–288. doi: https://doi.org10.1016/j.apcatb.2011.04.010

Voigt, W. (1928). *A determination of the elastic constants for beta-quartz*. Leipzig: Terubner. (Lehrbuch de Kristallphysik)

Vosko, S. H., Wilk, L., & Nusair, M. (1980). Accurate spin-dependent electron liquid correlation energies for local spin density calculations: A critical analysis. *Canadian Journal of Physics*, **58**(8): 1200–1211. doi: https://doi.org10.1139/p80-159

Wang, J.-X., Chen, Z., & Gao, Y. (2018). Phase stability, magnetic, electronic, half-metallic and mechanical properties of a new equiatomic quaternary heusler com-pound zrrhtiin: A first-principles investigation. *Journal of Physics and Chem-istry of Solids*, **116**: 72–78. doi: https://doi.org10.1016/j.jpcs.2018.01.003

Wang, Y., & Cheng, H.-P. (2013). Oxygen reduction activity on perovskite oxide surfaces: a comparative first-principles study of $LaMnO_3$, $LaFeO_3$, and $LaCrO_3$. *The Journal of Physical Chemistry C*, **117**(5): 2106–2112. doi: https://doi.org10.1021/jp309203k

Wei, J., Zhang, L., & Liu, Y. (2021). First-principles calculations study the mechanical and thermal properties of Cr-Al-B ternary borides. *Solid State Communications*, **326**: 114182–1–6. doi: https://doi.org10.1016/j.ssc.2020.114182

Wilk, G., & Wallace, R. (2000). Stable zirconium silicate gate dielectrics deposited directly on silicon. *Applied Physics Letters*, **76**(1): 112–114. doi: https://doi.org10.1063/1.125673

Wu, Y., Bao, L., Wang, X., Wang, Y., Peng, M., & Duan, Y. (2020). Insight into structural, electronic, elastic, and thermal properties of A15-type Nb_3X (X= Si,

Ge, Sn, and Pb) compounds. *Materials Today Communications*, **25**: 101410–1–41. doi: https://doi.org10.1016/j.mtcomm.2020.101410

Wu, Y., Ma, L., Zhou, X., Duan, Y., Shen, L., & Peng, M. (2022). Insights into Electronic Structures, Elastic Properties, Fracture Toughness, and Thermal Properties of $M_{23}C_6$ Carbides. *International Journal of Refractory Metals and Hard Materials*, **109**: 105985–1–10. doi: https://doi.org10.1016/j.ijrmhm.2022.105985

Xue, L., Ren, Y., He, J.-R., Zhao, Y., Xu, S.-L., Hu, Y., & Hua, C.-B. (2024). The mechanical and thermal parameters of two-dimensional hexagonal materials evaluated using elastic properties: monolayer MoS_2 as an example. *Results in Physics*, **57**: 107418–1–9. doi: https://doi.org10.1016/j.rinp.2024.107418

Yan, X. J., Li, W. Y., Zou, X., Liu, L. L., Wang, S. F., Wei, Y., & Hu, L. (2022). Janus B_2XY (X, Y= S, Se, Te) monolayers as piezoelectric materi-als: a first-principle study. *Chemical Physics Letters*, **806**: 140007–1–8. doi: https://doi.org10.1016/j.cplett.2022.140007

Yang, G., Yang, W., Gu, H., Fu, Y., Wang, B., & Cai, H. (2023). Perovskite-solar-cell-powered integrated fuel conversion and energy-storage devices. *Advanced Ma-terials*, **35**(44): 2300383–1–24. doi: https://doi.org10.1002/adma.202300383

Zaghrane, A., Ouhenou, H., Darkaoui, E., Agouri, M., Abbassi, A., Mekaoui, Y., & Manaut, B. (2024). First-principles investigation of structural, electronic, optical, and magnetic properties of a scintillating double perovskite halides (Cs_2LiCeX_6) with (X= F, Br, and I). *Chinese Journal of Physics*, **90**: 911–921. doi: https://doi.org10.1016/j.cjph.2023.08.001

Zhang, S., Li, F., Jiang, X., Kim, J., Luo, J., & Geng, X. (2015). Advantages and challenges of relaxor–pbtio$_3$ ferroelectric crystals for electroacoustic transducers-a review. *Progress in Materials Science*, **68**: 1–66. doi: https://doi.org10.1016/j.pmatsci.2014.10.002

Zheng, X., Du, A., Ye, Y., Chen, E., Xu, S., & Guo, T. (2024). Synthesis, structural and optical properties of a novel double perovskite for LED applications. *Ceramics International*, **50**(1): 1474–1487. doi: https://doi.org10.1016/j.ceramint.2023.10.237

APPENDIX

A1. Simulation and Software

In this section, we discuss our simulation work and the software used in the calculations. We performed first-principles calculations using the Quantum ESPRESSO (QE) software package (Malakkal et al., 2016), which is based on plane-wave basis sets.

Moreover, we used XCrySDen to visualize and interpret the crystal structure and the VESTA software package (Momma & Izumi, 2011) for visualization of the materials under consideration. XCrySDen, which stands for (X-window) Crystalline Structures and Densities, is open-source software. It is a crystalline and molecular structure visualization program, capable of visualizing crystal structures from the `pw.x` input and output files (Kokalj, 1999). We also used Xmgrace to plot graphs. It is open-source and quite flexible. It can read and write many different formats, including EPS, PDF, PNG, JPEG, and MIF, and it needs the.agrformat to modify graphs (Trangenstein, 2017).

Furthermore, we discuss different codes and their purposes as required for our calculations.

A2. Quantum ESPRESSO (QE).

Quantum ESPRESSO (QE) is an open-source program for modeling of materials and calculations of electronic structure (Giannozzi et al., 2009). It is very helpful for first-principles computations in materials research and condensed matter physics. The software is based on DFT and uses plane-wave basis sets and pseudopotentials to model how electrons and ions interact. We used QE to do several calculations, such as: Ground state calculations of conductors, semiconductors, and insulators, including self-consistent total energies, forces, stresses and structural optimization of the system.

Additionally, QE allows for ab-initio molecular dynamics (MD) simulations and is compatible with density functional perturbation theory (DFPT) for analyzing energy derivatives and related quantities (Baroni et al., 2001). For this work, we calculated the ground state energy of graphene and boron nitride unit cells using both norm-conserving and ultrasoft pseudopotentials. We found that ultrasoft pseudopotentials yielded lower ground state energies for both materials.

A3. Scf input file structure.

A3.1. Scf.in File

. . . . . .

```
&control
calculation = 'scf'
restart_mode='from_scratch',
prefix='ZrSiO',
pseudo_dir = '.',
outdir='.'
tprnfor = .true., tstress=.true.
/
&system
ibrav= 0, celldm(1)= 13.631359,
nat= 40, ntyp= 3
ecutwfc = 60.0, ecutrho = 600.0,
nspin=2,
starting_magnetization(1)= 0.0,
starting_magnetization(2)= 0.5,
starting_magnetization(3)= 0.0,
occupations='smearing', smearing='gauss', degauss=0.01,
/
&electrons
mixing_mode = 'plain'
mixing_beta = 0.3
conv_thr =  1.0d-6
mixing_fixed_ns = 0
/
CELL_PARAMETERS
1.000000    0.0000000   0.0000000
0.0000000   1.0000000   0.0000000
0.0000000   0.0000000    1.000000

ATOMIC_SPECIES
Zr 91.220 Zr.UPF [Zr.pbe-spn-rrkjus_psl.1.0.0.UPF]
Si 28.090 Si.UPF [Si.pbe-nl-rrkjus_psl.1.0.0.UPF]
O 15.999 O.UPF   [O.pbe-spn-rrkjus_psl.1.0.0.UPF]

ATOMIC_POSITIONS (crystal)
Zr       0.000000000   0.000000000   0.000000000
Zr       0.000000000   0.000000000   0.500000000
Zr       0.000000000   0.500000000   0.500000000
Zr       0.500000000   0.500000000   0.500000000
```

```
Zr       0.500000000   0.000000000   0.000000000
Zr       0.000000000   0.500000000   0.000000000
Zr       0.500000000   0.000000000   0.500000000
Zr       0.500000000   0.500000000   0.000000000
Si       0.749197069   0.750001044   0.750001044
Si       0.749197069   0.750001044   0.249998956
Si       0.250802931   0.249998956   0.750001044
Si       0.749197069   0.249998956   0.750001044
Si       0.250802931   0.750001044   0.249998956
Si       0.250802931   0.750001044   0.750001044
Si       0.749197069   0.249998956   0.249998956
Si       0.250802931   0.249998956   0.249998956
O        0.248990645   0.248849228   0.000000000
O        0.248745525   0.251258350   0.500000000
O        0.751009355   0.751150772   0.000000000
O        0.751009355   0.248849228   0.000000000
O        0.248990645   0.751150772   0.000000000
O        0.000000000   0.249802878   0.249802878
O        0.000000000   0.750197122   0.750197122
O        0.000000000   0.750197122   0.249802878
O       -0.000000000   0.249802878   0.750197122
O        0.248990645  -0.000000000   0.248849228
O        0.751009355   0.000000000   0.751150772
O        0.248990645   0.000000000   0.751150772
O        0.751009355   0.000000000   0.248849228
O        0.751254475   0.748741650   0.500000000
O        0.751254475   0.251258350   0.500000000
O        0.248745525   0.748741650   0.500000000
O        0.500000000   0.250090696   0.250090696
O        0.500000000   0.749909304   0.749909304
O        0.500000000   0.749909304   0.250090696
O        0.500000000   0.250090696   0.749909304
O        0.248745525   0.500000000   0.251258350
O        0.751254475   0.500000000   0.748741650
O        0.248745525   0.500000000   0.748741650
O        0.751254475   0.500000000   0.251258350
K_POINTS {automatic}
14 14 14 0 0 0
.........................
```

A3.2. PWscf Code

The **PWscf** code (Scandolo et al., 2005) was used to perform electronic structure calculations with plane-wave basis sets and pseudopotentials. It made structural relaxation, electronic structure calculations, and self-consistent computations easier. The primary components of the QE input file:

- **calculation**: Tells you what kind of calculation to do, such **relax**, **scf**, **nscf**, or **bands**.
- **ibrav**: ibrav tells you what kind of Bravais lattice is being used. We used `ibrav = 1` to represent the Simple cubic structure of $ZrSiO_3$.
- **nat**: denotes the total number of atoms in the simulated cell. In the present study, **nat = 5** is used for the primitive unit cell of $ZrSiO_3$, whereas **nat = 40** corresponds to the $2 \times 2 \times 2$ supercell of $ZrSiO_3$.
- **ntype**: This tells you how many different sorts of atoms are used. For Zirconium (Zr), Silicon (Si), and Oxygen (O), we have **ntype = 3**.
- **ecutwfc**: This is kinetic energy cut-off value. It cuts off total electronic wave function.
- **celldm(i)**: `i = 1, 2, 3` denote the lattice parameters of the crystal measured in atomic units.
- **Atomic_Species**: The name of the atom, together with its symbol, which is written with atomic mass (in amu) on the pseudopotential (PP) file.
- **Atomic_Positions**: These are the coordinates of the positions of atoms in the simulation cell that defines the correct structure.
- **k-points**: They are the number of points set used to take samples in reciprocal space. They are used to perform the self-consistent minimization of energy. Typically, **k-points** are determined by a convergence test.

A3.3. PostProc

The `PostProc` module has a lot of scripts for post-processing and assists in analyzing the data obtained from `PW-scf` calculations. These codes extract the data files produced by the `PWscf` calculation. Some important codes include:

- **bands.x**: This script retrieve the data sets generated by the **PWscf** calculation to obtain the electronic band structure.

- **plotband.x**: This script processes the output of the **bands.x** file into a simple format that can be plotted easily by programs like **xmgrace** or **gnuplot**, ultimately producing band structure.
- **dos.x**: This script is employed to evaluate the density of states (DOS) for various k-points.
- **projwfc.x**: This script uses atomic orbitals to project the wave functions in order to do population analysis and find the projected density of states (PDOS). It allows the contribution of various atomic orbitals to the total density of states.

A4. Convergence Tests

We independently determined three fundamental parameters for our calculations: the kinetic energy cut-off (ecutwfc), which signifies the threshold for wave function expansion; the k-points, which assess the efficacy of our discrete grid in approximating the continuous integral over the Brillouin zone (BZ); and the lattice parameter (a), which defines the cell dimensions in first-principles calculations.

SSO, the plane wave self-consistent field (PWscf) calculations employ an infinite set of basis functions, which represent the plane wave expansion of both the ground-state and electronic wave functions under periodic boundary conditions. This expansion is based on Bloch's theorem (Parmenter, 1952):

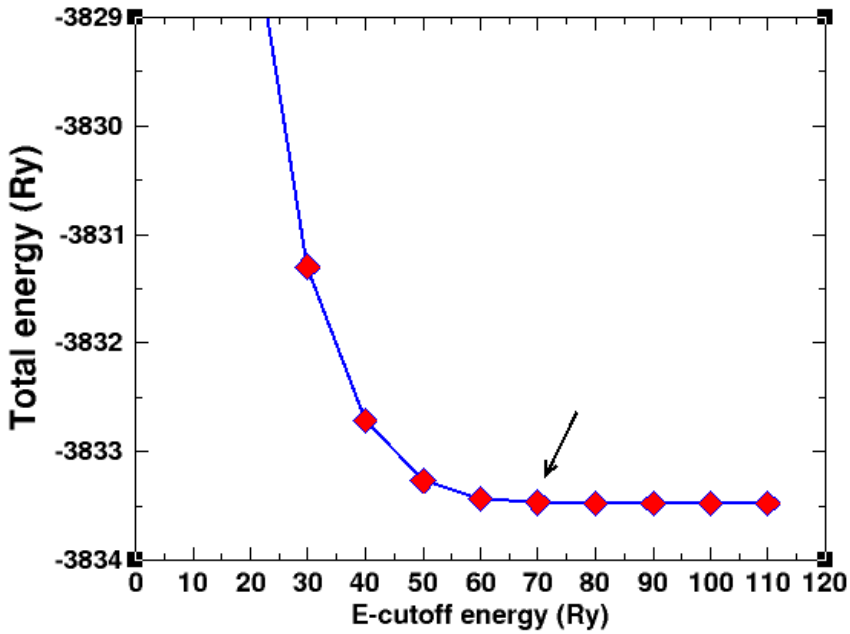

Figure A1: Total energy and kinetic energy cut-off for a $2 \times 2 \times 2$ supercell of $ZrSiO_3$

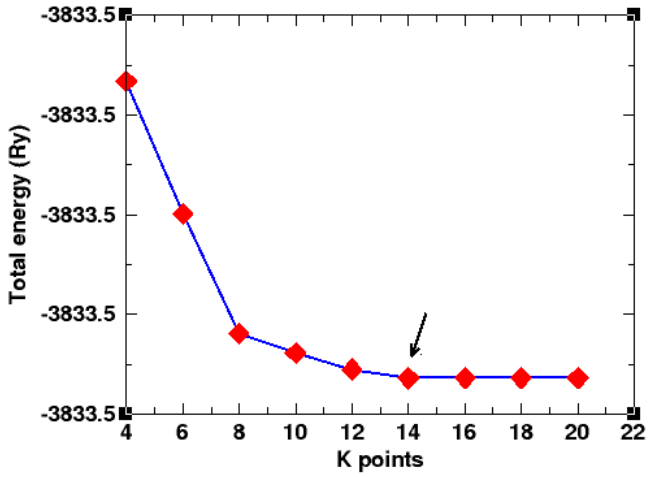

Figure A2: Total energy and k-points of $2 \times 2 \times 2$ supercell of $ZrSiO_3$.

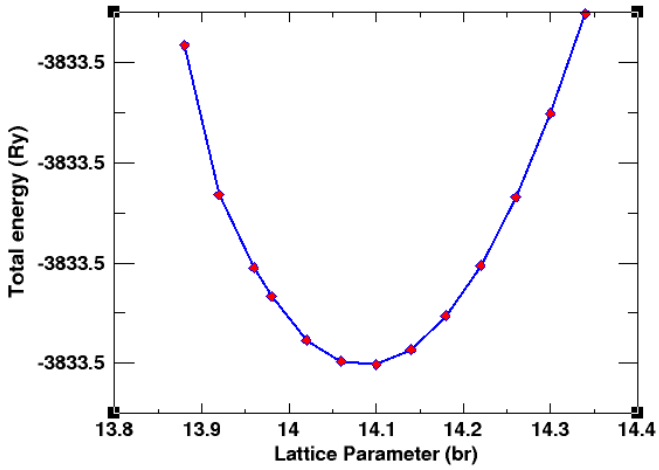

Figure A3: Total energy and lattice constant of 2x2x2 supercell of $ZrSiO_3$.

B: Paper published in international journals

Pokharel, P., Yadav, S. K., Pantha, N., & Adhikari, D. (2024a). First-Principles Investigations of Structural, Electronic, and Elastic Properties of $ZrSiO_3$ Perovskite: Layer Dependence, Surface Termination, and Pressure Effects. *physica status solidi (b)*, **261**(8): 2400156.

Pokharel, P., Yadav, S. K., Pantha, N., & Adhikari, D. (2024b). Strain-dependent electronic, mechanical and piezoelectric properties of $ZrSiO_3$ 2D monolayer: A first-principles approach. *Journal of Physics and Chemistry of Solids*, **193**: 112198–1–9. doi: https://doi.org10.1016/j.jpcs.2024.112198

Pokharel, P., Yadav, S. K., Pantha, N., Sharma, B., & Adhikari, D. (2025). Elastic

Anisotropy and Thermal Properties of Sr_2ZrMoO_6 Double Perovskite under Different Pressure. *physica status solidi (b)*, **262**(5): 2400625.

Pokharel, P., Yadav, S. K., Sharma, B., Pantha, N., & Adhikari, D. (2024c). Structural, electronic, optical, magnetic, and mechanical properties of $SmMnO_3$ perovskite with europium and yttrium doping: A first-principles study. *AIP Advances*, **14**(12): .

C: Paper published in national journals

Pokharel, P., Yadav, S. K., Adhikari, D., & Pantha, N. (2025). First Principles Study of the Electronic, Optical, Elastic, and Thermal Properties of Double Perovskite Sr_2MgWO_6 for Optoelectronic Applications. *Journal of Institute of Science and Technology*, **30**(2): 1–13. doi: https://doi.org10.3126/jist.v30i2.76851

C: Participation in Conferences and Workshops

Conferences

- **Gandaki University International Conference, 2023 (GUIC-2023)**, 13-15 June, 2023, **Gandaki University**, Pokhara, Nepal.
- 3^{rd} **International Conference on Condenced Matter & Applied Physics**, 09-10 October, 2023, **Department of Physics, Government Engineering College**, Bikaner, Rajsthan, India.
- 4^{th} **International Conference on Material Science(ICMS-2024)**, 31January-2February 2024, **Department of Physics, Tripura University**, Agartala, Tripura, India.
- **Association of Nepali Physicists in America Conference**, 14-16 July, 2023, **ANPA**, America.
- **APS March Meeting 2024**, 3 March- 8 March, 2024, **American Physical Society,** America.
- **Regional Conference on Science and Technology**, 2024, 7-8 May, 2024, **Central Campus of Technology (IoST),** Dharan, Nepal.
- **International Conference on Material Science and Characterization Technology (ICMSCT)**, 26 -28 September, 2021, **St. Xavier's College, Maitighar, Kathmandu, Nepal.**

Workshop Participation

- **Workshop on Experimental and Computational Approach of Metal Oxide Thin Film**, 18-19 March, 2021, **Department of Physics, Amrit Campus,** Kathmandu, Nepal.
- **Workshop on Density Functional Theory**, 18-21 February, 2023, **M. M. A. M. Campus, T. U.**, Biratnagar, Nepal.
- **Refresher course on Material Science–2021**, 15–19 September 2021, **Central Department of Physics, Tribhuvan University.** Kathmandu, Nepal.
- **Workshop on Emerging Computational Science, ECS-2024**, 20-25 May, 2024, **Department of Physics, IIT Goa**, Goa, India.
- **Workshop on Density Functional Theory based Studies on Nanomaterials for Optoelectronic Devices**, 06-06-2024 to 10-07 2024, **Chhatisgrah Swami Vivekanand Technical University (CSVTU)**, Bhilai, India.

RESEARCH ARTICLE

physica status solidi b

www.pss-b.com

First-Principles Investigations of Structural, Electronic, and Elastic Properties of $ZrSiO_3$ Perovskite: Layer Dependence, Surface Termination, and Pressure Effects

Peshal Pokharel, Shashit Kumar Yadav, Nurapati Pantha, and Devendra Adhikari**

Zirconium silicate ($ZrSiO_3$) perovskite is a promising material for various technological applications. The structural, electronic, and thermodynamic properties of $ZrSiO_3$ perovskite are studied under different conditions, including pressure and layer configuration variations using density functional theory. The present investigation includes a thorough analysis of 2D perovskite derivatives derived from its basic 3D structure. The bulk and surface-terminated silicon-dominant SiO_2 and zirconium-dominant ZrO compounds are found to be mechanically stable with an anisotropy factor above 1. The calculated indirect-bandgap values for the ZrO termination and SiO_2 termination are found to be 2.585 and 1.639 eV, respectively. Moreover, the pore size of the SiO_2-terminated slab model of $ZrSiO_3$ is calculated to be 105.39 μm and that for ZrO-termination to be 129.30 μm. Thus, the material considered for the study can have potential applications in bone regeneration and tissue engineering. Further, the possibilities for modifying $ZrSiO_3$ for uses in electrical devices, sensors, sustainable energy materials, and even biomedical applications like tissue engineering are intriguingly expanded by the present findings.

1. Introduction

Zirconium silicate ($ZrSiO_3$) perovskite is an interesting perovskite with a unique crystal structure and properties. The general formula for this perovskite is ABX_3, with zirconium (Zr), silicon (Si), and oxygen (X) as the A-site cations, B-site cations, and X-site anions, respectively.[1] The $ZrSiO_3$ perovskite attracts most modern-day scientific concerns due to its exceptional properties and potential applications in a wide range of technological fields. In this regard, researchers are interested in gathering more information related to its structural, electrical, magnetic, optical, and thermal properties. The study and characterization of 2D perovskites is carried out with the help of elementary knowledge of their 3D counterparts.[2] In 2D perovskites, the inorganic octahedral layers of the 3D structure are preserved, whereas the 'A' cations are confined within the organic or inorganic spacer layers, resulting in a layered structure.[3] The general formula for a 2D perovskite is (A)n (BX_3)m or (AX_3)n (B)m which represents the repeated layers of 'A' and BX_3 units or AX_3 and B units.[4] This maintains the stacking patterns AB, AB, AB, with the 'A' layers serving as spacers or insulating layers to separate the perovskite-type octahedral layers, denoted by 'B'. The surface termination of perovskite materials is the arrangement and composition of atoms or molecules on the outermost layers of the crystal structure. Surface termination of $ZrSiO_3$ perovskite depends on crystallographic orientation. On the (001) surface, oxygen (O) atoms terminate alternating layers of zirconium (Zr) and silicon (Si) atoms. This termination exposes Zr—O and Si—O bonds on a stable surface. There are two termination models: silicon-dominant SiO_2 and zirconium-dominant ZrO. The crystallographic orientation and growth conditions might enable alternative surface terminations like (110) or (111). The choice of surface termination has a significant effect on the characteristics of the material. By changing surface reconstruction, energy, and chemistry, it can affect surface reactivity, catalytic activity, and electrical characteristics.[5] In contrast to ZrO termination, the SiO_2-terminated slab model demonstrates promising material to be used as a scaffold material for bone tissue engineering[6] due to its narrow bandgap and comparable pore size compared to bone. In addition, the Bader charge distribution data is a valuable resource for explaining the arrangement of different atoms and their associated charges within a material's layers. These charges and their positions are crucial for understanding the electronic and structural properties of the material, including its conductivity, chemical reactivity, and catalytic behavior.[7] Moreover, pressure changes the electronic structure, bandgap energy, lattice density, velocity of sound, and Debye temperature of perovskite materials. Pressure-induced changes improve solar devices and perovskite-based electronics by

P. Pokharel, N. Pantha
Central Department of Physics
Tribhuvan University
Kritipur 44618, Nepal

P. Pokharel, S. K. Yadav, D. Adhikari
Department of Physics
Mahendra Morang Adarsh Multiple Campus
Tribhuvan University
Biratnagar 56613, Nepal
E-mail: sashit.yadav@mmamc.tu.edu.np;
devendra.adhikari@mmamc.tu.edu.np

P. Pokharel
Department of Physics
Central Campus of Technology
Tribhuvan University
Dharan 56700, Nepal

The ORCID identification number(s) for the author(s) of this article can be found under https://doi.org/10.1002/pssb.202400156.

DOI: 10.1002/pssb.202400156

controlling energy interactions.[8] Additionally, pressure can significantly alter the thermal properties, stability, and durability of perovskite materials, which are essential for their practical application. These layer-dependent perovskites are highly promising for use in solar cells, light emitting diodes, lasers, photodetectors, memory devices, and field-effect transistors[9] due to their unique properties, which include increased stability, variable bandgaps, high charge carrier mobility, and extended diffusion lengths. Therefore, several researchers have studied the pressure-dependent and surface termination effects on the structural, elastic, thermal, mechanical, and electronic properties of different perovskites using first-principle calculations.

Terki et al.[10] studied $BaZrO_3$ and $SrZrO_3$, revealing that they exhibit insulating characteristics characterized by wide bandgaps in their electronic structures. Li et al.[11] used Cambridge serial total energy package software and density functional theory (DFT)-based calculations with generalized gradient approximation for the study of structural stability and electronic properties of LaO- and NiO_2-terminated $LaNiO_3$ (001) surface. Their calculations showed the impact of surface termination, atomic relaxation, and the role of Ni 3d electrons in influencing the surface energy and electronic states of $LaNiO_3$ perovskite. Luo et al.[12] used the Vienna ab initio simulation program VASP, a DFT-based first-principles calculation for the comprehensive investigation of the electronic structure, surface energy, and charge distribution of the cubic perovskite $KNbO_3$ (001) surface with NbO_2 and KO terminations. They found that NbO_2 termination has a lower surface energy and a smaller bandgap compared to KO termination. Nazari et al.[13] analyzed the influence of halogen type and surface termination on the stability and electronic properties of $CsPbX_3$ (X = I, Br, Cl) perovskites. They found that these materials possessed superior stability and favorable band alignment of CsX-terminated surfaces, making them promising for photovoltaic applications. Zhao et al.[14] studied charge carrier mobilities, exciting binding energies, and optical properties of ultrathin 2D layered phenylethylammonium lead iodide perovskite to better understand its potential uses in photovoltaics and optoelectronic devices. Bakar et al.[15] investigated the structural, elastic, mechanical, and thermal properties of cubic perovskites $XCoO_3$ (X = Nd, Pr) under varying pressure conditions. Their findings revealed the mechanical stability, anisotropic nature, and changes in the materials' properties under pressure, such as the transition from ionic to covalent nature and from ductile-to-brittle behavior.

Previous investigations of Zr-based perovskite have focused primarily on its structural and electronic properties under normal conditions. Therefore, the effects of mechanical pressure on a material's structural stability and electronic properties were studied in the present work. The characteristics of layer-dependent $ZrSiO_3$ perovskite were also calculated. Moreover, the surface relaxations, structural features, electrical properties, and elastic properties of ZrO- and SiO_2-terminated $ZrSiO_3$ surfaces oriented with the (0 0 1) plane were calculated and predicted.

2. Computational Details

The geometrical stability and electronic properties of bulk and different layers of $ZrSiO_3$ perovskite were studied in this work. The structural properties of $ZrSiO_3$ were investigated using the Quantum ESPRESSO code[16] employing pseudopotential planewave approaches based on DFT.[17] The Perdew–Burke–Ernzerhof (PBE) exchange-correlation functional[18] was used for electronic exchange correlation, along with the revised correlation functional PBESOL.[19] Ultrasoft Vanderbilt-type pseudopotentials were used to implement the interaction between valence electrons and atomic cores.[20] The planewave basis set was given a cutoff energy of 70 Ry. Monkhorst–Pack method was used to calculate the bulk and surface properties of the systems.[21] A $14 \times 14 \times 14$ k-point mesh was employed for the calculations of bulk properties whereas a $14 \times 14 \times 1$ k-point mesh was used for the calculation of surface properties. To examine the surface relaxation of $ZrSiO_3$, slab models for various layer configurations were created and their geometries were optimized as described above. All atoms in various layers on each side of the slab were free to move in orthogonal directions to the slab surfaces until the forces exerted on each atom were minimized. To minimize contact between adjacent surfaces created by the periodic boundary condition of the model, a 15 Å vacuum gap was created between adjacent layers. To investigate the electronic properties of $ZrSiO_3$ with varying layer thicknesses, band structures and partial density of states (PDOS) were estimated. The stress–strain method was employed to calculate the elastic constants, including second-order elastic tensors. The Debye temperature was calculated to understand the thermal properties of the different terminations of $ZrSiO_3$. It was calculated using the average sound velocity obtained from the longitudinal and transverse elastic wave velocities.

3. Results and Discussion

3.1. Structural Properties

3.1.1. Bulk $ZrSiO_3$ at Different Pressures

The pressure-dependent structural parameters, such as lattice constant (a_0), ground-state energy (E_0), minimum volume (V_0), cohesive energy (ΔE), and bond lengths of the bulk $ZrSiO_3$, are calculated. It can be observed that the ratio of lattice parameter a/a_0 and unit cell volume V/V_0 of the compound decreases gradually with an increase in pressure (**Figure 1**a). This may be due to the linear compressibility of the compound with increasing pressure. The calculated values of E_0 increase gradually with the increase in pressure and are found to be −472.51209, −472.51211, −472.51249, −472.51273, −472.51363, and −472.51569 Ry at pressures 0, 20, 40, 60, 80, and 100 GPa, respectively. Cohesive energy values exhibit a nonlinear trend with the application of pressure (Figure 1b). $ZrSiO_3$ exhibits a covalent nature because of the presence of strong covalent connections within silicon–oxygen tetrahedra. These covalent bonds experience compression as the pressure of the compound is increased. As a result, the bond lengths decrease and the strength of interactions increases, thereby increasing the cohesive energy. Therefore, the estimated values of Zr—O, Si—O, and Zr—Si bond lengths (in Å) are (2.5472, 2.5469, 2.5468, 2.5468, 2.5422, 2.5402), (1.8013, 1.8011, 1.8010, 1.8009, 1.8009, 1.8007), and (3.1193, 3.1192, 3.1190, 3.0987, 3.0987, 3.0779) at pressures

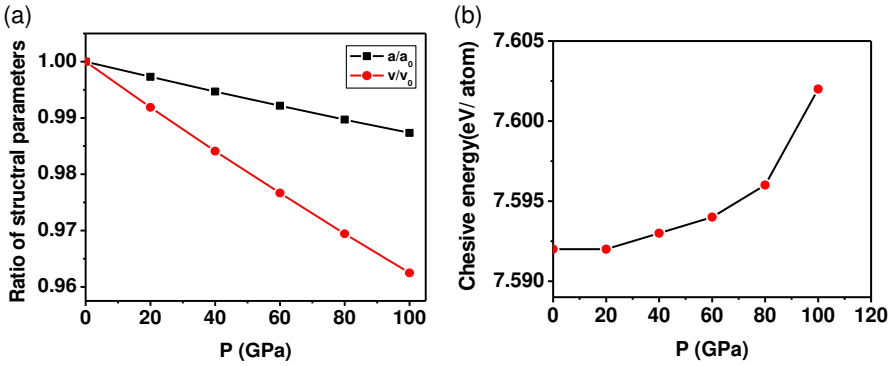

Figure 1. a) Ratios of structural parameters (a/a_0 and V/V_0) and b) cohesive energy at different pressures for the bulk $ZrSiO_3$.

(in GPa) (0, 20, 40, 60, 80, 100), respectively. Furthermore, comparable results are obtained when the pressure is reduced in the same manner, indicating that there was no hysteresis loss during expansion and compression.

3.1.2. Different Layer Configurations

In the perovskite structure of $ZrSiO_3$, the primitive unit cell has the chemical formula ABX_3 and is made up of three separate atomic sites. Zr is situated at site A, where it forms bonds with oxygen atoms in nearby regions and occupies the central octahedral coordination position. Si is found at site B, particularly at the corners, where it combines with oxygen (O) to form a tetrahedral network. When oxygen atoms are at the X sites, they make silicon–oxygen tetrahedra and the octahedral coordination around Zr (**Figure 2**a). The four-layered unit cell is composed of SiO_2 and ZrO layers that alternate in a particular sequence. A possible stacking order is SiO_2–ZrO–SiO_2–ZrO or vice versa. This alternating arrangement creates a layered structure with a repeating sequence of SiO_2 and ZrO layers. The SiO_2 layer consists of silicon–oxygen tetrahedra, forming a tetrahedral network.

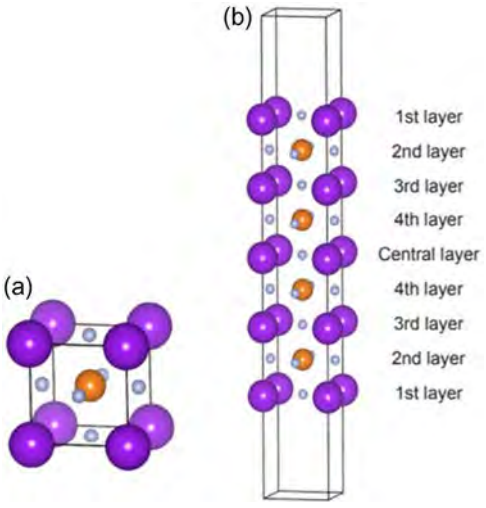

Figure 2. a) A primitive unit cell of cubic $ZrSiO_3$ and b) unit cell of four layers of $ZrSiO_3$ complex.

Si atoms are bonded to four oxygen atoms, creating a stable structure. ZrO layer is formed by oxygen atoms interacting with zirconium. In the ZrO layer, Zr atoms between SiO_2 layers improve the stability and structural integrity of the compound (Figure 2b).

The relaxation analysis is conducted on the (0 0 1) surfaces, where all atoms in the various layers on each side are allowed to move freely along orthogonal directions to the slab surfaces. The layered-dependent surface energies and bond lengths between different atoms and their cohesive energies have been calculated using the following expressions.[22]

$$\Delta E = \left[E_{ZrSiO_3} + \left(E_{Zr} + E_{Si} + E_{O_2}\right)\right] \quad (1)$$

where E_{ZrSiO_3} is the total energy per atom, and E_{Zr}, E_{Si}, and E_{O_2} are the energies of isolated atoms of Zr, Si, and O, respectively. The surface energy (γ) is given as[23]

$$\gamma = \frac{1}{2A}\left[E_{Slab}(N) - NE_{bulk}\right] \quad (2)$$

where $E_{Slab}(N)$ and E_{bulk} are slab layer energy and bulk energy, respectively.

The optimal number of layers for the slab model is determined by correlating the total energy per atom and surface energy per cell values with the number of layers. For this purpose, the surface area of each layer is taken to be $5.9155 \times 10^{-20}\,m^2$. The surface energy as a function of number of layers is plotted in **Figure 3**a. It can be observed that the surface energy increases gradually at first (up to layer 3) and then almost remains constant with the increase in the number of layers.

The bond lengths between different atoms (Zr—Si, Zr—O, and Si—O) and their respective cohesive energies are calculated for different slab configurations. The bond lengths for Zr—Si are calculated to be 3.1529, 3.0740, 3.0077, 2.7552, and 2.5722 Å for the first, second, third, fourth, and fifth slab layers, respectively. Similarly, those of Zr—O and Si—O are estimated to be 2.5556, 2.5182, 2.4558, 2.2496, 2.1012 Å, and 1.8184, 1.7982, 1.7365, 1.5908, 1.4850 Å, respectively, for the first, second, third, fourth, and fifth slab layers. Thus, the present investigations reveal that as the number of slab layers increases, the bond lengths decrease gradually. The cohesive energy per atom decreases gradually up to the number of layers equal to 3 and then it increases with an increase in the number of layers

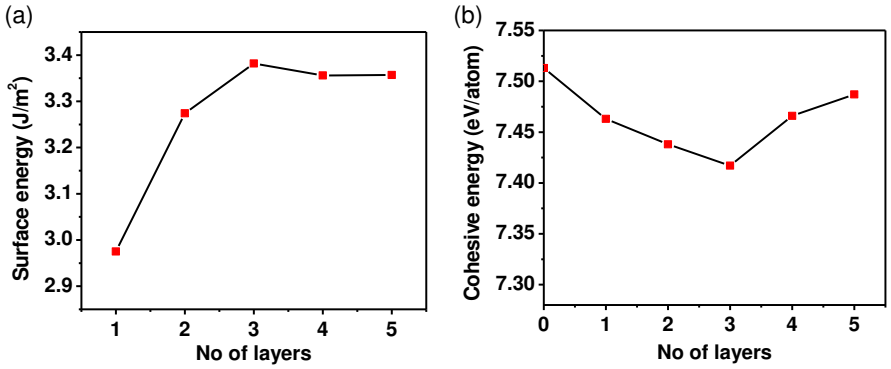

Figure 3. a) Surface energy per cell versus number of layers and b) cohesive energy per atom versus number of layers of different layers of $ZrSiO_3$.

(Figure 3b). This can be attributed to the relaxation process, which allows the atoms to move more freely and form more stable configurations resulting in the decrease in the cohesive energy. Once a certain number of layers (three in this case) is reached, interactions between levels intensify, potentially leading to energetically unfavorable configurations or increased structural instability, thereby influencing the overall cohesive energy.

3.1.3. Surface Relaxation of $ZrSiO_3$

The surface relaxation of a slab model refers to the atoms or ions that adjust their positions at the surface of the slab. This adjustment occurs due to the reduced coordination of surface atoms and their desire to minimize surface energy. Surface relaxation results in changes in the spacing between adjacent layers in the surface region of the slab.[24] The surface and atomic relaxations of $ZrSiO_3$ (0 0 1) surfaces and Bader charge distribution around each atom in different layer configurations are studied in this work.

The atomic relaxation (ΔZ_i) of the i^{th} layer from the surface is expressed as[25]

$$\Delta Z_i = Z_i - Z_{i,\text{bulk}} \tag{3}$$

where $Z_{i,\text{bulk}}$ is the unrelaxed z-coordinate and Z_i is the coordinate of individual atoms of Zr, Si, and O in the i^{th} layer after relaxation. If $\Delta Z_i > 0$, then it indicates relaxation toward the vacuum region, and if $\Delta Z_i < 0$, then it indicates relaxation toward the bulk.[26] In the first layer from the surface, the calculated values of Δz for each of Zr and O are 0.001 Å. This small and positive value of Δz reveals the displacements of both of the atoms toward the vacuum region and outward relaxation. Likewise, the Si ($\Delta z = 0.0358$ Å) atom also experiences a small outward relaxation. In the second layer from the surface, each of the atoms has a larger atomic displacement ($\Delta z = 0.0524$ Å) compared with the first layer predicting their displacements toward the vacuum region and outward relaxation. In the third layer from the surface, the calculated values of atomic displacements for each of the Zr and O atoms ($\Delta z = 0.001$ Å) are small, revealing their displacements toward the vacuum region with slightly outward relaxation. The Si ($\Delta z = 0.0136$ Å) atom in this layer also experienced a small outward relaxation. In the fourth layer from the surface, the small and positive values of atomic displacements were obtained for Zr and O atoms ($\Delta z = 0.001$ Å), indicating their respective displacements toward the vacuum region with slight outward relaxation. Further, the Si ($\Delta z = 0.9141$ Å) atom experiences a significant outward relaxation. More precisely, the present investigations have shown that on moving from the bulk to the surface layers of $ZrSiO_3$ perovskite, the atoms of the layer faced outward atomic relaxations, indicating that the atoms at the surface tend to adjust their positions to minimize surface energy.

The study of the Bader charge (Q) of each atom in the compound gives the information values about the localization of electronic charge around it. The Bader charge distributions for Zr, Si, and O atoms in the bulk material are estimated to be 0.27|e|, 1.02|e|, and −0.43|e|, respectively; indicating the localization of electronic charge around each atom. Similarly, the Bader charge distributions around Zr, Si, and O atoms are (0.32|e|, 1.08|e|, −0.48|e|), (0.51|e|, 1.19|e|, −0.47|e|), (0.56|e|, 1.07|e|, −0.44|e|), and (0.76|e|, 0.91|e|, −0.46|e|) for the first, second, third, and fourth layer configurations of $ZrSiO_3$ perovskite, respectively. The Bader charge analysis revealed that the electronic charges are localized around each atom in the different layers.

3.1.4. Surface Termination Models and Their Relaxations

The symmetrical slabs of alternating SiO_2 and ZrO layers are then created using the optimized cubic $ZrSiO_3$ crystal lattice structure. One of these slabs is terminated by ZrO planes, while the other is terminated by SiO_2 planes. These slabs are finite in the z-direction but periodic in the x- and y-directions and the unit cells representing both slabs are shown in **Figure 4**.

A model of the surface is constructed using a periodic slab consisting of seven layers. The slab is composed of alternating layers of SiO_2 and ZrO, with a vacuum region of 15 Å separating them. The ZrO-terminated slab contains a supercell with 17 atoms, while the SiO_2-terminated slab contains a supercell with 18 atoms. The surface energy for the thicknesses of several slabs is estimated to decide the size of the slab models. Surfaces with two possible terminations emerge concurrently when surface energy is distributed equally on both surfaces.

The relaxation analysis is conducted on the (0 0 1) surfaces, where all atoms in the various layers on each side are allowed to move freely along orthogonal directions to the slab surfaces. The optimal number of layers for the slab model is determined by correlating the surface energy values with the number of

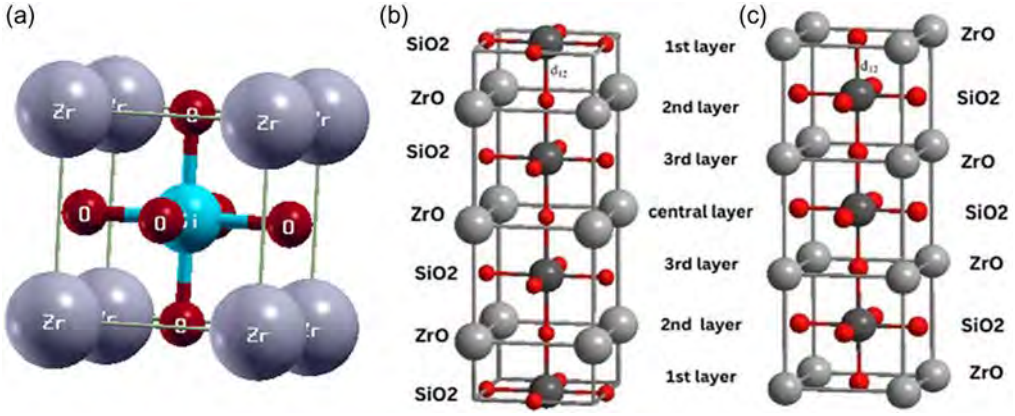

Figure 4. a) A primitive unit cell of cubic $ZrSiO_3$, b) SiO_2-terminated three-layered slabs, and c) ZrO-terminated slabs of $ZrSiO_3$ using VESTA and Canva.

layers. The surface and atomic relaxations of $ZrSiO_3$ (0 0 1) surfaces are examined with ZrO and SiO_2 terminations. Due to inherent symmetry, the atomic displacements (Δz) of the atoms in the top three layers are similar to those in the bottom three layers, Figure 4b,c. Specifically, on SiO_2-terminated surfaces, both O and Si atoms in the first layer ($\Delta z = -1.175$ Å for O and $\Delta z = -1.256$ Å for Si) and third layer ($\Delta z = -0.395$ Å for O and $\Delta z = -0.675$ Å for Si) experience inward relaxation whereas in the second layer, atoms of O ($\Delta z = 0.753$ Å) experience outward relaxation and that of Si ($\Delta z = -1.030$ Å) still experience inward relaxation, as shown in Figure 4b. In the case of ZrO-terminated slabs, atoms of O in all three layers exhibit outward relaxations ($\Delta z = 0.047, 0.061, 0.030$ Å for first, second, and third layers, respectively) whereas those of Zr exhibit inward relaxations, $\Delta z = -0.041, -0.098, -0.329$ Å for first, second, and third layers, respectively (Figure 4c). Notably, the second layer with ZrO termination shows the most significant atomic relaxations while the largest atomic relaxations are observed in the first-layered atoms in SiO_2-terminated surfaces.

The Bader charge distributions are also estimated at the bulk terminated geometry for different models to confirm the convergence of the charge distribution for the slab thickness.[27] Bader charge analysis indicates that the charge distributions converge to less than the formal ionic charges of 4|e|, 4|e|, and −2|e| for oxygen, silicon, and zirconium atoms, respectively. The difference between bulk and internal layer charges is minimal, less than 0.1|e|, 0.2|e|, and 0.1|e| for O, Si, and Zr atoms, respectively. The charge distribution within a SiO_2 molecule on the SiO_2-terminated surface model shows partial positive charges of 0.39|e| on Si and partial negative charges of −0.43|e| on O. This suggests the existence of polar covalent character in the Si—O bonds, indicating the unequal electron sharing, such that Si acquires a slight positive charge and O acquires a slight negative charge.[28] For the ZrO-termination model, partial positive charges of 1.19|e| are observed on Zr and partial negative charges of −0.43|e| are observed on O. These charge distributions suggest the presence of a partial covalent bond between them, similar to the SiO_2-terminated model. Both SiO_2- and ZrO-terminated surfaces exhibit a partial covalent character in the Si—O bonds, especially in the SiO_2-terminated surface layer. In the Zr—O bonds, a very low covalent character is observed.[28] The electron density maps in **Figure 5**a,b also confirm the existence of the partial covalent character of the Si—O bonds and Zr—O bonds on each slab layer.

The ground-state properties such as bond lengths and cohesive energies and surface characteristics are altered when a crystal is terminated with a particular atomic layer.[29] In $ZrSiO_3$, the

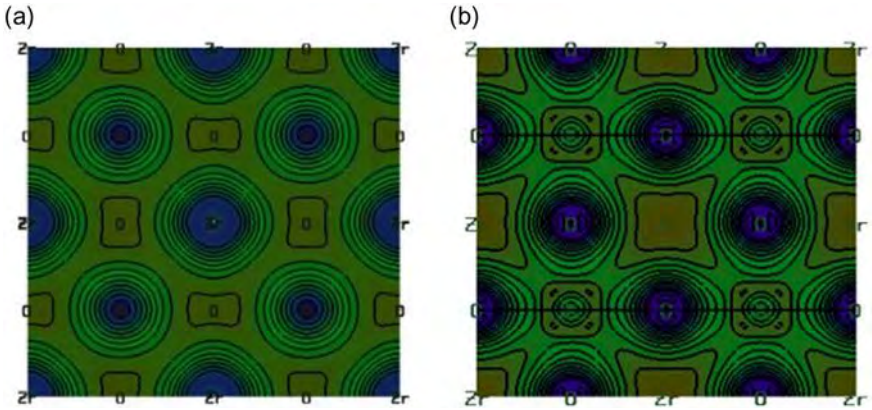

Figure 5. Electron density maps of different surface layers with a) ZrO terminations and b) SiO_2 terminations.

SiO_2- and ZrO-terminated slabs show different ground-state properties than that of its bulk phase. For the slab models, the bond lengths between the atoms and charge distribution around them differ from the bulk phase. Therefore, the cohesive energy values of the various termination models are estimated to comprehend their thermodynamic stability. Following a similar process, Meyer et al.[30] pointed that on $BaTiO_3$ and $SrTiO_3$ surfaces, both Ba/SrO-terminated and TiO_2-terminated surfaces are thermodynamically stable whereas for the $PbTiO_3$ surface, only the PbO-terminated has been found to be stable. The calculated values of cohesive energies for the SiO_2- and ZrO-terminated slabs of the $ZrSiO_3$ surface are 7.554 and 7.525 eV atom^{-1}, respectively, indicating them to be thermodynamically stable.

The dimension of the pores is a critical factor in the design of scaffolds used in tissue engineering. The strong effects of the scaffold on cellular adhesion and activity may make it an ideal material for the regeneration of bone tissue. The interconnection of pores is necessary to facilitate nutrient transport, cell migration, development, and migration.[31] Small pores create a cellular capsule along the edges of the scaffold, limiting cell movement. On the other hand, an increase in pore size leads to a decrease in surface area, which prevents cellular adhesion. Studies on porous implants show that the ideal pore size of range 100–135 mm is needed to contribute to effective bone formation.[32,33] In this regard, the pore sizes of ZrO- and SiO_2-terminated $ZrSiO_3$ slabs are calculated in the present work. The diameters of the pores for the ZrO- and SiO_2-terminated slab models are found to be 129.30 and 105.39 μm, respectively. Compared to the ZrO-terminated slab, the SiO_2-terminated slab exhibits smaller pore size; however, both of these values fall within the ideal range required for the bone regeneration materials.

3.2. Electronic Properties

3.2.1. The Bulk Material at Different Pressure

The pressure-responsive changes in the electronic band structure of bulk $ZrSiO_3$ with high-symmetry k-path in the irreducible Brillouin zone (Γ–X–M–Γ–R) are represented in **Figure 6**a–f. $ZrSiO_3$ has a 3.164 eV indirect bandgap at zero pressure. With increasing pressure, the bandgap increases. Their values are calculated to be 3.261, 3.287, 3.318, 3.328, and 3.339 eV at 20, 40, 60, 80, and 100 GPa, respectively. It is observed that an increase in pressure can influence the interactions between atoms, affecting the electronic states involved in the absorption and emission processes. Consequently, a blueshift may occur in the energy levels associated with the bandgap which may cause the shift to higher energy levels. A similar shift in the bandgap with the application of pressure was observed on cesium lead iodide perovskite.[34]

3.2.2. Different Layered Configurations

The analysis of the band structure of bulk $ZrSiO_3$ shows an indirect bandgap (**Figure 7**a). The valence band maximum is located at the high-symmetric Γ point, while the conduction band minimum is situated at the X point. A similar characteristic is shown by all $ZrSiO_3$ (0 0 1) surface layers (Figure 7b–e). It is a well-known fact that the interlayer interaction, potentially influences by Van der Waals forces, plays a vital role in determining the energy levels and bandgap. There is a significant decrease in the bandgap with the increase in the number of layers, ranging from 2.334 eV for the bulk material to 1.878 eV for the fourth layer (Figure 7f). Similar types of results related to the layer-dependent variation of bandgaps are also predicted by other researchers.[35,36]

The sharp peaks in the O-s state within the valence bands of the different layers of $ZrSiO_3$ PDOS plots are observed (**Figure 8**a–d). The observed peak indicates the existence of localized oxygen 2*p* orbitals, which actively participate in the bonding processes with the atoms of silicon and zirconium. A similar event is also observed where the conduction band contained sharp peaks in the Zr-d states, indicating the presence of localized zirconium 4*d* orbitals, which play a substantial role in the formation of the conduction band. Thus, it states that these localized d orbitals significantly influenced the conductivity of the material.

3.2.3. Surface Termination Models

Electronic Properties: The band structures of bulk $ZrSiO_3$, ZrO-terminated slabs, and SiO_2-terminated slabs are also studied and predicted in the present work (**Figure 9**a–c). The calculated values of indirect band gaps are 2.661, 2.585, and 1.639 eV for the bulk material, ZrO-terminated slab, and SiO_2-terminated slab, respectively. The energy levels of the material are observed to be affected by the specific surface termination, which affects its optical and electrical characteristics.

The projected DOS on all atomic orbitals of different atoms in the sample are calculated and plotted in **Figure 10**a,b. It is observed that in the SiO_2-termination slab, a higher peak is obtained for the Zr atom in the second layer than that in the central layer. This result indicates that the Zr atom in the former layer possesses a higher probability of containing electrons in its orbitals. Moreover, the higher values of energy levels of d orbitals compared with those in s and p suggest that the electrons in the later orbitals are found to be more stable. The PDOS of Si atoms shows that the first layer appears to have higher energy levels on the right side of the Fermi level whereas the third layer has a more stable arrangement with lower energy states on the left side of the Fermi level. Similarly, the PDOS plot of oxygen atoms in different layers shows that the third layer contained most electrons in its orbitals, the second layer has a lower electron density, and the first and central layers contained intermediate electron densities, Figure 10a.

In the case of the ZrO-termination slab, the higher peaks for the third-layer Zr atom in comparison to the first layer show that the third-layer Zr atom has a higher chance of electron presence in its orbitals, as shown in Figure 10b. The higher energy levels of the d orbitals suggest that electrons in the s and p orbitals are more stable or have lower energy levels. The PDOS plot of oxygen atoms in different layers shows that the second layer has more electrons in its orbitals, the orbitals of the first layer have a lower electron density, and the third and central layers have intermediate electron density. About Si atoms, the central layer appears to have higher energy levels on the right side of the Fermi level, whereas the second layer appears to have a more stable arrangement with lower energy states on the left side of the Fermi level.

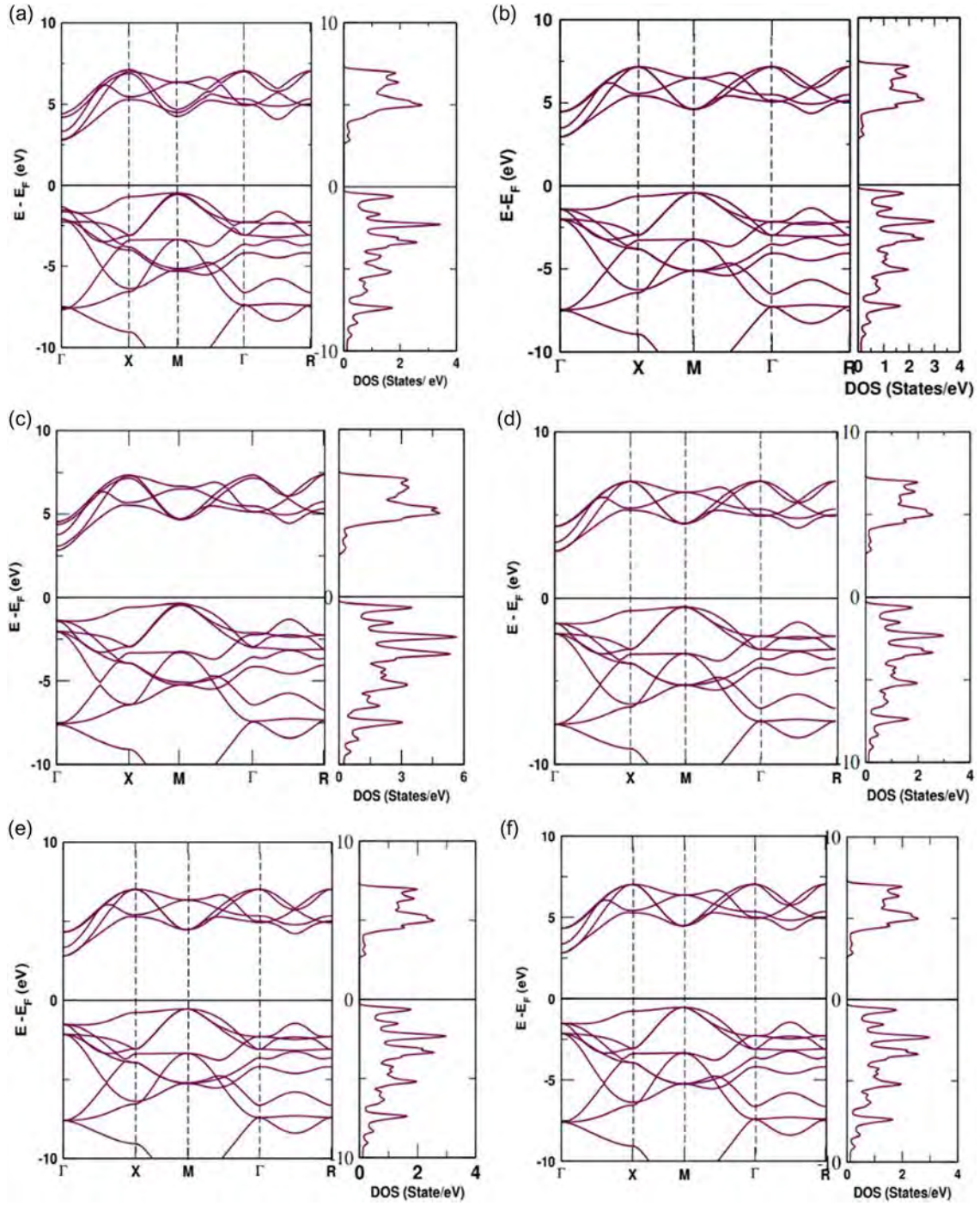

Figure 6. Band structures and density of states of bulk $ZrSiO_3$ at different pressures: a) at 0 GPa, b) at 20 GPa, c) 40 GPa, d) 60 GPa, e) 80 GPa, and f) 100 GPa.

3.3. Elastic Properties

The mechanical properties and dynamic stability of preferred perovskite materials are also calculated and studied. There are only three elastic constants for the simple cubic structure, namely, C_{11}, C_{12}, and C_{44}. Among these, C_{12} and C_{44} reflect elasticity in terms of shape, while C_{11} denotes elasticity in terms of length.[37] The pressure-dependent values of elastic constants for $ZrSiO_3$ are computed using the stress–strain method[38] using the following relations.

According to Hooke's law,[39] the relationship between stress (σ_{ij}) and strain (ε_{kl}) in terms of C_{ij} is expressed as

$$\sigma_{ij} = C_{ijkl}\varepsilon_{kl} \Rightarrow \sigma_{ij} = C_{ij}\varepsilon_{ij} \quad (4)$$

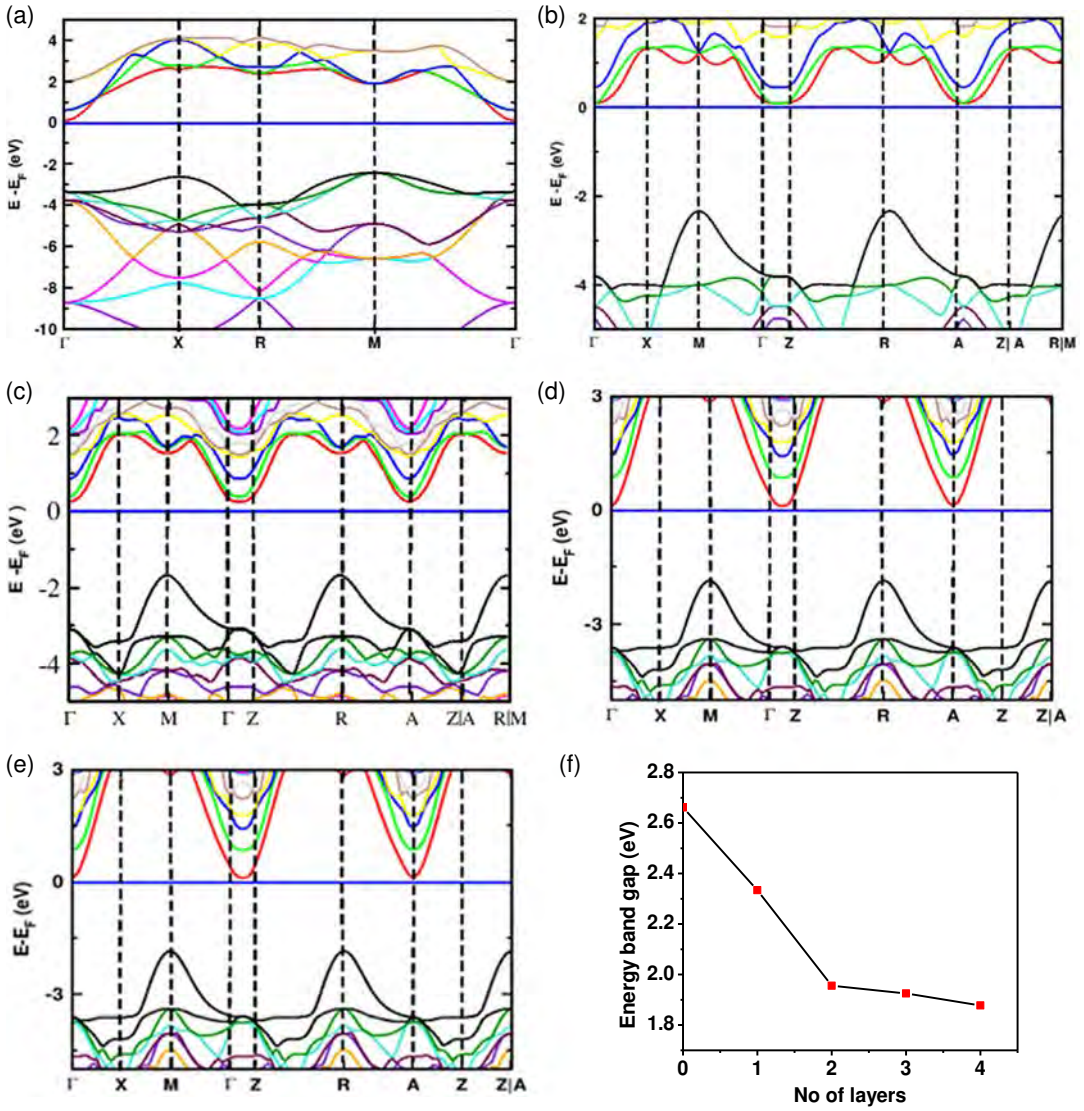

Figure 7. Band structure of a) bulk $ZrSiO_3$, b) first layer of $ZrSiO_3$, c) second layer of $ZrSiO_3$, d) third layer of $ZrSiO_3$, e) fourth layer of $ZrSiO_3$ and f) energy bandgap versus several layers of $ZrSiO_3$.

where σ_{ij} is the stress tensor component, C_{ij} is the stiffness or elastic tensor component, and ε_{ij} is the strain component.

The Voigt–Reuss–Hill approximation[40–42] has been employed for determining the bulk modulus (B), the shear modulus (G), and Young's modulus (E), which are calculated using the relations as follows.

$$B_{\mathrm{V}} = \frac{(C_{11} + 2C_{12})}{3} \text{ and } B_{\mathrm{R}} = \frac{1}{(3S_{11} + 6S_{12})} \tag{5a}$$

$$B_{\mathrm{H}} = \frac{B_{\mathrm{V}} + B_{\mathrm{R}}}{2} \tag{5b}$$

$$G_{\mathrm{V}} = \frac{(C_{11} - C_{12} + 3C_{44})}{5} \tag{6}$$

$$G_{\mathrm{R}} = \frac{5C_{44}(C_{11} - C_{12})}{4C_{44} + 3(C_{11} - C_{12})} \tag{7}$$

$$G_{\mathrm{H}} = \frac{(G_{\mathrm{V}} + G_{\mathrm{R}})}{2} \tag{8}$$

$$E = \frac{9B_H G_H}{3B_H + G_H} \tag{9}$$

The shear moduli of Voigt and Reuss generate isostrain upper and lower bounds, respectively.[43] Combining the Voigt and Reuss limits with a weight parameter is utilized for representing an intermediate condition.[44]

The following formulae are used to calculate the anisotropy factor (A), Poisson's ratio, and Cauchy's pressure. They are expressed as

$$A = 1 + \frac{C_{44} + C_{12}}{C_{11}} \tag{10}$$

$$\nu = \frac{3B_H - 2G_H}{2(3B_H + G_H)} \tag{11}$$

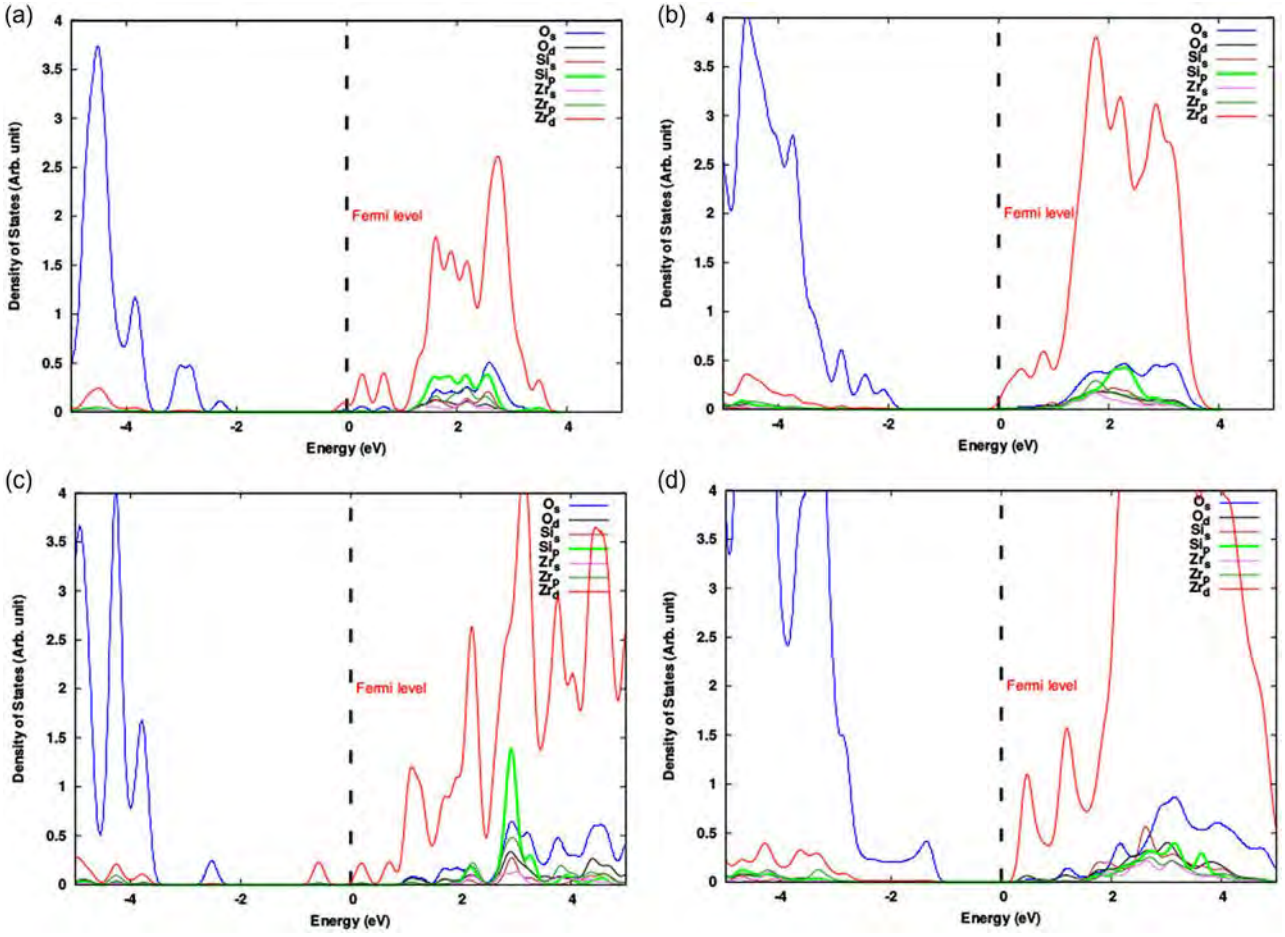

Figure 8. Plots of PDOS versus the energy of different layers of $ZrSiO_3$ a) first layer, b) second layer, c) third layer, and d) fourth layer.

and, Cauchy's pressure;

$$P_C = C_{12} - C_{44} \tag{12}$$

The types of bonds for a compound under examination can be interpreted using the sign of Cauchy's pressure[45] and the value of Poisson's ratio.[46] Cauchy's pressure is negative for the majority of covalent bonds whereas it is positive for the majority of ionic bonds. For a typical covalent compound, Poisson's ratio is substantially lower than 0.25 (about 0.1) whereas for a typical ionic compound, it is close to or greater than 0.25.[47]

It is observed that the values of C_{11} increase gradually with the increase in pressure of the compound, whereas those of C_{12} and C_{44} increase slightly with pressure which is due to a slight decrease in anisotropy of the substance with pressure (**Figure 11**a). The calculated value of $C_{11} > C_{44}$ throughout the entire pressure range indicates that the material became stiffer and resistant to compression with the increase in the pressure. Further, the material's resistance to isotropic compression is found to be stronger than its resistance to shear deformation at equivalent pressure levels in the simple cubic phase. The predicted values of elastic constants fulfilled the Born–Huang generalized elastic criterion[48] ($C_{11}-C_{12}>0$, $C_{11}+2C_{12}>0$, $C_{12}<B<C_{11}$and $C_{44}>0$), revealing the compound to be mechanically stable within the pressure range of 0–100 GPa.

As per Pugh's criteria, materials exhibit brittle behavior if the value of the Pugh ratio is less than 1.75 and ductile behavior if it is greater than 1.75.[49] At all applied pressures, the computed Pugh ratio for bulk $ZrSiO_3$ is found to be more than 1.75, indicating the material to be ductile in the applied pressure range.

The estimated values of Young's modulus and bulk modulus of the compound gradually increase with the increase in pressure whereas the shear modulus remains nearly constant due to the shear deformation of $ZrSiO_3$ (Figure 11b). These characteristics are critical for scaffold support, biomaterial–host tissue alignment, and transplanted cell activity. A positive Cauchy pressure signifies that the material exhibits greater compressibility when subjected to hydrostatic stress as opposed to shear stress. As the pressure of the sample is gradually increased, the Cauchy pressure remains almost constant (Figure 11c). This result predicts that the anisotropic behavior is stable over the given pressure range.

The study of elastic anisotropy (A) gives information related to the presence of variable bonding characteristics in different crystallographic directions and is associated with the potential to cause small cracks in materials.[50] For isotropic materials, $A=1$, and deviation from 1 is a measurement of the crystal's

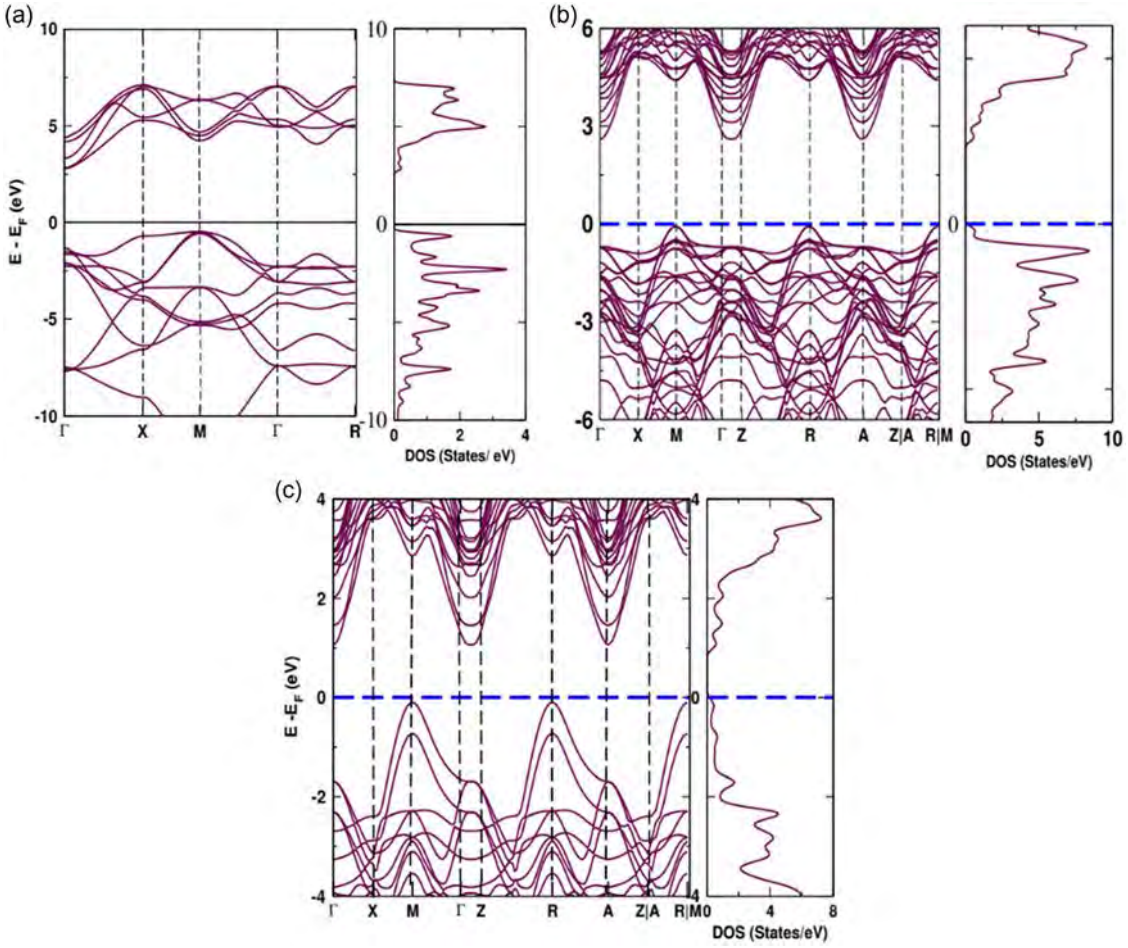

Figure 9. Band structure of a) bulk $ZrSiO_3$, b) ZrO-terminated slab, and c) SiO_2-terminated slab.

degree of elastic anisotropy. In the present study, the estimated value of A indicates that the preferred material is anisotropic (Figure 11d). As pressure is raised from 0 to 100 GPa, the Poisson's ratio decreases continuously (Figure 11e). This result reveals the material to be less compressible in the lateral direction compared to that of the axial direction. The Pugh ratio is a measure of the brittleness or ductility of a material. The Pugh ratio decreases gradually with the increase in the pressure of the sample, indicating a decrease in its ductility (Figure 11f).

The mechanical properties of tetragonal systems are also determined by the application of six second-order elastic constants. According to the mechanical requirements for tetragonal systems, the elastic constants are calculated by the following relations.[51]

$$C_{11} > 0, C_{33} > 0, C_{44} > 0, C_{66} > 0, C_{11} - C_{12} > 0, C_{11} + C_{33} - 2C_{12} > 0, 2C_{11} + 2C_{12} + C_{33} + 4C_{13} > 0 \quad (13)$$

The tetragonal Voigt bounds are derived from the Voigt approximation (uniform strain assumption).[52] The bulk modulus (B_v) is defined in terms of C, expressed as

$$B_V = \frac{1}{9}[2C_{11} + C_{33} + 2C_{12} + 4C_{13}] \quad (14)$$

According to Reuss approximation, B_R for lower bounds for all lattices can be given as

$$B_R = \frac{C^2}{M} \quad (15)$$

From Voigt and Reuss approximations, the shear constant (G_v) of an upper limit is given b

$$G_V = \frac{1}{30}[M + 3C_{11} - 3C_{12} + 12C_{44} + 6C_{66}] \quad (16)$$

with $M = [C_{11} + C_{12} + 2C_{33} - 4C_{44}]$
and $C^2 = (C_{11} + C_{12})C_{33} - 2C_{13}{}^2$
and its lower limit can be expressed in the form as

$$G_R = \frac{15}{\left[\frac{18B_V}{C^2} + \frac{6}{C_{11}+C_{12}} + \frac{6}{C_{44}} + \frac{3}{C_{66}}\right]} \quad (17)$$

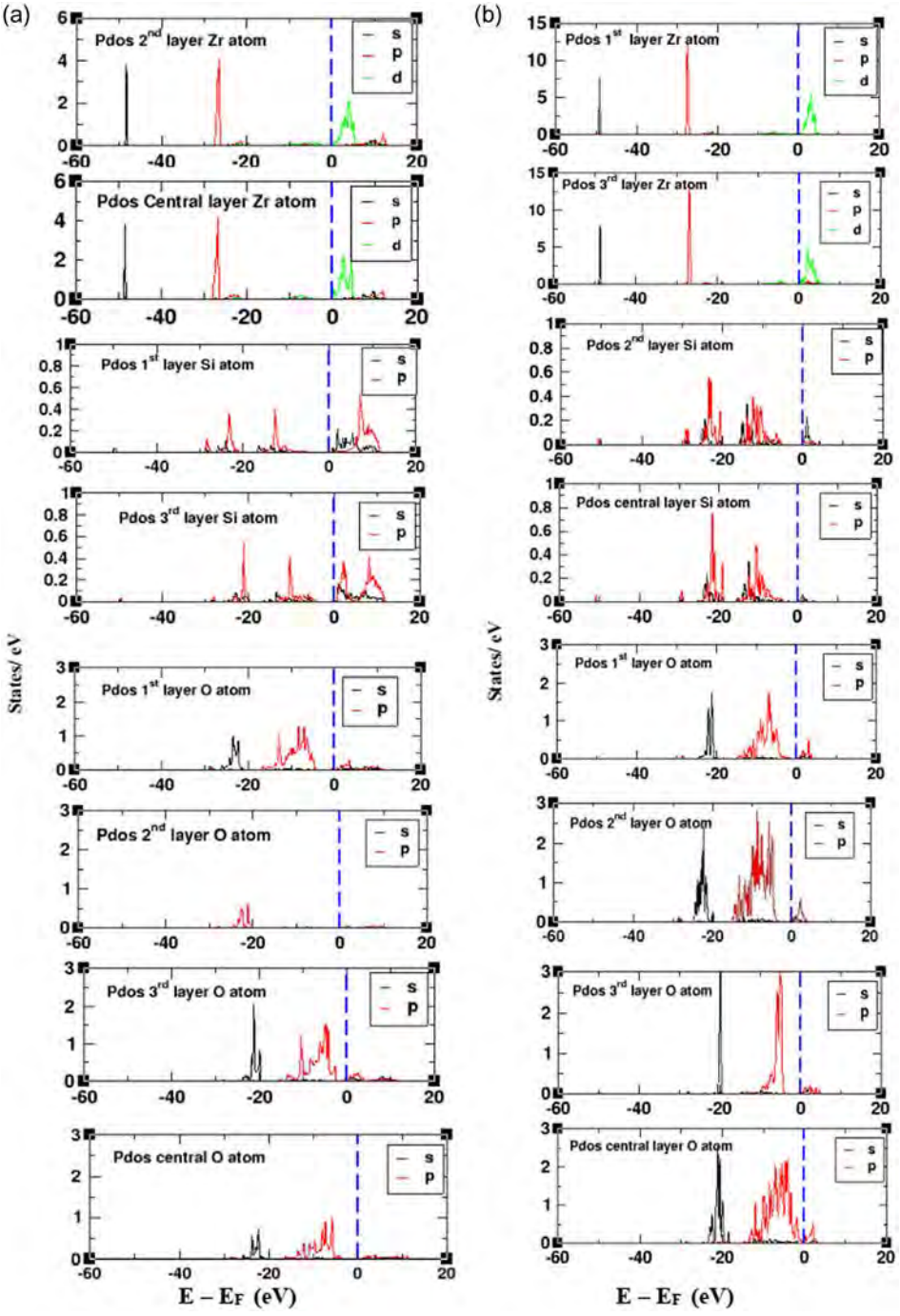

Figure 10. Projected DOS for different atoms in a) SiO_2-terminated slab models and b) ZrO-terminated slab models.

Finally, Voigt and Reuss's mean values are obtained by

$$B_H = \frac{(B_V + B_R)}{2} \text{ and } G_H = \frac{(G_V + G_R)}{2} \quad (18)$$

The values of the Poisson ratio and Young's modulus can be obtained using Equation (9) and (11), respectively. For the tetragonal system, Cauchy pressures along a- axis and b-axis are given by:

$$P_a^{Cauchy} = C_{13} - C_{44} \text{ and } P_b^{Cauchy} = C_{12} - C_{66} \quad (19)$$

The mechanical properties of tetragonal $ZrSiO_3$ and its ZrO- and SiO_2-terminated slabs are calculated and are displayed in **Figure 12**a,b. Both the ZrO- and SiO_2-terminated slab models are found to be mechanically stable and ductile. Compared to the ZrO-terminated slab, the SiO_2-terminated slab exhibits greater values of elasticity and stability. Additionally, the

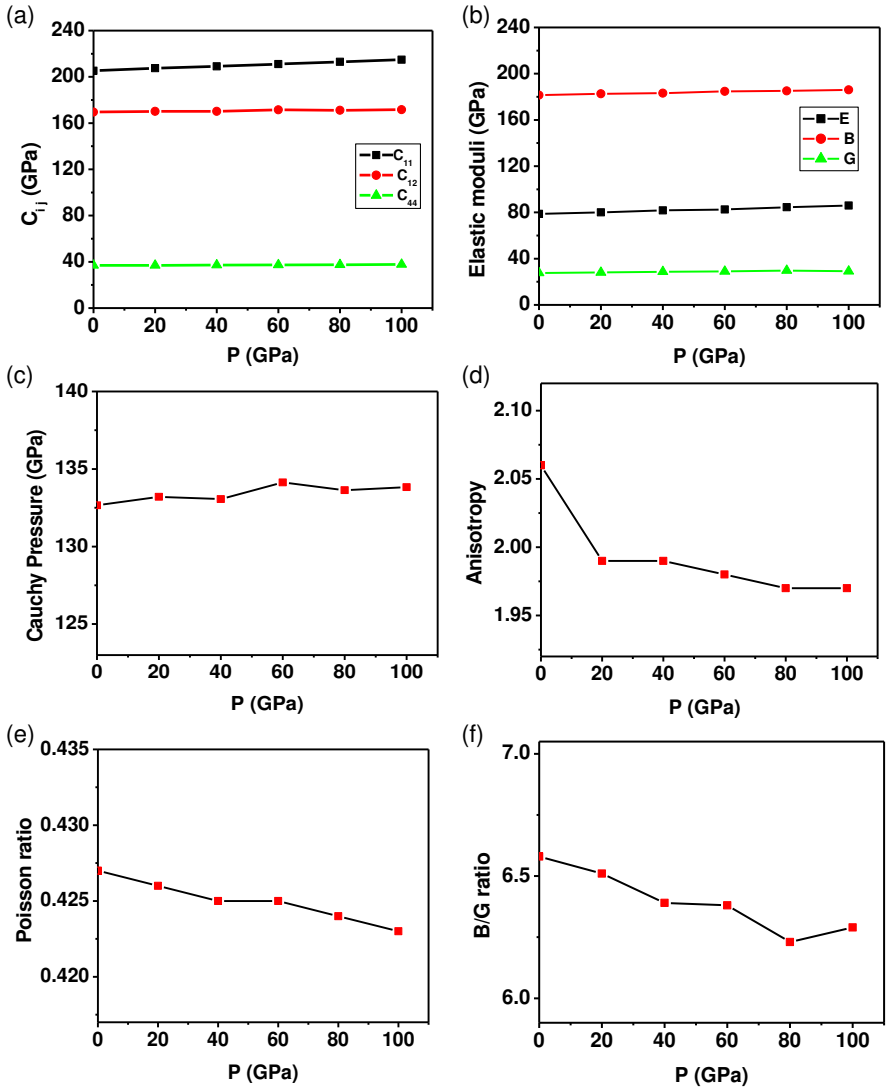

Figure 11. Elastic properties a) C_{ij}, b) elastic moduli (bulk modulus (B), the shear modulus (G), and Young's modulus (E)), c) Cauchy pressure, d) anisotropy (A), e) Poisson's ratio, and f) B/G ratio of $ZrSiO_3$ at different pressures.

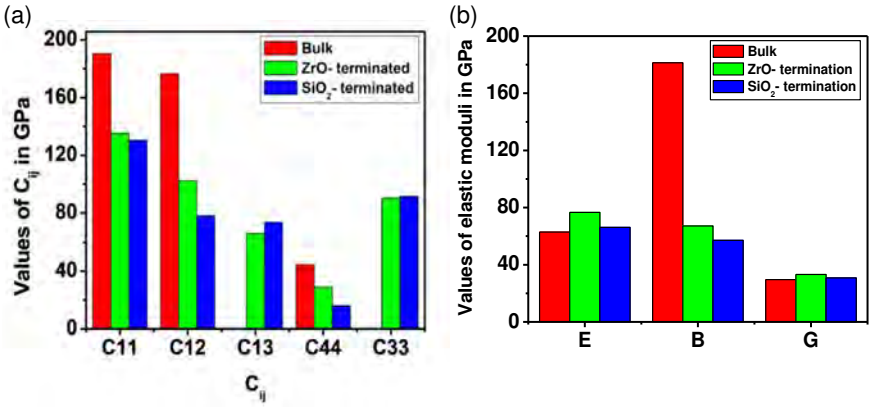

Figure 12. Different values of a) C_{ij} and b) elastic moduli for the bulk $ZrSiO_3$, ZrO-, and SiO_2-terminated slab models.

Table 1. Calculated values of the elastic modulus (B, G, E), Poisson's ratio (υ), G_H/B_H ratio, and Cauchy's pressure P_C of the bulk $ZrSiO_3$, ZrO-terminated slab, and that for SiO_2-terminated slab.

Compound	B_V [GPa]	B_R [GPa]	B_H [GPa]	G_V [GPa]	G_R [GPa]	G_H [GPa]	E [GPa]	ν	G_H/B_H	P_C [GPa]
Bulk	181.30	181.28	181.29	29.55	14.06	21.80	62.88	0.479	0.12	132.06
ZrO-terminated	92.19	42.06	67.12	33.22	25.34	29.28	76.69	0.309	0.44	37.16
SiO2-terminated	89.36	24.84	57.09	30.82	19.77	25.29	66.13	0.307	0.443	57.85

calculated values of Cauchy's pressure $P_C = C_{13} - C_{44} = 37.16$ GPa for ZrO-terminated slab models and $P_C = 57.85$ GPa for SiO_2-terminated slab models. Poisson's ratios (υ) of ZrO-terminated and SiO_2-terminated slab are calculated to be 0.334 and 0.379, respectively. Similarly, G_H/B_H ratios are found to be 0.373 and 0.264, respectively. These values of $P_C > 0$, G_H/B_H ratio <0.57, and Poisson's ratio $\upsilon > 0.33$ indicate both termination models are found to be ductile (**Table 1**).

The Debye temperature (θ_D) is an important parameter that gives information related to the thermal characteristics of materials, and it distinguishes between the high- and low-temperature states of solids. A higher value of (θ_D) indicates that the material possesses a higher thermal conductivity and has a high melting temperature.[53] The Debye temperature, which is effectively computed using the average sound velocity, has been determined in this study employing well-established methods and elastic constant data. The expression for θ_D can be given as[54]

$$\theta_D = \frac{h}{k_B}\left[\frac{3n}{4\pi}\left(\frac{N_A\rho}{M}\right)\right]^{\frac{1}{3}} v_m \tag{20}$$

where h represents Planck's constant, k_B is Boltzmann's constant, N_A is Avogadro's number, M is the molecular mass, ρ is the density, and v_m is the average sound velocity.

And v_m is calculated using the relation as follows.[55]

$$v_m = \left[\frac{1}{3}\left(\frac{2}{v_t^3} + \frac{1}{v_l^3}\right)\right]^{\frac{-1}{3}} \tag{21}$$

where v_l and v_t are the longitudinal elastic wave velocity and transversal elastic wave velocity, respectively, and can be obtained from Navier's equation[56] in terms of B and G as

$$v_l = \left[\frac{3B + 4G}{3\rho}\right]^{\frac{1}{2}}, \text{ and } v_t = \left[\frac{G}{\rho}\right]^{\frac{1}{2}} \tag{22}$$

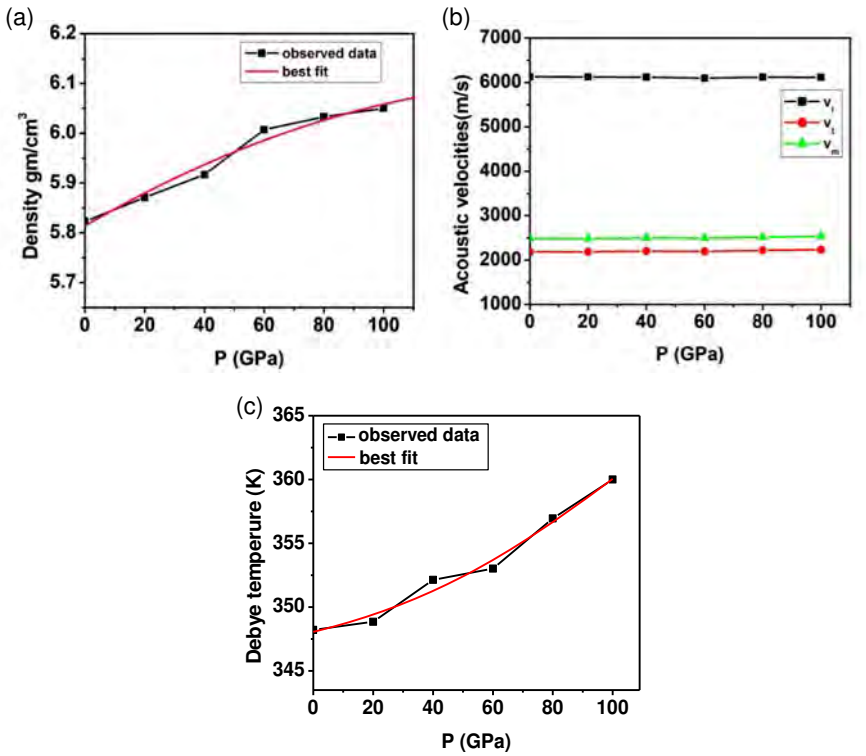

Figure 13. The calculated values of a) densities (ρ), b) longitudinal, transverse, and average sound velocities (v_l, v_t and v_m), and c) Debye temperature (θ_D) as a function of the pressure for the bulk $ZrSiO_3$.

The pressure-dependent values of densities (ρ), longitudinal velocity (v_l), transverse velocity (v_t), average sound velocity (v_m), and Debye temperature (θ_D) of the bulk $ZrSiO_3$ are calculated using Equation (20)–(22). The calculated value of density increases gradually with the increase in pressure, which is as expected (**Figure 13**a). The perusal of Figure 13b corresponds that the calculated sound velocities (v_l, v_t and v_m) of $ZrSiO_3$ at different pressures remain relatively constant regardless of the applied pressure, indicating that applied pressure has a minimal effect on the sound velocity. The estimated value of θ_D of the compound increases gradually with the increase in pressure of the compound (Figure 13c). As pressure increases, the atomic arrangement within a crystal structure gets compressed. This results in a reduction in the distances between atoms and an increase in the strength of the forces holding them together. This leads to increase in vibrational energy and frequencies, consequently increasing θ_D. Furthermore, the covalent bond strength in solids is proportional to θ_D. Therefore, computed values of θ_D revealed that the $ZrSiO_3$ complex exhibits the strongest covalent character up to 100 GPa. Similar types of variations were observed by Tian et al. in Al_7Cu_2Fe alloy[57] and Daoud in thallium–phosphide[58] using DFT.

Following a similar procedure, the values of ρ, v_l, v_t, v_m and θ_D are also estimated for ZrO- and SiO_2-terminated slab models. The calculated values of ρ are found to be 7.040 g cm^{-3} for the bulk $ZrSiO_3$, 2.724 g cm^{-3} for the ZrO-terminated slab, and 2.278 g cm^{-3} for the SiO_2-terminated slab. As expected, the density of the bulk compound is found to be the highest, followed by the ZrO-terminated slab model and the lowest for the SiO_2-terminated slab model. Likewise, the values of (v_l, v_t, v_m) are calculated to be (5974.06, 3206.22, 3550.02 ms^{-1}) for the bulk, (5877.07, 2935.30, 3293.08 ms^{-1}) for ZrO-terminated slab, and (7429.31, 3280.83, 3703.21 ms^{-1}) for SiO_2-terminated slab. Thus, the SiO_2-terminated slab model possesses the highest values of sound velocities followed by the bulk material and ZrO-terminated slab model.

The calculated values of θ_D are 438.04, 321.09, and 359.17 K, respectively for $ZrSiO_3$, ZrO-, and SiO_2-terminated slab models. These results suggest that the bulk compound exhibits the highest thermal conductivity and melting temperature, as indicated by its highest value of Debye temperature. The SiO_2-terminated compound has an intermediate value, while the ZrO-terminated compound has the lowest Debye temperature, indicating relatively lower thermal conductivity and melting temperature. These findings provide insights into the thermal properties of the studied compounds with different terminations.

4. Conclusion

The pressure and layered-dependent structural, mechanical, and electronic properties of $ZrSiO_3$ were studied using first-principle calculations in the present work. The important conclusions of the work are highlighted below. 1) With the rise in pressure, no significant variation in cohesive energy is estimated, but its value increases nonlinearly with an increase in layer thickness. 2) The study of elastic properties confirmed that the bulk $ZrSiO_3$ compound remains mechanically stable and ductile even at high pressures up to 100 GPa. Both ZrO-terminated and SiO_2-terminated models also show mechanical stability and ductility. In comparison to the ZrO-terminated slab, the SiO2-terminated form stands out for its greater elasticity and stability. 3) The calculated value of Debye temperature is found to be $(\theta_D)_{bulk} > (\theta_D)_{SiO_2-terminated\ slab} > (\theta_D)_{ZrO-terminated\ slab,}$ indicating the bulk material to have the highest thermal conductivity and melting temperature followed by SiO_2-terminated slab and the least for ZrO-terminated model. This makes it a valuable material for high-pressure uses, including high-pressure vessels, and other high-pressure and hydraulic systems, and ensures that it can bear mechanical stress and strain in bone tissue engineering applications. 4) Furthermore, the calculated electronic band structure identifies bulk $ZrSiO_3$ as an indirect-bandgap semiconductor. The bandgap increases with the rise in pressure whereas decreases with the increase in the number of layers. This type of variation of bandgap under pressure and layer thickness makes it promising for optoelectronic applications. It can be used in the development of high-pressure optical devices, such as sensors, modulators, and photodetectors. 5) Bader charge analysis revealed that termination types exhibit pronounced outward relaxation in the second atomic layer. Remarkably, SiO_2-terminated surfaces display the most substantial atomic relaxations in the first-layer atoms rather than the second layer. 6) The calculated values of pore sizes for SiO_2- and ZrO-terminated slabs of $ZrSiO_3$ are found to be small and within the ideal range required to be used in bone regeneration materials. The possibilities for modifying $ZrSiO_3$ material to be used in electrical devices, sensors, sustainable energy materials, and even biomedical applications like tissue engineering are intriguingly expanded by these findings.

Acknowledgements

The authors are grateful to Professor Dr. Narayan Prasad Adhikari (Central Department of Physics, TU) and Dr. Kapil Adhikari (Prithvi Narayan Campus, Pokhara) for the continuous support in pursuing the work. The authors also acknowledge the Department of Physics, Mahendra Morang Adarsh Multiple Campus, Biratnagar, TU, for providing necessary facilities to conduct the work.

Conflict of Interest

The authors declare no conflict of interest.

Author Contributions

P.P. conceptualization, methodology, software, visualization, validation, and writing the original draft. S.K.Y. resources and writing the review and editing. N.P. data curation and validation. D.A. resources, supervision, and formal analysis.

Data Availability Statement

The data that support the findings of this study are available from the corresponding author upon reasonable request.

Ethical Statement

The work is based on the authors' original research and the analysis presented is accurate.

Keywords

bandgap evolutions, biomedical applications, layer-dependent properties, surface relaxations, $ZrSiO_3$ perovskite

Received: March 28, 2024
Revised: May 6, 2024
Published online: May 19, 2024

[1] Q. A. Akkerman, L. Manna, *ACS Energy Lett.* **2020**, *5*, 604.
[2] X. Zhao, T. Liu, Y. L. Loo, *Adv. Mater.* **2022**, *34*, 2105849.
[3] G. Wu, R. Liang, Z. Zhang, M. Ge, G. Xing, G. Sun, *Small* **2021**, *17*, 2103514.
[4] K. S. Aleksandrov, J. Bartolomé, *Phase Transitions* **2001**, *74*, 255.
[5] P. F. Weck, E. Kim, V. Tikare, J. A. Mitchell, *Dalton Trans.* **2015**, *44*, 18769.
[6] S. Cao, Y. Zhao, Y. Hu, L. Zou, J. Chen, *Composites, Part B* **2020**, *202*, 108445.
[7] X. Lü, W. Yang, Q. Jia, H. Xu, *Chem. Sci.* **2017**, *8*, 6764.
[8] G. Liu, L. Kong, W. Yang, H. K. Mao, *Mater. Today* **2019**, *27*, 91.
[9] H. Ullah, F. S. Kayani, R. Khenata, *Mater. Res. Express* **2019**, *6*, 126105.
[10] R. Terki, H. Feraoun, G. Bertrand, H. Aourag, *Phys. Status Solidi B* **2005**, *242*, 1054.
[11] L. Guan, J. Zuo, G. Jia, Q. Liu, W. Wei, J. Guo, X. Dai, B. Liu, Y. Wang, G. Fu, *Appl. Surf. Sci.* **2013**, *264*, 570.
[12] B. Luo, X. Wang, E. Tian, G. Li, L. Li, *Appl. Surf. Sci.* **2015**, *351*, 558.
[13] S. Nazari, Y. T. Azar, A. Doroudi, *Mater. Today Commun.* **2020**, *24*, 100961.
[14] Y. Q. Zhao, Q. R. Ma, B. Liu, Z. L. Yu, J. Yang, M. Q. Cai, *Nanoscale* **2018**, *10*, 8677.
[15] A. Bakar, A. O. Alrashdi, M. M. Fadhali, A. Afaq, H. A. Yakout, M. Asif, *J. Mater. Res. Technol.* **2022**, *19*, 4233.
[16] P. Giannozzi, S. Baroni, N. Bonini, M. Calandra, R. Car, C. Cavazzoni, D. Ceresoli, G. L. Chiarotti, M. Cococcioni, I. Dabo, A. D. Corso, *J. Phys.: Condens. Matter* **2009**, *21*, 395502.
[17] J. P. Perdew, K. Burke, M. Ernzerhof, *Phys. Rev. Lett.* **1996**, *77*, 3865.
[18] M. Ropo, K. Kokko, L. Vitos, *Phys. Rev. B* **2008**, *77*, 195445.
[19] J. P. Perdew, A. Ruzsinszky, G. I. Csonka, O. A. Vydrov, G. E. Scuseria, L. A. Constantin, X. Zhou, K. Burke, *Phys. Rev. Lett.* **2008**, *100*, 136406.
[20] G. Kresse, D. Joubert, *Phys. Rev. B* **1999**, *59*, 1758.
[21] H. S. Patel, V. A. Dabhi, A. M. Vora, *Mater. Today: Proc.* **2022**, *57*, 275.
[22] P. H. T. Philipsen, E. J. Baerends, *Phys. Rev. B* **1996**, *54*, 5326.
[23] K. Ishikawa, T. Uemori, *Phys. Rev. B* **1999**, *60*, 11841.
[24] C. Q. Sun, B. K. Tay, X. T. Zeng, S. Li, T. P. Chen, J. Zhou, H. L. Bai, E. Y. Jiang, *J. Phys.: Condens. Matter* **2002**, *14*, 7781.
[25] B. Beeler, A. Casagranda, L. Aagesen, Y. Zhang, S. Novascone, *J. Nucl. Mater.* **2020**, *540*, 152271.
[26] H. L. Skriver, N. M. Rosengaard, *Phys. Rev. B* **1992**, *46*, 7157.
[27] F. Cargnoni, C. Gatti, E. May, D. Narducci, *J. Chem. Phys.* **2000**, *112*, 887.
[28] S. de Lazaro, E. Longo, J. R. Sambrano, A. Beltrán, *Surf. Sci.* **2004**, *552*, 149.
[29] Y. Sozen, S. Ozen, H. Sahin, *J. Magn. Magn. Mater.* **2021**, *531*, 167845.
[30] B. Meyer, J. Padilla, D. Vanderbilt, *Faraday Discuss.* **1999**, *114*, 395.
[31] C. M. Murphy, M. G. Haugh, F. J. O'Brien, *Biomaterials* **2010**, *31*, 461.
[32] S. F. Hulbert, F. A. Young, R. S. Mathews, J. J. Klawitter, C. D. Talbert, F. H. Stelling, *J. Biomed. Mater. Res.* **1970**, *4*, 433.
[33] J. J. Klawitter, J. G. Bagwell, A. M. Weinstein, B. W. Sauer, *J. Biomed. Mater. Res.* **1976**, *10*, 311.
[34] Y. Cao, G. Qi, C. Liu, L. Wang, Z. Ma, K. Wang, F. Du, G. Xiao, B. Zou, *J. Phys. Chem. C* **2018**, *122*, 9332.
[35] M. López-Suárez, I. Neri, R. Rurali, *J. Appl. Phys.* **2016**, *119*, 165105.
[36] Y. Cai, G. Zhang, Y. W. Zhang, *Sci. Rep.* **2014**, *4*, 6677.
[37] F. Birch, *Phys. Rev.* **1947**, *71*, 809.
[38] J. X. Wang, Z. B. Chen, Y. C. Gao, *J. Phys. Chem. Solids* **2018**, *116*, 72.
[39] R. Golesorkhtabar, P. Pasquale, S. Jurgen, P. Peter, D. Claudia, *Comput. Phys. Commun.* **2013**, *184*, 1861.
[40] S. Yip, L. Ju, T. Meijie, W. Jinghan, *Mater. Sci. Eng., A* **2001**, *317*, 236.
[41] W. Voigt, *Lehrbuch de Kristallphysik*, Terubner, Leipzig **1928**.
[42] A. Reuss, *J. Appl. Math. Mech.* **1929**, *9*, 49.
[43] R. Hill, *Proc. Phys. Soc., London, Sect. A* **1952**, *65*, 349.
[44] M. Jamal, M. S. Abu-Jafar, A. H. Reshak, *J. Alloys Compd.* **2016**, *667*, 151.
[45] Z. V. Poniznik, M. Basista, D. Gross, *Comput. Mater. Sci.* **2008**, *44*, 813.
[46] S. Pachori, R. Agarwal, B. Prakash, S. Kumari, A. S. Verma, *Energy Technol.* **2022**, *10*, 2100709.
[47] G. Surucu, C. Abdullah, G. Aysenur, I. Mehmet, *Int. J. Hydrogen Energy* **2019**, *44*, 30218.
[48] M. Jamal, S. J. Asadabadi, I. Ahmad, H. R. Aliabad, *Comput. Mater. Sci.* **2014**, *95*, 592.
[49] F. Mouhat, F. X. Coudert, *Phys. Rev. B* **2014**, *90*, 224104.
[50] S. A. Khandy, D. C. Gupta, *RSC Adv.* **2016**, *6*, 97641.
[51] C. Yang, Y. Duan, J. Yu, M. Peng, S. Zheng, M. Li, *Vacuum.* **2023**, *207*, 111626.
[52] Y. Wu, Y. Duan, X. Wang, M. Peng, L. Shen, H. Qi, *Mater. Today Commun.* **2022**, *33*, 104651.
[53] S. Sharma, A. S. Verma, R. Bhandari, V. K. Jindal, *Comput. Mater. Sci.* **2014**, *86*, 108.
[54] O. L. Anderson, *J. Phys. Chem. Solids* **1963**, *124*, 909.
[55] Y. Wu, L. Bao, X. Wang, Y. Wang, M. Peng, Y. Duan, *Mater. Today Commun.* **2020**, *25*, 101410.
[56] J. Wei, L. Zhang, Y. Liu, *Solid State Commun.* **2021**, *326*, 114182.
[57] J. Tian, Y. Zhao, Z. Wen, H. Hou, P. Han, *Solid State Commun.* **2017**, *257*, 6.
[58] S. Daoud, *Int. J. Adv. Res. Phys. Sci.* **2014**, *1*, 1.

Journal of Physics and Chemistry of Solids 193 (2024) 112198

Contents lists available at ScienceDirect

Journal of Physics and Chemistry of Solids

journal homepage: www.elsevier.com/locate/jpcs

Strain-dependent electronic, mechanical and piezoelectric properties of $ZrSiO_3$ 2D monolayer: A first principle approach

P. Pokharel [a,b,c], S.K. Yadav [b,**], N. Pantha [a], D. Adhikari [b,*]

[a] Central Department of Physics, Tribhuvan University, Kritipur, Nepal
[b] Department of Physics, Mahendra Morang Adarsha Multiple Campus, Tribhuvan University, Biratnagar, Nepal
[c] Department of Physics, Central Campus of Technology, Tribhuvan University, Dharan, Nepal

ARTICLE INFO

Keywords:
elastic anisotropy
Piezoelectricity
Stacking order
Compressional strain
Cohesive energy

ABSTRACT

This study investigated the mechanical stability, elastic anisotropy, electronic and piezoelectric properties of $ZrSiO_3$ 2D monolayer subjected to varying degrees of strain. The monolayer films were characterized under strains ranging from −6% to +6 %, and different material properties were analyzed to understand their response to mechanical deformation using density functional theory with the Quantum Espresso code. The calculated values of cohesive and strain energy revealed that the material exhibited a symmetrical response to tension and compression within a strain value range of −2% to +2 %. Electronic properties showed strain-induced modifications: the band gap of the material decreases under tensile strain and increases under compressive strain. The material remained mechanically stable and ductile under the applied strain range of −6% to +6 %. Present investigations conveyed the modifications produced by strain on elastic anisotropy and piezoelectric characteristics of the material, finding their applications in strain-sensitive sensors, actuators, and energy-harvesting devices.

1. Introduction

Zirconium silicate ($ZrSiO_3$) perovskite is an interesting perovskite with a unique crystal structure and rich properties. In $ZrSiO_3$, zirconium (Zr) occupies the A-site, silicon (Si) the B-site, and oxygen (O) the X-site, following the formula ABX_3 [1]. This material has gained interest for its potential applications in various technologies due to its structural, electronic, and mechanical properties. The study and characterization of 2D perovskites usually originate with an elementary knowledge of their 3D counterparts [2]. A 2D monolayer of perovskite is a thin sheet of material composed of a single layer of atoms or molecules [3]. This structure comprises one or more inorganic slabs composed of corner-sharing metal-oxide octahedral alternating with monovalent and divalent cations for the Dion-Jacobson (DJ) and Ruddlesden-Popper (RP) phases, respectively [4]. Monolayer perovskites differ from other 2D inorganic materials because they have a soft lattice and a dynamically disordered framework [5]. They exhibit various stacking orders, unlike graphene and transition metal dichalcogenides (TMDCs). Graphene has a single layer of carbon atoms in a hexagonal lattice, and TMDCs have layers of chalcogen and transition metal atoms. In contrast, 2D perovskite oxides can have octahedral, alternating, or mixed stacking orders. In octahedral stacking, layers maintain the octahedral coordination of the B-site cations, while alternating stacking produces a repeating pattern, and mixed stacking combines different configurations within one monolayer.

Experimentally, an oxide perovskite monolayer can be fabricated effectively by ion-exchange techniques [6] electrochemical deposition [7], spin coating [8], chemical vapor deposition [9], and pulsed laser deposition methods [10]. Three-dimensional perovskites are found to be less efficient due to factors such as moisture. However, reducing them to 2D layers supports to make the material more stable and prolong useable [11]. Maruyama et al. reported the first layered organic-inorganic halide perovskite in 1986. This discovery initiated the development of advanced two-dimensional hybrid perovskites [12]. In the 1990s, Mitzi and coworkers synthesized organic-based layered halide perovskites that transition from semiconducting to metallic behavior with increasing layers [13]. In 2009, Miyasaka et al. carried out extensive research on halide perovskites for photovoltaic applications by manipulating the properties of bulk organic-inorganic hybrid perovskites [14]. A decade later, perovskite solar cells reached 25.5 % efficiency from 3.8

* Corresponding author.
** Corresponding author.
E-mail addresses: sashit.yadav@mmamc.tu.edu.np (S.K. Yadav), devndra.adhikari@mmamc.tu.edu.np (D. Adhikari).

https://doi.org/10.1016/j.jpcs.2024.112198
Received 10 May 2024; Received in revised form 13 July 2024; Accepted 14 July 2024
Available online 25 July 2024

%. In 2015, Dou et al. studied bandgap engineering in organic-inorganic hybrid perovskites, highlighting their findings on the fabrication of highly efficient photodetectors [15]. In 2021, Ahmad et al. worked to improve the affordability and stability of perovskite solar cells by using transition metal dichalcogenides (TMDCs) and other two-dimensional materials, achieving an efficiency increase of 25.2 % [16]. Recently, scientists have extended their research on 2D perovskite monolayers into several application areas, including electronics, sensors, and catalysis. The electronic and mechanical characteristics of two-dimensional perovskite monolayers are significantly influenced by mechanical strain. Variations in the elastic modulus are brought about by mechanical strain, which impacts the resistance of the material to deformation. By increasing the elastic modulus, tensile strain improves flexibility; conversely, compressive strain increases stiffness. The modifications in the elastic modulus induced by strain are important for a wide variety of applications [17]. When mechanical stress is applied to piezoelectric materials such as quartz, they produce electrical energy. The piezoelectric properties of monolayers, mostly in two-dimensional materials like graphene [18], transition metal dichalcogenides (TMDs), and other 2D materials [19], are important for a variety of applications. Understanding how these materials react to mechanical stress is crucial for realizing their potential in applications such as energy harvesting, mobile devices, integrated circuits, nano-electromechanical systems, biomedical technologies, and optoelectronics.

This study addresses a literature gap by exploring the impact of strain on the structural stability, mechanical, electronic, and piezoelectric properties of the 2D monolayer of $ZrSiO_3$ perovskite, extending its potential applications in various fields. Our current research delves into strain-dependent structural parameters of a 2D monolayer of the compound, such as bond length, cohesive energy per atom, strain energy, electronic band structure, the total density of states (TDOS), projected density of states (PDOS), and elastic properties.

2. Computational detail

We used the Quantum ESPRESSO code [20] to study the mechanical stability, elastic anisotropy, electronic and piezoelectric properties of the 2D ZrSiO3 monolayer. This code employs pseudo-potential plane--wave approaches based on density functional theory (DFT) principles [21]. We adopt the generalized gradient approximation (GGA) in the scheme of the updated correlation functional PBESOL for electronic exchange-correlation [22,23]. Ultra-soft Vanderbilt-type pseudopotentials were used to implement the interaction between valence electrons and atomic cores [24]. In this computational study, a cutoff energy of 70 Ry was assigned to the plane-wave basis set. For surface calculations, a $12 \times 12 \times 1$ k-point mesh using the Monkhorst-Pack method was employed [25], with a $2 \times 2 \times 1$ grid used for 20-atom unit cells. The total energy calculations were systematically improved until convergence was achieved within 10^{-6} eV. The integration of bands at the Fermi level utilized the Fermi distribution function, incorporating a smearing parameter set at 0.2 eV. A consistent energy cutoff of 560 Ry was applied for charge density throughout the process. For monolayer materials, a 15 Å vacuum gap was introduced between adjacent layers. The structure is fully optimized for the ionic positions until the forces on all atoms are less than 0.01 eV/Å. Elastic constants for the 2D $ZrSiO_3$ monolayer were determined by inducing finite distortions and calculating the corresponding total energies at various strain levels. The determination of the piezoelectric stress coefficients (e_{ij}) was performed using the DFPT method [26].

3. Results and discussion

3.1. Structural properties

The cubic lattice configuration of the $ZrSiO_3$ perovskite consists of a network of corner-sharing BX_6 octahedra, with Zirconium (Zr) as large spheres at corners, silicon (Si) as the blue sphere in the center of the cube, and smaller red spheres representing oxygen anions forming the octahedral structure [Fig. 1(a)]. The respective material is found to be structurally and mechanically stable under different configurations when subjected to pressure in the range (0–100 GPa) [27]. A 2D crystal structure simply involves a connection between the BX_6 and the shared X anions in a single plane [Fig. 1(b)]. The general formula for 2D layered perovskites is $A'_mA_{n-1}B_nX_{3n+1}$, where A′ can be a divalent cation for $m = 1$ or a monovalent cation for $m = 2$, forming either a bilayer or monolayer. The parameter n represents the thickness of the layer or the number of layers of metal halide sheets. The surfaces of two-dimensional perovskite materials are enclosed by cations, with the lateral dimension ranging from a few hundred nanometers to a micrometer.

The stacking order in 2D monolayer configurations of $ZrSiO_3$ is significantly affected by the physical arrangement of the constituent particles. Crystal formations have well-defined stacking patterns, and $ZrSiO_3$ has several stacking orders. Perovskite structures, including 2D monolayer perovskite, have complex stacking arrangements that are determined by the arrangement of cations (A and B) and anions (X) in the crystal lattice. The ABC-type stacking sequence utilized in the simple cubic perovskite structure is frequently represented in scientific notation as [0 0 1], which indicates the stacking order in a particular direction. Octahedral stacking generates a layered structure characterized by a combination of B and X ions in octahedral layers, with A ions situated in between these layers.

The estimated values of Zr–O, Si–O and Zr–Si bond lengths (in Å) are found to be (2.5688, 2.5175, 2.4662, 2.4149), (1.9268, 1.8882, 1.8494, 1.8112) and (3.1821, 3.1206, 3.0462, 2.9367) at strain values of 0 %, −2%, −4% and −6%, respectively. These results reveal that when a compressional strain is applied within the material, strain forces the atoms closer together. Hence, the bond lengths between the atoms or molecules decreased [Fig. 2(a)]. Moreover, the calculated values of bond lengths (in Å) are found to be (2.5688, 2.6201, 2.6717, 2.7216), (1.9268, 1.9653, 2.0038, 2.0413) and (3.1821, 3.2083, 3.2347, 3.2647) at tensile strain values of 0 %, 2 %, 4 %, and 6 % respectively. These results corresponded that when the material is subjected to tensile strain, it causes the atoms or molecules to move farther apart from each other, and hence the bond lengths increase [Fig. 2(a)].

Cohesive energy is computed by subtracting the energies of each constituent atom from the total energy of the compound. The cohesive energy of a monolayer of $ZrSiO_3$ is calculated using the relation [28].

$$E_{coh} = E_{tot} - \sum_i n_i E_i \quad (1)$$

Where E_{coh} is the cohesive energy, E_{tot} is the total energy of the 2D monolayer, n_i is the total number of atoms and E_i is the total energy of an isolated i^{th} atom.

The cohesive energy trend in response to various strains offers valuable insights into the mechanical stability of the $ZrSiO_3$ monolayer. Strain-free systems are the most stable, as indicated by the observed

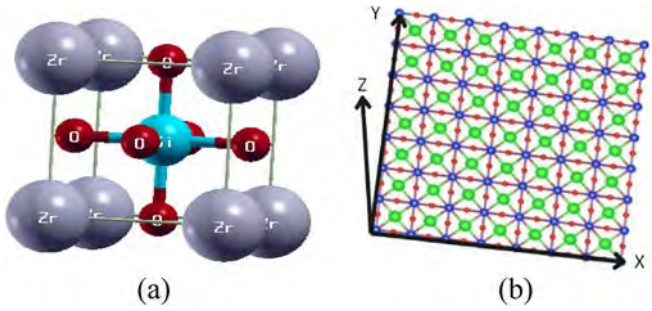

Fig. 1. (a) Unit cell of bulk $ZrSiO_3$ and (b) 2D monolayer of $ZrSiO_3$ perovskite.

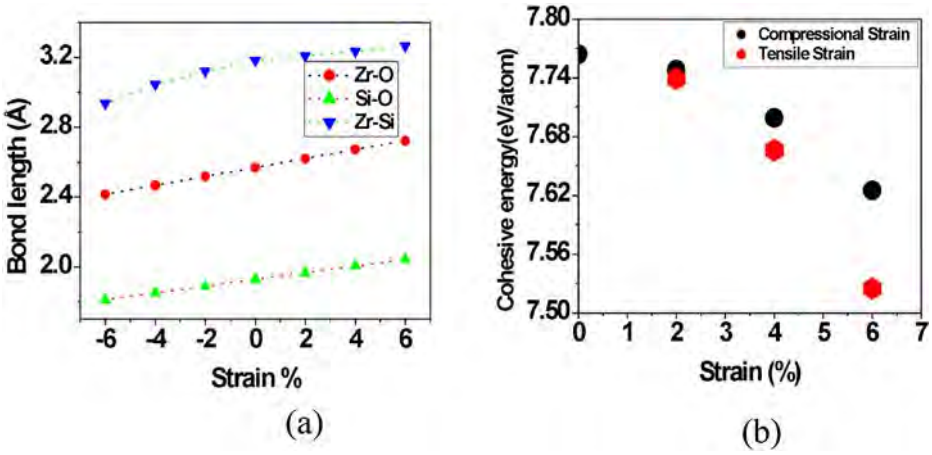

Fig. 2. (a) Variation of bond length and (b) cohesive energy with applied strain.

value of the cohesive energy of the material at 0 % strain (−7.764 eV/atom). In comparison to tensile strain, compressive strain shows less variation in cohesive energy [Fig. 2(b)]. Furthermore, the consistent values of cohesive energy per atom at −2% (−7.748 eV/atom) and +2 % (−7.743eV/atom) strains convey that the preferred material shows a symmetrical response to tension and compression strains [Fig. 2(b)].

3.1.1. Strain energy

The concept of strain energy provides valuable insights into how strain affects the structural and elastic properties of materials. The strain energy per atom (E_s) is expressed as [29]:

$$E_s = \frac{[E_{tot} - E_0]}{n} \quad (2)$$

where E_s denotes the strain energy per atom, E_{tot} stands for the total energy of the system under strain, E_o represents the total energy in the absence of strain and n denotes the number of atoms in the unit cell.

The uniaxial strain (ε_i) along a and b are systematically varied in an incremental manner of 2 % from −6% to +6 % as tension and compression strains. Fig. 3 illustrates the strain energy versus strain curves for strain types a and b. The curves demonstrate a monotonic increase in strain energy with increasing strain for both compressive and tensile stresses within the investigated range. Within the strain range of −2% to +2 %, the material exhibits behavior consistent with the harmonic approximation, following Hooke's Law. This implies a linear relationship between stress and strain. However, beyond this range, the strain energy versus strain curves deviate from harmonic behavior, suggesting the influence of higher-order terms in the strain energy expression. Fig. 3 reveals that both uniaxial a-strain and b-strain have similar effects on strain energy. However, the curve for the a-direction exhibits a smaller area under the strain energy (E_s) vs. strain curve. This

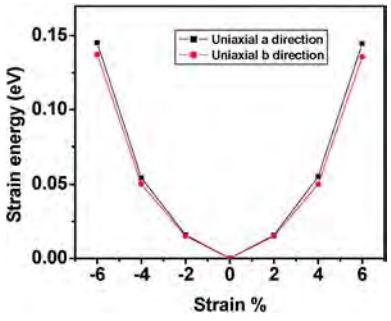

Fig. 3. Variation of strain energy of a 2D monolayer of $ZrSiO_3$ with applied strain.

observation suggests that the material is more stable under strain applied in the a-direction within the specified strain range. Additionally, it confirms that the equilibrium condition without applied strain ($\varepsilon = 0$) corresponds to the minimum energy state for the monolayer. This highlights the inherent stability of the unstrained configuration.

3.2. Electronic properties

This study investigates how strain affects the band gap of a two-dimensional $ZrSiO_3$ monolayer. We accomplish this by computing the partial density of states (PDOS) and analyzing spin-polarized electronic band structures. The electronic band structure analysis is conducted within the first Brillouin Zone along the high-symmetry directions Γ - X - M − Y - Γ, as illustrated in Fig. 4 (a). The symmetry observed in both the spin-up and spin-down band structures indicates the absence of magnetic characteristics [Fig. 4 (b)]. This symmetry suggests that the material is non-magnetic. Similarly, the symmetry observed in the partial density of states (PDOS) plot [Fig. 4(b)] further supports this conclusion. In magnetic materials, PDOS typically exhibits asymmetry due to the presence of magnetic moments. Therefore, the consistent symmetry in the PDOS further confirms the non-magnetic behavior of the material under study.

When subjected to tensile strain, the bandgap of the material expands from 2.29 eV to 2.59 eV. Conversely, the bandgap decreases from 2.29 eV to 1.87 eV under equivalent compressive strain [Figure (5)]. Under tensile strain, the bond length increases which reduces the overlap of orbitals. This has a different effect on the conduction band minimum (CBM) and valence band maximum (VBM). More precisely, the energy of the conduction band minimum (CBM) drops at a faster rate compared to the energy of the valence band maximum (VBM), which leads to a narrower bandgap. On the other hand, when subjected to compressive strain, the length of bonds reduces. Additionally, the energies of the conduction band minimum (CBM) and valence band maximum (VBM) change at different rates when the bandgap decreases. Therefore, the band structure is not consistently affected by the observed changes in bond length under different strain conditions [Fig. 6(a)] [30]. Due to its wide and tunable band gap semiconducting character, this material could be helpful in the design of strain-sensitive devices, optoelectronics [31,32], and flexible electronics.

From the total density of states (TDOS) plot in the energy range of −2 eV to +6 eV, we can observe a notable change in the peak of the conduction band minimum (CBM) in response to applied strain. As tensile strain increases from 0 % to +6 % [Fig. 6 (b)], the CBM peak gradually shifts towards the Fermi level, indicating a reduction in the bandgap. Under tensile strain, the reduction in band gap will likely occur due to the increased overlap of atomic orbitals and the

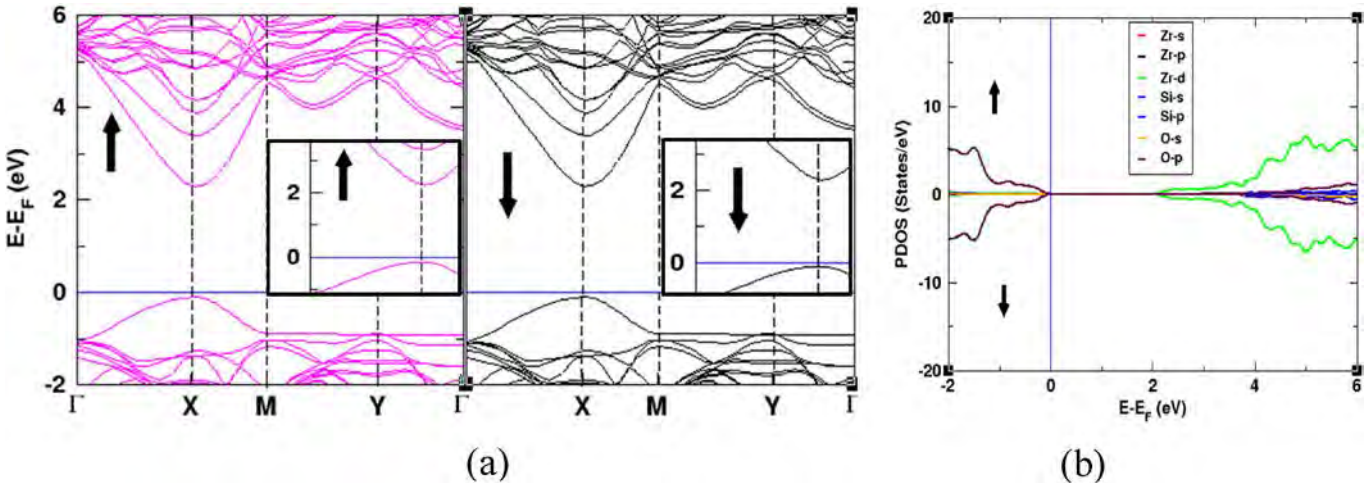

Fig. 4. (a) Band structure of spin-up and spin-down (left and right side) and, (b) the partial density of states (PDOS) of a 2D monolayer of $ZrSiO_3$.

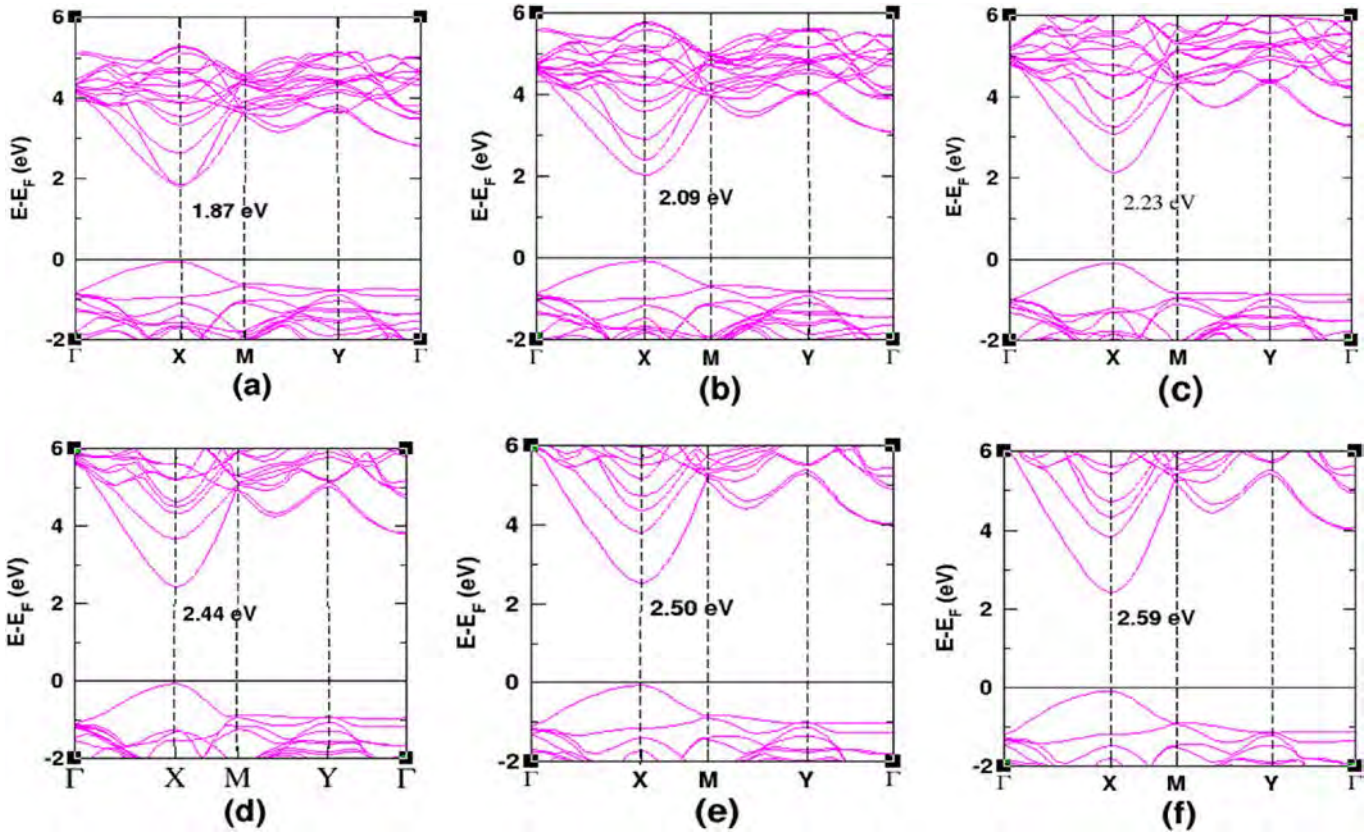

Fig. 5. Band structure of $ZrSiO_3$ monolayer at different strains (a) 6 %, (b) 4 %, (c) 2 %, (d) −2%, (e) −4%, and (f) −6%.

delocalization of electrons. Conversely, as compressional strain increases from 0 % to −6% [Fig. 6 (c)], the CBM peak shifts away from the Fermi level, leading to an increase in the band gap. Under compression strain, electrons move farther apart in atomic orbitals, and orbital overlap decreases. This results in an increase in the band gap. These trends can be seen in both the density of states and band structure calculations, demonstrating the significant impact of strain on the electronic properties of the material.

3.3. Mechanical properties of 2D monolayer $ZrSiO_3$

The formula for calculating elastic constants is as follows [33].

$$C_{ij} = \frac{1}{S_0}\left(\frac{\partial^2 E_s}{\partial\varepsilon_i \partial\varepsilon_j}\right) \tag{3}$$

Where, E_s, ε, and S_0 represent the strain energy, the applied strain, and the area of the strain-free monolayer, respectively. To examine the mechanical strength and stability of the 2D monolayer of $ZrSiO_3$, second-order elastic constants (C_{ij}) are computed using the finite distortion method [34]:

$$\begin{bmatrix}\sigma_1\\ \sigma_2\\ \sigma_6\end{bmatrix} = \begin{bmatrix}C_{11} & C_{12} & 0\\ C_{12} & C_{22} & 0\\ 0 & 0 & C_{66}\end{bmatrix}\begin{bmatrix}\varepsilon_1\\ \varepsilon_2\\ \varepsilon_6\end{bmatrix} \tag{4}$$

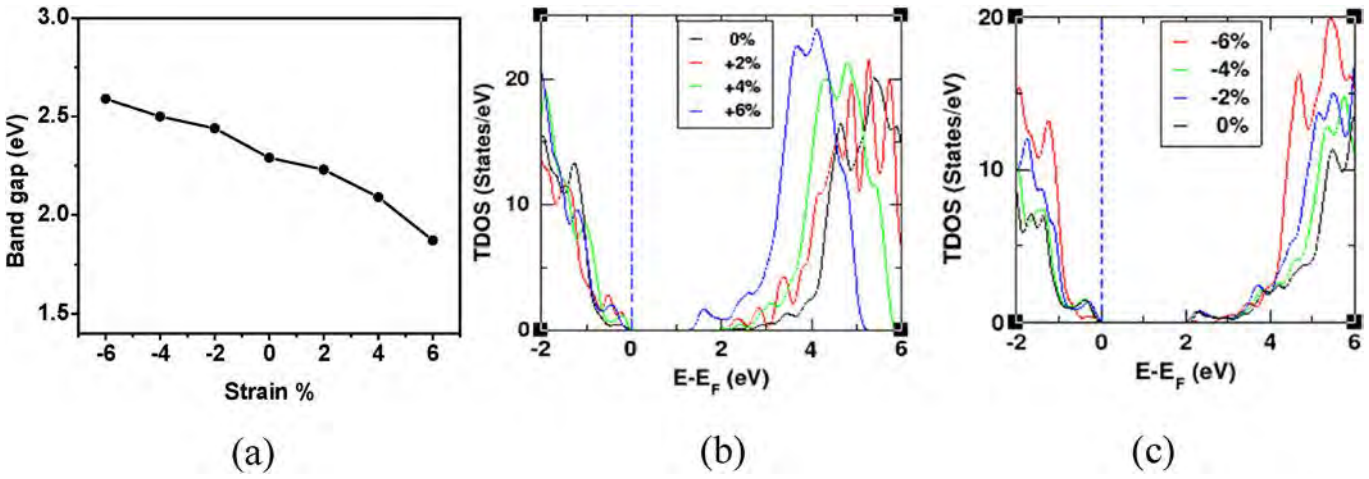

Fig. 6. (a) Variation of bandgap with strain, (b) TDOS plot with tensile strain (c) TDOS Plot with compressive strain for $ZrSiO_3$ monolayer.

For this crystal symmetry of the 2D square lattice, only C_{11}, C_{22}, C_{12}, and C_{66} are identified as significant independent elastic stiffness constants [35]. These constants are pivotal in assessing the mechanical strength criteria [36], namely

$$\left(C_{11}C_{22} - C_{12}^2\right) > 0 \text{ and } C_{66} > 0. \tag{5}$$

The expression for the total energy E as a function of strain for this crystal system is as follows:

$$\mathrm{E} = \frac{1}{2}\left(C_{11}\epsilon_{xx}^2 + C_{22}\epsilon_{yy}^2 + 2\,C_{12}\epsilon_{xx}\,\epsilon_{yy} + 2C_{66}\epsilon_{xy}^2\right) \tag{6}$$

Two-dimensional Young's modulus (Y_b and Y_b) along (100) and (010) directions are computed using the expressions [37]:

$$Y_a = \frac{\left(C_{11}^2 - C_{12}^2\right)}{C_{11}} \text{ and } Y_b = \frac{\left(C_{22}^2 - C_{12}^2\right)}{C_{11}}, \tag{7}$$

The corresponding Poisson's ratios are expressed as:

$$\nu_{xy} = \frac{C_{12}}{C_{11}} \text{ and } \nu_{yx} = \frac{C_{12}}{C_{22}} \tag{8}$$

Ranganathan [40], and Kube [41] anisotropy coefficients. For this purpose, the following expressions are used to determine the Voigt [42] and Reuss [43] estimated bulk (K^V and K^R) and shear moduli (G^V and G^R):

$$K^V = \frac{(C_{11}+C_{22}+2C_{12})}{4}, \tag{10(a)}$$

$$G^V = \frac{(C_{11}+C_{22}-2C_{12}+4C_{66})}{8}, \tag{10(b)}$$

$$K^R = \frac{1}{(S_{11}+S_{22}+2S_{12})}, \tag{10(c)}$$

$$G^R = \frac{1}{(S_{11}+S_{22}-2S_{12}+S_{66})}, \tag{10(d)}$$

In this case, S_{ij} represents the compliance matrix that is reciprocal to the C_{ij} matrix [44].

Additionally, the following expressions are used to compute additional mechanical anisotropy indices:

$$A^{SU} = \left(\left[\frac{1}{4}(C_{11}+C_{22}+2C_{12})(S_{11}+S_{22}+2S_{12}) - 1\right]^2 + 2\left[\frac{1}{16}(C_{11}+C_{22}-2C_{12}+4C_{66})\left(S_{11}+S_{22}-2S_{12}+S_{66}\right]^2\right)^{\frac{1}{2}} \tag{11(a)}$$

respectively, and the 2D shear modulus is:

$$\mathrm{G} = C_{66} \tag{9}$$

Subsequently, the in-plane stiffness (layer modulus) K, equivalent to the bulk modulus, and shear modulus G are given as a function of the Poisson's ratio ν and the 2D Young's modulus Y^{2D} [38]:

$$\mathrm{K} = \frac{Y^{2D}}{2(1-\nu)}, \text{and } \mathrm{G} = \frac{Y^{2D}}{2(1+\nu)} \tag{10}$$

Where the bulk modulus signifies resistance to compression, and the layer modulus represents the resistance of a 2D material to stretching. Stiffness, in this context, quantifies a material's resistance to elastic deformation.

In addition, Li's elastic anisotropy measurement methodologies [39] are utilized to compute the mechanical anisotropy. For mechanical anisotropy measurement, we specifically examine the universal,

$$A^{Ranganathan} = \frac{K^V}{K^R} + 2\,\frac{G^V}{G^R} - 3 \geq 0, \tag{11(b)}$$

$$A^{Kube} = \sqrt{\left(ln\frac{K^V}{K^R}\right)^2 + 2\left(ln\frac{G^V}{G^R}\right)^2}, \tag{11(c)}$$

Anisotropy is closely related to both Young's modulus Y and Poisson's ratio v of a material. These values are functions of the angles of direction θ. Which can be formulated as [45].

$$Y(\Theta) = \frac{\left[\,C_{11}C_{22} - C_{12}^2\,\right]}{\left[\,C_{22}\,cos^4(\Theta) + Acos^2(\Theta)sin^2(\Theta) + C_{11}\,sin^4(\Theta)\,\right]}, \tag{12}$$

$$\nu(\Theta) = \frac{\left[\,C_{12}\,cos^4(\Theta) - Bcos^2(\Theta)sin^2(\Theta) + C_{12}\,sin^4(\Theta)\,\right]}{\left[\,C_{22}\,cos^4(\Theta) + Acos^2(\Theta)sin^2(\Theta) + C_{11}\,sin^4(\Theta)\,\right]}, \tag{13}$$

Table 1
Calculated values of elastic stiffness coefficient (C_{ij}), elastic modulus (Y, K, G), Poisson's ratio (υ), and mechanical stability condition of $ZrSiO_3$ 2D monolayer.

Strain%	C_{ij} (N/m)				Y (N/m)		ν (N/m)		K (N/m)		Stability Yes/No
	C_{11}	C_{22}	C_{12}	$C_{66} = G_{xy}$	Y_a	Y_b	ν_a	ν_b	K_a	K_b	
6	156.74	139.01	49.92	77.02	140.84	107.39	0.318	0.349	103.25	82.48	Yes
4	158.57	141.41	50.39	78.65	142.56	110.09	0.317	0.356	104.36	85.48	Yes
2	169.52	148.82	52.24	80.73	153.42	114.55	0.308	0.351	100.85	88.29	Yes
0	196.52	159.82	59.63	81.33	178.43	111.88	0.303	0.373	127.99	88.22	Yes
−2	205.04	165.13	56.79	82.04	189.31	117.26	0.277	0.344	130.92	89.37	Yes
−4	211.04	171.53	57.39	82.54	195.43	123.81	0.272	0.334	134.27	92.95	Yes
−6	219.52	186.08	59.92	83.73	203.16	141.38	0.273	0.322	139.73	104.26	Yes

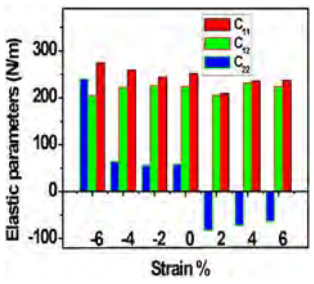

Fig. 7. Variation of elastic constants C_{ij} of a 2D monolayer of $ZrSiO_3$ with applied strain.

$$\frac{1}{G(\Theta)} = [S_{11}+S_{22}-S_{12}]cos^2(\Theta)sin^2(\Theta)+\frac{1}{4}S_{66}\left[cos^4(\Theta)+sin^4(\Theta) - 2\,cos^2(\Theta)sin^2(\Theta)\right] \quad (14)$$

where,

$$A=\frac{(C_{11}C_{22}-C_{12}^2)}{C_{66}}-2C_{11} \text{ and } B=C_{11}+C_{22}-\frac{(C_{11}C_{22}-C_{12}^2)}{C_{66}}. \quad (15)$$

The calculated values of elastic constants under zero strain [Table 1] are close to those reported for single-layer B_2SSe whereas they deviate significantly from those of α-Ga_2S_3 monolayer and α-Ga_2Se_3 monolayer [46,47]. Our calculations reveal a significant influence of strain on the elastic properties of the 2D $ZrSiO_3$ monolayer (see Fig. 7). Values for strains exceeding ±6 % are not reported due to mechanical instability in Table (1). Young's moduli (Y_a and Y_b) increase with increasing compressive strain, indicating a stiffening effect on the material under compression. Conversely, tensile strain leads to a decrease in Young's moduli, signifying a reduction in stiffness. The observed difference between Y_a and Y_b under both compressive and tensile strain highlights the anisotropic behavior of the monolayer. Specifically, under a uniform strain ranging from −6% to 6 %, Y_a continuously decreases from 203.16 N/m to 140.84 N/m. Similarly, Y_b decreases from 141.38 N/m to 107.39 N/m within this strain range. The bulk moduli (K_a and K_b) increase with compressive strain, indicating a stronger resistance to volume deformation under pressure. Conversely, tensile strain has the opposite effect, and reduces the material's resistance. The shear modulus typically increases with compressive strain, signifying higher resistance to shear deformation under compression. In contrast, tensile strain decreases shear modulus, implying a lower resistance to shear deformation under tension. Poisson's ratio values remain near 0.3 for both tensile and compressive strains, suggesting ductility and potential for use in biomedical devices due to their adaptability and flexibility. Notably, under a uniform tensile strain of 0 %–6 %, the calculated values of Poisson's ratio gradually increase from 0.303 to 0.318. This trend indicates lateral expansion tendencies within the material under tensile strain, suggesting potential applications in strain-sensitive sensors.

Table 2 presents the anisotropy indexes, which provide valuable insights into the anisotropic elastic behavior of the $ZrSiO_3$ monolayer. The calculated non-negative values for both $A^{Ranganathan}$ and A^{Kube} indicate the present material has mechanical stability and a high degree of anisotropy. According to Ranganathan's and Kube's rules, these positive values indicate that the $ZrSiO_3$ monolayer satisfies the mechanical stability criteria. The Polar plots (Fig. 8) graphically demonstrate its anisotropic nature and mechanical stability. These mechanical stability and anisotropy characteristics suggest that the $ZrSiO_3$ monolayer along the [010] direction, with the highest Young's modulus emerging as a highly promising candidate for diverse applications across various fields, including biomedical devices, electronics, advanced materials engineering, and even aerospace engineering.

3.3.1. *Piezoelectricity*

Piezoelectric materials, like $ZrSiO_3$, play a crucial role in various devices such as power generators, actuators, sensors, and switches. These materials exhibit a unique property where they can generate electric charges under mechanical strain due to their anisotropic crystallographic properties. The complex relationship between the polarization tensor (P_i), stress tensor (σ_{jk}), and strain tensor (ε_{jk}) can be described by the third-rank piezoelectric tensors (e_{ijk}) and (d_{ijk}) [48,49] as:

$$d_{ijk}=\frac{dP_i}{d\sigma_{jk}} \quad (16)$$

$$e_{ijk}=\frac{dP_i}{d\varepsilon_{jk}} \quad (17)$$

where the stress tensor, strain tensor, and polarization tensor are denoted by σ_{jk}, ε_{jk}, and P_i, respectively. By utilizing the stress-strain relationships and Voigt notation [Eq. (4)], we can simplify the equations further as:

Table 2
Elastic anisotropy, together with the Voigt and Reuss estimated bulk (K^V, K^R) and shear (G^V, G^R) moduli of the $ZrSiO_3$ 2D monolayer at different strains.

Strain%	G^V	G^R	K^V	K^R	A^{SU}	$A^{Ranganathan}$	A^{Kube}
6	62.998	59.729	98.898	98.497	0.188	0.114	0.033
4	64.225	60.847	100.190	99.820	0.186	0.115	0.033
2	67.098	64.144	105.705	105.204	0.181	0.097	0.028
0	70.300	68.093	118.900	117.479	0.175	0.077	0.020
−2	73.094	71.477	120.938	119.386	0.169	0.058	0.015
−4	74.744	73.449	124.338	122.880	0.167	0.047	0.012
−6	77.585	76.787	131.360	130.382	0.162	0.028	0.007

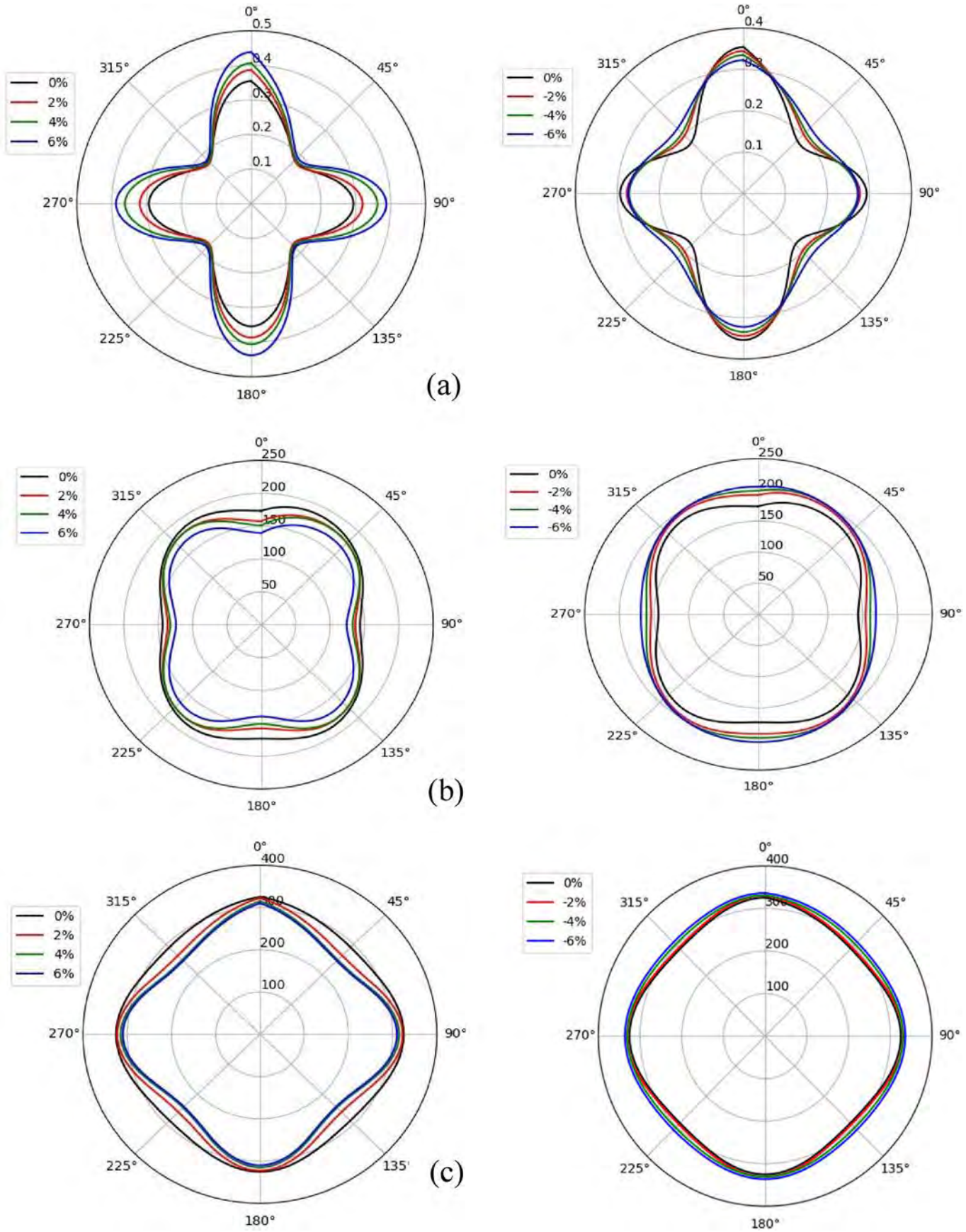

Fig. 8. The orientation dependent (a) Poisson's ratio, (b) Young's modulus, and (c) shear modulus for a 2D monolayer of $ZrSiO_3$ under tensile and compressional strains.

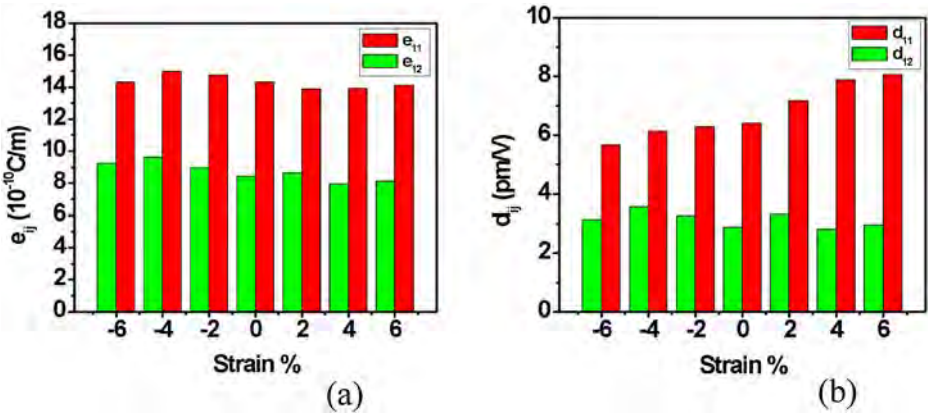

Fig. 9. Calculated (a) piezoelectric stress (e_{ij}) and (b) piezoelectric strain (d_{ij}) coefficients of a 2D monolayer of $ZrSiO_3$ with applied strain.

Table 3
Calculated values of the elastic constants C_{ij} (N/m), piezoelectric coefficients e_{ij} (10^{-10} C/m), and d_{ij} (pm/V) of $ZrSiO_3$ monolayer.

Strain%	C_{ij} (N/m)				e_{ij} ($\times 10^{-10}$ C/m)		d (pm/V)	
	C_{11}	C_{22}	C_{12}	C_{66}	e_{11}	e_{12}	d_{11}	d_{12}
6	156.74	139.01	49.92	77.02	14.12	8.13	8.07	2.95
4	158.57	141.41	50.39	78.65	13.92	7.95	7.88	2.81
2	169.52	148.82	52.24	80.73	13.89	8.67	7.17	3.31
0	196.52	159.82	59.63	81.33	14.31	8.43	6.41	2.88
−2	205.04	165.13	56.79	82.04	14.77	8.97	6.29	3.26
−4	211.04	171.53	57.39	82.54	14.98	9.62	6.13	3.56
−6	219.52	186.08	59.92	83.73	14.32	9.24	5.66	3.14

$$e_{ijk} = d_{ijk}.C_{jk} \tag{18}$$

where C_{jk} denotes elastic stiffness coefficients. Furthermore, the expressions for piezoelectric strain coefficients (d_{11}, d_{12}) in terms of independent elastic constants (C_{11}, C_{22}, C_{12}, C_{66}) and piezoelectric coefficients (e_{11}, e_{12}) are derived as [50,51]:

$$d_{11} = \frac{e_{11}C_{22} - e_{12}C_{12}}{(C_{11}C_{22} - C_{12}^2)} \tag{19}$$

$$d_{12} = \frac{e_{12}C_{11} - e_{11}C_{12}}{(C_{11}C_{22} - C_{12}^2)}. \tag{20}$$

The calculated data reveals some interesting trends, the piezoelectric coefficients (e_{ij}) generally increase with increasing positive strain percentages (tensile strain), Table 3 and Fig. 9(a). This indicates an enhanced ability of the material to convert mechanical energy into electrical energy under tension. Notably, the piezoelectric strain coefficient (d_{11}) demonstrates a significant rise under tensile strain, with values increasing from 6.41 p.m./V at 0 % strain to 8.07 p.m./V at 6 % tensile strain. These values are comparable to those observed in group IV transition-metal dichalcogenides [52] and are significantly larger than the value for α-quartz (2.3 p.m./V) [53]. Conversely, as the compressive strain increases, the value of d_{11} decreases due to the diminishing effect of compression on piezoelectricity, Fig. 9 (b). This strain-dependent behavior of the $ZrSiO_3$ 2D monolayer offers valuable insights for designing future high-performance piezoelectric devices.

4. Conclusions

The key findings of the study are summarized below.

i. The cohesive energy of the 2D monolayer exhibits optimal stability under strain-free conditions and responds symmetrically to −2% and +2 % strain values.
ii. The material shows linear elastic behavior up to ±2 % strain (harmonic region), then deforms plastically (inharmonic region).
iii. Electronic properties display strain-sensitive behavior, with the band gap decreasing under tensile strain and increasing under compressive strain.
iv. The material remains mechanically stable and ductile under applied strain conditions from −6% to +6 % and indicates lateral expansion under tensile strain.
v. Under tensile strain, the material demonstrates enhanced piezoelectricity that enables the efficient transformation of mechanical energy into electrical energy

CRediT authorship contribution statement

P. Pokharel: Writing – original draft, Software, Resources, Investigation, Formal analysis, Conceptualization. **S.K. Yadav:** Writing – review & editing, Validation, Project administration, Investigation, Formal analysis, Data curation. **N. Pantha:** Writing – review & editing, Supervision, Methodology, Investigation. **D. Adhikari:** Writing – review & editing, Validation, Supervision.

Declaration of competing interest

The authors declare that they have no known competing financial interests or personal relationships that could have appeared to influence the work reported in this paper.

Data availability

Data will be made available on request.

References

[1] Q.A. Akkerman, L. Manna, What defines a halide perovskite, ACS Energy Lett. 5 (2020) 604, https://doi.org/10.1021/acsenergylett.0c00039.

[2] X. Zhao, T. Liu, Y.L. Loo, Advancing 2D perovskites for efficient and stable solar cells: challenges and opportunities, Adv. Mater. 34 (2022) 2105849, https://doi.org/10.1002/adma.202105849.

[3] A.G. Ricciardulli, S. Yang, J.H. Smet, M. Saliba, Emerging perovskite monolayers, Nat. Mater. 20 (2021) 1325–1336, https://doi.org/10.1038/s41563-021-01029-9.

[4] R. Uppuluri, A.S. Gupta, A.S. Rosas, T.E. Mallouk, Soft chemistry of ion-exchangeable layered metal oxides, Chem. Soc. Rev. 47 (2018) 2401–2430, https://doi.org/10.1039/C7CS00290D.

[5] L. Mao, C.C. Stoumpos, M.G. Kanatzidis, Two-dimensional hybrid halide perovskites: principles and promises, J. Am. Chem. Soc. 141 (2018) 1171–1190, https://doi.org/10.1021/jacs.8b10851.

[6] G. Grimaldi, L.S.D. Antony, L. Helmbrecht, A. van der Weijden, S.W. van Dongen, I. Schuringa, et al., Microstructuring of 2D perovskites via ion-exchange fabrication, Appl. Phys. Lett. 119 (2021) 223102, https://doi.org/10.1063/5.0065070.

[7] J. Yadav, Q. Liang, S. Pan, Electrochemical deposition of organometallic halide perovskite single-crystal particles with density gradients and their stability, fluorescence, and Photoelectrochemical properties, J. Phys. Chem. C 124 (2020) 10659–10668, https://doi.org/10.1021/acs.jpcc.0c01536.

[8] B.P. Kore, J.M. Gardner, Water-resistant 2D lead (II) iodide perovskites: correlation between optical properties and phase transitions, Mater. Adv. 1 (2020) 2395–2400, https://doi.org/10.1039/D0MA00577K.

[9] X. Liu, L. Cao, Z. Guo, Y. Li, W. Gao, L. Zhou, A review of perovskite photovoltaic materials' synthesis and applications via chemical vapor deposition method, Materials 12 (2019) 3304, https://doi.org/10.3390/ma12203304.

[10] K.G. Brooks, M.K. Nazeeruddin, Laser processing methods for perovskite solar cells and modules, Adv. Energy Mater. 11 (2021) 2101149, https://doi.org/10.1002/aenm.202101149.

[11] D.T. Gangadharan, D. Ma, Searching for stability at lower dimensions: current trends and prospects of layered perovskite solar cells, Energy Environ. Sci. 12 (2019) 2860–2889, https://doi.org/10.1039/C9EE01591D.

[12] Y.I. Dolzhenko, T. Inabe, Y. Maruyama, In situ X-ray observation on the intercalation of weak interaction molecules into perovskite-type layered crystals $(C_9H_{19}NH_3)_2Pb_{I4}$ and $(C_{10}H_{21}NH_3)_2CdC_{l4}$, Bull. Chem. Soc. Jap. 59 (1986) 563–567, https://doi.org/10.1246/bcsj.59.563.

[13] D.B. Mitzi, C.A. Feild, W.T.A. Harrison, A.M. Guloy, Conducting tin halides with a layered organic-based perovskite structure, Nature 369 (1994) 467–469, https://doi.org/10.1038/369467a0.

[14] A. Kojima, K. Teshima, Y. Shirai, T. Miyasaka, Organometal halide perovskites as visible-light sensitizers for photovoltaic cells, J. Am. Chem. Soc. 131 (2009) 6050–6051, https://doi.org/10.1021/ja809598r.

[15] L. Dou, A.B. Wong, Y. Yu, M. Lai, N. Kornienko, S.W. Eaton, et al., Atomically thin two-dimensional organic-inorganic hybrid perovskites, Science 349 (2015) 1518–1521, https://doi.org/10.1126/science.aac7660.

[16] S.O.A. Ahmad, A. Ashfaq, M.U. Akbar, M. Ikram, K. Khan, F. Wang, et al., Application of two-dimensional materials in perovskite solar cells: recent progress, challenges, and prospective solutions, J. Mater. Chem. C 9 (2021) 14065–14092, https://doi.org/10.1039/D1TC02407H.

[17] S.-B. Chen, Z.-Y. Zeng, X.-R. Chen, X.-X. Yao, Strain-induced electronic structures, mechanical anisotropy, and piezoelectricity of transition-metal dichalcogenide monolayer CrS_2, J. Appl. Phys. 128 (2020) 125111, https://doi.org/10.1063/5.0022429.

[18] X. Song, F. Hui, T. Knobloch, B. Wang, Z. Fan, T. Grasser, M. Lanza, Piezoelectricity in two dimensions: graphene vs. molybdenum disulfide, Appl. Phys. Lett. 111 (2017) 083107, https://doi.org/10.1063/1.5000496.

[19] K.A.N. Duerloo, M.T. Ong, E.J. Reed, Intrinsic piezoelectricity in two-dimensional materials, J. Phys. Chem. Lett. 3 (2012) 2871–2876, https://doi.org/10.1021/jz3012436.

[20] P. Giannozzi, et al., Quantum espresso: a modular and open-source software project for quantum simulations of materials, J. Phy. Cond. Matt. 21 (2009) 395502, https://doi.org/10.1088/0953-8984/21/39/395502.

[21] J.P. Perdew, K. Burke, M. Ernzerhof, Generalized gradient approximation made simple, Phys. Rev. Lett. 77 (1996) 3865, https://doi.org/10.1103/PhysRevLett.77.3865.

[22] D.C. Langreth, J.P. Perdew, Theory of nonuniform electronic systems. I. Analysis of the gradient approximation and a generalization that works, Phys. Rev. B 21 (1980) 5469, https://doi.org/10.1103/PhysRevB.21.5469.

[23] J.P. Perdew, A. Ruzsinszky, G.I. Csonka, O.A. Vydrov, G.E. Scuseria, L. A. Constantin, X. Zhou, K. Burke, Phys. Rev. Lett. 100 (2008), https://doi.org/10.1103/PhysRevLett.100.136406, 136406-1-136406-4.

[24] G. Kresse, D. Joubert, From ultrasoft pseudopotentials to the projector augmented-wave method, Phys. Rev. B 59 (1999) 1758, https://doi.org/10.1103/PhysRevB.59.1758.

[25] H.J. Monkhorst, J.D. Pack, Special points for brillouin-zone integrations, Phys. Rev. B 13 (1976) 5188–5192, https://doi.org/10.1103/PhysRevB.13.5188.

[26] X. Wu, D. Vanderbilt, D.R. Hamann, Systematic treatment of displacements, strains, and electric fields in density-functional perturbation theory, Phys. Rev. B 72 (2005) 035105, https://doi.org/10.1103/PhysRevB.72.035105.

[27] P. Pokharel, S.K. Yadav, N. Pantha, D. Adhikari, First-principles investigations of structural, electronic, and elastic properties of $ZrSiO_3$ perovskite: layer dependence, surface termination, and pressure effects, Phys. Status Solidi B (2024) 2400156, https://doi.org/10.1002/pssb.202400156.

[28] A. Vig, E. Doan, K. Yang, First-principles investigation of size effects on cohesive energies of transition-metal nanoclusters, Nanomaterials 13 (2023) 2356, https://doi.org/10.3390/nano13162356.

[29] L. Huang, Z. Chen, J. Li, Effects of strain on the band gap and effective mass in two-dimensional monolayer GaX (X= S, Se, Te), RSC Adv. 5 (2015) 5788, https://doi.org/10.1039/C4RA12107D.

[30] X. Jiang, Y. Liu, Y. Zang, Y. Liu, T. Gao, N. Zheng, Y. Nie, Uniaxial strain-induced anisotropic bandgap engineering in freestanding $BiFeO_3$ films, Apl. Mater. 10 (2022) 095103, https://doi.org/10.1063/5.0095955.

[31] Deb, U. Sarkar, Boron-nitride and boron-phosphide doped twin-graphene: applications in electronics and optoelectronics, Appl. Surf. Sci. 541 (2021) 148657, https://doi.org/10.1016/j.apsusc.2020.148657.

[32] J. Deb, N.B. Singh, U. Sarkar, Density functional theory study of the electronic and optical properties of Pentagraphyne nanotubes, Phys. Chem. Chem. Phys. 26 (2024) 15484–15493, https://doi.org/10.1039/D3CP06341K.

[33] M. Faghihnasiri, H. Jafari, A. Ramazani, M. Shabani, S.M. Estalaki, R.G. Larson, Nonlinear elastic behavior and anisotropic electronic properties of two-dimensional borophene, J. Appl. Phys. 125 (2019) 145107, https://doi.org/10.1063/1.5079932.

[34] R. Li, Q. Shao, E. Gao, Z. Liu, Elastic anisotropy measure for two-dimensional crystals, Extrem. Mech. Lett. 34 (2020) 100615, https://doi.org/10.1016/j.eml.2019.100615.

[35] Y. Le Page, P. Saxe, Symmetry-general least-squares extraction of elastic data for strained materials from ab initio calculations of stress, Phys. Rev. B 65 (2002) 104104, https://doi.org/10.1103/PhysRevB.65.104104.

[36] F. Mouhat, F.X. Coudert, Necessary and sufficient elastic stability conditions in various crystal systems, Phys. Rev. B 90 (2014) 224104, https://doi.org/10.1103/PhysRevB.90.224104.

[37] S.B. Sharma, R. Bhatta, R. Adhikari, D. Paudyal, Strain-dependent electronic and optical responses of penta-BCN monolayer, Carbon Trends 7 (2022) 100162, https://doi.org/10.1016/j.cartre.2022.100162.

[38] A. Politano, G. Chiarello, Probing Young's modulus and Poisson's ratio in graphene/metal interfaces and graphite: a comparative study, Nano Res. 8 (2015) 1847–1856, https://doi.org/10.1007/s12274-014-0691-9.

[39] R. Li, Q. Shao, E. Gao, Z. Liu, Elastic anisotropy measure for two-dimensional crystals, Extreme Mech. Lett. 34 (2020) 100615, https://doi.org/10.1016/j.eml.2019.100615.

[40] S.I. Ranganathan, M. Ostoja-Starzewski, Universal elastic anisotropy index, Phys. Rev. Lett. 101 (2008) 055504, https://doi.org/10.1103/PhysRevLett.101.055504.

[41] C.M. Kube, M. De Jong, Elastic constants of polycrystals with generally anisotropic crystals, J. Appl. Phys. 120 (2016) 165105, https://doi.org/10.1063/1.4965867.

[42] W. Voigt, A Determination of the Elastic Constants for Beta-Quartz, Lehrbuch de Kristallphysik Terubner, Leipzig, 1928.

[43] A. Reuss, Calculation of the flow limits of mixed crystals based on the plasticity of monocrystals, J. Appl. Math. Mech. 9 (1929) 49.

[44] K.S. Nagy, D.J. Siegel, Anisotropic elastic properties of battery anodes, J. Electrochem. Soc. 167 (2020) 110550, https://doi.org/10.1149/1945-7111/aba54c.

[45] M. Yagmurcukardes, C. Sevik, F.M. Peeters, Electronic, vibrational, elastic, and piezoelectric properties of monolayer Janus MoSTe phases: a first-principles study, Phys. Rev. B 100 (2019) 045415, https://doi.org/10.1103/PhysRevB.100.045415.

[46] X.J. Yan, W.Y. Li, X. Zou, L.L. Liu, S.F. Wang, Y. Wei, L. Hu, Janus B_2XY (X, Y= S, Se, Te) monolayers as piezoelectric materials: a first-principle study, Chem. Phys. Lett. 806 (2022) 140007, https://doi.org/10.1016/j.cplett.2022.140007.

[47] L. Hu, X. Huang, Peculiar electronic, strong in-plane and out-of-plane second harmonic generation and piezoelectric properties of atom-thick α-M_2X_3 (M= Ga, In; X= S, Se): role of spontaneous electric dipole orientations, RSC Adv. 7 (2017) 55034–55043, https://doi.org/10.1039/C7RA11014F.

[48] N. Blonsky, H.L. Zhuang, A.K. Singh, R.G. Hennig, Ab initio prediction of piezoelectricity in two-dimensional materials, ACS Nano 9 (2015) 9885–9891, https://doi.org/10.1021/acsnano.5b03394.

[49] J.F. Nye. Physical Properties of crystaks : their representation by tensors and matrices, Oxford University Press, Oxford, 1985.

[50] S.D. Guo, Y.T. Zhu, W.Q. Mu, W.C. Ren, Intrinsic piezoelectricity in monolayer MSi2N4 (M= Mo, W, Cr, Ti, Zr, and Hf), Europhys. Lett. 132 (2020) 57002, https://doi.org/10.1209/0295-5075/132/57002.

[51] Y. Xu, Z. Li, C. He, J. Li, T. Ouyang, C. Zhang, et al., Intrinsic piezoelectricity of monolayer group IV–V MX_2: SiP_2, $SiAs_2$, GeP_2, and $GeAs_2$, Appl. Phys. Lett. 116 (2020), https://doi.org/10.1063/1.5135950.

[52] M.M. Alyoruk, Y. Aierken, D. Çakır, F.M. Peeters, C. Sevik, Promising piezoelectric performance of single layer transition-metal dichalcogenides and dioxides, J. Phys. Chem. C 119 (2015) 23231–23237, https://doi.org/10.1021/acs.jpcc.5b06428.

[53] J. Shi, C. Han, X. Wang, S. Yun, Electronic, elastic and piezoelectric properties of boron-V group binary and ternary monolayers, Physica B: Cond. Matt. 574 (2019) 311634, https://doi.org/10.1016/j.physb.2019.08.011.

RESEARCH ARTICLE | DECEMBER 04 2024

Structural, electronic, optical, magnetic, and mechanical properties of $SmMnO_3$ perovskite with europium and yttrium doping: A first-principles study

Peshal Pokharel ; Shashit Kumar Yadav ; Nurapati Pantha ; Bikash Sharma ; Devendra Adhikari

AIP Advances 14, 125309 (2024)
https://doi.org/10.1063/5.0232439

AIP Advances ARTICLE pubs.aip.org/aip/adv

Structural, electronic, optical, magnetic, and mechanical properties of $SmMnO_3$ perovskite with europium and yttrium doping: A first-principles study

Cite as: AIP Advances 14, 125309 (2024); doi: 10.1063/5.0232439
Submitted: 20 August 2024 • Accepted: 17 November 2024 •
Published Online: 4 December 2024

Peshal Pokharel,[1,2,3] Shashit Kumar Yadav,[2,a)] Nurapati Pantha,[1,a)] Bikash Sharma,[4] and Devendra Adhikari[2,a)]

AFFILIATIONS

[1] Central Department of Physics, Tribhuvan University, Kritipur, Nepal
[2] Department of Physics, Mahendra Morang Adarsha Multiple Campus, Tribhuvan University, Biratnagar, Nepal
[3] Central Campus of Technology, Tribhuvan University, Dharan, Nepal
[4] Department of Electronics and Communication Engineering, Sikkim Manipal Institute of Technology, Sikkim Manipal University, Majitar, Sikkim 737136, India

[a)] Authors to whom correspondence should be addressed: yadavshashit@yahoo.com; mrnurapati@gmail.com; and deven.bmhs@gmail.com

ABSTRACT

This paper explores the impact of europium (Eu) and yttrium (Y) doping on the electronic, magnetic, optical, elastic, and structural properties of $SmMnO_3$ perovskites using the Quantum ESPRESSO code. The cohesive energy and tolerance factor calculations revealed that the perovskite can maintain structural stability up to 25% doping of Eu and Y. Bandgap calculations suggest that when Eu and Y are doped, the energy bandgap of pure $SmMnO_3$ decreases significantly from 2.72 to 0.47 and from 2.72 to 0.76 eV, respectively. Doped $SmMnO_3$ exhibits a UV shift and increased intensity in the absorption coefficient, while the reflectivity peak decreases. These changes in optical properties and bandgap due to Eu and Y doping make $SmMnO_3$ a promising material for advanced applications in photovoltaics, UV photodetectors, and optoelectronic devices. The ferromagnetic property and total magnetic moment of $SmMnO_3$ are found to be increased by Eu doping. Meanwhile, the magnetic moment gets reduced by Y doping. Curie temperature calculations indicate that Eu doping increases the Curie temperature from 255.35 to 314.28 K, while Y doping reduces it from 255.35 to 187.69 K. These changes in magnetic moment and Curie temperature suggest that the doped material is suitable to be used in magnetic sensors and storage devices. The calculated elastic constants, Young's modulus, shear modulus, Poisson's ratio, and B/G ratio suggest that both pristine and doped compounds under study show a ductile behavior.

I. INTRODUCTION

The perovskite having a structure of type ABO_3 is one of the most commonly studied structures in condensed matter physics due to its natural abundance and remarkable properties. The study of structural, elastic, electrical, magnetic, optical, and thermoelectric properties of perovskites is essential for several industrial and biomedical applications.[1–4] These materials are primarily used as high-temperature electric and catalytic superconductors.[5,6] In recent years, the perovskites based on rare earth (RE) metals and their derivative compounds have emerged as exciting research areas. These materials are durable and possess simple crystal structures based on the chemical formula ABO_3, are cost-effective to produce in the laboratory, and exhibit exceptional optoelectronic and thermoelectric properties.[7,8] Samarium manganese oxide ($SmMnO_3$) is a perovskite compound in the RE oxide family and is fabricated by

using the sol-gel method and hydrothermal synthesis.[9,10] Pristine $SmMnO_3$, along with $NdMnO_3$, has been the subject of extensive study due to its remarkable magnetic and electronic transport properties.[11,12] Mahalik *et al.* investigated the oxygen reduction and evolution reactions in $REMnO_3$ (RE = Pr, Nd, Sm, Eu, and Gd) and then discovered that $SmMnO_3$ is more effective at both catalyzing reactions and storing energy.[13] Saad and Alsobhi reported the observation of ferromagnetic half-metallic behavior in the $SmMnO_3$ compound having high electrical conductivity. Their results suggest that $SmMnO_3$ could be useful in high-efficiency solar cells.[14] Butt *et al.* carried out an extensive investigation and explored the optical and spintronic properties of $SmMnO_3$ in greater depth.[15]

When cations of different sizes are substituted for either A or B site, the symmetry of the cubic type Pm3m changes to that of tetragonal, orthorhombic, and monoclinic forms.[16] Since europium (Eu) and yttrium (Y) have the same sizes as Sm, substituting cations of comparable size does not alter the space group but may result in a change in the cell parameters, tilt angles of BO_6 polyhedra, and displacement of A cations.[17] These changes may lead to significant variations in physical properties. Doping of Eu and Y atoms into the $SmMnO_3$ perovskite structure enhances its physical properties, thereby diversifying its potential applications. Due to its unique electronic configuration and magnetic properties, Eu has the potential to modify the basic characteristics of materials. Furthermore, it can alter the structural, thermodynamic, magnetic, and electronic properties of perovskite compounds. Ke *et al.* investigated Sr-doped $SmMnO_3$ as a potential material for converting CO_2 into fuel in a stable and efficient manner at moderate temperatures and under near isothermal conditions.[18] Gao *et al.* examined different doping ratios of Ca- and Al-doped $SmMnO_3$ to improve thermochemical CO_2 splitting performance and solar absorption for more efficient solar-driven CO_2 splitting.[19] In this regard, understanding how Eu and Y doping affects $SmMnO_3$ is crucial for maximizing the material's advantages and utilizing its changes in applications such as magnetoelectric devices, catalysis, and electrical devices.

Meanwhile, Y is a versatile element with industrial significance, often classified as a rare-earth element due to its chemical similarities with lanthanides. This transition metal is not naturally found in its pure form but is commonly found in combination with lanthanides in rare-earth minerals, emphasizing its rarity and importance in various industries.[20] Its unique properties make it valuable for technological advancements, such as in the fabrication of yttrium iron garnet (YIG) with ferrimagnetic characteristics, further expanding its applications in smart materials and magnetic devices.[21] In addition, studies have highlighted the environmental and health implications of yttrium exposure, showcasing the need for a comprehensive understanding of its effects on biological systems.[22]

In the present study, we compared the structural, electrical, magnetic, and mechanical properties of pristine and doped $SmMnO_3$ perovskites using Density Functional Theory (DFT). In addition, we examined the significant impact of Eu and Y doping on the various properties of this cubic perovskite material.

II. COMPUTATIONAL METHOD

In this study, calculations based on density functional theory (DFT)[23,24] were employed, utilizing pseudo-potential plane wave approaches with the Quantum ESPRESSO code.[25] These calculations aimed to investigate the geometrical stability and electronic, optical, mechanical, and magnetic properties of both pristine and substitutional doped $SmMnO_3$. For electron–electron interaction, the Perdew–Burke–Ernzerhof (PBE) functional was chosen,[26] while ultra-soft Vanderbilt-type pseudo-potentials[27] from the official Quantum ESPRESSO site were used for the interaction between valence electrons and atomic nuclei. A kinetic energy cutoff of 70 Ry was employed for the plane wave expansion. The convergence criteria for electronic and ionic relaxations were set at 10^{-6} eV and 10^{-3} eV/Å, respectively. A supercell of dimension 2 × 2 × 2 with 40 atoms was considered to enhance the convergence of the calculations. During the doping procedure, the Sm atom was replaced by one or two atoms of Eu and Y, resulting in an overall impurity content of 12.5% or 25.0%. The magnetic properties of pure and doped $SmMnO_3$ were studied using spin-polarized calculations. The spin-polarized electronic band structures of the compounds were determined using both the Generalized Gradient Approximation (GGA)[28,29] and GGA + U[30] approaches. We employed GGA + U for the partially filled 3d orbitals [$4s^2 3d^5$] in Mn atoms. A Monkhorst–Pack 14 × 14 × 14 k-point sampling mesh was selected for the Brillouin zone.[31] The irreducible tetrahedron method was utilized with a 120-point k-mesh for the integration of reciprocal space. The elastic constants, including second-order elastic tensors, were determined using the strain–stress relation technique based on optimized unit cells.[32]

III. RESULTS AND DISCUSSION

A. Structural properties

$SmMnO_3$ is a perovskite oxide with a general formula of ABO_3, where Sm occupies the A-site and Mn occupies the B-site in the structure. The ideal lattice parameter values for pure $SmMnO_3$ are given as a = b = c = 3.806 Å, indicating a cubic symmetry [Fig. 1(a)]. As the doping level of Eu or Y increases, the crystal lattice contracts, resulting in a decrease in lattice constant (a_o) (3.789 Å at 12.5% Eu, 3.725 Å at 25.0% Eu, 3.746 Å at 12.5% Y, and 3.704 Å at 25.0% Y). This indicates changes in unit cell size due to the replacement of the Sm atom [Fig. 1(b)]. The lattice parameters of both pure and doped $SmMnO_3$ differ noticeably due to the varying atomic radii of Eu, Y, and Sm.

In 1926, Victor Moritz Goldschmidt used the term "tolerance factor" (t) to describe the stability of perovskite ABO_3 structures.[33] It is defined by as follows:

$$t = \frac{r_A - r_O}{\sqrt{2}(r_B + r_O)}, \tag{1}$$

where r_A, r_B, and r_O are the ionic radii of the A-site cation, B-site cation, and oxygen anion, respectively, and for substitutional doping, r_A can be written as $r_A = (1-x)r_{A'} + xr_{A''}$ with $r_{A'}$ being the ionic radius of the initial A-site cation, $r_{A''}$ being the ionic radius of the new A-site cation, and x being the proportion of dopant in the new cation.

For a stable cubic perovskite structure, the tolerance factor lies within the range $0.8 \le t \le 1.0$. Since the atomic radii of Sm, Eu, and Y are very similar, the tolerance factor of pure, Eu-doped, and Y-doped

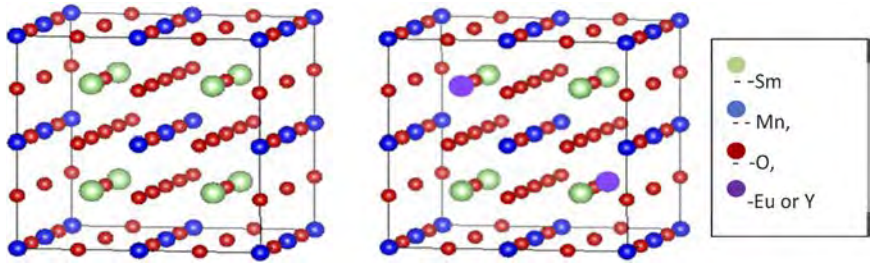

FIG. 1. Supercell of (a) pristine $SmMnO_3$ and (b) Eu- or Y-doped $SmMnO_3$.

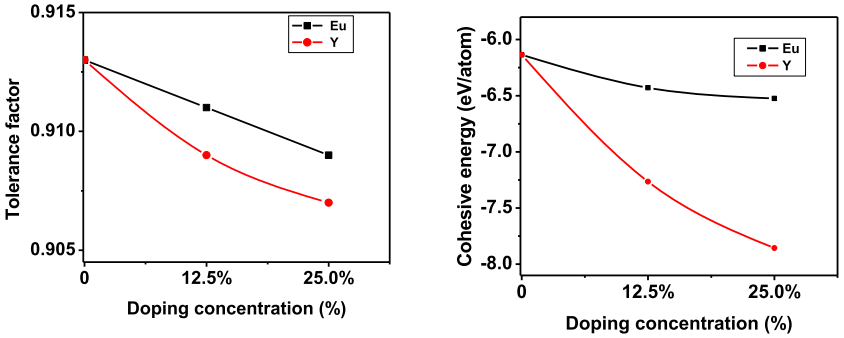

FIG. 2. Variation in the (a) tolerance factor and (b) cohesive energy of Eu- and Y-doped $SmMnO_3$ with doping concentration.

$SmMnO_3$ is about 0.9, which falls within the stability range. As the doping concentration of Eu or Y atoms in $SmMnO_3$ increases, the tolerance factor decreases linearly. The values for pure, 12.5%, and 25% doped with Eu atoms are 0.913, 0.911, and 0.909, respectively, and they drop non-linearly and rapidly with Y doping. The values for pristine, 12.5%, and 25% doped with Y atoms are found to be 0.913, 0.909, and 0.907, respectively [Fig. 2(a)].

The stability of the compound is assessed using cohesive energy, which measures the amount of energy required to break down a molecule into its constituent atoms. For perovskite compounds, the cohesive energy can be expressed as follows:[34]

$$\Delta E = [E_{ABO_3} - (E_A + E_B + E_{O_2})], \quad (2)$$

where E_{ABO_3} is the total energy per atom of the composite material and E_A, E_B, and E_{O_2} are the energies of isolated atoms of the A-site cation, B-site cation, and oxygen atom, respectively.

As the doping concentration of the dopant increases, the corresponding bond length decreases. Consequently, the cohesive energy of Eu- or Y-doped $SmMnO_3$ also increases, with the respective values of 6.135, 6.429, and 6.525 eV/atom for the Eu-doped sample and 6.135, 7.265, and 7.856 eV/atom for the Y-doped sample. These values suggest that the doped $SmMnO_3$ has improved structural stability [Fig. 2(b)]. Given that the atomic radii of the dopant elements (Eu and Y) are comparable to that of Sm, the cohesive energy values and tolerance factor indicate that 0%, 12.5%, and 25% Eu-/Y-doped $SmMnO_3$ is stable.

B. Electronic properties

The energy band structure and density of states (DOS) are two important features for describing the electronic properties of compounds. The GGA and GGA + U approximations are employed to calculate the spin-polarized distribution of pure and doped $SmMnO_3$ band structures along their high-symmetry k-points in the first Brillion zone. The GGA + U approach introduces a Hubbard U

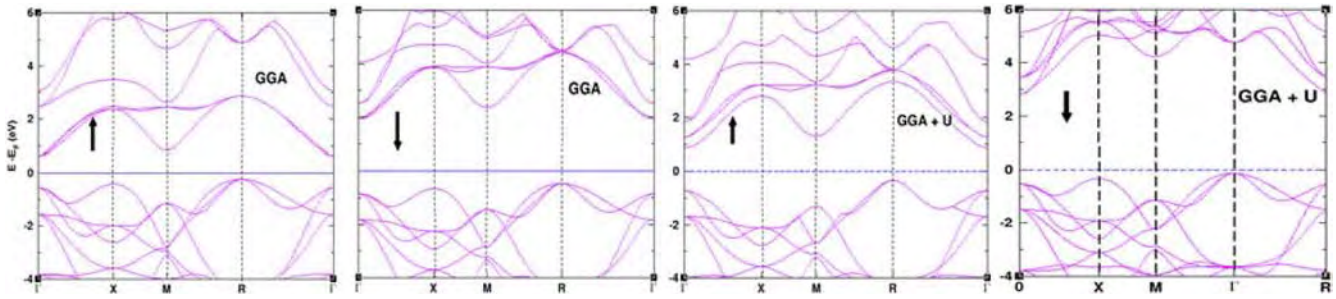

FIG. 3. Band structure of spin-up and spin-down states for pristine $SmMnO_3$ within (a) the GGA and (b) the GGA + U approaches.

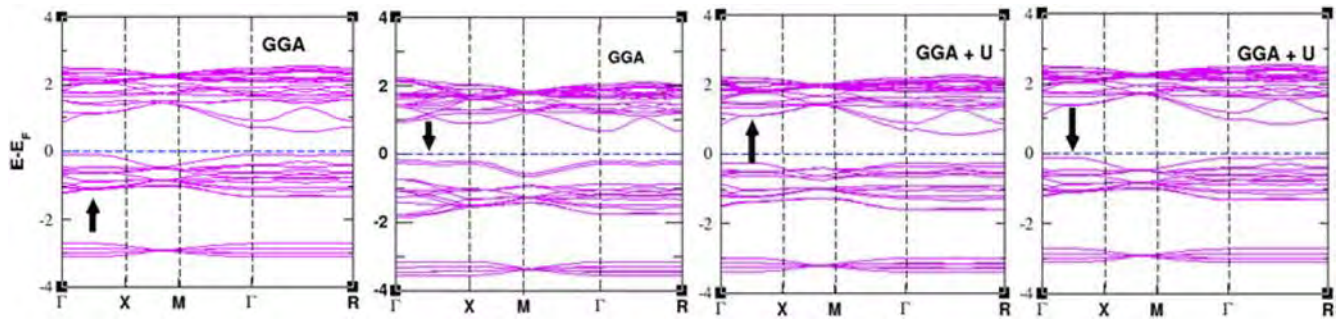

FIG. 4. Band structure of spin-up and spin-down states for 12.5% Eu-doped $SmMnO_3$ within (a) the GGA and (b) the GGA + U approaches.

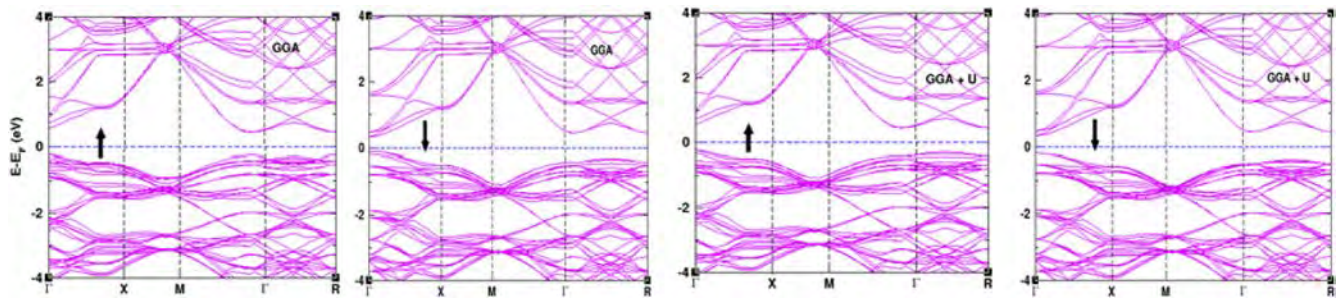

FIG. 5. Band structure of spin-up and spin-down states for 25.0% Eu-doped $SmMnO_3$ within (a) the GGA and (b) the GGA + U approaches.

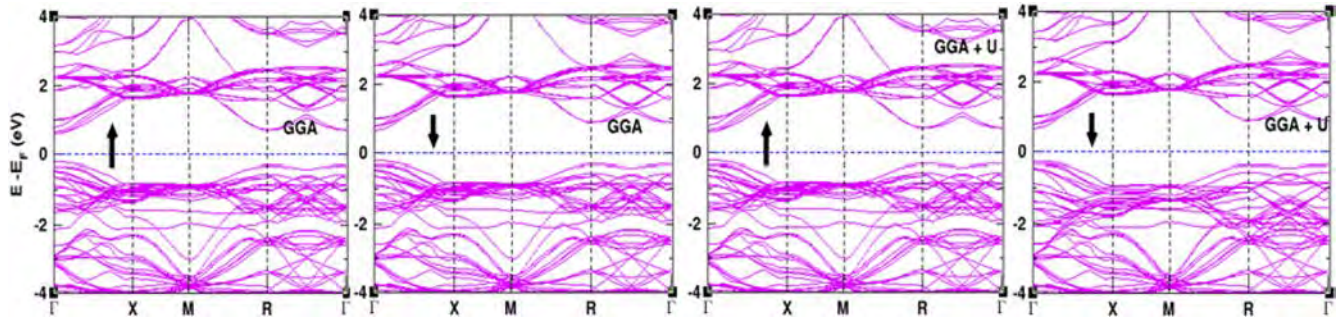

FIG. 6. Band structure of spin-up and spin-down states for 12.5% Y-doped $SmMnO_3$ within (a) the GGA and (b) the GGA + U approaches.

term to better account for localized electron interactions in the partially filled 3d orbitals of Mn and the partially filled 4f orbitals of Eu. By incorporating this term, GGA + U can more accurately describe the spin-polarized band structure and partial DOS (PDOS) of the perovskite.

For pure $SmMnO_3$, the calculated indirect bandgap is 2.31 eV using GGA [Fig. 3(a)] and 2.72 eV using GGA + U [Fig. 3(b)] and close to the experimental value of 2.8 eV.[14] When Eu ($[Xe]4f^7 6s^2$) is doped on $SmMnO_3$, the partially filled 4f orbital of Eu can lead to strong electron–electron and magnetic interactions. The new energy states interact with the existing electronic structure of $SmMnO_3$, resulting in a decrease in the bandgap. The bandgap shrinks to 1.03 eV at a doping level of 12.5% Eu [Figs. 4(a) and 4(b)]. When 25% Eu is added, the bandgap shrinks to 0.40 eV under both spin-up and spin-down conditions [Figs. 5(a) and 5(b)]. This indicates significant changes in the electrical structure for both the GGA and GGA + U methods. Similarly, for the partially filled 4d orbital of yttrium ($[Kr]4d^1 5s^2$) in pristine $SmMnO_3$, the electronic bandgap is found to be 1.30 eV at a doping level of 12.5% [Figs. 6(a) and 6(b)] and 0.76 eV at the 25.0% doping level of Y for both the GGA and GGA + U methods [Figs. 7(a) and 7(b)].

The PDOS analysis indicates that Sm-3d, Mn-3d, and O-2p play a dominant role in pristine $SmMnO_3$ [Figs. 8(a) and 8(b)]. In the spin-up scenario, the Sm-d and O-p states contribute most significantly to the valence band, while in the spin-down scenario,

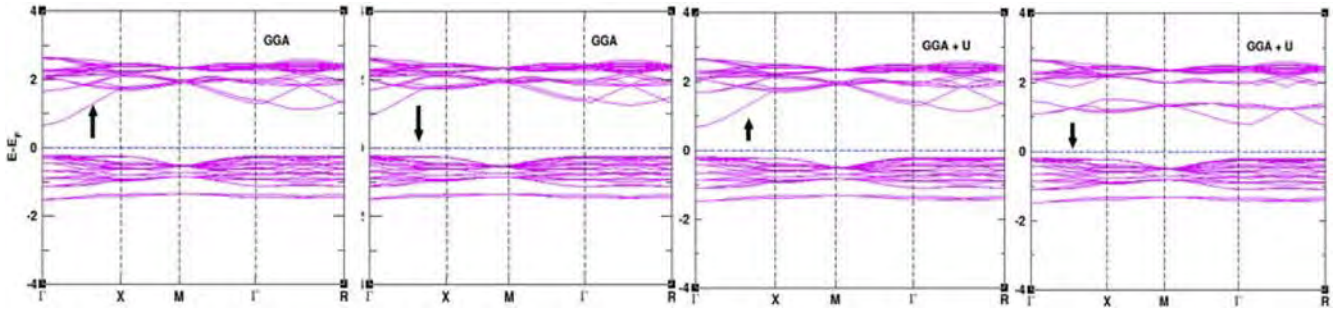

FIG. 7. Band structure of spin-up and spin-down states for 25.0% Y-doped $SmMnO_3$ within (a) the GGA and (b) the GGA + U approaches.

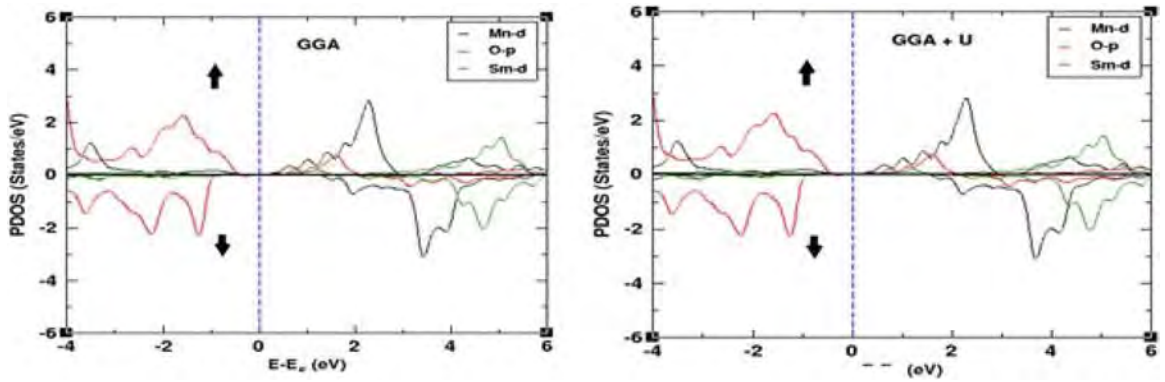

FIG. 8. PDOS of spin up and down states for pristine $SmMnO_3$ within (a) the GGA and (b) the GGA + U approaches.

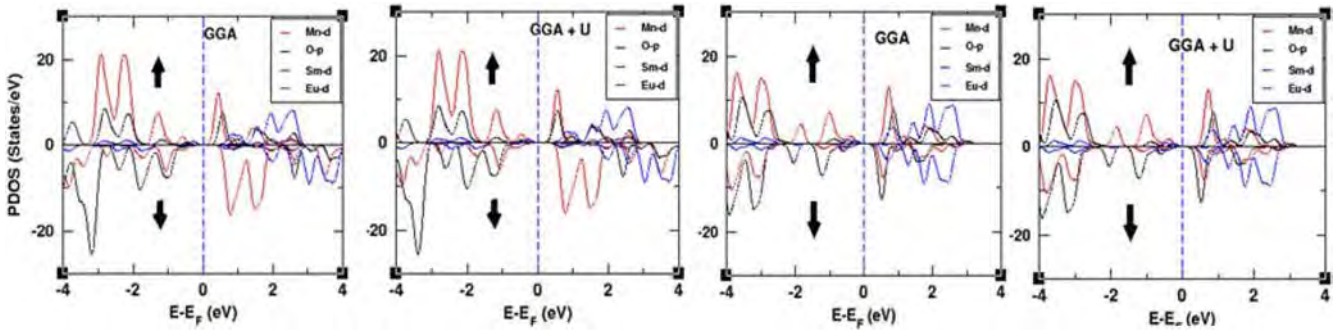

FIG. 9. PDOS of spin-up and spin-down states: (a) GGA for 12.5% Eu-doped, (b) GGA + U for 12.5% Eu-doped, (c) GGA for 25.0% Eu-doped, and (d) GGA + U for 25.0% Eu-doped $SmMnO_3$.

the Mn-d states contribute most significantly to the conduction band. After Eu doping, the O-p and Mn-d states to the valence and conduction bands decrease with increasing levels of doping of Eu [Figs. 9(a)–9(d)]. Similar phenomena are observed with varying levels of doping of Y [Figs. 10(a)–10(d)]. These results indicate that doping of $SmMnO_3$ with Eu and Y can reduce the bandgap or enhance its tunable bandgap capacity, thereby improving the potential applications of the material in various disciplines.

C. Optical properties

For a better understanding of the electronic properties of pristine and doped $SmMnO_3$, it is essential to examine their optical

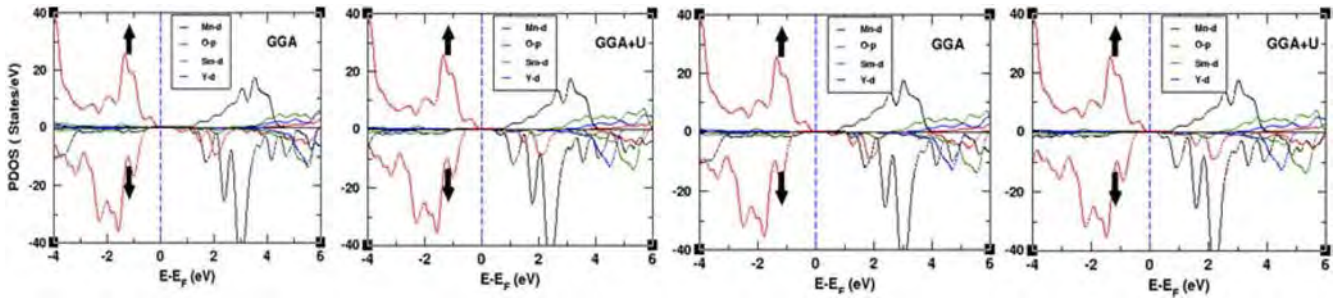

FIG. 10. PDOS of spin-up and spin-down states: (a) GGA for 12.5% Y-doped, (b) GGA + U for 12.5% Y-doped, (c) GGA for 25.0% Y-doped, and (d) GGA + U for 25.0% Y-doped $SmMnO_3$.

behavior. The interaction of these materials with light provides valuable insights into their potential applications. Fundamental optical parameters, such as the absorption coefficient, refractive index, and dielectric function, are critical in evaluating their viability for various optoelectronic technologies, such as solar cells, LEDs, and lasers. These characteristics not only affect how efficiently these materials can convert light into energy or emit light but also influence their overall performance in high-efficiency devices. Thus, studying these optical properties is essential for optimizing the practical applications of pristine and doped $SmMnO_3$ compounds. The dielectric function provides a comprehensive description of a material's optical and electronic behavior, capturing how it interacts with electromagnetic fields across different energy ranges. This function is crucial to understanding inter-band electronic transitions, which occur when electrons move between different energy bands in response to incident light.

The connection between the dielectric function and the wave vector or leap matrix allows for the determination of the dispersion relationship of dielectric functions.[35] The dielectric function is represented by the following equation:[36]

$$\varepsilon(\omega) = \varepsilon_1(\omega) + i\varepsilon_2(\omega). \tag{3}$$

The imaginary component of the dielectric function, $\varepsilon_2(\omega)$, is calculated using the following formula:[37]

$$\varepsilon_2(\omega) = \frac{8\pi^2 e^2}{2\omega^2 m^2} \sum_n \sum_{n'} \int_{BZ} |P_{nn'}(k)|^2 f_{kn}(1 - f_{kn'}) \times \partial\left(E_n^k - E_{n'}^k - h\omega\right) \frac{\partial^3 k}{2\pi^3}. \tag{4}$$

Here, f_{kn} represents the Fermi–Dirac distribution function, while $P^v_{nn'}(k)$ denotes the projection of the momentum dipole matrix elements on the direction of the field v for the initial and final states. The symbol $E_n^k(k)$ represents the energy of an individual electron, with m being the mass of the electron and e being the charge of the electron.

The real component of the dielectric function, $\varepsilon_1(\omega)$, can be calculated using the following expression obtained from the Kramers–Kronig transformation:[38]

$$\varepsilon_1(\omega) = 1 + \frac{2}{\pi} P \int_0^{\infty} \left[\frac{\omega' \varepsilon_2(\omega')}{\omega'^2 - \omega^2} \right] d\omega'. \tag{5}$$

Here, $\varepsilon_1(\omega)$ illustrates the ability of the material to disperse and polarize light, which in turn affects its refraction and the shift of light waves. In contrast, the imaginary part, $\varepsilon_2(\omega)$, represents the capacity of the material to absorb light energy. These properties collectively affect the efficiency of material in converting light to energy and its application in high-efficiency optoelectronic devices.

The linear optical properties, such as absorption coefficient $\alpha(\omega)$, refractive index $n(\omega)$, and reflectivity $R(\omega)$, are described by the following equations:

$$\alpha(\omega) = \sqrt{2\omega \sqrt{\{\varepsilon_1(\omega)\}^2 + \{\varepsilon_2(\omega)\}^2} - \varepsilon_1(\omega)}, \tag{6}$$

$$n(\omega) = \sqrt{\frac{1}{2} \sqrt{\{\varepsilon_1(\omega)\}^2 + \{\varepsilon_2(\omega)\}^2} + \varepsilon_1(\omega)}, \tag{7}$$

$$R(\omega) = \left| \frac{\sqrt{\varepsilon_1(\omega) + i\varepsilon_2(\omega)} - 1}{\sqrt{\varepsilon_1(\omega) + i\varepsilon_2(\omega)} + 1} \right|^2. \tag{8}$$

The values for various optical parameters, calculated over a photon energy range of 0–30 eV, are illustrated in Figs. 11(a)–11(e). They provide detailed insights into the behavior of the material's optical properties across this energy spectrum. At static frequency, the value of $\varepsilon_1(0)$ provides knowledge about the polarization response of the material at various doping levels, with values of 2.96 for pristine $SmMnO_3$, 2.55 for 12.5% Eu-doped, 2.50 for 25.0% Eu-doped, 2.18 for 12.5% Y-doped, and 2.05 for 25.0% Y-doped $SmMnO_3$. These changes in polarization behavior support the reduction in the electronic bandgap of Eu/Y-doped $SmMnO_3$. As photon energy increases, the peaks in $\varepsilon_1(\omega)$ for Eu- and Y-doped $SmMnO_3$ occur around 5.0 eV, while for the pristine material, the peak energy is at 1.45 eV. The lower energy peak at 1.45 eV suggests that the pristine material interacts strongly with longer wavelength light,

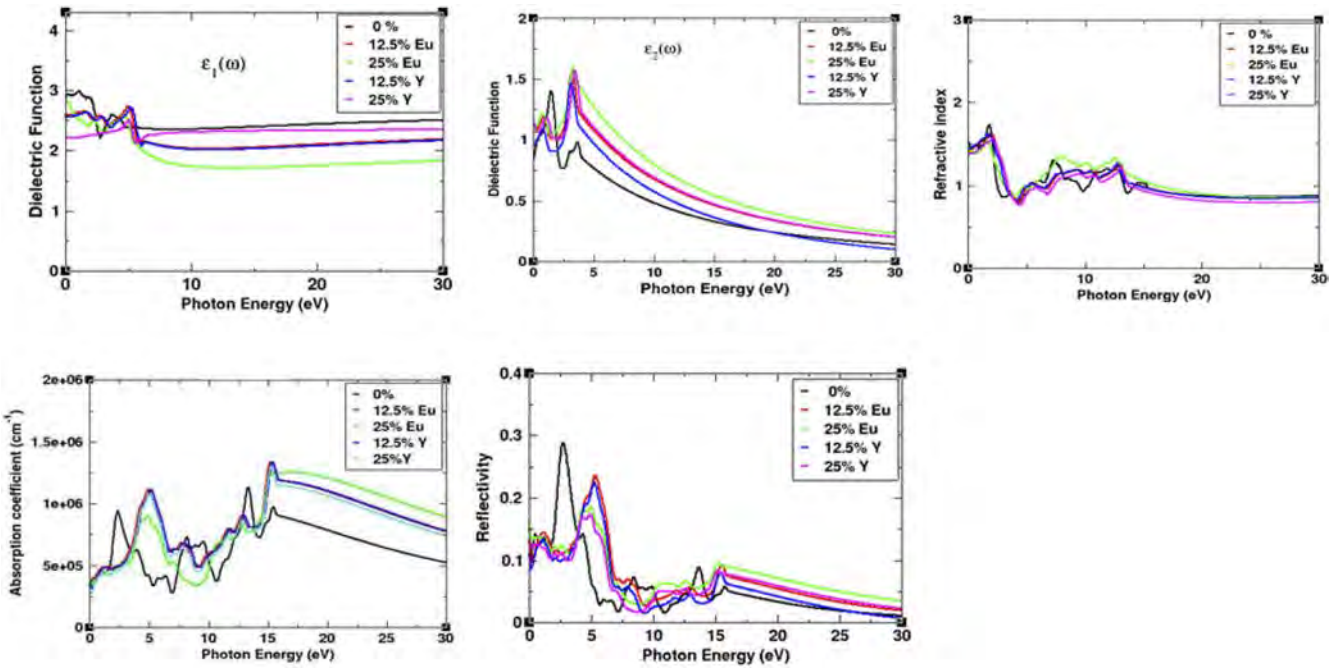

FIG. 11. Variation in the (a) real and (b) imaginary parts of the dielectric function, (c) refractive index, (d) absorption coefficient, and (e) reflectivity of pure and Eu-/Y-doped $SmMnO_3$.

corresponding to visible or near-infrared light. In contrast, the higher energy peak at 5.0 eV indicates that the doped material exhibits maximum polarizability at a much higher energy, corresponding to ultraviolet light. This suggests potential applications in UV filtering, optoelectronics, or high-frequency applications, as discussed in Sec. III B on electronic properties.

Figure 11(c) shows the trends of the refractive index $n(\omega)$ with photon energy, and it follows a trend similar to that of $\varepsilon_1(\omega)$. Furthermore, the refractive index decreases with Eu/Y doping on $SmMnO_3$, which reflects how doping affects the optical characteristics of the material.

Figure 11(b) shows that both Eu-doped $SmMnO_3$ and Y-doped $SmMnO_3$ exhibit an initial increase in the $\varepsilon_2(\omega)$ spectrum, which indicates efficient photon absorption at lower energies. This initial rise can be attributed to electronic transitions from the localized f orbitals of Eu or the d orbitals of Y to unoccupied states that involve the Mn-3d and O-2p orbitals, thereby enhancing the absorption behavior of the material. After this initial increase, a subsequent decrease in $\varepsilon_2(\omega)$ is observed for both Eu-/Y-doped materials, a behavior commonly observed in small bandgap semiconductors. This decrement suggests that at higher photon energies, electronic transitions to higher energy states become less favorable due to the saturation of available states or the reduced probability of such transitions.

The reflectivity spectrum of pristine and Eu-/Y-doped $SmMnO_3$, as shown in Fig. 11(e), provides valuable insights into the reflection and transmission properties of light. At zero energy, the reflectivity of both pristine and doped materials is relatively low, around 0.1, indicating that these materials have a moderate ability to reflect light in the absence of external energy. This suggests that, at lower energies, the materials primarily absorb light rather than reflecting it. At higher energies, the reflectivity of the materials also rises, with distinct peaks appearing in the spectra. For the pristine $SmMnO_3$, the reflectivity peak of 0.3 is observed at ~2.34 eV. In contrast, the Eu-doped $SmMnO_3$ and Y-doped $SmMnO_3$ show a reflectivity peak of 0.22 at 5.1 eV for both dopants. This indicates that pristine $SmMnO_3$ is more effective at reflecting light at lower energies, while the doped variants demonstrate enhanced reflectivity at higher photon energies. The low reflectivity at lower energies makes these materials suitable for light absorption in photovoltaic applications, while the peak reflectivity at higher energies suggests potential for use in optoelectronics.

The absorption coefficient measures how efficiently a material absorbs light as photon energy increases. Both pristine and doped $SmMnO_3$ exhibit significant absorption once photon energy exceeds their respective bandgaps. A peak appears around 15 eV for both doped and pristine material, with a slightly higher intensity in the doped variants. This peak is attributed to inter-band transitions, where photons with sufficient energy excite electrons from the valence band to the conduction band, thereby increasing absorption. As shown in Fig. 11(d), doping with Eu and Y shifts this peak to higher photon energies, reduces the bandgap, and introduces localized states near both the valence band maximum and conduction band minimum. These trends highlight the potential of doped $SmMnO_3$ materials for optoelectronic applications, where their

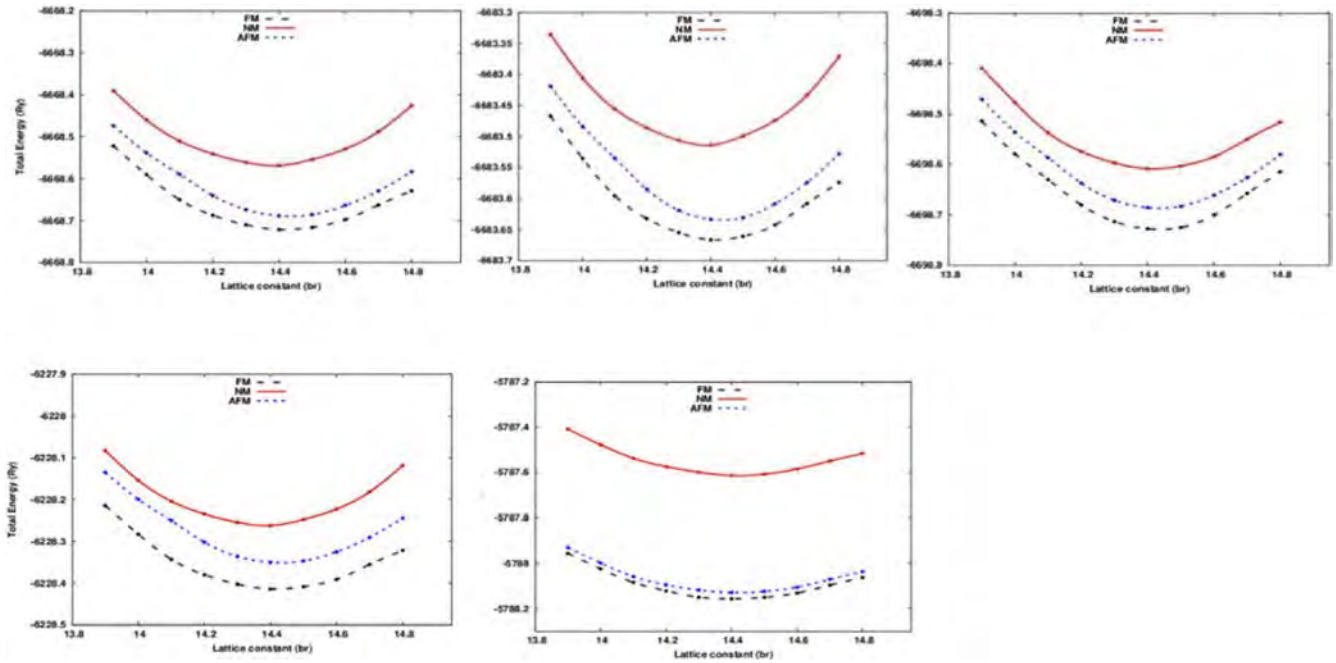

FIG. 12. Energy vs lattice constant plots of (a) pristine, (b) 12.5% Eu-doped, (c) 25.0% Eu-doped, (d) 12.5% Y-doped, and (e) 25.0% Y-doped $SmMnO_3$ at different magnetic configurations.

tunable absorption characteristics could be utilized for advanced technologies.

D. Magnetic properties

Using structure optimization based on Birch–Murnaghan's equation of state,[39] this study thoroughly investigates the magnetic properties of the $SmMnO_3$ compounds with varying levels of Eu and Y doping. The equilibrium volume vs energy curve for pure and doped compounds in the non-magnetic, ferromagnetic, and antiferromagnetic phases has been used to determine the optimized lattice constant. Figures 12(a)–12(e) clearly illustrate that the FM (ferromagnetic) configuration is the most stable phase for all compounds, and the ground state energies associated with these phases are presented in Table II. These results indicate that the ferromagnetic phase is the most stable magnetic phase across all doping levels.

Eu with partially filled 4f orbitals is typically paramagnetic[40] and alters the magnetic properties of $SmMnO_3$ when introduced as a dopant, inducing ferromagnetic characteristics. Similarly, Y, in its pure state, is also paramagnetic; however, its incorporation into $SmMnO_3$ leads to the emergence of ferromagnetic properties. This modification arises from specific interactions between the partially filled d orbital of manganese (Mn) and the f orbital of samarium (Sm), as well as the partially filled f orbital of europium or the partially filled d orbital of yttrium. These interactions can align magnetic moments in parallel, enhancing magnetization and inducing a ferromagnetic state. Consequently, doping of both europium and yttrium into $SmMnO_3$ significantly alters its magnetic properties and enhances its ferromagnetic behavior.

The GGA + U method incorporates an additional Hubbard U parameter that specifically addresses the strong electron–electron interactions within the partially filled d and f orbitals. This correction improves the accuracy of the estimated magnetic moments by better representing the localization of electrons in these orbitals. As a result, the GGA + U method provides a more accurate and reliable presentation of the magnetic properties of materials such as Eu-doped $SmMnO_3$. It yields ~10% greater magnetic moments at each site and for the total magnetic moment compared to the GGA method. In contrast, for Y-doped $SmMnO_3$, there is no significant change in the total magnetic moment between the GGA and GGA + U methods. Spin–orbit coupling (SOC) is a quantum mechanical phenomenon where the orbital motion of electrons around the nucleus interacts with their spin. In our study, we observed negative orbital moments at the Mn and Eu sites, indicating that the orbital contribution opposes the spin contribution, which in turn affects the overall magnetic properties. Incorporating SOC with the GGA + U method is essential for accurately calculating magnetic properties. It effectively accounts for magnetic anisotropy, provides a realistic description of materials with significant electron correlation and relativistic effects, and offers a comprehensive and precise representation of the magnetic behavior and electronic structure of the material. For pristine $SmMnO_3$, the magnetic moment of the Mn site calculated using the GGA + U + SOC method is 3.583 μ_B, with a negative orbital moment of −0.9847 μ_B. This indicates a strong ferromagnetic moment with a notable reduction in

TABLE I. Calculated total magnetic moment (M_{Tot}) and atomic magnetic moment of each site within Sm (M_{Sm}), Mn (M_{Mn}), Eu (M_{Eu}), Y(M_Y), and O (M_O), obtained using the GGA, GGA + U, and GGA + U + SOC approaches of $SmMnO_3$ with different doping levels of Eu and Y.

Configuration	Compound	M_{Sm} (μ_B)	M_{Eu} (μ_B)	M_Y (μ_B)	M_{Mn} (μ_B)	M_O (μ_B)	M_{Tot} (μ_B)
GGA	Bulk $SmMnO_3$	0.0111	⋯	⋯	2.9352	0.0543	3.620
	12.5% Eu doped	0.0115	0.0122	⋯	2.9412	0.0558	3.661
	25% Eu doped	0.0115	0.0121	⋯	2.9573	0.0548	3.767
	12.5% Y doped	0.0112	⋯	0.0134	2.5070	0.0542	3.248
	25.0% Y doped	0.0111	⋯	0.0131	2.5008	0.0544	3.224
GGA + U	Bulk $SmMnO_3$	0.0111	⋯	⋯	3.2763	0.0019	4.000
	12.5% Eu doped	0.0185	0.0192	⋯	3.2923	0.0052	4.045
	25.0% Eu doped	0.0184	0.0194	⋯	3.2928	0.0048	4.081
	12.5% Y doped	0.0144	⋯	0.0139	2.5262	0.0547	3.248
	25.0% Y doped	0.0113	⋯	0.0137	2.5176	0.0549	3.229
GGA + U + SOC	Bulk $SmMnO_3$	0.0111	⋯	⋯	3.583/−0.9847	0.0019	3.886
	12.5% Eu doped	0.0185	0.0192	⋯	3.849/−0.4299	0.0052	3.908
	25.0% Eu doped	0.0184	0.0192	⋯	3.855/−0.4532	0.0048	3.916
	12.5% Y doped	0.0144		0.0139	2.572/−0.0423	0.0547	3.234
	25.0% Y doped	0.0113		0.0137	2.441/−0.014 43	0.0549	3.207

TABLE II. Calculated ground state energy (E_O) in the PM, FM, and AFM phases of $SmMnO_3$ with different doping levels of Eu and Y.

Compounds	Non-magnetic phase (Ry)	Ferromagnetic phase (Ry)	Antiferromagnetic phase (Ry)	$\Delta E = (\mathbf{E_{FM}} - \mathbf{E_{AFM}})$ (Ry)	Curie temperature (K)
Bulk $SmMnO_3$	−6667.3857	−6668.6942	−6668.6591	0.0351	255.35
12.5% Eu doped	−6682.6319	−6683.7510	−6683.7141	0.0369	268.63
25% Eu doped	−6697.2358	−6698.6994	−6698.6562	0.0432	314.28
12.5% Y doped	−6227.8531	−6228.3948	−6228.3635	0.0313	227.70
25% Y doped	−5787.6143	−5788.1557	−5788.129 94	0.0258	187.69

the orbital moment due to SOC. For Eu-doped $SmMnO_3$, the magnetic moments for 12.5% and 25.0% Eu doping are 3.849 and 3.855 μ_B, respectively, with the corresponding negative orbital moments of −0.429 and −0.4532 μ_B. In the case of Y-doped $SmMnO_3$, the magnetic moments for 12.5% and 25.0% Y doping are 2.572 and 2.441 μ_B, respectively, with the corresponding negative orbital moments of −0.0423 and −0.0144 μ_B. Here, the negative orbital moment indicates the antiparallel alignment of the orbital moment with the spin moment, which reduces the total magnetic moment and influences the magnetic behavior of the material.

When Eu is added to $SmMnO_3$, the overall magnetic moment, as well as the magnetic moment at each site of the compound, increases under all three approximations (GGA, GGA + U, and GGA + U + SOC) [Table I]. This increase occurs because Eu, with a partially filled f orbital, replaces the Sm atom in $SmMnO_3$. The additional electrons interact with Mn through a super-exchange interaction, which improves the alignment of magnetic moments and increases the overall magnetic properties of the material. In contrast, yttrium ($[Kr]4d^15s^2$) does not contribute additional magnetic electrons when it replaces samarium in $SmMnO_3$. This substitution can disrupt the magnetic ordering in $SmMnO_3$, leading to a reduction in the overall magnetic moment.

1. Curie temperature

The Curie temperature is the temperature at which the magnetic properties of certain substances undergo significant changes. Below the Curie temperature, magnetic dipoles are aligned, resulting in ferromagnetic order. However, the thermal energy above this temperature disrupts this alignment, causing the dipoles to become randomly oriented. Most perovskites exhibit a low Curie temperature. To calculate the Curie temperature, the following equation is used:[41]

$$K_B T_C = \frac{2}{3}\sum_{ij} J_{ij} \tag{9}$$

with

$$\sum_{ij} J_{ij} = \frac{\Delta E}{2} = \frac{E_{FM} - E_{AFM}}{2}, \tag{10}$$

where K_B represents the Boltzmann constant and J_{ij} represents the exchange interaction, that is, the energy difference between the ferromagnetic (E_{FM}) and antiferromagnetic states (E_{AFM}).

The calculated values of Curie temperature (T_C) for pristine, 12.5% Eu-doped, and 25% Eu-doped $SmMnO_3$ are 255.35,

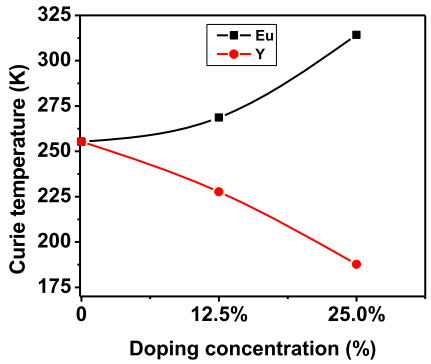

FIG. 13. Variation in the Curie temperature with Eu/Y doping concentration on $SmMnO_3$.

268.63, and 314.28 K, respectively [Table II]. In contrast, for Y-doped samples, the values are 227.70 and 187.69 K. The Curie temperature increases rapidly with Eu doping, while it decreases significantly with Y doping. As the doping level rises, notable changes occur in the magnetic properties and Curie temperature of the material.

Figure 13 illustrates that the Curie temperature of $SmMnO_3$ decreases nearly linearly with increasing Y doping concentration. This is attributed to the slightly smaller atomic radius of yttrium than that of samarium, which introduces significant lattice distortion and reduces magnetic exchange interactions between Mn ions. Conversely, europium, having a similar ionic radius as compared to Sm and partially filled 4f orbitals, causes less lattice distortion and enhances magnetic interactions. Thus, the Curie temperature initially increases with increasing Eu concentration as the magnetic exchange interactions strengthen.

E. Elastic properties

Here, the mechanical properties and dynamic stability of $SmMnO_3$ with varying europium doping are discussed. The relevant elastic constants for the simple cubic structure include C_{11}, C_{12}, and C_{44}. Among these, C_{12} and C_{44} reflect elasticity in terms of shape, while C_{11} denotes elasticity in terms of length.[42] The stress–strain method has been employed to calculate these constants for both pure and doped $SmMnO_3$ (Table III).

According to Hooke's law,[43] the relationship between stress (σ_{ij}) and strain (ε_{kl}) in terms of C_{ij} can be expressed as

$$\sigma_{ij} = C_{ijkl}\varepsilon_{kl} \Rightarrow \sigma_{ij} = C_{ij}\varepsilon_{ij}, \tag{11}$$

where σ_{ij} is the stress tensor component, C_{ij} is the stiffness or elastic tensor component, and ε_{ij} is the strain component.

The Voigt–Reuss–Hill approximation[44–46] has been used to determine the bulk modulus (B), the shear modulus (G), and Young's modulus (E), which are calculated using the following relations:

$$B_V = \frac{(C_{11} + 2C_{12})}{3}, \quad \text{and} \quad B_R = \frac{1}{(3S_{11} + 6S_{12})} \tag{12a}$$

$$B_H = \frac{B_V + B_R}{2}. \tag{12b}$$

The shear moduli of Voigt and Reuss provide upper and lower bounds, respectively,[47] and combining these with a weight parameter represents an intermediate condition,[48]

$$G_V = \frac{(C_{11} - C_{12} + 3C_{44})}{5}, \tag{13a}$$

$$G_R = \frac{5C_{44}(C_{11} - C_{12})}{4C_{44} + 3(C_{11} - C_{12})}, \tag{13b}$$

$$G_H = \frac{(G_V + G_R)}{2}, \tag{13c}$$

$$E = \frac{9B_H G_H}{3B_H + G_H}. \tag{14}$$

The following formulas are used to calculate the anisotropy factor (A), Poisson's ratio, and Cauchy's pressure:

$$A = 1 + \frac{C_{44} + C_{12}}{C_{11}}, \tag{15}$$

$$\upsilon = \frac{3B_H - 2G_H}{2(3B_H + G_H)}, \tag{16}$$

and, Cauchy's pressure;

$$P_C = C_{12} - C_{44}. \tag{17}$$

The elastic constants (C_{ij}) of pristine and doped compounds, specifically C_{11}, C_{12}, and C_{44}, are critical for describing their mechanical

TABLE III. Calculated elastic constants (C_{ij}), Young's modulus (E), shear modulus (G), Poisson's ratio (υ), and G_H/B_H ratio of $SmMnO_3$ with different doping levels of europium and yttrium.

Compounds	C_{11} (GPa)	C_{12} (GPa)	C_{44} (GPa)	B_V (GPa)	B_R (GPa)	B_H (GPa)	G_V (GPa)	G_R (GPa)	G_H (GPa)	E (GPa)	υ	G_H/B_H
Bulk SmMnO3	240.52	112.08	78.32	154.89	154.89	154.89	72.68	71.99	72.34	187.78	0.323	0.471
12.5% Eu doped	229.71	185.99	70.95	200.56	200.56	200.56	51.31	37.38	44.34	123.90	0.365	0.221
25% Eu doped	235.7	183.78	76.95	201.09	201.09	201.09	56.55	43.09	49.82	138.07	0.386	0.248
12.5% Y doped	247.84	153.72	119.04	185.09	185.09	185.09	90.25	73.85	82.05	214.46	0.307	0.443
25% Y doped	246.65	150.38	117.68	182.47	182.47	182.47	89.86	74.58	82.22	214.45	0.304	0.450

behavior. These constants are listed in Table III, and the results confirm that both the doped and pristine compounds studied satisfy the Born stability criteria for mechanical stability,[49] making them suitable for various technological applications,

$$C_{11} - |C_{12}| > 0, \tag{18a}$$

$$C_{11} + 2C_{12} > 0, \tag{18b}$$

$$C_{12} < B < C_{11}, \tag{18c}$$

and

$$C_{44} > 0.$$

The bulk modulus (B), shear modulus (G), Young's modulus (E), Pugh ratio (G/B), and Poisson's ratio of both pristine and doped perovskites are summarized in Table III. These moduli are crucial in determining the material's behavior under various mechanical conditions. The bulk modulus indicates the material's resistance to uniform compression under pressure. The shear modulus reflects the material's ability to withstand deformation in response to shear stress. Young's modulus measures the material's resistance to longitudinal deformation under tensile or compressive forces. Understanding these properties is essential for predicting the material's mechanical performance.

From the tabulated values of C_{11} and C_{44}, it is observed that Y-doping results in higher values compared to both Eu-doped and pristine $SmMnO_3$, suggesting that Y-doping enhances the material's resistance to both compression and shear deformation. This indicates greater mechanical stability and improved suitability for structural applications.

The bulk modulus (B) displays a clear trend with doping in $SmMnO_3$ compounds. For pristine $SmMnO_3$, B = 154.89 GPa, indicating moderate resistance to uniform compression. Europium (Eu) doping significantly increases the bulk modulus, with B rising to 200.56 GPa for 12.5% Eu and 201.09 GPa for 25% Eu, suggesting improved structural stability under pressure. In contrast, yttrium (Y) doping decreases the bulk modulus, with B falling to 185.09 GPa for 12.5% Y and 182.47 GPa for 25% Y, indicating lower resistance to compression compared to Eu-doped compounds.

Shear modulus (G) trends are also affected by doping. Pristine $SmMnO_3$ has a shear modulus of 65.47 GPa. Europium doping leads to a reduction in shear modulus, with values of 44.34 GPa for 12.5% Eu and 49.82 GPa for 25% Eu, indicating decreased resistance to shear stress compared to the pristine material. Meanwhile, yttrium doping significantly enhances the shear modulus, with G increasing to 82.05 GPa for 12.5% Y and 82.22 GPa for 25% Y, surpassing both the pristine and Eu-doped $SmMnO_3$ compounds.

Young's modulus (E) shows a significant variation with doping. Yttrium doping results in the highest E values among the studied compounds, with 214.46 GPa for 12.5% Y and 214.45 GPa for 25% Y, reflecting a substantial increase in stiffness compared to pristine $SmMnO_3$, which has E = 187.78 GPa. In contrast, europium doping reduces E considerably, with values dropping to 123.90 GPa for 12.5% Eu and 138.07 GPa for 25% Eu, indicating a marked decrease in stiffness compared to both pristine and Y-doped $SmMnO_3$. The Poisson's ratio values indicate that europium doping results in greater lateral expansion under tension, while yttrium doping leads to less lateral expansion. According to Pugh's criteria, materials with a Pugh ratio $G/B < 0.57$ are considered ductile. All calculated values of G/B for both pristine and doped compounds are below 0.57, confirming that these materials are ductile.

1. Elastic anisotropy

Elastic anisotropy, an important parameter describing how mechanical properties vary with direction, is assessed using the universal anisotropy index (A^U).[50] The Zener anisotropy index (A^Z) measures the degree of elastic anisotropy in cubic crystals,[51] while percent compression and shear anisotropy indices (A_{comp} and A_{shear})[52] describe the elastic anisotropy of both pristine and doped compounds as follows:[53]

$$A^U = 5\frac{B_V}{B_R} + \frac{G_V}{G_R} - 6, \tag{19a}$$

$$A^Z = 5\frac{2C_{44}}{C_{11} - C_{12}}, \tag{19b}$$

$$A_{comp} = \frac{B_V - B_R}{B_V + B_R}, \tag{19c}$$

$$A_{shear} = \frac{G_V - G_R}{G_V + G_R}. \tag{19d}$$

Isotropic characteristics are indicated by $A^U = 0$, $A^Z = 1$, and $A_{comp} = A_{shear} = 0$, while all other values indicate anisotropy. In addition, the extent of elastic anisotropy increases with the magnitudes of A^U, A^{comp}, A^{shear}, and $|A^Z - 1|$. The calculated anisotropy indices (A^U, A^Z, A_{comp}, and A_{shear}) for pure and Eu- or Y-doped $SmMnO_3$ compounds are presented in Table IV. These compounds exhibit an isotropic bulk modulus due to their A_{comp} values of zero, resulting in a perfect spherical shape [Fig. 14(a)]. The cubic structure of these compounds means that they deform uniformly in all [100], [010], and [001] directions when subjected to the same hydrostatic pressure. The calculated values of A_{shear} and A^Z convey that these cubic complexes are not identical. The Eu-doped compounds demonstrate relatively greater elastic anisotropy compared to their pure and Y-doped counterparts.

To better visualize the elastic anisotropy of these complexes, we have constructed two-dimensional polar plots of Young's modulus and shear modulus (Fig. 14). These plots are based on the elastic compliance constants (S_{ij}) and directional cosines (l_i) with the following expressions for Young's modulus and shear modulus:[54]

$$\frac{1}{E} = S_{11} - 2\left(S_{11} - S_{12} - \frac{S_{44}}{4}\right)\left(l_1^2 \cdot l_2^2 + l_2^2 \cdot l_3^2 + l_1^2 . l_3^2\right), \tag{20a}$$

$$\frac{1}{G} = S_{11} + 4\left(S_{11} - S_{12} - \frac{S_{44}}{4}\right)\left(l_1^2 \cdot l_2^2 + l_2^2 \cdot l_3^2 + l_1^2 . l_3^2\right). \tag{20b}$$

2. Debye temperature (θ_D)

The Debye temperature (θ_D) is an important parameter that determines the thermal properties of materials, distinguishing between their high- and low-temperature states. A higher value of θ_D indicates that the material has a higher melting temperature and enhanced thermal conductivity.[55] In this study, we employed established techniques and elastic constant data to compute the Debye

TABLE IV. Calculated elastic anisotropy indices (A^U, A^Z, A_{comp}, and A_{shear}) of $SmMnO_3$ with different doping levels of Eu and Y.

Compounds	A^U	A^Z	A_{comp}	A_{shear}
Bulk $SmMnO_3$	0.0095	6.0978	0.00	0.0047
12.5% Eu doped	0.3729	16.2283	0.00	0.1571
25% Eu doped	0.3124	14.8209	0.00	0.1351
12.5% Y doped	0.2219	12.6477	0.00	0.0999
25% Y doped	0.2049	12.2239	0.00	0.0929

temperature. The value of θ_D can be efficiently calculated using the average sound velocity (v_m) as follows:

$$\theta_D = \frac{h}{K_B}\left[\frac{3n}{4\pi}\left(\frac{N_A \cdot \rho}{M}\right)\right]^{\frac{1}{3}} v_m, \tag{21}$$

where h, K_B, N_A, n, M, ρ, and v_m are Planck's constant, Boltzmann's constant, Avogadro's number, the number of atoms per formula unit, the molecular mass per formula unit, the density, and the average sound velocity, respectively. The average sound velocity is calculated using the following relation:[56]

$$v_m = \left[\frac{1}{3}\left(\frac{2}{v_t^3} + \frac{1}{v_l^3}\right)\right]^{\frac{-1}{3}}, \tag{22}$$

where v_l and v_t are the longitudinal and transversal elastic wave velocities in an isotropic material, respectively, and can be obtained from Navier's equation as follows:[57]

$$v_l = \left[\frac{3B + 4G}{3\rho}\right]^{\frac{1}{2}} \text{ and } v_t = \left[\frac{G}{\rho}\right]^{\frac{1}{2}}. \tag{23}$$

The introduction of europium atoms into $SmMnO_3$ generally decreases the longitudinal, transverse, and average sound velocities [Fig. 15(a)]. In contrast, yttrium doping enhances acoustic velocities, longitudinal, transverse, and average sound velocities. The value of θ_D decreases significantly upon the addition of Eu and continues to decline linearly with increasing doping levels. However, its value consistently decreases with an increase in the doping level of Y [Fig. 15(b)]. Overall, yttrium doping enhances the longitudinal, transverse, and average sound velocities, as well as the Debye temperature, which improves both the mechanical stiffness and thermal properties of $SmMnO_3$. This makes Y-doped $SmMnO_3$ more suitable for applications requiring high resistance to deformation and better thermal conductivity. The tabulated values of longitudinal (v_l), transverse (v_t), and average (v_m) sound velocities, along with the Debye temperature (θ_D) for Eu- and Y-doped $SmMnO_3$, presented in Table V, as well as the anisotropic index in Table IV, exhibit trends that are consistent with the general behavior observed in ABO_3 perovskites, such as $KSnO_3$, $RbSnO_3$, $CsSnO_3$, $KSbO_3$, $RbSbO_3$, and $CsSbO_3$, as reported by Ülkü Bayhan and İnanç Yilmaz in their study.[58]

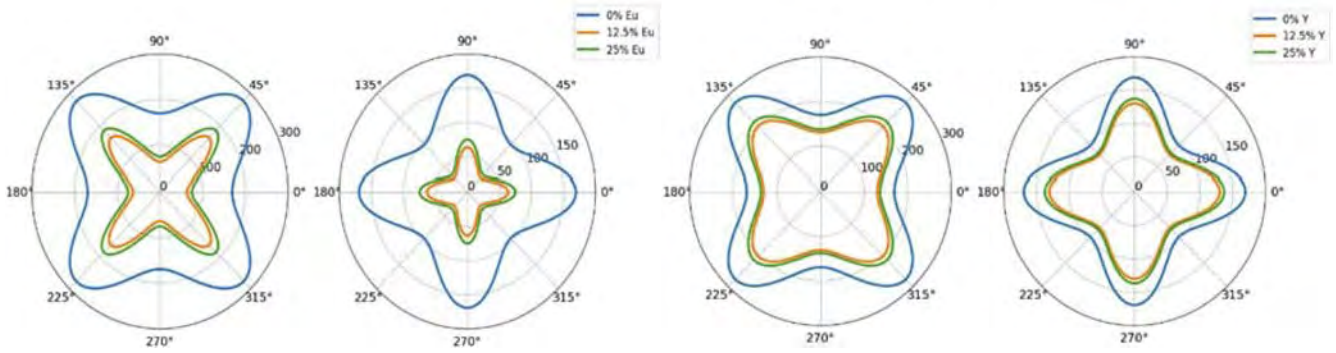

FIG. 14. Two-dimensional polar plots of (a) Young's modulus and (b) shear modulus of Eu-doped $SmMnO_3$ and (c) Young's modulus and (d) shear modulus of Y-doped $SmMnO_3$ at different concentrations.

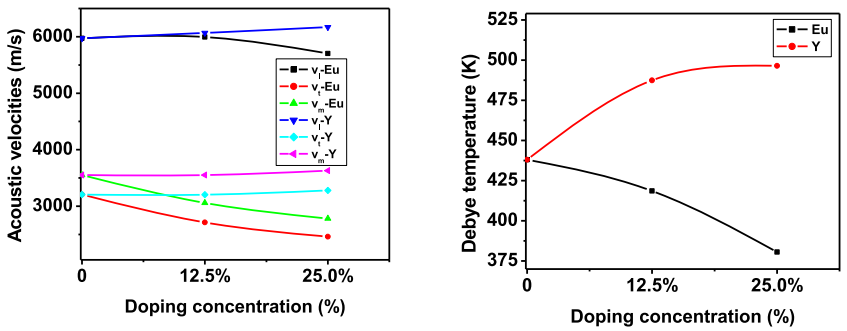

FIG. 15. Variation in (a) acoustic velocities and (b) Debye temperature of $SmMnO_3$ with different doping levels of Eu and Y.

TABLE V. Calculated density (ρ), longitudinal, transverse, and average sound velocities ($v_l, v_t, \wedge v_m$), and Debye temperature (θ_D) of $SmMnO_3$ with different doping levels of Eu and Y.

Compounds	σ	P (g cm^{-3})	v_l (m s^{-1})	v_t (m s^{-1})	v_m (m s^{-1})	θ_D (K)
Bulk $SmMnO_3$	0.323	7.042	5974.06	3206.22	3550.00	438.04
12.5% Eu doped	0.365	8.194	5994.44	2711.99	3058.01	418.62
25% Eu doped	0.386	8.225	5703.09	2461.14	2780.55	380.55
12.5% Y doped	0.307	7.996	6068.78	3203.36	3551.98	487.39
25% Y doped	0.304	7.676	6168.66	3278.78	3628.80	496.44

IV. CONCLUSIONS

The important takeaways from this work are listed as follows:

i. Tolerance factors of ~0.9 are observed in pure, Eu-doped, and Y-doped $SmMnO_3$, suggesting that these materials are stable up to a 25% doping level. As the doping concentration increases, the tolerance factor decreases non-linearly for Y-doped $SmMnO_3$ and decreases linearly for Eu-doped $SmMnO_3$.
ii. Electronic and magnetic calculations show that pristine $SmMnO_3$ exhibits a ferromagnetic half-metallic behavior. The band reduces significantly on Eu and Y doping. Eu doping increases the magnetic moment and Curie temperature, while these properties are reduced by Y doping.
iii. Eu and Y doping shifts the peak of the real part of the dielectric function $\varepsilon_1(\omega)$ from 1.5 eV (pristine $SmMnO_3$) to 5.0 eV (doped compounds) and increases the peaks of the imaginary part $\varepsilon_2(\omega)$, indicating enhanced optical absorption.
iv. The refractive index $n(\omega)$ decreases rapidly at low energies and stabilizes at higher energies. Doped $SmMnO_3$ shows a UV shift with increased absorption intensity and decreased reflectivity. These modifications in optical properties due to Eu and Y doping suggest potential applications in advanced photovoltaics, UV photodetectors, optoelectronic devices, and broad-spectrum sensors.
v. Eu doping causes a decrease in Young's modulus and shear modulus, with an increase in the bulk modulus. Conversely, Y doping leads to increased shear and Young's moduli. Furthermore, Eu doping has been shown to increase Poisson's ratio (up to 0.386), while Y doping results in a slight decrease in Poisson's ratio (~0.304–0.307). Finally, Eu doping increases elastic anisotropy while decreasing the Debye temperature, whereas Y doping has the opposite effect.

AUTHOR DECLARATIONS

Conflict of Interest

The authors have no conflicts to disclose.

Author Contributions

Peshal Pokharel: Formal analysis (equal); Investigation (equal); Methodology (equal); Writing – original draft (equal). **Shashit Kumar Yadav**: Conceptualization (equal); Data curation (equal); Investigation (equal); Methodology (equal); Writing – original draft (equal). **Nurapati Pantha**: Conceptualization (equal); Investigation (equal); Visualization (equal); Writing – review & editing (equal). **Bikash Sharma**: Conceptualization (equal); Software (equal); Validation (equal); Visualization (equal). **Devendra Adhikari**: Supervision (equal); Visualization (equal); Writing – review & editing (equal).

DATA AVAILABILITY

Data of the present work will be made available by corresponding authors on request.

REFERENCES

[1] M. A. Rahman, W. Hasan, M. Z. Hasan, A. Irfan, S. C. Mouna, M. A. R. Sarker *et al.*, "Structural, mechanical, electronic, optical, and thermodynamic features of lead-free oxide perovskites $AMnO_3$ (A = Ca, Sr, Ba): DFT simulation-based comparative study," Physica B **668**, 415215 (2023).
[2] S. Rahman, A. Hussain, S. Noreen, N. Bibi, S. Arshad, J. U. Rehman, and M. B. Tahir, "Structural, electronic, optical and mechanical properties of oxide-based perovskite ABO_3 (A = Cu, Nd and B = Sn, Sc): A DFT study," J. Solid State Chem. **317**, 123650 (2023).
[3] S. R. Bhandari, S. Kc, S. Lawaju, R. K. Thapa, G. C. Kaphle, and M. P. Ghimire, "Electronic structure and estimation of Curie temperature in Ca_2BIrO_6 (B = Cr, Fe) double perovskites," J. Appl. Phys. **130**(17), 173902 (2021).
[4] P. Pokharel, S. K. Yadav, N. Pantha, and D. Adhikari, "First-Principles investigations of structural, electronic, and elastic properties of $ZrSiO_3$ perovskite: Layer dependence, surface termination, and pressure effects," Phys. Status Solidi B **261**, 2400156 (2024).
[5] A. Žužić, A. Ressler, and J. Macan, "Perovskite oxides as active materials in novel alternatives to well-known technologies: A review," Ceram. Int. **48**(19), 27240 (2022).
[6] N. U. Khan, U. A. Khan, V. Tirth, J. Y. Al-Humaidi, M. S. Refat, A. Algahtani, and A. Zaman, "Investigation of structural, optoelectronic, and thermoelectric properties of titanium-based chloro-perovskites $XTiCl_3$ (X = Rb, Cs): A first-principles calculation," RSC Adv. **13**(9), 6199 (2023).
[7] B. O. Alsobhi, "First-principles calculations to investigate structural, electronic, magnetic, optical, mechanical, and thermoelectric properties of rare-earth aluminate perovskite $XAlO_3$ (X = Ce, Nd, Gd) compounds," Mater. Chem. Phys. **301**, 127691 (2023).
[8] Q. Tao, P. Xu, M. Li, and W. Lu, "Machine learning for perovskite materials design and discovery," npj Comput. Mater. **7**(1), 23 (2021).
[9] W. Amdouni, M. Otoničar, P. Gemeiner, V. Butin, N. Guiblin, H. Maghraoui-Meherzi, and B. Dkhil, "A general synthetic route to high-quality perovskite oxide nanoparticles and their enhanced solar photocatalytic activity," Angew. Chem. **135**, 202215700 (2023).
[10] A. E. Hannora and F. F. Hanna, "Preparation of nanostructured manganites $SmMnO_3$ and $Sm_{0.5}Sr_{0.5}MnO_3$ by mechanochemical synthesis method," J. Mater. Sci.: Mater. Electron. **30**, 12456–12464 (2019).

[11] C. A. da Silva, R. S. Silva, E. J. R. Plaza, and N. O. Moreno, "Magnetic state and magnetocaloric effect of $SmMnO_3$," J. Supercond. Novel Magn. **26**, 2497–2499 (2013).
[12] A. Nandy and S. K. Pradhan, "Effects of monovalent cation doping on the structure, microstructure, lattice distortion and magnetic behavior of single crystalline $NdMnO_3$ compounds," Dalton Trans. **44**(39), 17229–17240 (2015).
[13] R. R. Mahalik, S. Soren, I. Hota, A. K. Debnath, K. P. Muthe, and P. Parhi, "$REMnO_3$ (RE = Pr, Nd, Sm, Eu, Gd) perovskite as efficient catalysts for the oxygen reduction reaction," J. Rare Earths **42**, 2078 (2024).
[14] M. M. Saad and B. O. Alsobhi, "Consequences of tuning rare-earth RE^{3+}-Site and exchange–correlation energy U on the optoelectronic, mechanical, and thermoelectronic properties of cubic manganite perovskites $REMnO_3$ for spintronics and optoelectronics applications," ACS Omega **7**(32), 27903–27917 (2022).
[15] M. K. Butt, M. Yaseen, S. A. Aldaghfag, A. Murtaza, and S. Saleem, "Investigation of structural, electromagnetic, and optical properties of cubic $SmXO_3$ (X = Fe, Mn, Cr) perovskites," Phys. Scr. **98**(11), 115970 (2023).
[16] V. B. Jayakrishnan, S. K. Mishra, and P. U. Sastry, "Role of A and B site doping on antiferrodistortive phase transition in sodium bismuth titanate," Mater. Res. Bull. **144**, 111499 (2021).
[17] R. H. Mitchell and R. P. Liferovich, "A structural study of the perovskite series $Na_{0.75}Ln_{0.25}Ti_{0.5}Nb_{0.5}O_3$," J. Solid State Chem. **178**(9), 2586–2593 (2005).
[18] K. Gao, X. Liu, Z. Jiang, H. Zheng, C. Song, X. Wang *et al.*, "Direct solar thermochemical CO_2 splitting based on Ca-and Al-doped $SmMnO_3$ perovskites: Ultrahigh CO yield within small temperature swing," Renewable Energy **194**, 482 (2022).
[19] K. Gao, X. Liu, T. Wang, Z. Zhu, P. Li, H. Zheng *et al.*, "Sr-doped $SmMnO_3$ perovskites for high-performance near-isothermal solar thermochemical CO_2-to-fuel conversion," Sustainable Energy Fuels **5**(17), 4295 (2021).
[20] B. J. Tickner, G. J. Stasiuk, S. B. Duckett, and G. Angelovski, "The use of yttrium in medical imaging and therapy: Historical background and future perspectives," Chem. Soc. Rev. **49**(17), 6169–6185 (2020).
[21] K. Zhang, A. N. Kleit, and A. Nieto, "An economics strategy for criticality—Application to rare earth element Yttrium in new lighting technology and its sustainable availability," Renewable Sustainable Energy Rev. **77**, 899–915 (2017).
[22] Z. Liu, Y. Ding, S. Xie, Y. Hu, H. Xiao, X. Liu, and X. Fan, "Chronic exposure to yttrium induced cell apoptosis in the testis by mediating Ca^{2+}/IP3R1/Ca MKII signaling," Front. Public Health **11**, 1104195 (2023).
[23] W. Koch and M. C. Holthausen, *A Chemist's Guide to Density Functional Theory*, 2nd ed. (Wiley-VCH Verlag GmbH, 2001).
[24] R. G. Parr and W. Yang, *Density Functional Theory of Atoms and Molecules* (Oxford University Press, New York, 1989).
[25] P. Giannozzi *et al.*, QUANTUM ESPRESSO: A modular and open-source software project for quantum simulations of materials, J. Phys.: Condens. Matter, **21**(39), 395502 (2009).
[26] D. C. Langreth and J. P. Perdew, "Theory of nonuniform electronic systems. I. Analysis of the gradient approximation and a generalization that works," Phys. Rev. B **21**(12), 5469 (1980).
[27] D. Vanderbilt, "Soft self-consistent pseudopotentials in a generalized eigenvalue formalism," Phys. Rev. B **41**, 7892 (1990).
[28] P. Pokharel, S. K. Yadav, N. Pantha, and D. Adhikari, "Strain-dependent electronic, mechanical and piezoelectric properties of $ZrSiO_3$ 2D monolayer: A first principle approach," J. Phys. Chem. Solids **193**, 112198 (2024).
[29] J. P. Perdew, K. Burke, and M. Ernzerhof, "Generalized gradient approximation made simple," Phys. Rev. Lett. **77**, 3865 (1996).
[30] V. I. Anisimov, J. Zaanen, and O. K. Andersen, "Band theory and Mott insulators: Hubbard *U* instead of Stoner *I*," Phys. Rev. B **44**, 943 (1991).
[31] J. D. Pack and H. J. Monkhorst, "Special points for Brillouin-zone integrations—A reply," Phys. Rev. B **16**, 1748 (1977).
[32] R. Golesorkhtabar, P. Pavone, J. Spitaler, P. Puschnig, and C. Draxl, "ElaStic: A tool for calculating second-order elastic constants from first principles," Comput. Phys. Commun. **184**, 1861 (2013).
[33] S. C. Tidrow, "Mapping comparison of Goldschmidt's tolerance factor with Perovskite structural conditions," Ferroelectrics **470**(1), 13–27 (2014).
[34] P. H. T. Philipsen and E. J. Baerends, "Cohesive energy of 3*d* transition metals: Density functional theory atomic and bulk calculations," Phys. Rev. B **54**(8), 5326 (1996).
[35] C. Yang, Y. Wu, and Y. Duan, "Theoretical predictions of the electronic, optical and thermodynamic properties of the C40-type $TMSi_2$ (TM= V, Nb and Ta)," Mater. Today Commun. **30**, 103115 (2022).
[36] Y. Wu, X. Wang, Y. Wang, Y. Duan, and M. Peng, "Insights into electronic and optical properties of $AGdS_2$ (A= Li, Na, K, Rb, and Cs) ternary gadolinium sulfides," Opt. Mater. **114**, 110963 (2021).
[37] Y. Lu, Y. Duan, M. Peng, J. Yi, and C. Li, "First-principles calculations of electronic, optical, phononic and thermodynamic properties of C40-type $TMSi_2$ (TM= Cr, Mo, W)," Vacuum **191**, 110324 (2021).
[38] V. Lucarini, J. J. Saarinen, K. E. Peiponen, and E. M. Vartiainen, *Kramers-Kronig Relations in Optical Materials Research* (Springer Science & Business Media, 2005), Vol. 110.
[39] F. Birch, "Finite elastic strain of cubic crystals," Phys. Rev. **71**(11), 809 (1947).
[40] N. G. Nereson, C. E. Olsen, and G. P. Arnold, "Magnetic structure of europium," Phys. Rev. **135**(1A), A176 (1964).
[41] J. Kubler, G. H. Fecher, and C. Felser, "Understanding the trend in the Curie temperatures of Co_2-based Heusler compounds: *Ab initio* calculations," Phys. Rev. B **76**, 24414 (2007).
[42] V. Sinko, "Ab initio calculations of the second order elastic constants of crystals under arbitrary isotropic pressure," Phys. Rev. B **77**(10), 104118 (2008).
[43] S. Yip, J. Li, M. J. Tang, and J. G. Wang, "Mechanistic aspects and atomic-level consequences of elastic instabilities in homogeneous crystals," Mater. Sci. Eng., A **317**, 236 (2001).
[44] W. Voigt, "A determination of the elastic constants for beta-quartz," *Lehrbuch de Kristallphysik* (Terubner, Leipzig, 1928).
[45] A. Reuss, "Calculation of the flow limits of mixed crystals based on the plasticity of monocrystals," J. Appl. Math. Mech. **9**, 49 (1929).
[46] R. Hill, "The elastic behaviour of a crystalline aggregate," Proc. Phys. Soc., Sect A **65**(5), 349 (1952).
[47] M. Jamal, M. S. Abu-Jafar, and A. H. Reshak, "Revealing the structural, elastic, and thermodynamic properties of $CdSe_xTe_{1-x}$ (x = 0, 0.25, 0.5, 0.75, 1)," J. Alloys Compd. **667**, 151 (2016).
[48] Z. Poniznik, V. Salit, M. Basista, and D. Gross, "Effective elastic properties of interpenetrating phase composites," Comput. Mater. Sci. **44**(2), 813 (2008).
[49] F. Mouhat and F. X. Coudert, "Necessary and sufficient elastic stability conditions in various crystal systems," Phys. Rev. B **90**(22), 224104 (2014).
[50] S. I. Ranganathan and M. Ostoja-Starzewski, "Universal elastic anisotropy index," Phys. Rev. Lett. **101**, 055504 (2008).
[51] C. Zener, *Elasticity and Anelasticity of Metals* (University of Chicago, Chicago, 1948).
[52] N. Miao, B. Sa, J. Zhou, and Z. Sun, "First-principles study of magnetic properties in CO_2-based Heusler compounds," Comput. Mater. Sci. **50**, 1559 (2011).
[53] J. F. Nye and R. B. Lindsay, *Physical Properties of Crystals: Their Representation by Tensors and Matrices* (Oxford University Press, Oxford, UK, 1984).
[54] J. Nordmann, M. Aßmus, and H. Altenbach, "Visualising elastic anisotropy: Theoretical background and computational implementation," Continuum Mech. Thermodyn. **30**, 689 (2018).
[55] O. L. Anderson, "A simplified method for calculating the Debye temperature from elastic constants," J. Phys. Chem. Solids **24**, 909 (1963).
[56] Y. Wu, L. Bao, X. Wang, Y. Wang, M. Peng, and Y. Duan, "Insight into structural, electronic, elastic, and thermal properties of A15-type Nb_3X (X = Si, Ge, Sn, and Pb) compounds," Mater. Today Commun. **25**, 101410 (2020).
[57] J. Wei, L. Zhang, and Y. Liu, "First-principles calculations study the mechanical and thermal properties of Cr-Al-B ternary borides," Solid State Commun. **326**, 114182 (2021).
[58] Ü. Bayhan and İ. Yilmaz, "Prediction of structural, electronic, and lattice dynamical properties of ABO_3 [A= K, Rb, Cs; B= Sn, Sb] perovskite compounds," Physica B **649**, 414355 (2023).

RESEARCH ARTICLE

physica status solidi b

www.pss-b.com

Elastic Anisotropy and Thermal Properties of Sr_2ZrMoO_6 Double Perovskite under Different Pressure

Peshal Pokharel, Shshit Kumar Yadav, Nurapati Pantha, Bikash Sharma, and Devendra Adhikari**

This study investigates the elastic and thermal properties of the double perovskite Sr_2ZrMoO_6 under different pressures from 0 to 80 GPa using first-principles calculations within the generalized gradient approximation of density functional theory. The calculated second-order elastic constants confirm the mechanical stability of the compound up to 80 GPa. The material exhibits significant elastic anisotropy, with elastic constants C_{11}, C_{33}, and C_{44} showing distinct pressure-dependent behavior. The elastic properties, including bulk modulus, shear modulus, Young's modulus, and Poisson's ratio, all increase with a rise in pressure, which enhances the material's stiffness and rigidity, improving its resistance to deformation or fracture. The Pugh ratio greater than 0.57, a negative Cauchy constant, and a low Poisson's ratio suggest that the material remains brittle within the examined pressure range. The calculated tolerance factor and formation energy confirm its thermodynamic stability. The minimum thermal conductivity k_{min} of the material increases slightly with pressure across all directions, maintaining the anisotropic order $k_{[001]} > k_{[110]} > k_{[100]}$, indicating improved phonon transport under compression. The specific heat capacity increases with pressure at low temperatures and approaches the Dulong–Petit limit at higher temperatures. These findings suggest Sr_2ZrMoO_6 holds potential for high-performance optical waveguides and optoelectronic applications.

1. Introduction

Perovskite materials have gained considerable interest from the scientific community for their broad range of applications to advancements in solar cells,[1,2] photovoltaics,[3] sensors,[4,5] spintronics,[6] data storage,[7] advanced electronic devices,[8] and high-temperature superconductors.[9] Double perovskites were first studied in the early 1950s[10] and gained popularity between the late 1950s and mid-1980s.[11] Their structure can be derived from the simple perovskite and has the formula $A_2B\ B'X_6$, where A cations occupy the octahedral sites, B and B' cations are located at the tetrahedral and octahedral positions, respectively, and X anions are situated at the interstitial sites (**Figure 1**). In strontium zirconium molybdate (Sr_2ZrMoO_6), Sr ions are located at the A site. Meanwhile, Zr and Mo are situated at the B and B' sites, and O anions occupy the X site. Sr_2ZrMoO_6, with its double perovskite structure, has gained significant attention due to its pronounced elastic anisotropy and unique thermal properties (Figure 1). The elastic anisotropy of this material plays a crucial role in its mechanical performance, as it exhibits different elastic moduli depending on the crystallographic direction. This anisotropy influences the material's structural stability and makes it more promising for high-performance applications where directional mechanical characteristics are essential.[12] Sr_2ZrMoO_6 is particularly noted for its excellent mechanical and thermal stability, making it suitable for use in extreme conditions. Furthermore, its thermal properties make it an attractive candidate for thermal management and energy-related applications. With these characteristics, the material finds its utility in advanced technological fields such as electronics, catalysis, and thermoelectric devices, where precise structural stability and heat transport control are required. The pressure-dependent mechanical properties of double perovskite Sr_2MnTaO_6 were

P. Pokharel, N. Pantha
Central Department of Physics
Tribhuvan University
Kritipur 44600, Nepal

P. Pokharel, S. K. Yadav, D. Adhikari
Department of Physics
Mahendra Morang Adarsha Multiple Campus
Tribhuvan University
Biratnagar 56613, Nepal
E-mail: sashit.yadav@mmamc.tu.edu.np;
devendra.adhikari@mmamc.tu.edu.np

P. Pokharel
Department of Physics
Central Campus of Technology
Tribhuvan University
Dharan 56700, Nepal

B. Sharma
Department of Electronics and Communication Engineering
Sikkim Manipal Institute of Technology
Sikkim Manipal University
Majitar, Sikkim 737136, India

The ORCID identification number(s) for the author(s) of this article can be found under https://doi.org/10.1002/pssb.202400625.

DOI: 10.1002/pssb.202400625

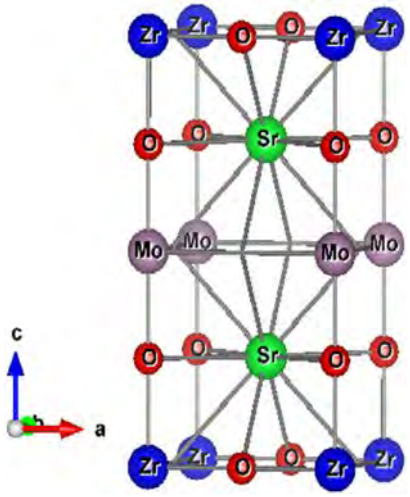

Figure 1. Unit cell of Sr_2ZrMoO_6 double perovskite.

explored through first-principle calculations for applications in optoelectronics and photovoltaics.[13] Recently, double perovskite oxides with Sr, Ca, and Ba atoms have been extensively investigated using density functional theory (DFT).[14,15] Specifically, strontium (Sr) and barium (Ba)-based double perovskites have attracted considerable attention due to their unique half-metallic behavior, high electrical conductivity, and strong magnetic ordering.[4,16,17] Feng et al. studied the elastic anisotropic and thermal properties of $Ln_2SrAl_2O_7$ (Ln = La, Nd, Sm, Eu, Gd, Dy) compounds using DFT and the Debye quasiharmonic approximation.[18]

In the present study, we intend to study the elastic anisotropy and thermal anisotropy of double perovskite Sr_2ZrMoO_6 under different isotropic pressure conditions within 0–80 GPa using DFT.

2. Results and Discussion

2.1. Structural Properties

The pressure-dependent structural properties of the tetragonal perovskite Sr_2ZrMoO_6, such as lattice parameters (a_0, c_0), ground state energy (E_0), minimum volume (V_0), and heat of formation energy (ΔH), have been systematically calculated at various pressures and presented in **Table 1**. As pressure increases, the ratios a/a_0, c/c_0, and V/V_0 decrease gradually, as illustrated in **Figure 2**a. It can be observed that the *c*-axis undergoes greater compression relative to the *a*-axis with the rise in pressure. But the ratio of parameter c/a is constant; also, the a/a_0 and c/c_0 curves exhibit a linear decrement. However, as pressure increases, the resistance to further compression causes a nonlinear response, resulting in a parabolic fall in the unit cell volume. To calculate the tolerance factor for a perovskite material such as Sr_2ZrMoO_6, the following formula has been used.[19]

$$t = \frac{r_A - r_O}{\sqrt{2}(r_B + r_O)} \quad (1)$$

Table 1. Calculated values of the lattice constants, a_0, and c_0, minimum volume (V_0), a/a_0, c/c_0, V/V_0, heat of formation (ΔH), for the tetragonal Sr_2ZrMoO_6 perovskite under different pressures.

P [Gpa]	*a* [Å]	*c* [Å]	*V* [Å]^3	a/a_0	c/c_0	V/V_0	ΔH [eV atom^{-1}]
0	4.066	8.232	136.086	1	1	1	−3.251
20	4.046	8.174	133.908	0.995	0.993	0.984	−3.249
40	4.025	8.133	132.819	0.99	0.988	0.976	−3.248
60	4.009	8.092	132.04	0.986	0.983	0.9703	−3.244
80	3.993	8.059	131.459	0.982	0.979	0.966	−3.240

where r_A, r_B, and r_O represent the ionic radii of the Sr cation, the average ionic radius of the Zr and Mo cations, and the oxygen anion, respectively. The calculated tolerance factor for the material is ≈0.978, which falls within the stability range of a tetragonal perovskite structure ($0.9 \leq t \leq 0.98$), showing its stability.

The ground state stability has also been evaluated by calculating the formation energy using the following relation.[20]

$$\Delta H_f = \frac{E_{total(Sr_2ZrMoO_6)} - (2E_{Sr} + E_{Zr} + E_{Mo} + 6E_o)}{6} \quad (2)$$

Here, $E_{total(Sr_2ZrMoO_6)}$ is the equilibrium energy of the Sr_2ZrMoO_6 perovskite, and E_{Sr}, E_{Zr}, E_{Mo}, and E_o are the respective energies of strontium, zirconium, molybdenum, and oxygen atoms in their bulk forms. The calculated formation energy for Sr_2ZrMoO_6 varies in the range of −3.251 to −3.240 eV atom^{-1} with the application of pressure (Figure 2b). This negative formation energy value shows the thermal stability of the compound and can be synthesized experimentally within the given pressure range. As pressure increases, the balance of Coulomb force between cations and anions becomes less effective because of distorted bond length and angles. As a result, the formation energy of the compound becomes less negative, which indicates a reduction in the thermodynamic stability of the material under high-pressure conditions. Furthermore, similar results were observed when the pressure was reduced, demonstrating the absence of hysteresis loss during both compression and expansion.

2.2. Elastic Properties

The study of elastic properties of double perovskite is important because it offers fundamental insights into the mechanical stability, dynamic behavior, and strength of materials under different pressure conditions. This section discusses the mechanical properties and dynamic stability of Sr_2ZrMoO_6 at different pressure conditions. The tetragonal structure is characterized by six distinct elastic constants (C_{11}, C_{12}, C_{13}, C_{33}, C_{44}, and C_{66}), which were determined using the stress–strain method. Pressure-dependent C_{ij} values of Sr_2ZrMoO_6 are presented in **Table 2**. From these values, the elastic compliance constants, S_{ij} ($=C_{ij}^{-1}$), were calculated (see Table ST1, Supporting Information).

The elastic constants provide insight into how a material resists stress from different directions. Specifically, C_{11}, C_{22},

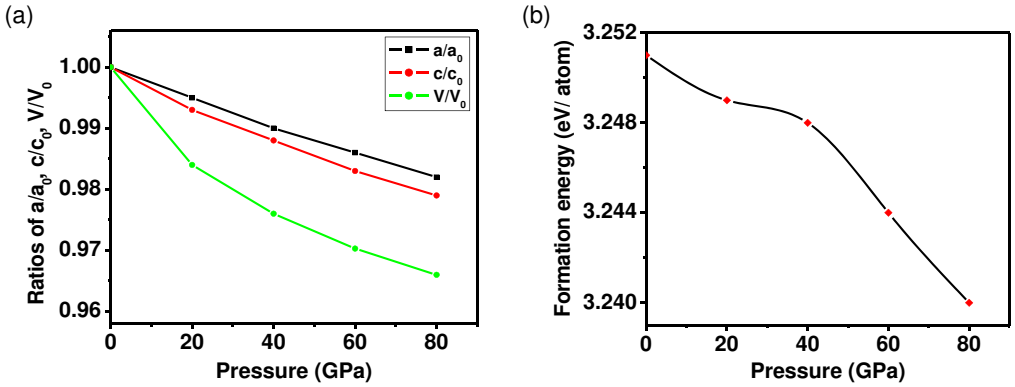

Figure 2. a,b) The variation of ratios of structural parameters and formation energy of Sr_2ZrMoO_6 at different pressures.

Table 2. Calculated elastic constants (C_{ij}) (in GPa) of Sr_2ZrMoO_6 at different pressures.

P [GPa]	C_{11}	C_{12}	C_{13}	C_{22}	C_{23}	C_{33}	C_{44}	C_{55}	C_{66}
0	313.21	95.11	85.66	313.21	85.66	332.62	98.46	98.46	135.32
20	321.71	95.83	87.72	321.71	87.72	335.16	98.24	98.24	137.45
40	327.66	96.19	90.49	327.66	90.49	341.69	98.09	98.09	140.22
60	330.85	96.85	93.32	330.85	93.32	343.29	97.83	97.83	143.22
80	332.57	97.03	95.66	332.57	95.66	350.04	97.67	97.67	147.89

and C_{33} describe how well the material resists deformation along the [100], [010], and [001] directions of the crystal. For the tetragonal perovskite Sr_2ZrMoO_6, it is observed that C_{11} is consistently larger than the corresponding C_{33} values at all pressures. This indicates that the bonding strength along the [100] direction is greater than that along the [001] direction. As shown in Table 2, C_{44} values at different pressures are significantly lower than the corresponding C_{11} and C_{33} values. This indicates that the compound in its tetragonal phase is more likely to deform than under unidirectional stress along the main crystallographic axes.[21] The elastic constant C_{66} denotes the degree of resistance to shear deformation in the *xy*-plane along the *x*- and *y*-axes. The elastic constant C_{66} represents the resistance to shear deformation within the [100] plane along the [110] direction. Also, a higher C_{66} value compared to C_{44}, as shown in Table 2 for all pressure, indicates the anisotropic shear behavior of the material.

The variation of the elastic constants (C_{ij}) of Sr_2ZrMoO_6 with pressure is shown in **Figure 3**a. The values of C_{11}, C_{12}, C_{13}, C_{33}, and C_{66} increase with an increase in pressure, while C_{44} exhibits the opposite trend. Additionally, C_{11} and C_{33} consistently show the highest values across all pressure levels, indicating that the material demonstrates strong resistance to uniaxial compression. Furthermore, it is observed that C_{33} consistently exceeds C_{11} across the entire pressure range, suggesting that atomic bonds along the [001] direction are stronger than those along the [100] direction. Additionally, the shear response of the material along the [001] direction in the (100) plane is characterized by the C_{44} value, while the shear response along the [110] direction in the (100) plane is represented by the C_{66} value. The calculated values of C_{44} and C_{66} vary significantly with pressure, and the variations are not equal, indicating that the shear moduli exhibit strong anisotropy, which are discussed in Section 2.2.1.

The mechanical stability criteria of materials were determined using Born–Huang's lattice dynamics theory.[22] The pressure-dependent form of mechanical stability criteria for the tetragonal system can be expressed as follows.[23]

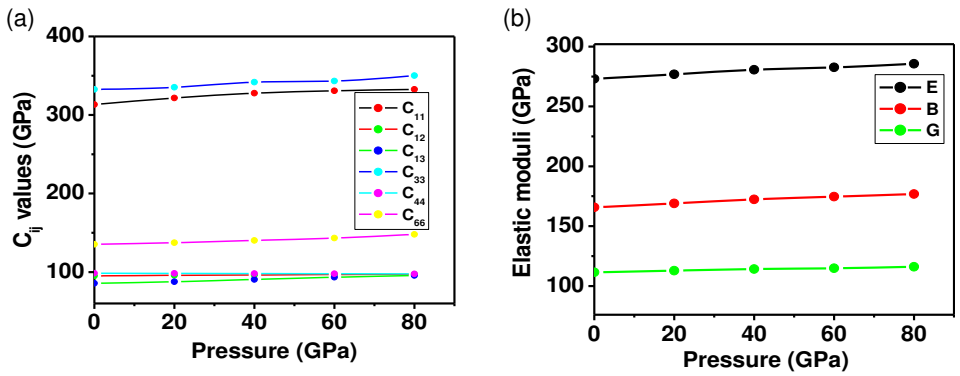

Figure 3. a,b) The variation of C_{ij} values and elastic constants (*E*, *B*, *G*) of Sr_2ZrMoO_6 at different pressures.

$$\begin{aligned} &C_{11} - P > 0 \\ &C_{33} - P > 0 \\ &C_{44} - P > 0 \\ &C_{66} - P > 0 \\ &C_{11} - C_{12} - 2P > 0 \\ &C_{11} + C_{33} - 2C_{13} - 4P > 0 \\ &2C_{11} + 2C_{12} + C_{33} + 4C_{13} + 3P > 0 \end{aligned} \tag{3}$$

All mechanical stability criteria are satisfied by the calculated values of (C_{ij}) listed in Table 2 for the tetragonal phases of the studied double perovskite Sr_2ZrMoO_6. This confirms that the material is mechanically stable under applied static pressures in tetragonal configurations.

Hooke's law[24] describes the dependence of stress (σ_{ij}) on strain (ε_{kl}) in terms of C_{ij} as follows.

$$\sigma_{ij} = C_{il}\varepsilon_{kl} \Rightarrow \sigma_{ij} = C_{ij}\varepsilon_{ij} \tag{4}$$

where σ_{ij} is the stress tensor component, C_{ij} is the stiffness or elastic tensor component, and ε_{ij} is the strain component.

The Voigt–Reuss–Hill method[25–27] can be used to determine the values of B and G for the tetragonal system, and they are given as

$$B_V = \frac{1}{9}[2C_{11} + C_{33} + 2C_{12} + 4C_{13}] \tag{5a}$$

$$B_R = \frac{C^2}{M} \tag{5b}$$

The shear constant (G_v) of an upper limit is

$$G_V = \frac{1}{30}[M + 3C_{11} - 3C_{12} + 12C_{44} + 6C_{66}] \tag{5c}$$

with $M = [C_{11} + C_{12} + 2C_{33} - 4C_{44}]$ and $C^2 = (C_{11} + C_{12})C_{33} - 2C_{13}{}^2$

and its lower limit can be expressed in the form as

$$G_R = \frac{15}{\left[\frac{18B_V}{C^2} + \frac{6}{C_{11}+C_{12}} + \frac{6}{C_{44}} + \frac{3}{C_{66}}\right]} \tag{5d}$$

Finally, Voigt and Reuss's mean values are obtained by

$$B_H = \frac{(B_V + B_R)}{2} \text{ and } G_H = \frac{(G_V + G_R)}{2} \tag{5e}$$

$$E = \frac{9B_H G_H}{3B_H + G_H} \tag{5f}$$

$$\nu = \frac{3B_H - 2G_H}{2(3B_H + G_H)} \tag{5g}$$

$$P_a^{cauchy} = C_{13} - C_{44}, \quad \text{and} \quad P_b^{cauchy} = C_{12} - C_{66} \tag{5h}$$

The elastic constants listed in Table 2 were utilized to calculate additional mechanical parameters, including the bulk modulus (B), Young's modulus (Y), and shear modulus (G), using Equation (5a–g). The computed values, such as elastic moduli (E, B, G), Poisson's ratio (ν), and Pugh's ratio (G/B), for the Sr_2ZrMoO_6 double perovskite under varying pressures, are presented in **Table 3**.

The elastic modulus represents the resistance to structural deformation of the material. A higher bulk modulus value compared to shear modulus suggests that Sr_2ZrMoO_6 exhibits greater resistance to volumetric deformation than to shape changes. Furthermore, the high Y and G values of double perovskite indicate the significant mechanical properties and stiffness of the material.

Figure 3b shows that all three elastic moduli (E, B, G) increase steadily with pressure up to 80 GPa. The increasing pressure compresses the crystal structure, strengthening atomic bonds and reducing interatomic distances. This enhances the material's stiffness and rigidity, improving its resistance to deformation or fracture under high-pressure conditions.

The tabulated values of elastic moduli (E, B, G), presented in Table 3, as well as the elastic constants (C_{ij}) in Table 2, exhibit trends that are consistent with the general behavior observed in half-metallic double perovskite oxide Sr_2MnTaO_6, as reported by Dar et al. in their study.[13]

The G/B ratio is a critical parameter for evaluating whether materials exhibit ductile or brittle behavior.[28] The materials with $\frac{G}{B} > 0.57$ are considered brittle, while those with $\frac{G}{B} < 0.57$ are classified as ductile. For the material under study, the calculated G/B ratio consistently exceeds 0.57 across a pressure range of 0–80 GPa (Table 3). This indicates that tetragonal Sr_2ZrMoO_6 retains brittle behavior even under high pressure. Additionally, the negative Cauchy constant and low Poisson's ratio (ranging from 0.225 to 0.231 up to 80 GPa) further support the brittle nature of the material.

The linear increase in C_{ij}, and elastic moduli (B, G, and E) with pressure, as illustrated in Figure 3a,b, shows that Sr_2ZrMoO_6 is stiffer under compression. This behavior arises from stronger interatomic bonds and reduced atomic distances, which improve

Table 3. Calculated values of pressure-dependent elastic moduli (B, G, E), Poisson's ratio (ν), and G_H/B_H ratio of Sr_2ZrMoO_6 double perovskites.

P [GPa]	B_V [GPa]	B_R [GPa]	B_H [GPa]	G_V [GPa]	G_R [GPa]	G_H [GPa]	E [GPa]	ν	G_H/B_H
0	165.76	165.73	165.75	112.31	110.51	111.41	273.04	0.225	0.67
20	169.01	169.00	169.01	113.78	111.82	112.79	276.81	0.227	0.67
40	172.37	172.35	172.36	115.27	113.09	114.18	280.58	0.229	0.66
60	174.66	174.64	174.65	116.04	113.67	114.86	282.62	0.230	0.66
80	176.88	176.79	176.84	117.42	114.68	116.05	285.66	0.231	0.66

the resistance to compression and shape deformation of the material. The steady rise in B and G with pressure shows that the material can handle both uniform compression and shape changes, while the rise in E indicates increased rigidity and reduced flexibility. These properties make Sr_2ZrMoO_6 highly suitable for high-pressure applications in advanced technological applications.

The Vickers hardness test is a common method for determining the hardness of materials by determining their resistance to plastic deformation. This method works well with many different types of materials, like metals, ceramics, and thin films. Vickers hardness H_V of Sr_2ZrMoO_6 double perovskite can be obtained using a relatively semiempirical equation of hardness proposed by Tian et al.[29]

$$H_V = 0.92(G/B)^{1.137}G^{0.708} \tag{6}$$

Here, B and G represent the bulk and shear moduli, respectively.

Fracture toughness K_{IC} reflects the resistance to crack expansion, which is an important mechanical property. Fracture toughness K_{IC} of the compound can be measured in the following formula.[30]

$$K_{IC} = (V_0)^{1/6}G \cdot \left(\frac{B}{G}\right)^{1/2} \tag{7}$$

where V_0 is the volume of a single atom (in m^3), B and G are the bulk and shear moduli (in MPa), respectively.

For assessing the damage resistance of the compound, the brittleness index M is used and obtained by H_V and K_{IC}[31]

$$M = \frac{H_V}{K_{IC}} \tag{8}$$

For K_{IC}, a material with a large K_{IC} possesses a strong resistance to crack expansion and a material with a small M shows a great damage tolerance. From **Table 4**, the calculated value of fracture toughness (K_{IC}) of Sr_2ZrMoO_6 ranges from 3.61 to 3.73 Mpa $m^{1/2}$ under the pressure of 0–80 GPa, indicating moderate toughness. These values suggest that Sr_2ZrMoO_6 possesses a level of toughness that is greater than many superhard materials, such as diamond,[32] but slightly lower than cubic boron nitride (c-BN).[33] This illustrates how Sr_2ZrMoO_6 balances toughness and brittleness and offers greater resistance to crack propagation in comparison to brittle ceramics and the majority of superhard materials. Furthermore, the calculated brittleness index (M) values for Sr_2ZrMoO_6 range from 4.60 to 4.64 $\mu m^{-1/2}$, which are significantly lower than those of typical superhard materials such as diamond or cubic boron nitride (c-BN), with M values $>10\ \mu m^{-1/2}$. This lower M value indicates that Sr_2ZrMoO_6 is less brittle and exhibits moderate toughness. The combination of reduced brittleness and excellent fracture toughness highlights its potential for high-performance applications in structural, thermal, and electronic fields.

2.2.1. Elastic Anisotropy

The anisotropy indices are an important tool for evaluating the mechanical, thermal, and electrical properties of a material. The universal anisotropy index (A^U) provides a thorough evaluation of overall anisotropy.[34] Furthermore, the shear anisotropy indices (A_{shear}) and bulk anisotropy (A_{comp}) offer important information about how the material behaves under shear strains and compression, respectively.[35] These parameters are important for the analysis of the elastic anisotropy of double perovskites under isotropic pressure.[36] These indices are defined as follows.

$$A^U = 5\frac{B_V}{B_R} + \frac{G_V}{G_R} - 6 \tag{9a}$$

$$A^Z = 5\frac{2C_{44}}{C_{11} - C_{12}} \tag{9b}$$

$$A_{comp} = \frac{B_V - B_R}{B_V + B_R} \tag{9c}$$

$$A_{shear} = \frac{G_V - G_R}{G_V + G_R} \tag{9d}$$

Isotropic behavior is indicated when A^U, A_{comp}, and A_{shear} are all equal to 0, while any nonzero values indicate the presence of anisotropy. Moreover, the degree of elastic anisotropy increases with higher values of A^U, A_{comp}, and A_{shear}. The calculated anisotropy indices (A^U, A_{comp}, and A_{shear}) for Sr_2ZrMoO_6 double perovskites at different pressures are presented in **Table 5**. The compound exhibits an isotropic bulk modulus as indicated by $A_{comp} = 0$. However, the nonzero values of A^U and A_{shear} in Table 5 suggest that the shear modulus and Young's modulus vary across different crystallographic directions, indicating elastic anisotropy in shear and stiffness. In a tetragonal crystal, the anisotropy factors $A_{\{100\}}$, $A_{\{010\}}$, and $A_{\{010\}}$ are defined as[37]

$$A_1 = A_{\{100\}} = \frac{4C_{44}}{C_{11} + C_{33} - 2C_{13}} \tag{10a}$$

Table 4. Calculated fracture toughness K_{IC} (in MPa $m^{1/2}$) and brittleness index M (in $\mu m^{-1/2}$) of Sr_2ZrMoO_6 perovskite.

P [GPa]	H_v [GPa]	K_{IC} [MPa $m^{1/2}$]	M [$\mu m^{-1/2}$]
0	16.64	3.61	4.61
20	16.76	3.64	4.60
40	16.97	3.66	4.64
60	17.02	3.67	4.64
80	17.02	3.73	4.61

Table 5. Calculated elastic anisotropy indices (A^U, A^Z, A_{comp}, A_{shear}, A_1, A_2, A_3) of the Sr_2ZrMoO_6 double perovskites.

P [GPa]	A^U	A_{comp}	A_{shear}	A_1	A_2	A_3
0	0.0817	0.0	0.0081	0.8233	0.8233	1.2408
20	0.0875	0.0	0.0086	0.8128	0.8128	1.2170
40	0.0966	0.0	0.0096	0.8034	0.8034	1.2116
60	0.1042	0.0	0.0103	0.8061	0.8061	1.2241
80	0.1199	0.0002	0.0118	0.8016	0.8016	1.2558

$$A_2 = A_{\{010\}} = \frac{4C_{55}}{C_{22} + C_{33} - 2C_{23}} \tag{10b}$$

$$A_3 = A_{\{010\}} = \frac{2C_{66}}{C_{11} - C_{12}} \tag{10c}$$

These equations further illustrate the anisotropic nature of the shear modulus in different crystallographic directions.

A crystal shows isotropic behavior if $A_1 = A_2 = A_3 = 1$, any deviation from 1 indicates the level of elastic anisotropy. Table 5 displays the values of A_1, A_2, and A_3; the universal anisotropy index (A^U); and shear anisotropy (A_{shear}) for Sr_2ZrMoO_6 under various pressures. It is observed that values of both A[100] and A[010] decrease with increasing pressure. However, A[001] initially decreases up to 40 GPa and then increases, similar to the behavior reported for tetragonal WN_2.[38] The reduction in A[100] with increasing pressure can be explained by the rise in longitudinal modes C_{11} and C_{33}, alongside the decrease in C_{44}. These results suggest that higher pressure leads to increased elastic anisotropy of Sr_2ZrMoO_6 (**Figure 4**a).

Acoustic velocities have a close relationship with elastic constants and are influenced by the direction of propagation and crystal symmetry. In a tetragonal structure, transverse and longitudinal wave modes are only feasible along specific symmetry directions, such as [001], [001], and [110]. In other directions, the waves are a combination of transverse and longitudinal modes, and their behavior can be expressed as the combination of these modes.[39] We have

$$v_l^{[100]} = v_l^{[010]} = \sqrt{C_{11}/\rho}, \quad v_{t1}^{[001]} = \sqrt{C_{44}/\rho}, \quad v_{t2}^{[001]} = \sqrt{C_{66}/\rho} \tag{11a}$$

$$v_l^{[001]} = \sqrt{C_{33}/\rho}, \quad v_{t1}^{[100]} = v_{t2}^{[010]} = \sqrt{C_{66}/\rho} \tag{11b}$$

$$v_l^{[100]} = \sqrt{(C_{11} + C_{12} + 2.C_{66})/\rho}, \quad v_{t1}^{[001]} = \sqrt{C_{44}/\rho}, v_{t2}^{[110]} = \sqrt{C_{11} - C_{12}/\rho} \tag{11c}$$

The variation of sound velocities along different crystallographic directions ([100], [001], and [110]) of the material under increasing pressure (see Table ST2, Supporting Information) is presented in Figure 4b. These sound velocities depend on the crystallographic direction, and the rate of increase in sound velocity with pressure varies among the different directions ([100], [001], and [110]).

To better visualize the elastic anisotropy of the compound at different pressures, we have constructed 2D polar plots of Young's and shear moduli, as shown in **Figure 5**. These plots are based on the elastic compliance constants (S_{ij}) and directional cosines (l_i).[40]

$$\frac{1}{E} = S_{11}(l_1^4 + l_2^4) + (2.S_{13} + S_{44})(l_2^2 \cdot l_3^2 + l_1^2 \cdot l_3^2) + S_{33} \cdot l_3^4 + (2.S_{12} + S_{66})l_1^2 \cdot l_2^2 \tag{12a}$$

$$\frac{1}{B} = (S_{11} + S_{12} + S_{13}) - (S_{11} + S_{12} - S_{13} - S_{33}) \cdot l_3^2 \tag{12b}$$

$$\frac{1}{G} = \frac{1}{2}(S_{44} + S_{66})(l_1^4 + l_2^4) + S_{44}l_3^4 + l_1^2 \cdot l_2^2[4(S_{11} - S_{12}) + (S_{44} - S_{66})] + l_3^2(1 - l_3^2) \tag{12c}$$

These plots show that the elastic moduli are highly direction dependent, indicating that their values change according to the specific crystallographic orientation within the material. As pressure increases, the plot representing the bulk modulus is more circular. This suggests that under higher pressure, the bulk modulus remains nearly isotropic, implying that its value is almost uniform in all directions across the pressure range. In contrast, the plots of Young's modulus and shear modulus exhibit different behavior. As pressure increases, these moduli display moderate levels of anisotropy, indicating that their values vary significantly with direction. This directional dependence elastic modulus illustrates the complex mechanical response of the material, where stiffness and shear resistance vary in different crystallographic orientations under pressure.

Similar results are observed in the 3D plots, which illustrate the elastic anisotropy of a material at different levels of pressure (**Figure 6**). The 3D plot of the bulk modulus surface is more spherical, which indicates a relatively lower degree of anisotropy. Meanwhile, the shear modulus surface shows a moderate level of anisotropy, falling between the behavior of Young's and bulk moduli.

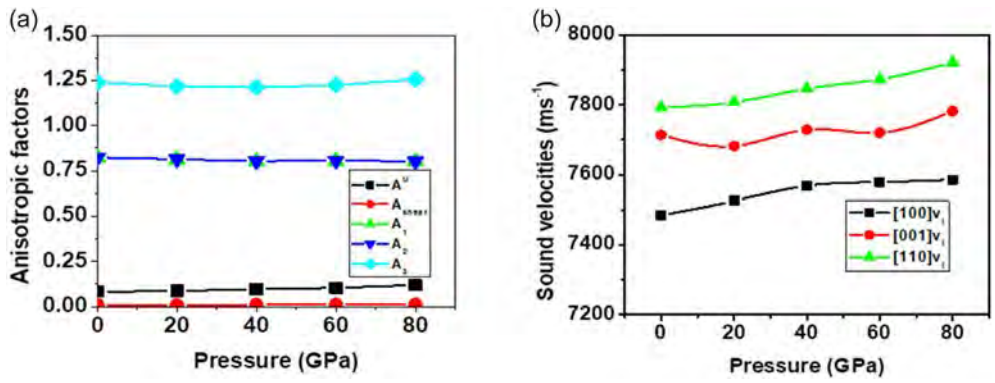

Figure 4. a,b) The variation of anisotropic factor values and sound velocities at different isotropic directions of Sr_2ZrMoO_6 at different pressures.

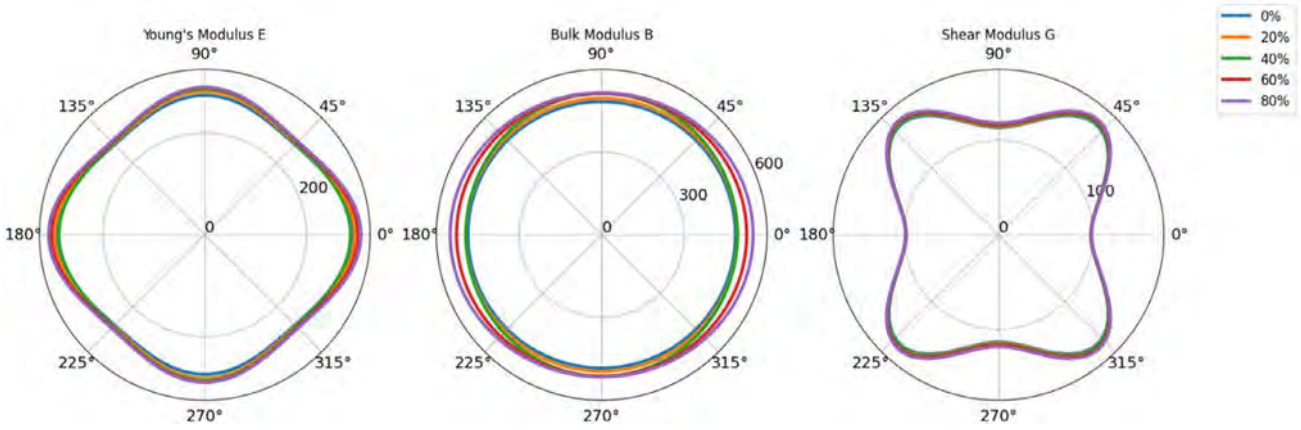

Figure 5. The orientation-dependent elastic moduli (E, B, G) of Sr_2ZrMoO_6 double perovskite at different pressures.

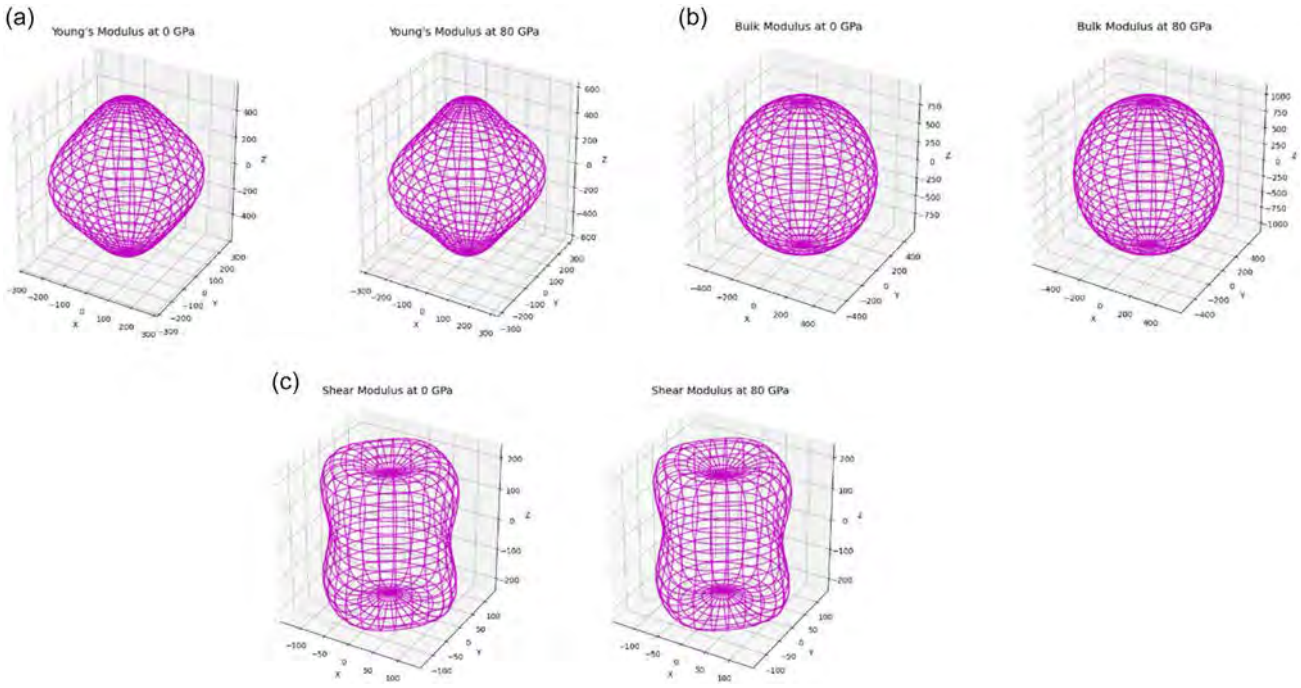

Figure 6. a–c) 3D representation of Young's modulus, bulk modulus, and shear modulus of Sr_2ZrMoO_6 at 0 and 80 GPa.

2.3. Debye Temperature

The Debye temperature (θ_D) is a key temperature that represents the vibrational characteristics of a solid. Above the θ_D, all vibrational modes are active, below which quantum effects play a significant role. DFT phonon dispersions can in principle provide a more direct and more informative approach but due to computational considerations are replaced with approximations provided here. A higher value of θ_D indicates that the material has a higher melting temperature and enhanced thermal conductivity.[41,42] In this study, we employed established techniques and elastic constant data to compute the Debye temperature. The equation below accurately estimates the θ_D value based on the average sound velocity (ν_m).

$$\theta_D = \frac{h}{K_B}\left[\frac{3n}{4\pi}\left(\frac{N_{A\cdot}\rho}{M}\right)\right]^{\frac{1}{3}}\nu_m \tag{13}$$

where h is Planck's constant, K_B is Boltzmann's constant, n is the number of atoms in each formula unit, N_A is Avogadro's number, M is the molecular weight, ρ is density, and ν_m is the average sound velocity, respectively. Furthermore, the average sound velocity is calculated using the following relation.[43]

$$\nu_m = \left[\frac{1}{3}\left(\frac{2}{\nu_t^3} + \frac{1}{\nu_l^3}\right)\right]^{\frac{-1}{3}} \quad (14)$$

Here, ν_l and ν_t represent the velocities of longitudinal and transverse elastic waves, respectively, and can be obtained from Navier's equation.[44]

$$\nu_l = \left[\frac{3B + 4G}{3\rho}\right]^{\frac{1}{2}}, \quad \text{and} \quad \nu_t = \left[\frac{G}{\rho}\right]^{\frac{1}{2}} \quad (15)$$

As shown in **Table 6**, the Sr_2ZrMoO_6 compound becomes more compact and denser with increasing pressure. Additionally, as the material's resistance to longitudinal and shear deformation increases with pressure, the velocities of longitudinal, transverse, and average sound waves slightly rise across the pressure range (**Figure 7**a). The Debye temperature θ_D also increases significantly with pressure. However, in a tetragonal system, the presence of anharmonic effects and structural phase transitions causes θ_D to increase nonlinearly with pressure (Figure 7b).

2.4. Thermal Conductivities

Thermal conductivity is a measure of a material's ability to transfer heat, which represents the heat flux through a material for a specific temperature gradient. The minimum thermal conductivity, k_{min}, refers to the lowest possible thermal conductivity of a material, where the ability to conduct heat is significantly restricted, often due to strong phonon scattering. This concept is crucial in designing materials for thermal management, where lower heat transfer is essential. In this study, the anisotropy in k_{min} for the Sr_2ZrMoO_6 double perovskite at various pressures can be determined using the Cahill model, which is based on the sum of one longitudinal and two transverse sound velocities.[45,46]

$$k_{min} = \frac{K_B}{2.48}\, n^{\frac{2}{3}} (\nu_l + \nu_{t1} + \nu_{t2}) \quad (16)$$

where n is the number density of atoms per volume.

The minimum thermal conductivity of Sr_2ZrMoO_6 is affected by pressure as well as anisotropy in the elastic and acoustic characteristics of the material as presented in **Table 7**. The minimum thermal conductivity increases slightly with pressure, indicating pressure-induced modifications in lattice dynamics and sound velocity. This trend points to increased phonon transfer during compression. The anisotropic nature of k_{min} arises from changes in sound velocities along different crystallographic directions. The values of k_{min} are in the order [001] > [110] > [100] direction, indicating directional variations in heat transmission. A higher k_{min} along the [001] direction indicates better acoustic transport, whereas lower values along the [110] and [100] directions reflect better acoustic dispersion. The minimum thermal conductivity of Sr_2ZrMoO_6 at 0 GPa, evaluated using Cahill's method, exhibits values nearly identical to those observed in Ga_3BN_4 nitrides, as reported by Yang et al.[47]

The thermodynamic properties, including the specific heat capacity (C_V), were calculated using the quasiharmonic Debye model[48] across a temperature and pressure range of 0–800 K and 0–80 GPa, respectively. These computations were performed based on the equation of state derived from the quasiharmonic approximation of the Debye model. The specific heat capacity is given by the following expression

Table 6. Calculated density (ρ); longitudinal, transverse, and average sound velocities (ν_l, ν_t, ν_m); and Debye temperature (θ_D) of Sr_2ZrMoO_6 at different pressures.

P [GPa]	ν	ρ [g cm^{-3}]	ν_l [m s^{-1}]	ν_t [m s^{-1}]	ν_m [m s^{-1}]	θ_D [K]
0	0.225	5.59	7498.32	4464.33	4942.32	531.55
20	0.227	5.68	7498.79	4456.16	4934.17	533.50
40	0.229	5.72	7533.14	4467.83	4948.01	536.25
60	0.230	5.76	7543.82	4465.53	4946.36	537.32
80	0.231	5.78	7574.01	4480.83	4963.57	539.81

Table 7. The minimum thermal conductivity in (WmK^{-1}) of Sr_2ZrMoO_6 at different pressures evaluated by Cahill's method.

P [GPa]	n [10^{28}]	$K_{min}^{[100]}$	$K_{min}^{[001]}$	$K_{min}^{[110]}$	k_{min}
0	8.79	1.826	1.932	1.804	1.854
20	8.79	1.827	1.932	1.807	1.856
40	8.79	1.834	1.945	1.815	1.865
60	8.79	1.838	1.956	1.818	1.871
80	8.79	1.846	1.971	1.825	1.881

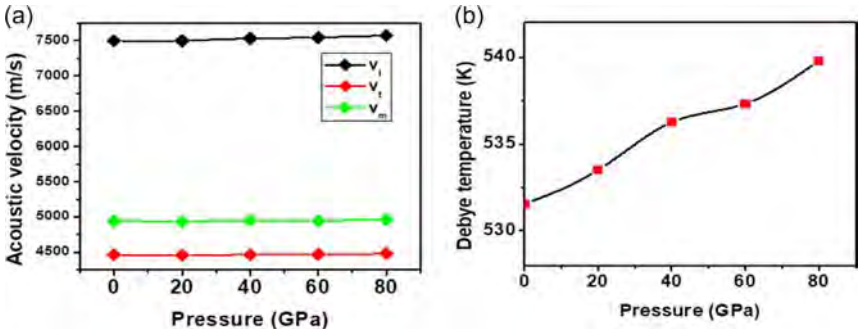

Figure 7. a,b) Variation of acoustic velocities and Debye temperature of Sr_2ZrMoO_6 at different pressures.

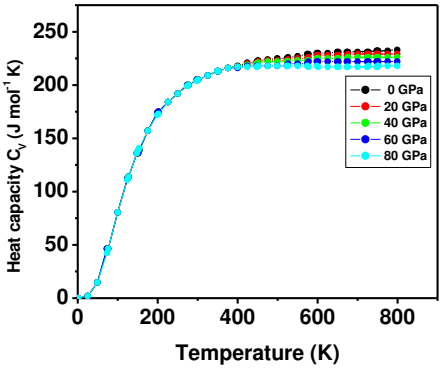

Figure 8. Variation of specific heat capacity of Sr_2ZrMoO_6 double perovskite with temperature.

$$C_V = 3K\left[4D(\theta/T)\left(\frac{\theta_D}{T}\right) - \frac{\frac{3\theta_D}{T}}{e^{\frac{\theta_D}{T}} - 1}\right] \tag{17}$$

where n represents the number of atoms per formula unit, K is the Boltzmann constant, θ_D is the Debye temperature, and $D(\theta/T)$ is the Debye integral and is defined as

$$D(\theta/T) = \frac{3}{\left(\frac{\theta}{T}\right)^3}\int_0^{\theta/T}\frac{x^3}{e^x - 1}dx \tag{18}$$

Figure 8 presents the variation of specific heat (C_V) as a function of temperature (0–800 K) at constant volume for Sr_2ZrMoO_6 under different applied pressures (0–80 GPa). The specific heat at constant volume represents the material's ability to store thermal energy via vibrational modes in the crystal lattice. At low temperatures (<340 K), C_V increases rapidly with temperature across all pressures. The gradual increase in vibrational modes is responsible for this behavior, as thermal energy becomes sufficient to excite lower-frequency phonons. At higher temperatures (>340 K), C_V approaches a plateau near the Dulong–Petit limit ($3R$, where R is the gas constant). However, the exact plateau value decreases with increasing pressure due to pressure-induced effects on the lattice dynamics. The specific heat (C_V) decreases systematically as pressure increases, with values of 231.41 J $(mol{\cdot}K)^{-1}$ at 0 GPa, 228.26 J $(mol{\cdot}K)^{-1}$ at 20 GPa, 225.15 J $(mol{\cdot}K)^{-1}$ at 40 GPa, 221.95 J $(mol{\cdot}K)^{-1}$ at 60 GPa, and 218.28 J $(mol{\cdot}K)^{-1}$ at 80 GPa. This decrease in C_V corresponds to the compression of the lattice under pressure.

3. Conclusion

This study explores the structural properties, elastic anisotropy, and thermal anisotropy of double perovskite Sr_2ZrMoO_6 under isotropic pressures ranging from 0 to 80 GPa. The results reveal significant elastic anisotropy, with the elastic constants C_{11}, C_{33}, and C_{44} exhibiting distinct pressure-dependent behavior. The material demonstrates strong resistance to uniaxial compression, particularly along the [001] direction, which indicates strong atomic bonding along this axis. As pressure increases, the bulk, shear, and Young's moduli rise, indicating improved mechanical stability. The consistently high G/B ratio, negative Cauchy constant, and low Poisson's ratio suggest that the compound remains brittle under high pressure, characterized by strong covalent bonding. Furthermore, the thermal conductivity of the compound exhibits anisotropy, influenced by different sound velocities along different crystallographic directions. This anisotropic behavior is supported by the calculated minimum thermal conductivities, which also vary with pressure and become more pronounced at higher pressure. This anisotropy in κ_{min} follows the order [001] > [110] > [100] direction, with better acoustic transport along [001] and greater acoustic scattering along [110] and [100] directions. The specific heat (C_V) of Sr_2ZrMoO_6 under pressures ranging from 0 to 80 GPa demonstrates notable dependencies on both pressure and temperature. At lower temperatures (<340 K), C_V increases rapidly due to the excitation of low-frequency phonons. At higher temperatures (>340 K), C_V approaches the Dulong–Petit limit, with the plateau value decreasing as pressure increases, indicating pressure-induced alterations in lattice dynamics. The thermal properties of the material are significantly influenced by lattice compression, as evidenced by the systematic decrease in C_V from 231.41 J $(mol{\cdot}K)^{-1}$ at 0 GPa to 218.28 J $(mol{\cdot}K)^{-1}$ at 80 GPa.

4. Experimental Section

The geometrical stability, as well as the elastic and thermal anisotropy of the Sr_2ZrMoO_6, was examined through computational methods using Quantum ESPRESSO code[49] based on DFT.[50,51] To deal with the electronic exchange and correlation,[52,53] we used the Perdew–Burke–Ernzerhof method along with the generalized gradient approximation. Vanderbilt's nonlocal ultrasoft pseudopotentials[54] were used for the ion-electron interactions. A plane wave basis set with an energy cutoff of 70 Ry to represent the wave functions accurately was used. The k-point sampling was carried out with a density of $8 \times 8 \times 8$ for structural optimization and $12 \times 12 \times 12$ for the calculation of elastic and thermal properties.[55] The convergence thresholds for total energy and atomic forces were set at 10^{-6} eV and 10^{-3} eV Å^{-1}, respectively. We evaluated the elastic values using the stress–strain approach, which introduced slight deformations in strain and calculated the resulting stress tensors.[56] The pressure-dependent properties of the material were evaluated by applying isotropic pressure ranging from 0 to 80 GPa. For thermal property calculations, the Debye temperature was calculated using the average sound velocity obtained from the longitudinal and transverse elastic wave velocities.[41] The minimum thermal conductivity was calculated using Cahil's model, considering the anisotropic sound velocities along different crystallographic directions.[45]

Supporting Information

Supporting Information is available from the Wiley Online Library or from the author.

Conflict of Interest

The authors declare no conflict of interest.

Author Contributions

Peshal Pokharel: contributed to conceptualization, methodology, software, visualization, validation, and writing—original draft. **Shshit Kumar Yadav**: contributed to resources and writing—review and editing. **Nurapati Pantha**: contributed to data curation and writing—review and editing.

Bikash Sharma: contributed to data curation and validation. **Devendra Adhikari**: contributed to resources, supervision, and formal analysis.

Data Availability Statement

The data that support the findings of this study are available from the corresponding author upon reasonable request.

Ethical Statement

The work is based on the authors' original research, and the analysis presented is accurate.

Keywords

double perovskites, elastic anisotropies, optical anisotropies, sound velocities, thermal conductivities

Received: November 20, 2024
Revised: January 22, 2025
Published online: February 2, 2025

[1] M. Manzoor, M. W. Iqbal, M. Imran, N. A. Noor, A. Mahmood, Y. M. Alanazi, S. Aftab, *J. Mater. Res. Technol.* **2022**, *18*, 4775.
[2] M. W. Iqbal, M. Manzoor, S. Gouadria, M. Asghar, M. Zainab, N. N. Ahmad, T. Zahid, *Mater. Sci. Eng., B* **2023**, *290*, 116338.
[3] H. Zhou, Q. Chen, G. Li, S. Luo, T. B. Song, H. S. Duan, Y. Yang, *Science* **2014**, *345*, 542.
[4] M. Manzoor, D. Bahera, R. Sharma, F. Tufail, M. W. Iqbal, S. K. Mukherjee, *Int. J. Energy Res.* **2022**, *46*, 23698.
[5] P. Pokharel, S. K. Yadav, N. Pantha, D. Adhikari, *Phys. Status Solidi B* **2024**, *261*, 2400156.
[6] M. Husain, N. Rahman, N. Sfina, N. H. Al-Shaalan, S. Alharthi, S. A. Alharthy, M. Y. Khan, *Opt. Quantum Electron.* **2023**, *55*, 920.
[7] Y. Wang, Z. Lv, L. Zhou, X. Chen, J. Chen, Y. Zhou, V. A. L. Roy, S. T. Han, *J. Mater. Chem. C* **2018**, *6*, 1600.
[8] Y. Meng, X. Li, S. Wang, C. Lau, H. Hu, Y. Ke, Y. Long, *Nano Energy* **2022**, *91*, 106632.
[9] Q. Tang, X. Zhu, *J. Mater. Chem. C* **2022**, *10*, 15301.
[10] R. Roy, J. Am, *Ceram. Soc.* **1954**, *37*, 581.
[11] T. Nakamura, J. H. Choy, *J. Solid State Chem.* **1977**, *20*, 233.
[12] R. Li, Q. Shao, E. Gao, Z. Liu, *Extreme Mech. Lett.* **2020**, *34*, 100615.
[13] S. A. Dar, V. Srivastava, U. K. Sakalle, *J. Magn. Magn. Mater.* **2019**, *484*, 298.
[14] T. Saha-Dasgupta, *Mater. Res. Express* **2020**, *7*, 014003.
[15] M. J. Cao, Y. Ji, Z. Shao, *Energy Environ. Sci.* **2022**, *15*, 2200.
[16] K. W. Kim, S. Ghosh, S. Buvaev, S. Mhin, J. L. Jones, A. F. Hebard, D. P. Norton, *J. Appl. Phys.* **2012**, *112*, 083909.
[17] N. A. Teli, B. Want, *J. Magn. Magn. Mater.* **2024**, *601*, 172183.
[18] J. Feng, B. Xiao, R. Zhou, W. Pan, D. R. Clarke, *Acta Mater.* **2012**, *60*, 3380.
[19] S. C. Tidrow, *Ferroelectrics* **2014**, *470*, 13.
[20] R. B. Ray, G. C. Kaphle, R. K. Rai, D. K. Yadav, R. Paudel, D. Paudyal, *J. Alloys Compd.* **2021**, *867*, 158906.
[21] L. Bao, Z. Kong, D. Qu, Y. Duan, *Mater. Today Commun.* **2020**, *24*, 101337.
[22] P. Li, L. Ma, M. Peng, B. Shu, Y. Duan, *J. Alloys Compd.* **2018**, *747*, 905.
[23] Z. Jiao, Q. J. Liu, F. S. Liu, W. P. Wang, Y. G. Wang, Y. Li, Z. T. Liu, *Braz. J. Phys.* **2016**, *46*, 213.
[24] S. Yip, J. Li, M. J. Tang, J. G. Wang, *Mater. Sci. Eng., A* **2001**, *317*, 236.
[25] W. Voigt, *Lehrbuch der Kristallphysik*, Teubner, Leipzig **1928**.
[26] A. Reuss, *J. Appl. Math. Mech.* **1929**, *9*, 49.
[27] R. Hill, *Proc. Phys. Soc. London* **1952**, *65*, 349.
[28] R. P. Thompson, W. J. Clegg, *Curr. Opin. Solid State Mater. Sci.* **2018**, *22*, 100.
[29] Y. J. Tian, B. Xu, Z. S. Zhao, *Int. J. Refract. Met. Hard Mater.* **2012**, *33*, 93.
[30] Y. Wu, L. Ma, X. Zhou, Y. Duan, L. Shen, M. Peng, *Int. J. Refract. Met. Hard Mater.* **2022**, *109*, 105985.
[31] A. R. Boccaccini, *J. Mater. Process. Technol.* **1997**, *65*, 302.
[32] J. E. Field, C. J. Freeman, *Philos. Mag. A* **1981**, *43*, 595.
[33] S. N. Monteiro, A. L. D. Skury, M. G. de Azevedo, G. S. Bobrovnitchii, *J. Mater. Res. Technol.* **2013**, *2*, 68.
[34] S. I. Ranganathan, M. Ostoja-Starzewski, *Phys. Rev. Lett.* **2008**, *101*, 055504.
[35] N. Miao, B. Sa, J. Zhou, Z. Sun, *Comput. Mater. Sci.* **2011**, *50*, 1559.
[36] J. F. Nye, R. B. Lindsay, *Physical Properties of Crystals: Their Representation by Tensors and Matrices*, Oxford University Press, Oxford, UK **1984**.
[37] H. C. Zhai, X. F. Li, J. Y. Du, *Mater. Trans.* **2012**, *53*, 1247.
[38] H. Zhai, X. Li, J. Du, *Mater. Trans.* **2012**, *53*, 1247.
[39] J. Wei, L. Zhang, Y. Liu, *Solid State Commun.* **2021**, *326*, 114182.
[40] Y. H. Duan, Y. Sun, M. J. Peng, *Comput. Mater. Sci.* **2014**, *92*, 258.
[41] O. L. Anderson, *J. Phys. Chem. Solids* **1963**, *24*, 909.
[42] P. Pokharel, S. K. Yadav, N. Pantha, D. Adhikari, *J. Phys. Chem. Solids* **2024**, *193*, 112198.
[43] Y. Wu, L. Bao, X. Wang, Y. Wang, M. Peng, Y. Duan, *Mater. Today Commun.* **2020**, *25*, 101410.
[44] W. Z. Bao, D. Liu, P. Li, Y. H. Duan, *Ceram. Int.* **2019**, *45*, 1857.
[45] D. G. Cahill, S. K. Watson, R. O. Pohl, *Phys. Rev. B* **1992**, *46*, 6131.
[46] J. Ji, H. Bu, Y. Duan, M. Peng, H. Qi, X. Wang, L. Shen, *Vacuum* **2023**, *214*, 112232.
[47] C. Yang, Y. Duan, J. Yu, M. Peng, S. Zheng, M. Li, *Vacuum* **2023**, *207*, 111626.
[48] M. A. Blanco, E. Francisco, V. Luania, *Comput. Phys. Commun.* **2004**, *158*, 57.
[49] P. Giannozzi, S. Baroni, N. Bonini, M. Calandra, R. Car, C. Cavazzoni, D. Ceresoli, G. L. Chiarotti, M. Cococcioni, I. Dabo, A. Dal Corso, *J. Phys.: Condens. Matter* **2009**, *21*, 395502.
[50] W. Koch, M. C. Holthausen, *A Chemist's Guide to Density Functional Theory*, 2nd ed., Wiley-VCH Verlag GmbH, Germany **2001**.
[51] R. G. Parr, W. Yang, *Density Functional Theory of Atoms and Molecules*, Oxford University Press, New York, NY **1989**.
[52] D. C. Langreth, J. P. Perdew, *Phys. Rev. B* **1980**, *21*, 5469.
[53] J. P. Perdew, K. Burke, M. Ernzerhof, *Phys. Rev. Lett.* **1996**, *77*, 3865.
[54] D. Vanderbilt, *Phys. Rev. B* **1990**, *41*, 7892.
[55] H. J. Monkhorst, J. D. Pack, *Phys. Rev. B* **1977**, *16*, 1748.
[56] R. Golesorkhtabar, P. Pavone, J. Spitaler, P. Puschnig, C. Draxl, *Comput. Phys. Commun.* **2013**, *184*, 1861.

Journal of Institute of Science and Technology, 30(2), 01-13 (2025)
ISSN: 2467-9062 (print), e-ISSN: 2467-9240
https://doi.org/10.3126/jist.v30i2.76851

Research Article

FIRST PRINCIPLES STUDY OF THE ELECTRONIC, OPTICAL, ELASTIC, AND THERMAL PROPERTIES OF DOUBLE PEROVSKITE Sr_2MgWO_6 FOR OPTOELECTRONIC APPLICATIONS

Peshal Pokharel [1,2,3], Shashit Kumar Yadav[2*], Devendra Adhikari[2], Nurapati Pantha[1*]
[1]Central Department of Physics, Tribhuvan University, Kritipur, Nepal.
[2]Department of Physics, Mahendra Morang Adarsh Multiple Campus, Tribhuvan University, Biratnagar, Nepal.
[3]Central Campus of Technology, Tribhuvan University, Dharan, Nepal.
**Correspondence: yadavshashit@yahoo.com, mrnurapati@gmail.com*

***(Received:** May 31, 2025; **Revised:** October 14, 2025; **Accepted:** October 16, 2025)*

ABSTRACT

The double perovskite Sr_2MgWO_6 exhibits outstanding mechanical, electronic, and optical properties, making it a potential candidate for high-performance optical and optoelectronic applications. In this regard, we investigated the electronic, magnetic, optical, elastic, and structural properties of the double perovskite Sr_2MgWO_6 using the Quantum ESPRESSO code. Structural stability has been confirmed through calculations of formation energy and the tolerance factor. The material exhibited a wide-band-gap (3.18 eV) semiconductor with intense polarization ($\varepsilon_1(\omega) = 12.46$) and a decreasing $\varepsilon_2(\omega)$ peak with photon energy. Elastic parameters, including elastic constants, bulk modulus, shear modulus, and Young's modulus, were determined using the stress-strain method. The calculated elastic constants satisfied Born-Huang criteria for mechanical stability. Calculated high value of bulk modulus (B), and Young's modulus (E) indicated the material's high resistance to volumetric deformation and stiffness, with a moderate shear modulus. A G/B ratio greater than 0.57, a negative Cauchy constant, and a low Poisson's ratio collectively indicated brittle behavior. The calculated Debye temperature of 492.34 K and specific heat capacity (C_v) of 373.4 J/mol-K further emphasized the mechanical strength, thermal stability, and high thermal conductivity of the material. These findings suggest that Sr_2MgWO_6 could be an excellent material for optical waveguides, light-emitting devices, and other optoelectronic technologies.

Keywords: Dielectric, Double perovskite, Electronic properties, Formation energy, Structural stability, Tolerance factor

INTRODUCTION

Perovskite materials have garnered significant attention due to their remarkable structural versatility and wide-ranging applications in photovoltaics (Rahman *et al.*, 2023), thermoelectrics (Aziz *et al.*, 2022), spintronics (Wang *et al.*, 2018), and optoelectronics (Lu *et al.*, 2020). Among these, double perovskites ($A_2BB'O_6$) are particularly noteworthy for their unique structural, electronic, magnetic, and optical properties (Manzoor *et al.*, 2022). The structural flexibility of perovskites enables the incorporation of a diverse array of elements, allowing for the customization of properties tailored to specific technological applications. Recent advances have underscored their potential in renewable energy, data storage, and high-performance electronic systems, establishing them as vital materials in modern materials science (Pokharel *et al.*, 2024a).

Double perovskites were first explored in the early 1950s (Meng *et al.*, 2022) and became widely studied from the late 1950s to the mid-1980s (Tang & Zhu, 2022). Their structure is an extension of simple perovskites, represented by the formula $A_2BB'X_6$. In this structure, A-site cations occupy octahedral positions, B and B' cations are found in tetrahedral and octahedral sites, and X anions fill the spaces between them [Figure 1]. In strontium magnesium tungstate (Sr_2MgWO_6), Sr^{2+} ions occupy the A-site, Mg^{2+}, and W^{6+} ions are situated at the B and B' sites, respectively, and O^{2-} anions are positioned at the X sites. Sr_2MgWO_6, known for its pronounced elastic anisotropy and unique thermal properties, crystallizes in the tetragonal I4/m space group, making it a promising material for further study. Its crystal structure features Sr^{2+} ions coordinated by twelve O^{2-} atoms, forming distorted SrO_{12} cuboctahedra that share corners and faces with adjacent MgO_6 and WO_6 octahedra. The Sr–O bond lengths range from 2.62 Å to 3.01 Å, contributing to the material's elastic and thermal anisotropy. Mg^{2+} ions form MgO_6 octahedra with uniform Mg–O bond lengths of 2.06 Å, while W^{6+} ions are coordinated within WO_6 octahedra, with bond lengths ranging from 1.92 Å to 1.93 Å. These structural characteristics, including corner-sharing

octahedral tilts between 0° and 16°, play a critical role in defining the mechanical stability and electronic properties of Sr_2MgWO_6.

Many double perovskites, particularly those that are environmentally friendly and lead-free, remain underexplored, despite the substantial progress that has been made. These materials provide safer and more sustainable alternatives to the noxious compounds currently used in optoelectronic and thermoelectric applications. Among them, Sr_2MgWO_6 has garnered attention due to its composition of earth-abundant, non-toxic elements. In addition, it has the potential to demonstrate exceptional mechanical stability, a wide band gap, and desirable optical properties.

In this work, we employ density functional theory (DFT) to investigate the ground-state properties of Sr_2MgWO_6, focusing on its elastic anisotropy, thermal stability, and optical characteristics. Our study aims to elucidate the interplay between structural distortions and the material's mechanical and electronic properties under varying pressure conditions. By exploring these properties, we provide new insights into potential applications of the material in thermal management, spintronics, and optoelectronics, contributing to the broader pursuit of eco-friendly, high-performance perovskite materials.

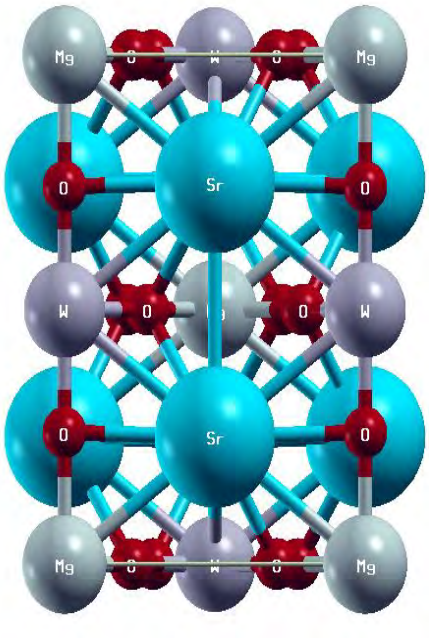

Figure 1. Unit cell of Sr_2MgWO_6 double perovskite.

MATERIALS AND METHODS

The geometrical stability, as well as the elastic and thermal anisotropy of Sr_2ZrMoO_6, was examined through computational methods using the Quantum ESPRESSO code (Giannozzi *et al.*, 2009) based on Density Functional Theory (Koch *et al.*, 2015; Parr *et al.*, 1989) . The spin-polarised electronic band structure of Sr_2MgWO_6 was calculated using both the Generalized Gradient Approximation (GGA) (Langreth & Perdew, 1980; Perdew *et al.*, 1996) and the GGA + U approach (Pokharel *et al.*, 2024). The GGA + U method was applied to account for the on-site Coulomb interactions in the partially filled 5d orbitals of W atoms. Vanderbilt's non-local ultra-soft pseudopotentials (Vanderbilt, 1990) were used for the ion-electron interactions. A plane wave basis set with an energy cutoff of 70 Ry was employed to represent the wave functions precisely. The k-point sampling was carried out with a density of 8 × 8 × 8 for optimization of the structure and the calculation of elastic and thermal properties, a 12 × 12 × 12 grid was employed (Pack & Monkhorst, 1977). The convergence thresholds for total energy and atomic forces were taken at 10^{-6} eV and 10^{-3} eV/Å, respectively. We evaluated the elastic values using the stress-strain approach, which introduced slight deformations in strain and calculated the resulting stress tensors (Golesorkhtabar *et al.,* 2013). The pressure-dependent properties of the material were evaluated by applying isotropic pressure ranging from 0 to 80 GPa. For thermal property calculations, the Debye temperature was estimated using the acoustic velocity derived from the longitudinal and transverse elastic wave velocities (Anderson, 1963). The thermodynamic properties, such as the specific heat capacity (C_V), were calculated using the quasiharmonic Debye model (Blanco *et al.*, 2004).

RESULTS AND DISCUSSION

Structural Properties

In the present calculations, the optimized lattice parameters of the compound are obtained by minimizing the total energy for the unit cell volume. A complete structural optimization is achieved for tetragonal Sr_2MgWO_6 as shown in Figure 2. From the optimized structure, value of lattice parameter is 5.59 Å, and the estimated values of Sr-O, W-O, and Mg-O bond lengths (in Å) were found to be 2.8023, 1.9341, and 2.0698, respectively.

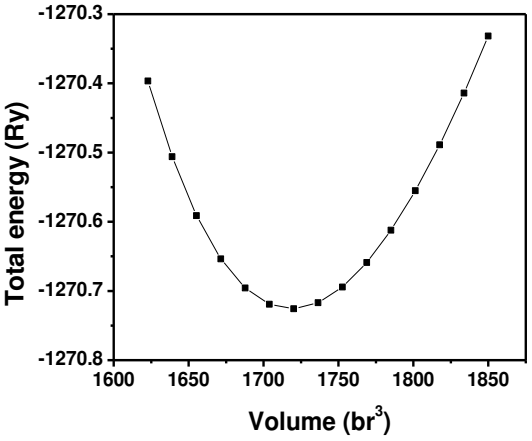

Figure 2. Optimization plots of Sr_2MgWO_6 double perovskite using GGA.

The tolerance factor t helps determine the stable configuration of the material in its ground state (Tidrow, 2014). For a double perovskite material, it is calculated as:

$$t = \frac{r_A + r_O}{\sqrt{2}\,(r_B + r_O)} \qquad (1)$$

Where r_A, r_B, and r_O represent the ionic radii of the Sr cation, the average ionic radius of the Mg and W cations, and the oxygen anion, respectively. The calculated tolerance factor for the material is approximately 0.917, which falls within the stability range of a tetragonal perovskite structure ($0.85 \leq t \leq 0.98$), showing its stability.

Formation energy is an important concept in materials science and solid-state physics, particularly the study of defects, doping, and phase stability. It is defined as the energy required to form a compound, defect, or structure from its constituent elements. The ground state stability has also been evaluated by calculating the formation energy using the following relation (Ray *et al.*, 2021).

$$\Delta H_f = \frac{E_{\text{total}(Sr_2MgWO_6)} - (2E_{Sr} + E_{Mg} + E_W + 6E_O)}{6} \qquad (2)$$

Here, $E_{\text{total}(Sr_2ZrMoO_6)}$ is the equilibrium energy of the Sr_2MgWO_6 perovskite, and E_{Sr}, E_{Mg}, E_W, and E_O are the respective energies of strontium, magnesium, tungsten, and oxygen atoms in their bulk forms. The calculated formation energy for the compound is −7.981 eV/atom. This negative value indicates that the compound is thermodynamically stable, suggesting it is likely to be synthesizable under appropriate experimental conditions (Patwe *et al.*, 2005).

Electronic Properties and Optical Anisotropy

The energy band structure is an important feature for describing the electronic properties of compounds. The electronic states of the transition metal ions are influenced by crystal field splitting and the symmetry of the crystal structure. In this study employs GGA and GGA+U approximations to determine the spin-polarized band structure of double perovskite at high-symmetry k-points. The GGA+U method includes a Hubbard U term, which helps to better represent the localized interactions of electrons in the partially filled 5d orbitals of W (tungsten). This adjustment allows GGA+U to describe the band structure and PDOS of the material more accurately. Using both GGA and GGA + U methods, the calculated band gap of 3.18 eV and also symmetry on the spin-up and spin-down band structure indicate that the non-magnetic nature of the material [Figure 3(a, b)], which matches well with those reported by Dar *et al.* for a wide band gap semiconductor (4.0 eV) double perovskite Ba_2InTaO_6 (Dar *et al.*, 2019).

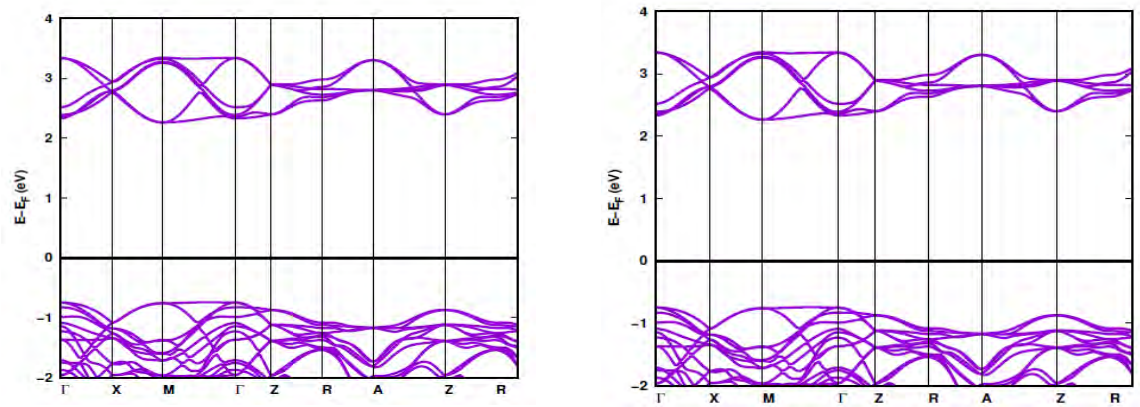

Figure 3. Spin-polarized band structure of Sr_2MgWO_6 double perovskite (a) spin up and (b) spin down within the GGA +U approach.

The PDOS plot [Figure 4] illustrates the contributions of different orbitals (s, p, d) from specific atoms (Sr, Mg, W) to the total density of states (DOS) in the material. The Sr-s and Sr-p orbitals show a relatively minor contribution, while the Mg-d, W-s, and W-d orbitals play a more prominent role, with pronounced peaks indicating a higher density of states at specific energy levels. The substantial contributions of the W-s and W-d orbitals highlight the critical role of tungsten in shaping the electronic properties of the material. The W-d orbitals, in particular, dominate near the Fermi level, making them the primary contributors to the conduction band. Both W-s and W-d orbitals also contribute to the valence band, with W-s orbitals influencing the lower-energy regions and W-d orbitals affecting the higher-energy regions.

The significant presence of W-d orbitals in both the conduction and valence bands suggests that tungsten is a key factor in the material's electrical conductivity. As shown in Figure 4, the observed spin-up/spin-down symmetry confirms the nonmagnetic nature of the perovskite. Its semiconducting character suggests potential for applications in optoelectronic devices such as solar cells.

Optical Properties

Exploring the optical behavior of Sr_2MgWO_6 provides valuable insights into its electronic properties. The interaction of these materials with light provides useful information about their possible applications. Fundamental optical factors like the absorption coefficient, refractive index, and dielectric function are important in determining the feasibility of many optoelectronic devices such as solar cells, LEDs, and lasers. The dielectric function describes the material's optical and electrical properties, including how it interacts with electromagnetic fields at various energy levels. This function is important to understanding how electrons move between energy bands when light is incident on the material.

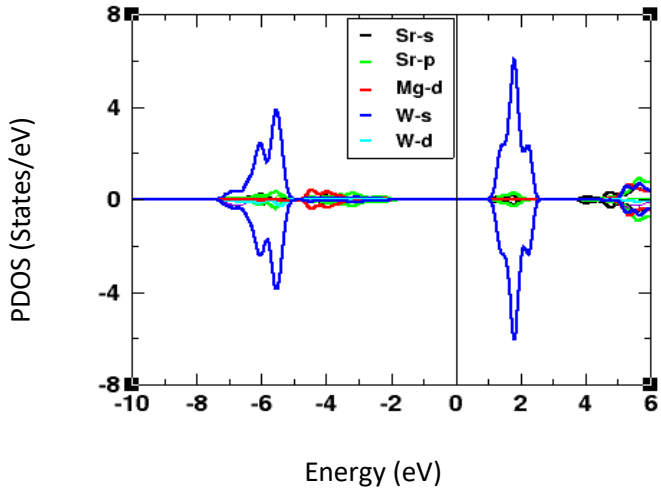

Figure 4. Spin-polarized PDOS plot of Sr_2MgWO_6 double perovskite within the GGA + U approach.

The dispersion relationship of dielectric functions can be determined by examining the connection between the wave vector or leap matrix and the dielectric function (Yang *et al.*, 2022).

The dielectric function is expressed as (Wu *et al.*, 2021):

$$\varepsilon(\omega) = \varepsilon_1(\omega) + i\varepsilon_2(\omega) \qquad (3)$$

And the imaginary component of the dielectric function, $\varepsilon_2(\omega)$, is given as (Lu *et al.*, 2021).

$$\varepsilon_2(\omega) = \frac{8\pi^2 e^2}{2\omega^2 m^2} \sum_n \sum_{n'} \int_{BZ} |P_{nn'}(k)|^2 f_{kn}(1 - f_{kn'})\, \partial(E_n^k - E_{n'}^k - h\omega) \frac{\partial^3 k}{2\pi^3} \qquad (4)$$

Here, f_{kn} is the Fermi-Dirac distribution function, $P_{nn'}(k)$ is the projection of the momentum dipole matrix elements on the direction of the field. $E_n^k(k)$ is the energy of an electron.

An expression derived from the Kramers-Kronig transformation (Lucarini *et al.*, 2005) can be used to compute the real component of the dielectric function, $\varepsilon_1(\omega)$.

$$\varepsilon_1(\omega) = 1 + \frac{2}{\pi} P \int_0^{\infty} \left[\frac{\omega' \varepsilon_2(\omega')}{\omega'^2 - \omega^2}\right] d\omega' \qquad (5)$$

The real part, $\varepsilon_1(\omega)$, describes the ability to disperse and polarize light through the material. On the other

hand, the imaginary part, $\varepsilon_2(\omega)$, indicates the capability to absorb light energy by the material.

These combined optical properties play a crucial role in determining how well the material converts light into energy and its potential for use in high-performance optoelectronic devices.

The other optical parameters, such as absorption coefficient $\alpha(\omega)$, refractive index $n(\omega)$, and reflectivity $R(\omega)$ are expressed in terms of $\varepsilon_1(\omega)$ and $\varepsilon_2(\omega)$ as;

$$\alpha(\omega) = \sqrt{2\omega\sqrt{\{\varepsilon_1(\omega)\}^2 + \{\varepsilon_2(\omega)\}^2} - \varepsilon_1(\omega)} \quad (6)$$

$$n(\omega) = \sqrt{\frac{1}{2}\sqrt{\{\varepsilon_1(\omega)\}^2 + \{\varepsilon_2(\omega)\}^2} + \varepsilon_1(\omega)} \quad (7)$$

$$R(\omega) = \left|\frac{\sqrt{\varepsilon_1(\omega)+i\varepsilon_2(\omega)}-1}{\sqrt{\varepsilon_1(\omega)+i\varepsilon_2(\omega)}+1}\right|^2 \quad (8)$$

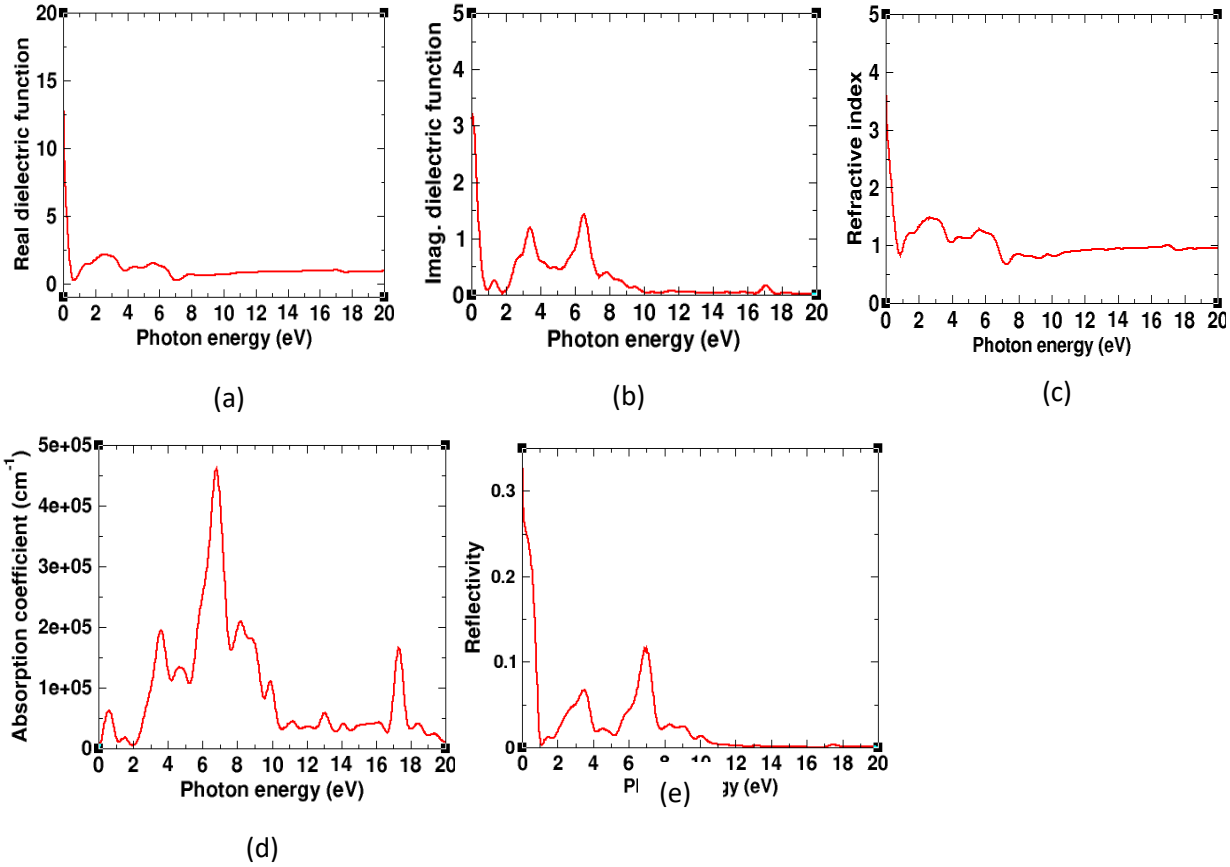

Figure 5. Variation of (a) real and (b) imaginary part of dielectric function (c) refractive index (d) absorption coefficient; (e) reflectivity of Sr_2MgWO_6 double perovskite with photon energy.

Figure 5(a–e) shows the optical parameters that were computed over a photon energy range of 0–20 eV. As shown in Figure 5(a), at static frequency, the polarization response of the material is indicated by the dielectric constant $\varepsilon_1(\omega)$ of 12.46. As photon energy increases, peaks in the dielectric function appear around 2.5 eV, indicating strong interaction with longer wavelengths of light, such as those in the visible or near-infrared regions. The other energy peak at 5.8 eV demonstrates reduced polarizability, corresponding to ultraviolet (UV) light, suggesting potential applications in UV filtering, optoelectronics, and high-frequency devices.

Figure 5(b) illustrates the behavior of $\varepsilon_2(\omega)$ with an initial rise in $\varepsilon_2(\omega)$ which suggests efficient photon absorption at lower energies. This is a result of electronic transitions from the f-orbitals of W or d-orbitals of Mg to unoccupied Sr-3d and O-2p orbitals. The initial increase in $\varepsilon_2(\omega)$ is followed by a decrease, which is a common trend in wide-band-gap semiconductors. These trends emphasize the potential of Sr_2MgWO_6 for optoelectronic applications, where its tunable absorption characteristics could enhance advanced technologies.

Figure 5(c) shows a variation of refractive index, $n(\omega)$ with photon energy. The trend closely follows the real part $\varepsilon_1(\omega)$, highlighting a direct correlation between

the R.I. of material and its polarization response. The R.I. decreases with increasing photon energy, indicating how doping influences the optical characteristics of the material. The absorption coefficient, which is illustrated in Figure 5(d), is a measure that indicates how well a material can absorb light as the energy of the photon increases. It is the interband transitions, which occur when photons with sufficient energy drive electrons to move from the valence band to the conduction band, that are responsible for the significant absorption peak that occurs at approximately 7 eV. This improves the absorption capacity of the material.

Figure 5(e) illustrates the reflectivity spectrum, which offers critical information regarding the light transmission and reflection characteristics of the material. At zero photon energy, the reflectivity is relatively low (0.27), indicating moderate light reflection and suggesting that the material primarily absorbs light at lower energies. As photon energy increases, reflectivity decreases, with distinct peaks at approximately 3.8 eV (0.07) and 6.9 eV (0.12), demonstrating less effective light reflection at higher energies as compared to zero energy. The low reflectivity at lower energies positions the material as a promising candidate for photovoltaic applications, while the peaks at higher energies suggest potential utility in optoelectronic devices.

Elastic Properties

Analysis of the elastic behavior of double perovskite proves essential because it offers fundamental insights into the mechanical stability, dynamic behavior, and strength of materials. This section discusses the mechanical properties and dynamic stability of Sr_2MgWO_6. The tetragonal structure is characterized by six distinct elastic constants (C_{11}, C_{12}, C_{13}, C_{33}, C_{44}, and C_{66}), which were determined using the stress-strain method. These C_{ij} values of Sr_2MgWO_6 are (C_{11} = 228.6 GPa, C_{12} = 69.86 GPa, C_{13} = 101.08 GPa, C_{33} = 229.94, C_{44} =86.96 GPa and C_{66} = 71.58 GPa). The elastic constants provide insight into how a material resists stress from different directions. Specifically, C_{11}, C_{22}, and C_{33} describe how well the material resists deformation along the [100], [010] and [001] directions of the crystal. C_{11} (228.6 GPa) and C_{33} (229.94 GPa) are nearly identical, suggesting that Sr_2MgWO_6 is elastically isotropic along the different directions. The data of C_{44} and C_{66} shows that Sr_2MgWO_6 exhibits moderate shear resistance. The calculated values of C_{ij} that satisfy Born-Huang's mechanical stability criteria (Pokharel *et al.*, 2025) for a tetragonal system

$$C_{11} > 0,\ C_{33} > 0,\ C_{44} > 0,\ C_{66} > 0,\ C_{11}–C_{12} > 0,$$

$$C_{11}+ C_{33}– 2C_{13} > 0,\ 2C_{11}+2C_{12}+ C_{33}+ 4C_{13} > 0 \quad (9)$$

Hooke's law (Bao *et al.*, 2020) describes the dependence of stress (σ_{ij}) to strain (ε_{kl}) in terms of C_{ij} as follows

$$\sigma_{ij} = C_{ijkl}\varepsilon_{kl} \Rightarrow \sigma_{ij} = C_{ij}\varepsilon_{ij} \quad (10)$$

where σ_{ij} is the stress tensor, C_{ij} is the stiffness tensor and ε_{ij} is the strain component.

The Voigt-Reuss-Hill method (Voigt, 1928) (Reuss, 1929) (Hill, 1952) can be used to determine the values of B and G for the tetragonal system and are given as

$$B_V = \frac{1}{9}[2C_{11} + C_{33} + 2C_{12} + 4C_{13}] \quad 11(a)$$

$$B_R = \frac{C^2}{M} \quad 11(b)$$

the shear constant (G_v) of an upper limit is

$$G_V = \frac{1}{30}[M + 3C_{11} - 3C_{12} + 12C_{44} + 6C_{66}] \quad 11(c)$$

with $M = [C_{11} + C_{12} + 2C_{33} - 4C_{44}]$

and $C^2 = (C_{11} + C_{12})C_{33} - 2{C_{13}}^2$

and its lower limit can be expressed in the form as

$$G_R = \frac{15}{[\frac{18B_V}{C^2}+\frac{6}{C_{11}+C_{12}}+\frac{6}{C_{44}}+\frac{3}{C_{66}}]} \quad 11(d)$$

Finally, Voigt and Reuss's mean values are obtained by

$B_H = \frac{(B_V+B_R)}{2}$ and $G_H = \frac{(G_V+G_R)}{2}$

$$E = \frac{9B_HG_H}{3B_H+G_H} \quad 11(e)$$

$$v = \frac{3B_H-2G_H}{2(3B_H+G_H)} \quad 11(f)$$

$$P_C = C_{13}- C_{44} \quad 11(g)$$

The elastic constants listed above were utilized to calculate additional mechanical parameters, including the bulk modulus (B), Young's modulus (Y), and shear modulus (G), using equations 11(a-g). The computed values, such as elastic moduli (E, B, G), Poisson's ratio (ν), and Pugh's ratio (G/B), for the Sr_2MgWO_6 double perovskite, are displayed in Table 1. The high bulk modulus value implies good resistance to volumetric deformation and indicates the material is relatively incompressible. The moderate shear modulus suggests that the compound has a balance between rigidity and flexibility. Furthermore, the high Y values indicate the stiffness of the material, illustrating its strong mechanical abilities as a double perovskite.

Table 1. Calculated values of elastic moduli (B, G, E), Poisson's ratio (υ), G_H/B_H ratio of Sr_2MgWO_6 double perovskites.

B_V (GPa)	B_R (GPa)	B_H (GPa)	G_V (GPa)	G_R (GPa)	G_H (GPa)	E (GPa)	υ	G_H/B_H
129.84	129.39	129.61	78.84	77.60	78.22	195.36	0.249	0.603

The tabulated values of elastic moduli (E, B, G), and the elastic constants (C_{ij}) described above, demonstrate patterns that follow the common behavior noticed in half-metallic double perovskite oxide Sr_2MnTaO_6, as reported by Dar *et al.* (2019) in their study (Dar *et al.,* 2019).

The G/B ratio is a critical parameter for evaluating whether materials exhibit ductile or brittle behavior (Thompson & Clegg, 2018). The materials with $\frac{G}{B} > 0.57$ are considered brittle, while those with $\frac{G}{B} < 0.57$ are classified as ductile. For the material under study, the calculated G/B ratio consistently exceeds 0.57. This indicates that the material retains brittle behavior even under high pressure. Additionally, the negative Cauchy constant further supports the brittle nature of the material.

Elastic Anisotropy

Anisotropy indexes are useful for assessing the mechanical, thermal, and electrical characteristics of a material. The universal anisotropy index (A^U) provides a thorough evaluation of overall anisotropy (Ranganathan & Ostoja-Starzewski, 2008). Furthermore, the shear anisotropy indexes (A_{shear}) and bulk anisotropy (A_{comp}) offer important information about how the material behaves under shear strains and compression, respectively (Miao *et al.*, 2011). These parameters are important for the analysis of the elastic anisotropy of double perovskites under isotropic pressure (Nye, 1985). These indices are defined as follows.

$$A^U = 5\frac{B_V}{B_R} + \frac{G_V}{G_R}6 \qquad 12(a)$$

$$A^Z = \frac{2C_{44}}{C_{11}-C_{12}} \qquad 12(b)$$

$$A_{comp} = \frac{B_V-B_R}{B_V+B_R} \qquad 12(c)$$

$$A_{shear} = \frac{G_V-G_R}{G_V+G_R} \qquad 12(d)$$

Isotropic behavior is indicated when A^U, A_{comp}, and A_{shear} are all equal to 0, while any non-zero values indicate the presence of anisotropy. Moreover, the degree of anisotropy rises as the values of A^U, A_{comp}, and A_{shear} are increased. The compound exhibits an isotropic bulk modulus as indicated A_{comp} = 0. However, the non-zero values of A^U and A_{shear} in Table 2 suggest that the shear modulus and Young's modulus vary across different crystallographic directions, indicating elastic anisotropy in shear and stiffness. In a tetragonal crystal, the anisotropy factors $A_{\{100\}}$, $A_{\{010\}}$ and $A_{\{010\}}$ are defines as (Zhai *et al.*, 2012):

$$A_1 = A_{\{100\}} = \frac{4C_{44}}{C_{11}+C_{33}-2C_{13}} \qquad 13(a)$$

$$A_2 = A_{\{010\}} = \frac{4C_{55}}{C_{22}+C_{33}-2C_{23}} \qquad 13(b)$$

$$A_3 = A_{\{010\}} = \frac{2C_{66}}{C_{11}-C_{12}} \qquad 13(c)$$

These equations further illustrate the anisotropic nature of the shear modulus in different crystallographic directions.

Table 2. Calculated elastic anisotropy indexes ($A^U, A^Z, A_{comp}, A_{shear}, A_1, A_2, A_3$) of the Sr_2MgWO_6 double perovskites.

A^U	A_{comp}	A_{shear}	A_1	A_2	A_3
1.0956	0.00173	0.0079	1.357	1.357	0.902

As reported in Table 2, the calculated values of A^U, A_1 and A_2 are greater than 1, while that of A_3 is less than 1. They collectively indicate a significant deviation from isotropic behaviour. To further illustrate this anisotropy, 2D polar plots of B, G, and ν were constructed, which offer a more precise visualization of their directional dependence across different crystallographic planes. These parameters are expressed in terms of the elastic compliance constants (S_{ij}) and directional cosines (l_i) (Pokharel *et al.*, 2024b).

$$\frac{1}{E} = S_{11}(l_1^4 + l_2^4) + (2.S_{13} + S_{44})(l_2^2.l_3^2 + l_1^2.l_3^2) + S_{33}.l_3^4 + (2.S_{12} + S_{66})\, l_1^2.l_2^2. \quad 14(a)$$

$$\frac{1}{B} = (S_{11} + S_{12} + S_{13}) - (S_{11} + S_{12} - S_{13} - S_{33}).l_3^2 \quad 14(b)$$

$$\frac{1}{G} = \frac{1}{2}(S_{44} + S_{66})(l_1^4 + l_2^4) + S_{44}l_3^4 + l_1^2.l_2^2[4(S_{11} - S_{12}) + (S_{44} - S_{66})] + l_3^2(1 - l_3^2)\left[2(S_{11} + S_{12} - 2S_{13}) + \frac{1}{2}(S_{66} - S_{44})\right]. \quad 14(c)$$

$$\text{and } (\Theta) = \frac{[\,C_{12}cos^4(\Theta) - Bcos^2(\Theta)sin^2(\Theta) + C_{12}sin^4(\Theta)\,]}{[\,C_{22}cos^4(\Theta) + Acos^2(\Theta)sin^2(\Theta) + C_{11}sin^4(\Theta)\,]} \quad 14(d)$$

$$\text{where, } A = \frac{(C_{11}C_{22} - C_{12}^2)}{C_{66}} - 2C_{11} \text{ and } B = C_{11} + C_{22} - \frac{(C_{11}C_{22} - C_{12}^2)}{C_{66}}. \quad 14(e)$$

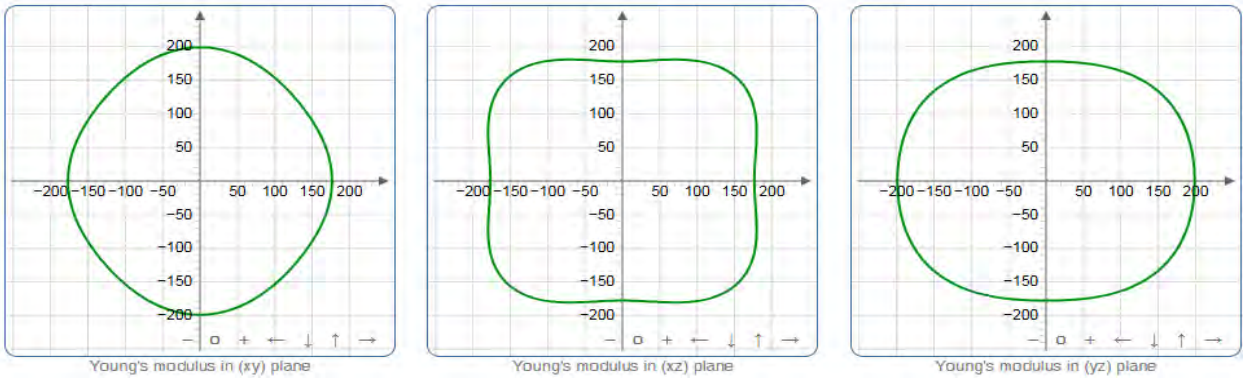

Figure 6: Polar plots of the variation of Young's modulus of Sr_2MgWO_6.

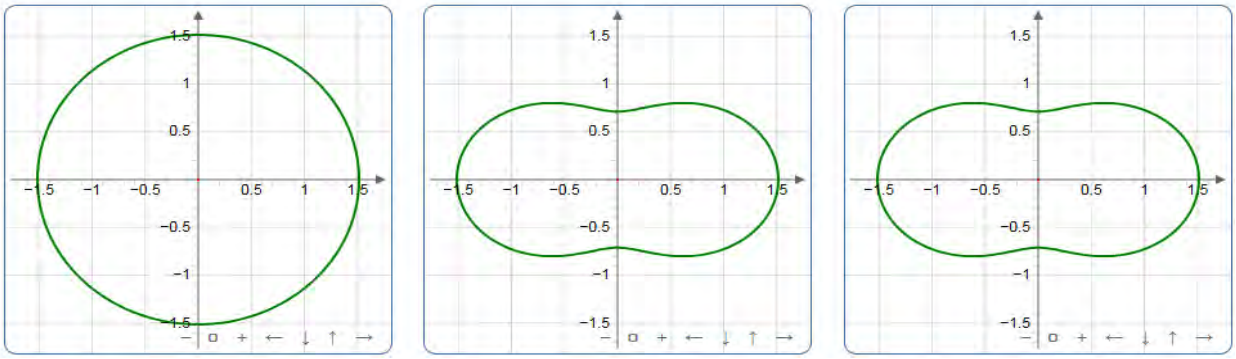

xy plane xz plane yz plane

Figure 7. Polar plots of the variation of bulk modulus of Sr_2MgWO_6.

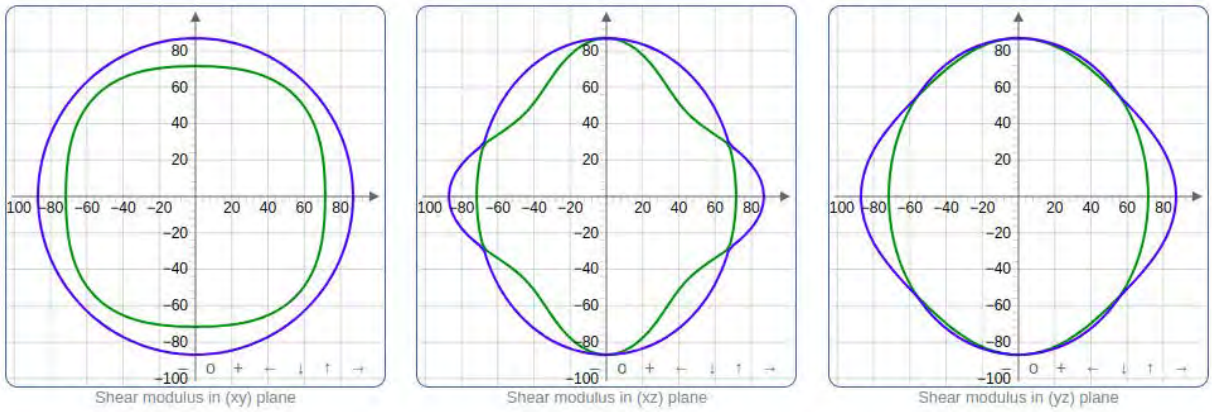

Figure 8. Polar plots of the variation of the shear modulus of Sr_2MgWO_6.

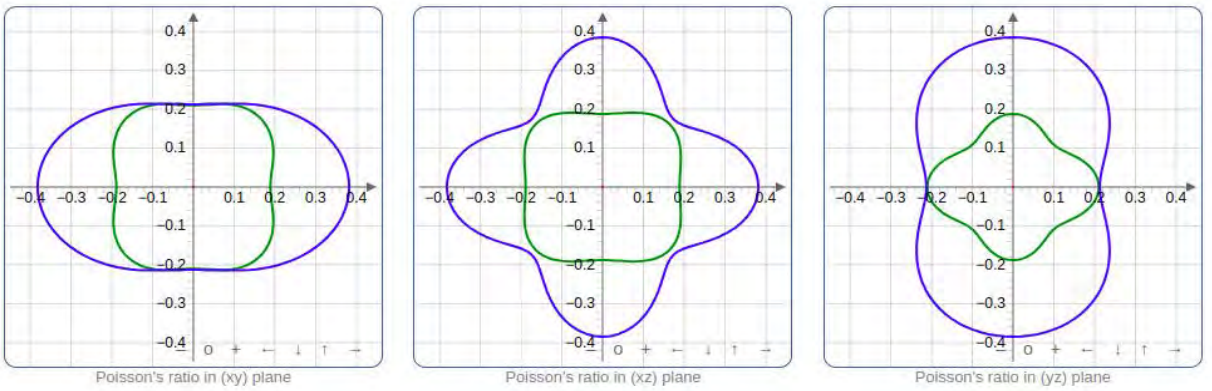

Figure 9. Polar plots of the variation of Poisson's ratio of Sr_2MgWO_6.

Figures 6, 7, 8, and 9 present polar plots illustrating the variation of E, B, G, and Poisson's ratio for Sr_2MgWO_6. These plots reveal a strong directional dependence of the elastic moduli, indicating that their values vary with specific crystallographic orientations within the material. The nearly circular plot of Young's modulus in the xy plane suggests an almost isotropic response, indicating the material offers uniform resistance to deformation in all directions within this plane. However, the elliptical plots in the xz and yz planes reflect anisotropic behavior. This anisotropic behavior shows that Young's modulus changes with the orientation of the applied stress in these planes [Figure 6]. The circular plot of bulk modulus in the xy plane indicates an almost isotropic volumetric response, suggesting that the material exhibits uniform resistance to compression in all directions within this plane. In contrast, the elliptical shapes observed in the xz and yz planes reflect anisotropic compressibility, showing that the bulk modulus varies with the direction of applied stress [Figure 7]. The shear modulus polar plot in the xy plane exhibits a nearly circular shape, indicating isotropic shear behavior within this plane. This reflects a uniform resistance to shear deformation in all directions of the xy plane. In contrast, the elliptical contours observed in the xz and yz planes reveal anisotropic shear behavior [Figure 8], with the resistance to shear deformation varying with direction. Figure 9 shows the directional variation of Poisson's ratio, with non-circular contour shapes indicating that the material is not perfectly isotropic. Overall, these findings reveal that the mechanical properties of Sr_2MgWO_6 are highly sensitive to crystallographic direction.

Debye Temperature

The Debye temperature (θ_D) is a key temperature that represents the vibrational characteristics of a solid. Above the θ_D all vibrational modes are active; below which quantum effects play a significant role. The expression of Debye temperature is established from acoustic velocities and elastic constant data (Anderson, 1963; Pokharel *et al.*, 2024b). The equation below accurately estimates the θ_D value based on the average sound velocity (v_m).

$$\theta_D = \frac{h}{K_B}\left[\frac{3n}{4\pi}\left(\frac{N_A.\rho}{M}\right)\right]^{\frac{1}{3}} v_m \qquad (15)$$

Where h is Planck's constant, K_B is Boltzmann's constant, n is the number of atoms in each formula unit, N_A is Avogadro's number, M is the molecular weight, ρ is density, and v_m is the average sound velocity. The average sound velocity is given by (Wu *et al.*, 2020)

$$v_m = \left[\frac{1}{3}\left(\frac{2}{v_t^3} + \frac{1}{v_l^3}\right)\right]^{\frac{-1}{3}} \qquad (16)$$

Here, v_l and v_t represent the velocities of longitudinal and transverse elastic waves, respectively, and can be obtained from Navier's equation (Bao *et al.*, 2019)

$$v_l = \left[\frac{3B+4G}{3\rho}\right]^{\frac{1}{2}}, \text{ and } v_t = \left[\frac{G}{\rho}\right]^{\frac{1}{2}} \qquad (17)$$

The longitudinal velocity v_l, transverse velocity v_t, and average sound velocity v_m are determined to be 6145.95 m s^{-1}, 3466.32 ms^{-1}, and 3844.87 ms^{-1}, respectively.

The longitudinal velocity is significantly greater than the transverse velocity, which highlights the material's inherent anisotropy in wave propagation between compressive and shear modes. The Debye temperature θ_D is 492.34 K. Overall, the high sound velocities and Debye temperature indicate that the material exhibits excellent mechanical strength, thermal resistance, and potentially high thermal conductivity, making it a promising candidate for applications in high-performance electronics and thermal management technologies.

Thermodynamic Properties

The thermodynamic properties, including the specific heat capacity (C_V), were calculated using the quasiharmonic Debye model (Blanco *et al.*, 2004) across a temperature range of 0 - 800 K. These computations were performed based on the equation of state-derived from the quasiharmonic approximation of the Debye model. The specific heat capacity is given by the following expression:

$$C_V = 3nK[4\mathrm{D}(\theta/\mathrm{T})\left(\frac{\theta_D}{T}\right) - \frac{\frac{3\theta_D}{T}}{e^{\frac{\theta_D}{T}}-1}] \qquad (18)$$

Where n represents the number of atoms per formula unit, K is Boltzmann constant, θ_D the Debye temperature, and D(θ/T) is the Debye integral and is defined as

$$\mathrm{D}(\theta/\mathrm{T}) = \frac{3}{\left(\frac{\theta}{T}\right)^3}\int_0^{\theta/\mathrm{T}} \frac{x^3}{e^x-1}\,dx \qquad (19)$$

Figure 10 presents the variation of specific heat (C_V), as a function of temperature (0–800 K) at constant volume for Sr_2MgWO_6 perovskite. The specific heat at constant volume represents the material's ability to store thermal energy via vibrational modes in the crystal lattice. At low temperatures (< 300 K), C_V increases rapidly with temperature. The gradual increase in vibrational modes is responsible for this behavior, as thermal energy becomes sufficient to excite lower-frequency phonons. At higher temperatures (> 300 K), C_V approaches a plateau near the Dulong-Petit limit. The specific heat C_V from equation 15 is found to be 373.42 J/(mol·K).

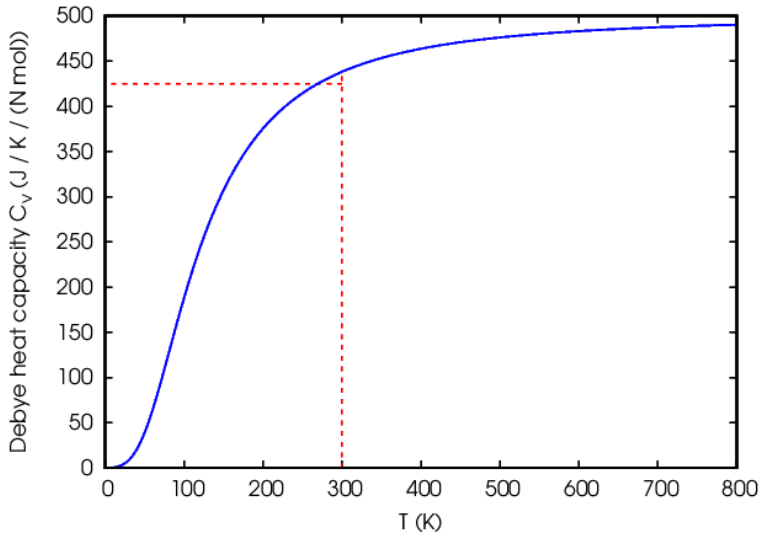

Figure 10. Variation of specific heat capacity of Sr_2MgWO_6 double perovskite with temperature.

CONCLUSIONS

This study demonstrates that the double perovskite Sr_2MgWO_6 possesses significant elastic, thermal, and optical anisotropy. This material exhibits strong resistance to uniaxial compression, particularly along the [001] direction, indicating strong atomic bonding along this axis. The rise in bulk, shear, and Young's moduli indicates enhanced mechanical stability of the material. However, the high G/B ratio, negative Cauchy constant, and low Poisson's ratio indicate that Sr_2MgWO_6 remains brittle under compression, characterized by strong covalent bonding.

Thermal conductivity of the material is direction-dependent, reflecting anisotropic phonon transport. The minimum thermal conductivity ($k_{\min}$) varies with pressure and crystallographic direction, following the order [001] > [110] > [100], suggesting more efficient acoustic transport along [001] and increased phonon scattering along [110] and [100]. The high Debye temperature (θ_D) = 492.34 K) supports the material's strong interatomic forces and thermal stability. Additionally, the specific heat capacity (C_V) increases rapidly below 300 K due to low-frequency phonon excitation and saturates at higher temperatures, reaching a value of 373.42 J/mol·K. These findings highlight Sr_2MgWO_6 as a mechanically stable, thermally resistant, and directionally anisotropic material, making it a promising candidate for applications in thermal management and high-performance electronic devices.

ACKNOWLEDGEMENTS

The authors are grateful to the Department of Physics, Mahendra Morang Adarsh Multiple Campus, Tribhuvan University, Biratnagar, Nepal, for providing computational facilities.

AUTHOR CONTRIBUTIONS

Conceptualization: PP; Investigation: KKB, DNC; Methodology: PP, SKY; Data curation: DA; Data analysis: NP, DA; Writing - original draft: PP, SKY; Writing - review and editing: DA, NP, SKY.

CONFLICT OF INTEREST

The authors declare that they have no known competing financial interests or personal relationships that could have appeared to influence the work reported in this paper.

DATA AVAILABILITY STATEMENT

The data of the present work will be made available by the corresponding authors upon request.

REFERENCES

Anderson, O. L. (1963). A simplified method for calculating the Debye temperature from elastic constants. *Journal of Physics and Chemistry of Solids*, *24*(7), 909–917. https://doi.org/10.1016/0022-3697(63)90067-2.

Aziz, A., Aldaghfag, S. A., Zahid, M., Iqbal, J., Yaseen, M., & Somaily, H. H. (2022). Theoretical investigation of X_2NaIO_6 (X= Pb, Sr) double perovskites for thermoelectric and optoelectronic applications. *Physica B: Condensed Matter*, *630*, 413694. https://doi.org/10.1016/j.physb.2022.413694.

Bao, L., Kong, Z., Qu, D., & Duan, Y. (2020). Revealing the elastic properties and anisotropies of Mg_2X (X = Si, Ge and Sn) with different structures from a first-principles calculation. *Materials Today Communications*, *24*, 101337. https://doi.org/10.1016/j.mtcomm.2020.101337.

Bao, W., Liu, D., Li, P., & Duan, Y. (2019). Structural properties, elastic anisotropies and thermal conductivities of tetragonal LnB_2C_2 (Ln = Rare Earth) compounds from first-principles calculations. *Ceramics International*, *45*(2), 1857–1867. https://doi.org/10.1016/j.ceramint.2018.10.077.

Blanco, M. A., Francisco, E., & Luaña, V. (2004). GIBBS: Isothermal-isobaric thermodynamics of solids from energy curves using a quasi-harmonic Debye model. *Computer Physics Communications*, *158(1)*, 57–72. https://doi.org/10.1016/j.comphy.2003.12.001.

Dar, S. A., Sharma, R., Srivastava, V., & Sakalle, U. K. (2019). Investigation on the electronic structure, optical, elastic, mechanical, thermodynamic and thermoelectric properties of wide band gap semiconductor double perovskite Ba_2InTaO_6. *RSC Advances*, *9*(17), 9522–9532. https://doi.org/10.1039/C9RA00313D.

Dar, S. A., Srivastava, V., & Sakalle, U. K. (2019). Structural, elastic, mechanical, electronic, magnetic, thermoelectric and thermodynamic investigation of half-metallic double perovskite oxide Sr_2MnTaO_6. *Journal of Magnetism and Magnetic Materials*, *484*, 298–306. https://doi.org/10.1016/j.jmmm.2019.04.048.

Giannozzi, P., Baroni, S., Bonini, N., Calandra, M., Car, R., Cavazzoni, C., Ceresoli, D., Chiarotti, G. L., Cococcioni, M., Dabo, I., Dal Corso, A., de Gironcoli, S., Fabris, S., Fratesi, G., Gebauer, R., Gerstmann, U., Gougoussis, C., Kokalj, A., Lazzeri, M., Wentzcovitch, R. M. (2009). QUANTUM ESPRESSO: A modular and open-

source software project for quantum simulations of materials. *Journal of Physics: Condensed Matter*, *21(*39*),* 395502. https://doi.org/10.1088/0953-8984/21/39/395502.

Golesorkhtabar, R., Pavone, P., Spitaler, J., Puschnig, P., & Draxl, C. (2013). Elastic: A tool for calculating second-order elastic constants from first principles. *Computer Physics Communications*, *184*(8), 1861–1873. https://doi.org/10.1016/j.cpc.2013.03.010.

Hill, R. (1952). The Elastic Behaviour of a Crystalline Aggregate. *Proceedings of the Physical Society. Section A*, *65*(5), 349–354. https://doi.org/10.1088/0370-1298/65/5/307.

Nye, J. F. (1985). *Physical properties of crystals: Their representation by tensors and matrices*. Oxford university press.

Koch, W., & Holthausen, M. C. (2015). *A chemist's guide to density functional theory*. John Wiley & Sons.

Lucarini, V., Peiponen, K. E., Saarinen, J. J., & Vartiainen, E. M. (2005). Kramers-Kronig relations in optical materials research. Berlin, Heidelberg: Springer Berlin Heidelberg.

Langreth, D. C., & Perdew, J. P. (1980). Theory of nonuniform electronic systems. I. Analysis of the gradient approximation and a generalization that works. *Physical Review B*, *21*(12), 5469–5493. https://doi.org/10.1103/PhysRevB.21.5469.

Lu, L., Pan, X., Luo, J., & Sun, Z. (2020). Recent Advances and Optoelectronic Applications of Lead-Free Halide Double Perovskites. *Chemistry – A European Journal*, *26*(71), 16975–16984. https://doi.org/10.1002/chem.202000788.

Lu, Y., Duan, Y., Peng, M., Yi, J., & Li, C. (2021). First-principles calculations of electronic, optical, phononic and thermodynamic properties of C40-type $TMSi_2$ (TM = Cr, Mo, W) disilicides. *Vacuum*, *191*, 110324. https://doi.org/10.1016/j.vacuum.2021.110324.

Manzoor, M., Bahera, D., Sharma, R., Tufail, F., Iqbal, M. W., & Mukherjee, S. K. (2022). Investigated the structural, optoelectronic, mechanical, and thermoelectric properties of Sr_2BTaO_6 (B = Sb, Bi) for solar cell applications. *International Journal of Energy Research*, *46*(15), 23698–23714. https://doi.org/10.1002/er.8669.

Meng, Y., Li, X., Wang, S., Lau, C., Hu, H., Ke, Y., Tan, G., Yang, J., & Long, Y. (2022). Flexible smart photovoltaic foil for energy generation and conservation in buildings. *Nano Energy*, *91*, 106632. https://doi.org/10.1016/j.nanoen.2021.106632.

Miao, N., Sa, B., Zhou, J., & Sun, Z. (2011). Theoretical investigation on the transition-metal borides with Ta_3B_4-type structure: A class of hard and refractory materials. *Computational Materials Science*, *50*(4), 1559–1566. https://doi.org/10.1016/j.commatsci.2010.12.015.

Pack, J. D., & Monkhorst, H. J. (1977). Special points for Brillouin-zone integrations—a reply. *Physical Review B*, *16*(4), 1748–1749. https://doi.org/10.1103/PhysRevB.16.1748.

Parr, R. G., & Yang, W. (1989). *Density functional theory of atoms and molecules* (2nd ed.). Oxford University Press.

Patwe, S. J., Achary, S. N., Mathews, M. D., & Tyagi, A. K. (2005). Synthesis, phase transition and thermal expansion studies on M_2MgWO_6 ($M=Ba^{2+}$ and Sr^{2+}) double perovskites. *Journal of Alloys and Compounds*, *390*(1–2), 100–105. https://doi.org/10.1016/j.jallcom.2004.05.093.

Perdew, J. P., Burke, K., & Ernzerhof, M. (1996). Generalized Gradient Approximation Made Simple. *Physical Review Letters*, *77*(18), 3865–3868. https://doi.org/10.1103/PhysRevLett.77.3865.

Pokharel, P., Yadav, S. K., Pantha, N., & Adhikari, D. (2024a). First-Principles Investigations of Structural, Electronic, and Elastic Properties of $ZrSiO_3$ Perovskite: Layer Dependence, Surface Termination, and Pressure Effects. *Physica Status Solidi (b)*, *261*(8) 2400156. https://doi.org/10.1002/pssb.202400156.

Pokharel, P., Yadav, S. K., Pantha, N., & Adhikari, D. (2024b). Strain-dependent electronic, mechanical and piezoelectric properties of $ZrSiO_3$ 2D monolayer: A first principles approach. *Journal of Physics and Chemistry of Solids*, *193*, 112198. https://doi.org/10.1016/j.jpcs.2024.112198.

Pokharel, P., Yadav, S. K., Pantha, N., Sharma, B., & Adhikari, D. (2024). Structural, electronic, optical, magnetic, and mechanical properties of $SmMnO_3$ perovskite with europium and yttrium doping: A first-principles study. *AIP Advances*, *14*(12), 125309 https://doi.org/10.1063/5.0232439.

Pokharel, P., Yadav, S. K., Pantha, N., Sharma, B., & Adhikari, D. (2025). Elastic Anisotropy and Thermal Properties of Sr_2ZrMoO_6 Double Perovskite under Different Pressures. *Physica Status Solidi (b)*, 262(5), 2400625. https://doi.org/10.1002/pssb.202400625.

Rahman, Md. A., Hasan, W., Hasan, Md. Z., Irfan, A., Mouna, S. C., Rukaia khatun, Razzaque Sarker, Md. A., Rahaman, Md. Z., & Rahman, M. (2023). Structural, mechanical, electronic, optical and thermodynamic features of lead-free oxide perovskites $AMnO_3$ (A=Ca, Sr, Ba): DFT simulation based comparative study. *Physica B:*

Condensed Matter, *668*, 415215. https://doi.org/10.1016/j.physb.2023.415215.

Ranganathan, S. I., & Ostoja-Starzewski, M. (2008). Universal Elastic Anisotropy Index. *Physical Review Letters*, *101*(5), 055504. https://doi.org/10.1103/PhysRevLett.101.055504.

Ray, R. B., Kaphle, G. C., Rai, R. K., Yadav, D. K., Paudel, R., & Paudyal, D. (2021). Strain induced electronic structure, and magnetic and structural properties in quaternary Heusler alloys ZrRhTiZ (Z = Al, In). *Journal of Alloys and Compounds*, *867*, 158906. https://doi.org/10.1016/j.jallcom.2021.158906.

Reuss, A. (1929). Berechnung der Fließgrenze von Mischkristallen auf Grund der Plastizitätsbedingung für Einkristalle . *ZAMM - Journal of Applied Mathematics and Mechanics / Zeitschrift Für Angewandte Mathematik Und Mechanik*, *9*(1), 49–58. https://doi.org/10.1002/zamm.19290090104.

Tang, Q., & Zhu, X. (2022). Half-metallic double perovskite oxides: recent developments and future perspectives. *Journal of Materials Chemistry C*, *10*(41), 15301–15338. https://doi.org/10.1039/D2TC03199J

Thompson, R. P., & Clegg, W. J. (2018). Predicting whether a material is ductile or brittle. *Current Opinion in Solid State and Materials Science*, *22*(3), 100–108. https://doi.org/10.1016/j.cossms.2018.04.001

Tidrow, S. C. (2014). Mapping Comparison of Goldschmidt's Tolerance Factor with Perovskite Structural Conditions. *Ferroelectrics*, *470*(1), 13–27. https://doi.org/10.1080/00150193.2014.922372.

Vanderbilt, D. (1990). Soft self-consistent pseudopotentials in a generalized eigenvalue formalism. *Physical Review B*, *41*(11), 7892–7895. https://doi.org/10.1103/PhysRevB.41.7892.

Wang, Y., Lv, Z., Zhou, L., Chen, X., Chen, J., Zhou, Y., Roy, V. A. L., & Han, S.-T. (2018). Emerging perovskite materials for high density data storage and artificial synapses. *Journal of Materials Chemistry C*, *6*(7), 1600–1617. https://doi.org/10.1039/C7TC05326F.

Wu, Y., Bao, L., Wang, X., Wang, Y., Peng, M., & Duan, Y. (2020). Insight into structural, electronic, elastic and thermal properties of A15-type Nb_3X (X = Si, Ge, Sn and Pb) compounds. *Materials Today Communications*, *25*, 101410. https://doi.org/10.1016/j.mtcomm.2020.101410.

Wu, Y., Wang, X., Wang, Y., Duan, Y., & Peng, M. (2021). Insights into electronic and optical properties of $AGdS_2$ (A = Li, Na, K, Rb and Cs) ternary gadolinium sulfides. *Optical Materials*, *114*, 110963. https://doi.org/10.1016/j.optmat.2021.110963.

Voigt, W. (1928). *A determination of the elastic constants for beta-quartz,* Lehrbuch der Kristallphysik. Terubner Leipzig, 40, 2856-2860.

Yang, C., Wu, Y., & Duan, Y. (2022). Theoretical predictions of the electronic, optical and thermodynamic properties of the C40-type $TMSi_2$ (TM = V, Nb and Ta) disilicides. *Materials Today Communications*, *30*, 103115. https://doi.org/10.1016/j.mtcomm.2021.103115.

Zhai, H., Li, X., & Du, J. (2012). First-Principles Calculations on Elasticity and Anisotropy of Tetragonal Tungsten Dinitride under Pressure. *Materials Transactions*, *53*(7), 1247–1251. https://doi.org/10.2320/matertrans.M2011373.

Certificate of Participations

4TH INTERNATIONAL CONFERENCE ON CONDENSED MATTER & APPLIED PHYSICS

ICC2023

Paper ID : K1-0001

Certificate

This is to certify that

Mr. PESHAL POKHAREL

of

Central Department of Physics, Tribhuvan University

has participated in 4th International Conference on Condensed Matter & Applied Physics (ICC 2023) organized by Govt. Engineering College, Bikaner in joint auspices of Condensed Matter Research Society (CMRS) during Oct. 09-10, 2023 and presented a paper entitled

First Principle Study of Effects of Pressure Variation on the Structural and Mechanical Properties of ZrSiO3 Perovskite

Dr. Ravindra Mangal
President,
Condensed Matter Research Society

Dr. Manoj S. Shekhawat
Convener, ICC 2023
Govt. Engineering College, Bikaner

www.iccindia.in

09-10 Oct, 2023

Gandaki University

GANDAKI UNIVERSITY INTERNATIONAL CONFERENCE, 2023 (GUIC-2023)

Mainstreaming Innovation and Research in Academia

CERTIFICATE

OF PARTICIPATION

This certificate is given to Mr. Peshal Pokharel, Tribhuvan University for his oral presentation entitled "Electronic structure elasticity, Debye temperature and ferromagnetism of SmMnO3 perovskite from the First principle calculation" at the Gandaki University International Conference, 2023 organized by Gandaki University, Nepal on June 13-15, 2023.

Prof. Naba Raj Devkota, PhD
Vice-Chancellor
Gandaki University
Pokhara, Nepal

Prof. Ganesh Man Gurung, PhD
Chancellor
Gandaki University
Pokhara, Nepal

4th International Conference on Material Science [ICMS-2024]

31st January -2nd February 2024

Certificate of Participation

Certified that Prof./Dr./Mr./Ms. Mr. Peshal Pokharel has participated / presented a paper entitled "Strain Effect on Mechanical and Electronic Properties of $ZrSiO_3$ 2D Monolayer" in the Fourth International Conference on Material Science (ICMS-2024) organized by Department of Physics, Tripura University (A Central University) during 31st January-2nd February, 2024.

(Prof. Debajyoti Bhattacharjee)
Chairman
ICMS-2024

(Prof. Syed Arshad Hussain)
Convener
ICMS-2024

St. Xavier's College

Maitighar, Kathmandu, Nepal

Department of Physics

This e-certificate of appreciation is awarded to **Mr Upendra Mehta** of Mahendra Morang Adarsh Multiple Campus, Biratnagar for oral presentation on the title

Thermodynamics surface and viscous properties of Cu-Fe-Ti liquid ternary alloys in the

"International Conference on Material Science and Characterization Technology (ICMSCT)"

held on **September 26-28, 2021**

Mr. Drabindra Pandit
Head,
Department of Physics

Fr. Dr. Augustine Thomas, S.J.
Principal
St. Xavier's College

Prof. Dr. Bhim Prasad Subedi
Chairperson, University Grants Commission Nepal

SSMSCP-2023 (June 8-12, 2023)

Certificate of Participation

Birendra Multiple Campus

IEEE ELECTRON DEVICES SOCIETY

Dr./Mr./Ms Peshal Pokharel, CDP, TU

has participated and presented oral/poster paper entitled Layer-Dependent Structural and Electronic Properties of 2D $ZrSi_2O_2$ Perovskite

on **Summer School on Materials Science and Computational Physics-2023 (SSMSCP-2023),** held from **June 8-12, 2023** organized by **IEEE EDS Nepal Chapter** and **Central Department of Physics, TU** in support with Lumbini Engineering, Management and Science College (LEMSC), PU and Birendra Multiple Campus, Bharatpur, TU.

Prof. Dr. Binod P. Dhakal	Prof. Dr. O. P. Niraula	Prof. Dr. B. R. Sharel	Dr. G. C. Kaphle
(Vice-Chancellor)	(Head)	(President)	(Secretary)
Lumbini Technological University	CDP, Tribhuvan University	IEEE EDS Nepal Chapter	SSMSCP-2023

Workshop on Emerging Computational Sciences (ECS), Goa - 2024

This certificate is awarded to MR. PESHAL POKHAREL OF TRIBHUVAN UNIVERSITY, NEPAL in recognition of his/her active participation in the workshop held from May 20 to May 25, 2024. His/her enthusiasm, dedication, and contribution were instrumental to the workshop's success, and we are delighted to acknowledge his/her involvement.

Dr. Mantu Santra	Dr. Santosh K Das	Dr. Sudipta Kanungo
Organizer	Organizer	Organizer

Certificate of Acknowledgement

Association of Nepali Physicists in America

ANPA

is presented to

Peshal Pokharel

for presenting research titled

First-principles study of Structural, Electronic and Elastic Properties of ZrSiO3 Slab Model

during ANPA Conference, July 14-16, 2023.

Raju Timsina, PhD Conference Co-Chair	08/06/2023 Date	Indra Dev Sahu, PhD Conference Chair

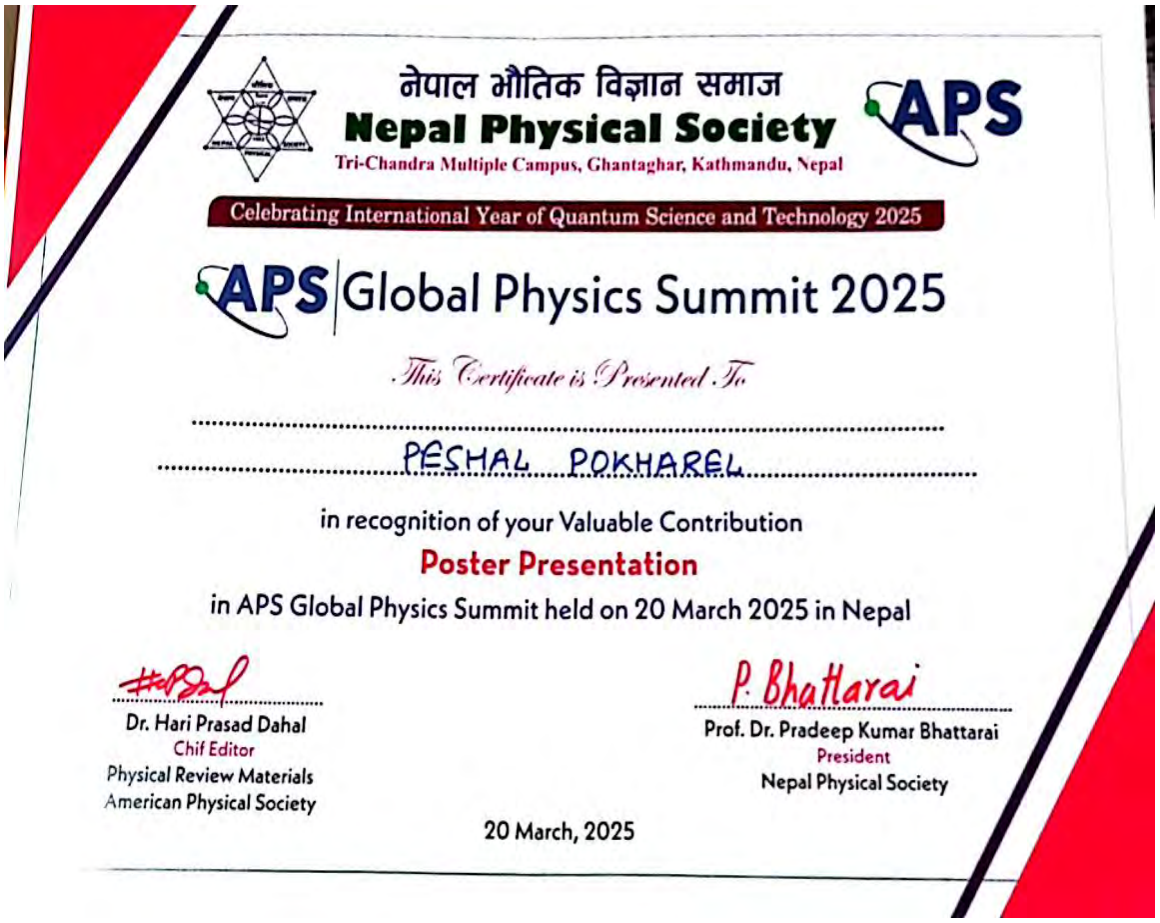

नेपाल भौतिक विज्ञान समाज

Nepal Physical Society

Tri-Chandra Multiple Campus, Ghantaghar, Kathmandu, Nepal

APS

Celebrating International Year of Quantum Science and Technology 2025

APS Global Physics Summit 2025

This Certificate is Presented To

PESHAL POKHAREL

in recognition of your Valuable Contribution

Poster Presentation

in APS Global Physics Summit held on 20 March 2025 in Nepal

Dr. Hari Prasad Dahal
Chif Editor
Physical Review Materials
American Physical Society

P. Bhattarai
Prof. Dr. Pradeep Kumar Bhattarai
President
Nepal Physical Society

20 March, 2025

Certificate of Attendance

APS March Meeting 2024 3/3/2024 - 3/8/2024

This is to certify that

Peshal Pokharel

attended the American Physical Society's
APS March Meeting 2024.

Ligette Rogers
APS Meetings Department

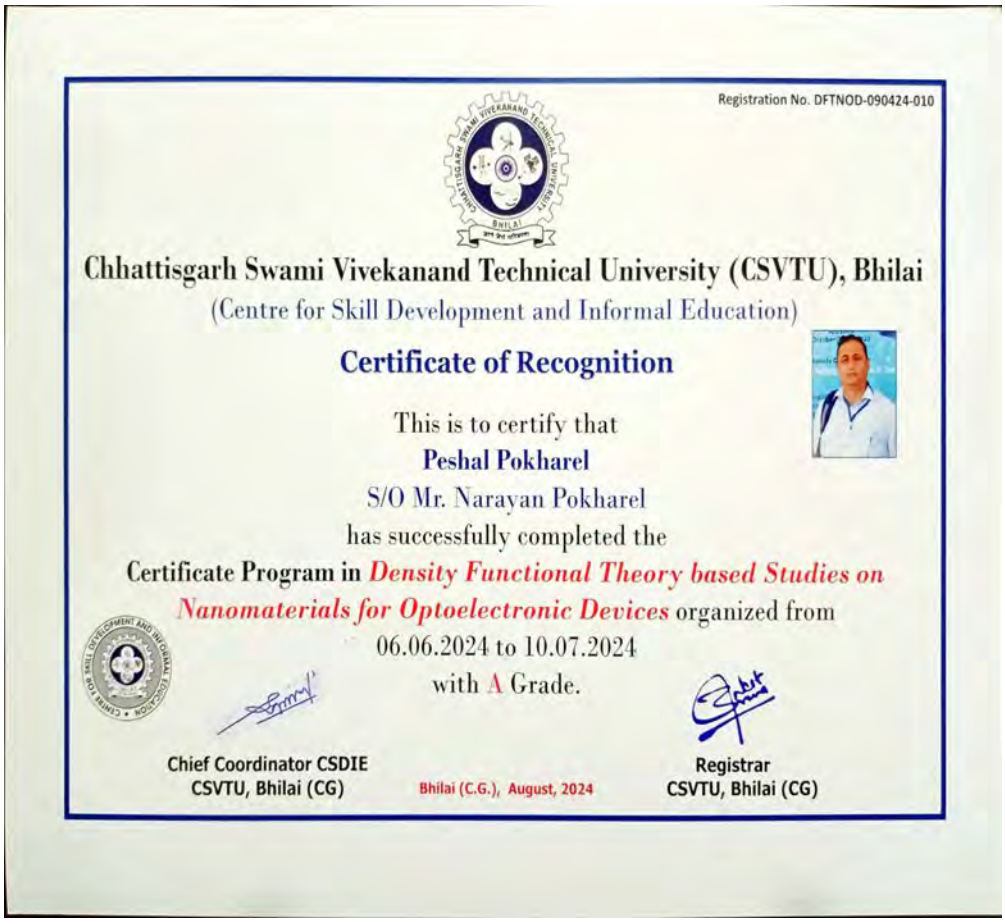

Registration No. DFTNOD-090424-010

Chhattisgarh Swami Vivekanand Technical University (CSVTU), Bhilai

(Centre for Skill Development and Informal Education)

Certificate of Recognition

This is to certify that

Peshal Pokharel

S/O Mr. Narayan Pokharel

has successfully completed the

Certificate Program in *Density Functional Theory based Studies on Nanomaterials for Optoelectronic Devices* organized from 06.06.2024 to 10.07.2024 with A Grade.

Chief Coordinator CSDIE
CSVTU, Bhilai (CG)

Bhilai (C.G.), August, 2024

Registrar
CSVTU, Bhilai (CG)

REGIONAL CONFERENCE
ON
SCIENCE AND TECH

Certificate of Participation

It is to certify that

Peshal Pokharel

Central Campus of Technology, TU, Dharan

presented a research paper in the RCST2024, held on May 7-8, 2024 Organized by the Central Campus of Technology (CCT), Institute of Science and Technology (IOST), Tribhuvan University (TU), Dharan, Nepal.

2024

Dr. Lalit K. Rai
Coordinator
RCST2024

Dr. Dil K. Limbu
Campus Chief
CCT, Dharan

Prof. Dr. Binil Aryal
Dean
IOST, TU

REFRESHER COURSE ON MATERIAL SCIENCE

Certificate of Participation

This certificate is awarded to Prof. Dr. / Dr. / Mr. /Ms. Peshal Pokharel for participating in the five days program from September 15th - 19th, 2021 on **"Refresher Course on Material Science"** organized by Central Department of Physics, Tribhuvan University. This program is supported by University Grants Commission, Nepal and Advanced Materials Research Laboratory of the Central Department of Physics.

Dr. Madhav Prasad Ghimire
Convener
Central Department of Physics
Tribhuvan University

Prof. Dr. Om Prakash Niraula
Head
Central Department of Physics
Tribhuvan University

(Patron)
Prof. Dr. Binil Aryal
Dean
Institute of Science & Technology
Tribhuvan University

(Chief Guest)
Prof. Dr. Shiva Lal Bhusal
Rector
Tribhuvan University

This is to Certify that

MR. PESHAL POKHAREL

has Successfully Completed

Workshop on Density Functional Theory

(Series-I)

February 18 - 21, 2023

Organized by

Mahendra Morang Adarsh Multiple Campus, Tribhuvan University, Biratnagar

Co-Organized by

Department of Physics
M.M.A.M.C., T.U., Biratnagar

Nepal Physical Society
Province-1

Research Management Cell (RMC)
M.M.A.M.C., T.U., Biratnagar

Dr. Rajendra Pd. Adhikari
Facilitator
Kathmandu University, Dhulikhel, Nepal

Prof. Dr. Devendra Adhikari
President
RMC, MMAMC, T.U., Biratnagar, Nepal

Dr. Baburam Timilsina
Campus Chief
MMAMC, T.U., Biratnagar, Nepal